LONG-TERM FATE OF ZINC IN CONTAMINATED SOILS: ZINC SPECIATION BY SYNCHROTRON SPECTROSCOPY AND CHEMICAL EXTRACTIONS

by Olivier Jacquat

Diss. ETH ZURICH NO. 17992, 2008

DISS. ETH NO. 17992

LONG-TERM FATE OF ZINC IN CONTAMINATED SOILS: ZINC SPECIATION BY SYNCHROTRON SPECTROSCOPY AND CHEMICAL EXTRACTIONS

A dissertation submitted to the

SWISS FEDERAL INSTITUTE OF TECHNOLOGY ZURICH

for the degree of

DOCTOR OF SCIENCES

presented by

OLIVIER JACQUAT

Dipl. Sciences de la Terre, University of Neuchâtel
born August 16, 1979
citizen of Fontenais, Jura

accepted on the recommendation of

Prof. Dr. Ruben Kretzschmar, ETH Zurich, examiner
Dr. Andreas Voegelin, ETH Zurich, co-examiner
Dr. Farid Juillot, Université Paris 7, co-examiner
Prof. Dr. Evert Elzinga, Rutgers University, co-examiner

2008

Cover layout: www.marie-veya.ch

Printed in Spring 2009, Zurich

Table of content

Abstract

Contamination of soils with heavy metals is widespread and still increasing due to anthropogenic activities. Among the heavy metals, zinc (Zn) is one of the most extensively used. High Zn concentrations in soils can pose a long-term risk to ecosystems and human health, e.g., by affecting soil fertility or causing groundwater contamination. In order to develop accurate risk assessments and effective remediation strategies, knowledge of the mechanisms that control Zn behavior in soils is required. Recent laboratory and field studies using extended X-ray absorption fine structure (EXAFS) spectroscopy reported the formation of different Zn-bearing phases with a high immobilization potential for Zn, such as Zn-layered double hydroxide (Zn-LDH) and Zn-phyllosilicates. At present, the abundance and stability of these Zn-bearing phases is unknown due to the limited number of contaminated soils considered. In addition, no information on the relations between soil properties, Zn speciation (i.e., its chemical form), and Zn fractionation are available.

The objectives of this work were (i) to establish the link between soil physical and chemical properties and the dominant Zn species forming, (ii) to relate the molecular-level speciation to the fractionation of Zn in contaminated soils, and (iii) to assess the speciation and reactivity of Zn due to changing soil chemical conditions during weathering in naturally Zn-rich soils. The speciation of Zn was determined using bulk and micro-focused (μ-) EXAFS spectroscopy and the fractionation of Zn was investigated by single and sequential extractions.

Forty-nine soils were sampled close to foundations of galvanized electricity towers across different geologic and climatic regions in Switzerland. The soils covered a wide range in soil pH (4.1 to 7.7), organic carbon content (9 to 102 g/kg), and clay content (38 to 451 g/kg). Input of aqueous Zn with runoff waters from electricity towers during 17 to 74 years resulted in total Zn contents of 251 up to 30090 mg/kg. Thirty of 49 soils studied are considered to be strongly contaminated as their Zn content is above the Swiss remediation limit of 2000 mg/kg. Based on bulk EXAFS and μ-EXAFS spectra, the number, type and proportion of Zn species occurring in contaminated soils were derived using principal component analysis, target testing, and linear combination fitting. Incorporation of Zn into hydroxy-interlayered minerals (Zn-HIM) or formation of Zn-precipitates such as Zn-LDH, Zn-phyllosilicates and hydrozincite were identified

as important mechanisms for Zn retention. The occurrence of these Zn bearing phases was strongly related to soil pH, potential cation exchange capacity (PCEC, calculated from clay and organic carbon content), and total Zn content. The good agreement between sequential extraction data and Zn speciation confirmed that soil pH and Zn loading (i.e., ratio of total Zn content in charge equivalent over PCEC) are dominant factors controlling Zn fractionation and demonstrated that Zn fractionation depends on Zn speciation.

Formation of Zn-HIM was relevant in acidic to neutral soils with moderate contamination levels (<2000 mg/kg). In these soils, Zn-HIM accounted for 29-84% of total Zn. EXAFS data suggested that soil HIM are loaded with Zn close to their sorption maximum and single and sequential extractions demonstrated the refractory nature of Zn-HIM in soils. Analysis of the bonding environment of Zn in synthetic HIM showed that the coordination of Zn changes with Zn content and that the sorption capacity of HIM for Zn is limited. Consequently, HIM may substantially contribute to Zn sequestration in soils with less than about 2000 mg/kg Zn but do not allow to retain large amount of Zn in response to continuous Zn inputs.

In contrast to Zn-HIM, Zn precipitates have been detected primarily in strongly contaminated soils (>2000 mg/kg). With soil pH and Zn loading, the amount of Zn precipitates formed gradually increased from 12 to 89% of total Zn, and dominated over adsorbed/complexed Zn species. In parallel, Zn precipitate speciation shifted from Zn-phyllosilicates over Zn-LDH to hydrozincite. Overall, Zn-LDH was the dominant Zn-precipitate. In sequential extraction experiments, synthetic Zn-phyllosilicate, Zn-LDH, and hydrozincite readily dissolved in comparison to Zn-HIM, suggesting that Zn is only transiently immobilized in Zn precipitates, and that these precipitates likely control the mobility and bioavailability of Zn in soils. Hence, the formation of Zn precipitates allows for the accumulation of large amounts of Zn in excess to soil's capacity of Zn adsorption, but the potential of Zn precipitates for long-term immobilization of Zn in soils is limited.

In soils developed over geologic times (~10000 years) from Zn-rich limestones, soil-formed Zn-HIM and Zn-kaolinite, and geogenic Zn-substituted goethite were detected. In oxic contaminated soils, the formation of these Zn species would therefore likely result in long-term Zn sequestration.

The trends in Zn speciation and reactivity observed for the studied soils are expected to apply also to soils where Zn contamination is caused by Zn in solid form rather than by aqueous Zn. While initially the mobility and bioavailability of Zn is determined by the solid contaminant, its decomposition will eventually cause the release of aqueous Zn into soil.

The results from this study are also relevant for other elements such as nickel (Ni) and cobalt (Co), which partially exhibit similar geochemical behavior as zinc.

Zusammenfassung

Bodenkontamination infolge Schwermetalleintrag ist ein weit verbreitetes Phänomen, welches infolge antropogener Aktivitäten stetig zunimmt. Zink (Zn) ist eines der industriell am meisten genutzten Schwermetalle. Hohe Zn-Konzentrationen in Böden stellen ein hohes Risiko für Mensch und Natur dar, beispielsweise durch die Reduzierung der Bodenfruchtbarkeit oder infolge von Grundwasserkontamination. Um genaue Risikoabschätzungen und effektive Sanierungsstrategien entwickeln zu können, sind Kenntnisse über die Mechanismen und Angaben über die Verbindungen welche das Verhalten von Zn im Boden kontrollieren nötig. Neuere Labor- und Feldstudien zeigten unter Verwendung von Röntgenabsorptionspektroskopie (EXAFS) die Bildung verschiedener Zinkphasen, wie z.B. "Zn-layered double hydroxide" (Zn-LDH) oder Zn-Schichtsilikate. Diese Phasen verfügen über ein potentiell hohes Immobilisierungsvermögen für Zn. Aufgrund der geringen Anzahl bisheriger Untersuchungen ist derzeit jedoch wenig über ihr Auftreten und ihre Stabilität in Böden bekannt. Ferner sind keine Information über das Verhältnis zwischen den Bodeneigenschaften, der Zn-Speziierung (chemische Zn-Form), und Zn-Reaktivität im Boden verfügbar.

Die Ziele dieser Arbeit waren daher (i) den Zusammenhang zwischen physikalischen und chemischen Bodeneigenschaften und dominierenden Zn-Phasen herzustellen, (ii) die molekulare Zn-Speziierung mit der Reaktivität von Zn in kontaminierten Böden zu vergleichen, sowie (iii) Änderungen in der Speziierung und Reaktivität von Zn während der Pedogenese natürlicher Zn-reicher Böden abzuleiten. Zink wurde mittels bulk und mikro (μ-) EXAFS-Spektroskopie in Bodenproben speziiert und quantifiziert. Zusätzlich wurde die Reaktivität von Zn mittels chemischen Extraktionen untersucht.

Entlang eines geologischen und klimatischen Gradienten in der Schweiz wurden 49 Zn-belastete Böden in unmittelbarer Umgebung von Hochspannungsmasten beprobt. Die Böden wiesen ein breites Spektrum im pH-Wert (4.1-7.7), organischen Kohlenstoff- (9-102 g/kg) und Tongehalt (38 to 451 g/kg) auf. Der Eintrag von gelöstem Zn aus den Hochspannungsmasten über einen Zeitraum von 17 bis 74 Jahren resultierte in einem Gesamtzinkgehalt des Bodens zwischen 251 bis 30090 mg/kg. In 30 der insgesamt 49 Böden wurde in der Schweiz gültige Sanierungswert von 2000 mg/kg überschritten, weshalb die Böden als schwer belastet einzustufen sind.

Basierend auf bulk und μ-EXAFS-Spektren wurden Zn-Phasen sowie ihre Anteile am Gesamtzinkgehalt mittels Hauptkomponentenanalyse, "target testing", und linearen Konbinationsfits abgeleitet.

Der Einbau von Zn in die Struktur von Mineralen mit Hydroxo-Zwischenschicht (Zn-HIM) und die Bildung von Zn-Präzipitaten wie Zn-LDH, Zn-Schichtsilikate und Hydrozinkit wurden als wichtige Mechanismen für die Retention von Zn in Böden identifiziert. Das Auftreten dieser Zn-Phasen hing vom pH-Wert, der potentiellen Kationenaustauschkapazität (KAK_{pot}, kalkuliert aus Ton und organischen Kohlenstoff Gehalten), sowie vom Gesamtzinkgehalt ab. Die gute Übereinstimmung zwischen den Ergebnissen der sequentiellen Extraktion und der Zn-Speziierung mittels EXAFS zeigte, dass pH-Wert und Zn-Belastung (Gesamtzinkgehalt in Ladungsäquivalenten normalisiert auf KAK_{pot}) die Reaktivität von Zn im Boden kontrollieren, und diese von der Zn-Speziierung abhängt.

Die Bildung von Zn-HIM ist bedeutend für sauere und neutrale Böden mit mässigem Kontaminationsgrad (<2000 mg/kg). In diesen Böden trug Zn-HIM 29-84% zum Gesamtzinkgehalt bei. EXAFS-Daten zeigten, dass bodenbürtige HIM fast vollständig mit Zn beladen waren. Der refraktäre Charakter von Zn-HIM im Boden wurde mittels chemischen Extraktionen bestätigt. Die Analyse der Bindungsumgebung von Zn in synthetischen HIM ergab, dass sich die Koordination von Zn mit dem Zn-Gehalt ändert, und die Sorptionskapazität von HIM für Zn limitiert ist. Folglich können HIM zu einer signifikanten Retention von Zn in Böden beitragen, welche weniger als ca. 2000 mg/kg Zn enthalten. Kontinuierliche Zn-Einträge, die zu stärkerer Zn-Belastung des Bodens führen, können HIM jedoch nicht abpuffern.

Im Gegensatz zu Zn-HIM wurden Zn-Präzipitate hauptsächlich in stark kontaminierten Böden (>2000 mg/kg) nachgewiesen. Mit steigendem pH-Wert und steigender Zn-Belastung nahm die Menge der gebildeten Zn-Präzipitate graduell von 12 auf 89% des Gesamtzinkgehaltes zu, und übertraf dabei die Menge an adsorbiertem Zn. Gleichzeitig änderte sich die Speziierung der Zn-Präzipitate von Zn-Schichtsilikaten über Zn-LDH zu Hydrozinkit. Insgesamt war Zn-LDH das wichtigste Zn-Präzipitat. Synthetische Zn-Präzipitate (Zn-Schichtsilikate, Zn-LDH, Hydrozinkit) wurden im Vergleich zu Zn-HIM in sequentiellen Extraktionsexperimenten leichter aufgelöst. Dies deutet darauf hin, dass Zn im Boden nur vorübergehend in Zn-Präzipitaten immobilisiert wird, und dass diese Präzipitate die Mobilität und Bioverfügbarkeit von Zn im Boden steuern. Die Bildung von Zn-Präzipitaten kann zur starken Anreicherung von Zn im Boden führen, und dabei dessen Adsorptionskapazität für Zn überschreiten. Aufgrund der geringen geochemischen Stabilität dieser Präzipitate ist jedoch ihr Potential für eine längerfristige Immobilisierung von Zn im Boden beschränkt.

In Böden, die sich über geologische Zeiträume (~10000 Jahre) aus Zn-reichem Kalkstein gebildet haben, wurden pedogener Zn-HIM und Zn-Kaolinit, sowie geogener Zn-Goethit identifiziert. Aufgrund unserer Erkenntnisse könnten diese Phasen in oxischen Zn-kontaminierten Böden zu einer längerfristigen Immobilisierung von Zn beitragen.

Es wird erwartet, dass der beobachtete Zusammenhang zwischen Zn-Speziierung und Reaktivität auch für Böden gilt, in denen die Zn-Kontamination nicht durch Eintrag von gelöstem Zn, sondern durch den Eintrag von Zn-Festphasen erfolgt. Während in solchen Böden die Mobilität und Bioverfügbarkeit von Zn intial von der Festphase bestimmt wird, führt deren Abbau langfristig zu einer Freisetzung von gelöstem Zn.

Die Ergebnisse dieser Studie sind auch auf andere Elemente wie Nickel (Ni) und Cobalt (Co) übertragbar, da diese ein ähnliches geochemisches Verhalten wie Zink aufweisen.

Résumé

La contamination des sols par les métaux lourds est un phénomène répandu et en constante augmentation en raison des activités anthropogènes. Parmi les métaux lourds, le zinc (Zn) est un des plus largement utilisés. Des teneurs élevées en Zn dans les sols peuvent poser un risque à long terme pour l'environnement et l'homme, par exemple en réduisant la fertilité du sol ou en contaminant les eaux souterraines. Afin d'estimer précisément les risques et développer des stratégies d'assainissement, une connaissance des mécanismes qui contrôlent le comportement du Zn dans les sols est nécessaire. Des études récentes réalisées en laboratoire ou sur le terrain et utilisant la spectroscopie d'absorption rayons X (EXAFS) ont montré la formation de différentes phases porteuses ayant un haut potentiel d'immobilisation du Zn, comme les hydroxydes doubles zincifères (Zn-LDH) ou les phyllosilicates zincifères (Zn-phyllosilicate). L'abondance et la stabilité de ces phases zincifères est inconnue car un nombre limité de sols contaminés a été analysée. De plus, il n'existe aucune information sur les relations entre la spéciation du Zn (i.e., formes chimiques du Zn), la réactivité du Zn et les propriétés du sol.

Les objectifs de ce travail étaient (i) d'établir le lien entre les propriétés physiques et chimiques du sol et les phases zincifères dominantes formées, (ii) de mettre en relation la spéciation moléculaire avec la réactivité du Zn dans les sols contaminés, et (iii) de dériver les changements de réactivité possible des phases zincifères durant la pédogenèse dans les sols naturellement riches en zinc. La spéciation du Zn a été déterminée par bulk et micro (μ-) spectroscopie EXAFS et la réactivité du Zn a été exploré par des extractions simples et séquentielles.

Quarante-neuf sols ont été échantillonnés à proximité des fondations de pylônes galvanisés supportant des lignes électriques à travers différentes régions géologiques et climatiques de Suisse. Les sols couvrent un large éventail en potentiel hydrogène (pH 4.1 à 7.7), teneur en carbone organique (9 à 102 g/kg) et teneur en argile (38 à 451 g/kg). L'apport de Zn aqueux avec les eaux d'écoulement des pylônes électriques pendant 17 à 74 ans a conduit à une teneur totale en Zn allant de 251 jusqu'à 30090 mg/kg dans les sols. Trente des quarante-neuf sols étudiés sont considérés comme étant extrêmement contaminés puisque leur teneur en Zn excède la limite suisse d'assainissement fixée à 2000 mg/kg. Sur la base de spectres bulk EXAFS et μ-EXAFS, le nombre, le type et

la proportion des phases zincifères survenant dans les sols contaminés a été dérivée par analyse en composante principale, "target testing", et simulation par combinaison linéaire. L'incorporation du Zn dans les minéraux hydroxy-interstratifiés (Zn-HIM) ou la formation de précipités de Zn comme Zn-LDH, Zn-phyllosilicate et hydrozincite ont été identifiées comme mécanismes importants pour la rétention du Zn. La présence de ces phases zincifères a été reliée au pH du sol, à la capacité potentielle d'échange cationique (CPEC, calculée par la teneur en argile et carbone organique) et à la teneur total en Zn. L'excellente relation entre les résultats d'extraction séquentielle et la spéciation du Zn ont confirmé que le pH du sol et la charge en Zn (i.e., le rapport entre la teneur total en Zn en charge équivalence et la CPEC) sont les principaux facteurs contrôlant la réactivité du Zn et ont démontré que la réactivité du Zn dépend de la spéciation du Zn.

La formation de Zn-HIM a été détectée dans les sols acides et neutres ayant un niveau de contamination modéré (<2000 mg/kg). Dans ces sols, les Zn-HIM renfermaient 29 à 84% de la teneur totale en Zn. Les données EXAFS ont suggéré que les HIM du sol contenaient des teneurs en Zn proche de leur capacité d'absorption maximale et des extractions simples et séquentielles ont démontré la nature réfractaire des Zn-HIM. L'analyse de l'environnement atomique du Zn dans des HIM synthétiques a montré que la coordination du Zn change avec la teneur en Zn et que la capacité d'absorption du Zn par les HIM est limitée. En conséquence, les HIM peuvent substantiellement contribuer à la séquestration du Zn dans les sols contenant moins d'environ 2000 mg/kg, mais ne permettent pas de retenir de grandes quantités de Zn en réponse à un apport continu de Zn.

Contrairement aux Zn-HIM, les précipités de Zn ont été détecté primairement dans les sols extrêmement contaminés (>2000 mg/kg). Avec une augmentation du pH du sol et de la charge en Zn, la quantité de précipités de Zn formés augmenta graduellement de 12 à 89% de la teneur totale en Zn, dominant les phases zincifères adsorbées/complexées. En parallèle, la spéciation des précipités de Zn changea de Zn-phyllosilicate via Zn-LDH à hydrozincite. De manière générale, Zn-LDH fut le précipité de Zn le plus souvent détecté. Des expériences d'extraction séquentielles ont montré que les phases synthétiques de Zn-phyllosilicate, Zn-LDH et hydrozincite se dissolvent facilement en comparaison à Zn-HIM, suggérant que le Zn est seulement immobilisé de manière transitoire dans les précipités de Zn et que ces précipités contrôlent vraisemblablement la mobilité et la biodisponibilité du Zn dans les sols. Ainsi, la formation de précipités de Zn permet l'accumulation de larges quantités de Zn en excès de la capacité d'adsorption du Zn par le sol, mais, à long terme, le potentiel d'immobilisation du Zn par les précipités de Zn est limité dans les sols.

Dans les sols formés depuis plus de 10000 ans sur calcaires riches en Zn, la présence de Zn-HIM et de Zn-kaolinite d'origine pédogénique et de goethite zincifère d'origine géogénique a été identifiée. Dans les sols oxiques contaminés, la formation de ces phases zincifères pourrait donc très probablement résulter en une séquestration du Zn à long terme.

Il est jugé que les relations entre la spéciation et la réactivité du Zn observées pour les sols étudiés sont aussi applicable aux sols où la contamination du Zn est causée par du Zn sous forme solide plutôt que sous forme aqueuse. Bien que la mobilité et la biodisponibilité du Zn soient initialement déterminées par le contaminant solide, la décomposition de celui-ci induit finalement la libération de Zn aqueux dans le sol.

Les résultats de cette étude pourraient, par analogie, être appliqués à d'autres éléments comme le nickel (Ni) ou le cobalt (Co), ceux-ci ayant un comportement géochimique partiellement semblable à celui du zinc (Zn).

1. Introduction

Heavy metals are present in surface and subsurface environments as a result of both, natural and anthropogenic processes. Weathering of rocks and sediments and human activities such as mining, smelting, industrial production, military activities and agriculture continuously release heavy metals into the environment. Some heavy metals, like Co, Cu, and Zn are essential for organisms and may be limiting factors in soil environments. However, at elevated concentrations most heavy metals are toxic. Zinc, which is one of the most extensively used heavy metals, inhibits microbial activity and causes phytotoxicity at high concentrations. This in turn may lead to reduced soil fertility, to decreasing crop yields and, in severe cases, even to soil degradation and erosion [1, 2]. The toxicity of Zn in soils depends not only on its total concentration, but also strongly on its chemical speciation.

Zinc, like other contaminants, interacts with the solid soil components through a variety of sorption processes (i.e., cation exchange, surface complexation, polymerization, surface precipitation) [3-5] leading to the formation of distinct Zn species. These species differ in their chemical form (i.e., local coordination environment) and in their stability (i.e., solubility and desorption kinetics). Most important sorbents for Zn in soils are organic matter, clay minerals, and Al-, Fe-, Mn-(hydr)oxides [1, 2]. In general, the extent of Zn adsorption to soil increases with pH. In acidic soils, non-specific reversible cation exchange reactions significantly contribute to the adsorption of Zn, which competes with other cations for exchange sites. In neutral to alkaline soils, on the other hand, specific adsorption processes becomes more important and may strongly retain Zn due to the occurrence of high-affinity sorption sites. The progressive (co) precipitation and diffusion of specifically adsorbed heavy metals into soil components at elevated pH may lead to a substantial depletion of the pool of readily available heavy metals over time [6, 7].

Determining and quantifying the speciation of Zn in contaminated soils and its variation with time are prerequisites for reliable long-term risk assessments and evaluations of soil remediation strategies. Synchrotron based spectroscopic techniques such as extended X-ray absorption fine structure (EXAFS) spectroscopy provide information on the coordination environment of an atom with the necessary elemental specificity [8, 9] and are thus powerful methods for assessing the molecular level

speciation of heavy metals.

An alternative approach for studying heavy metals in soils is the quantification of the most mobile and bioavailable heavy metal fractions, by using single salt and sequential batch extraction schemes [10-13]. However, due to limited extractant selectivity, element redistribution during extraction and presence of mineral phases not explicitly considered in the extraction schemes, fractionation data cannot unequivocally be interpreted in terms of speciation [14-19]. So far, the relationship between heavy metal reactivity as determined by sequential extraction and heavy metal speciation inferred from EXAFS spectroscopy has not been established on a large number of soils for which both information is available. Such knowledge is required to assess the availability of heavy metals as a function of their chemical speciation. Eventually, this would allow selecting adapted measures for remediation in contaminated areas based solely on rapid and economical laboratory experiments.

Numerous synchrotron-based studies on the sorption of Zn to pure minerals have shown that the formation of Zn-bearing precipitates represent an important sequestration mechanism for Zn in soils and sediments. At slightly acidic to alkaline pH, the sorption of Zn onto Al-containing phases such as kaolinite, pyrophyllite and gibbsite lead to the formation of layered double hydroxides (LDH) and at high Zn concentrations to hydroxides [20-23]. Likewise, laboratory studies using soil material packed into columns and reacted with Zn-containing solutions indicated the formation of Zn-LDH [24, 25]. Sorption studies involving clay mineral-suspensions further show that Zn also forms trioctahedral Zn-bearing phyllosilicates in the presence of dissolved Si [26, 27]. The formation of Zn-LDH as well as Zn-phyllosilicates in soils contaminated from mining or smelting activities and sewage sludge applications has been confirmed [28-35]. In acidic soils, Zn incorporation into the gibbsitic sheets of hydroxy-interlayered clay minerals (Zn-HIM) or the phyllomanganate lithiophorite (Zn-lithiophorite) has been suggested to be an important retention mechanism [36-39]. The common features of all these recently identified Zn species is the incorporation of Zn into the octahedral sheets of layered minerals. The formation of such Zn-bearing mineral phases may lead to a substantial depletion of the readily available Zn in soil. However, this attenuating effect depends on the physical and chemical properties of the specific soil and on the resistance of the newly formed phases against acidification. To date, the knowledge on the type of layered Zn species forming in different types of soils and on their effect on the availability and mobility of Zn in soils is still limited. Furthermore, fundamental understanding of the long-term fate of these layered Zn species is still incomplete.

In this work, the speciation and reactivity of Zn in a wide variety of contaminated soils were investigated using EXAFS spectroscopy and sequential extractions, respectively.

The overall objectives were (i) to establish the link between soil physicochemical properties and the dominant Zn species occurring, (ii) to relate the molecular-level speciation to the fractionantion of Zn in contaminated soils, and (iii) to understand the long-term fate of Zn mineral phases through weathering and pedogenesis in naturally Zn-rich soils.

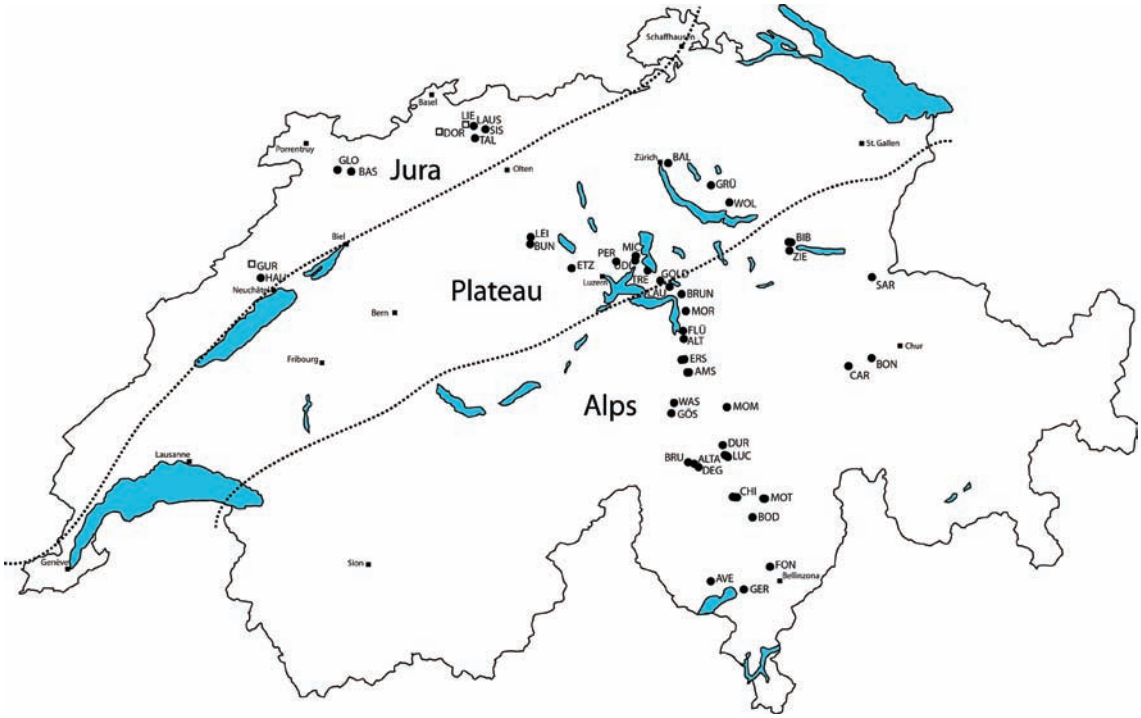

Figure 1.1. Sampling sites in the three important geographic divisions of Switzerland. Black points represent sampling sites under power line towers. Open squares are locations of the investigated geogenically Zn-rich soils.

Chapters 2, 3 and 4 deal with the speciation and fractionation of Zn in soils contaminated from the runoff water of galvanized power line towers. Like other steel constructions, power line towers are coated with Zn to slow corrosion. With time, Zn on the steel surface oxidizes and is washed off with the rainwater, leading to the contamination of the surrounding soils [40]. Soils below power line towers therefore present an ideal field system to investigate the speciation and reactivity of Zn in relation to soil properties, because the contamination is the same for different sites with different soil properties. In addition, the contaminant enters the environment as a dissolved species, (i.e., not in the form of primary Zn-bearing minerals), which facilitates the spectroscopic identification of newly formed Zn-bearing phases. For this project, fourty-nine soils were sampled below Zn-coated power line towers (74 to 17 years of contamination) across Switzerland. Samples were thus collected over a wide range of

soils developed from different parent rock material (fluvioglacial sediments, limestone, sandstone, granite, gneiss, etc) under different climatic conditions. The speciation and fractionation of Zn in contaminated calcareous soils is examined specifically in Chapter 2. The uptake mechanism and quantitative relevance of hydroxy-interlayered minerals for Zn retention in soils are analyzed in Chapter 3. Chapter 4 focuses on the relation between soil properties, Zn speciation and Zn fractionation in contaminated soils.

Chapter 5 is concerned with the speciation of Zn in geogenically Zn-rich soils. At numerous sites in the Swiss Jura Mountains, high Zn contents in soils originate from the weathering of the underlying Zn-rich limestones. Zn released from the limestones is transformed in the soil over timescales of thousand years. By studying the speciation of Zn in such soils, information on Zn species forming over geological times is obtained. These data complement the investigations on contaminated soils below power line towers, which cover a timescale of 10-100 years.

References

[1] Adriano, D. C., *Trace Elements in Terrestrial Environments: Biogeochemistry, Bioavailability, and Risks of Metals.* 2nd ed.; Springer: New York, 2001.

[2] Alloway, B. J., *Heavy Metals in Soils*. Chapman & Hall: London, 1995.

[3] McBride, M. B., Chemisorption and precipitation reactions. In *Handbook of Soil Science*, Summer, M. E., Ed. CRC Press: Boca Raton, B/265-B/302, 2000.

[4] Sparks, D. L., *Environmental Soil Chemistry*. 2nd ed.; Academic Press: London, 2003.

[5] Sposito, G., *The Chemistry of Soils*. Oxford University Press: New York, 2008.

[6] Axe, L.; Anderson, P. R., Intraparticle diffusion of metal contaminants in amorphous oxide minerals. In *Adsorption of Metals by Geomedia*, Jenne, E. A., Ed. Academic Press, 427-443: 1998.

[7] Sparks, D. L., Kinetics and mechanisms of chemical reactions at the soil mineral/water interface. In *Soil Physical Chemistry*, Sparks, D. L., Ed. CRC Press: Boca Raton, 135-191, 1998.

[8] Bertsch, P. M.; Hunter, D. B., Elucidating fundamental mechanisms in soil and environmental chemistry. The role of advanced analytical, spectroscopic and microscopic methods. In *Future Prospects for Soil Chemistry*, Huang, P. M.; Sparks, D. L.; Boyd, S. A., Eds. Soil Science Society of America Special Pubication: Madison, 103-122, 1998.

[9] Brown, B. E.; Parks, G. A.; O'Day, P., Sorption at mineral-water interfaces: macroscopic and microscopic perspectives. In *Mineral Surfaces*, Vaughan, D.

J.; Pattrick, R. A. D., Eds. Chapman and Hall: London, 129-183, 1995.

[10] Pickering, W. F., Metal ion speciation: soils and sediments (a review). *Ore Geol. Rev.* 1986, 1, 83-146.

[11] Shuman, L. M., Fractionation method for soil microelements. *Soil Sci.* 1985, 140, 11-22.

[12] Tessier, A.; Campbell, P. G. C.; Bisson, M., Sequential extraction procedure for the speciation of particulate trace metals. *Anal. Chem.* 1979, 51, 844-851.

[13] Zeien, H.; Brümmer, G. W., Chemische Extraktionen zur Bestimmung von Schwermetallbindungsformen in Böden. *Mitt. Dtsch. Bodenkundl. Ges.* 1989, 59, 505-510.

[14] Gleyzes, C.; Tellier, S.; Astruc, M., Fractionation studies of trace elements in contaminated soils and sediments: a review of sequential extraction procedures. *Trac-Trend Anal. Chem.* 2002, 21, 451-467.

[15] Kheboian, C.; Bauer, C. F., Accuracy of selective extraction procedures for metal speciation in model aquatic sediments. *Anal. Chem.* 1987, 59, 1417-1423.

[16] Shan, X. Q.; Bin, C., Evaluation of sequential extraction for speciation of trace-metals in model soil containing natural minerals and humic acid. *Anal. Chem.* 1993, 65, 802-807.

[17] Voegelin, A.; Tokpa, G.; Jacquat, O.; Barmettler, K.; Kretzschmar, R., Zinc fractionation in contaminated soils by sequential and single extractions: Influence of soil properties and zinc content. *J. Environ. Qual.* 2008, 37, 1190-1200.

[18] Whalley, C.; Grant, A., Assessment of the phase selectivity of the European Community Bureau of Reference (BCR) sequential extraction procedure for metals in sediment. *Anal. Chim. Acta* 1994, 291, 287-295.

[19] Young, S. D.; Zhang, H.; Tye, A. M.; Maxted, A.; Thums, C.; Thornton, I., Characterizing the availability of metals in contaminated soils. I. The solid phase: sequential extraction and isotopic dilution. *Soil Use Manag.* 2005, 21, 450-458.

[20] Ford, R. G.; Sparks, D. L., The nature of Zn precipitates formed in the presence of pyrophyllite. *Environ. Sci. Technol.* 2000, 34, 2479-2483.

[21] Nachtegaal, M.; Sparks, D. L., Effect of iron oxide coatings on zinc sorption mechanisms at the clay-mineral/water interface. *J. Colloid Interface Sci.* 2004, 276, 13-23.

[22] Roberts, D. R.; Ford, R. G.; Sparks, D. L., Kinetics and mechanisms of Zn complexation on metal oxides using EXAFS spectroscopy. *J. Colloid Interface Sci.* 2003, 263, 364-376.

[23] Trainor, T. P.; Brown, G. E.; Parks, G. A., Adsorption and precipitation of aqueous Zn(II) on alumina powders. *J. Colloid Interface Sci.* 2000, 231, 359-372.

[24] Voegelin, A.; Scheinost, A. C.; Bühlmann, K.; Barmettler, K.; Kretzschmar, R., Slow formation and dissolution of Zn precipitates in soil - A combined column-transport and XAFS study. *Environ. Sci. Technol.* 2002, 36, 3749-3754.

[25] Voegelin, A.; Kretzschmar, R., Formation and dissolution of single and mixed Zn and Ni precipitates in soil: Evidence from column experiments and extended X-ray absorption fine structure spectroscopy. *Environ. Sci. Technol.* 2005, 39, 5311-5318.

[26] Schlegel, M. L.; Manceau, A.; Charlet, L.; Chateigner, D.; Hazemann, J.-L., Sorption of metal ions on clay minerals III. Nucleation and epitaxial growth of Zn phyllosilicate on the edges of hectorite. *Geochim. Cosmochim. Acta* 2001, 65, 4155-4170.

[27] Schlegel, M. L.; Manceau, A., Evidence for the nucleation and epitaxial growth of Zn phyllosilicate on montmorillonite. *Geochim. Cosmochim. Acta* 2006, 70, 901-917.

[28] Isaure, M.-P.; Laboudigue, A.; Manceau, A.; Sarret, G.; Tiffrau, C.; Trocellier, P.; Lamble, G. M.; Hazemann, J. L.; Chateigner, D., Quantitative Zn speciation in a contaminated dredged sediment by μ-PIXE, μ-SXRF, EXAFS spectroscopy and principal component analysis. *Geochim. Cosmochim. Acta* 2002, 66, 1549-1567.

[29] Juillot, F.; Morin, G.; Ildefonse, P.; Trainor, T. P.; Benedetti, M.; Galoisy, L.; Calas, G.; Brown, G. E., Occurrence of Zn/Al hydrotalcite in smelter-impacted soils from northern France: Evidence from EXAFS spectroscopy and chemical extractions. *Am. Mineral.* 2003, 88, 509-526.

[30] Kirpichtchikova, T. A.; Manceau, A.; Spadini, L.; Panfili, F.; Marcus, M. A.; Jacquet, T., Speciation and solubility of heavy metals in contaminated soil using X-ray microfluorescence, EXAFS spectroscopy, chemical extraction, and thermodynamic modeling. *Geochim. Cosmochim. Acta* 2006, 70, 2163-2190.

[31] Manceau, A.; Lanson, B.; Schlegel, M. L.; Harge, J. C.; Musso, M.; Eybert-Berard, L.; Hazemann, J. L.; Chateigner, D.; Lamble, G. M., Quantitative Zn speciation in smelter-contaminated soils by EXAFS spectroscopy. *Am. J. Sci.* 2000, 300, 289-343.

[32] Nachtegaal, M.; Marcus, M. A.; Sonke, J. E.; Vangronsveld, J.; Livi, K. J. T.; Van der Lelie, D.; Sparks, D. L., Effects of in situ remediation on the speciation and bioavailability of zinc in a smelter contaminated soil. *Geochim. Cosmochim.*

Acta 2005, 69, 4649-4664.

[33] Panfili, F. R.; Manceau, A.; Sarret, G.; Spadini, L.; Kirpichtchikova, T.; Bert, V.; Laboudigue, A.; Marcus, M. A.; Ahamdach, N.; Libert, M. F., The effect of phytostabilization on Zn speciation in a dredged contaminated sediment using scanning electron microscopy, X-ray fluorescence, EXAFS spectroscopy, and principal components analysis. *Geochim. Cosmochim. Acta* 2005, 69, 2265-2284.

[34] Schuwirth, N.; Voegelin, A.; Kretzschmar, R.; Hofmann, T., Vertical distribution and speciation of trace metals in weathering flotation residues of a zinc/lead sulfide mine. *J. Environ. Qual.* 2007, 36, 61-69.

[35] Voegelin, A.; Pfister, S.; Scheinost, A. C.; Marcus, M. A.; Kretzschmar, R., Changes in zinc speciation in field soil after contamination with zinc oxide. *Environ. Sci. Technol.* 2005, 39, 6616-6623.

[36] Manceau, A.; Tamura, N.; Celestre, R. S.; MacDowell, A. A.; Geoffroy, N.; Sposito, G.; Padmore, H. A., Molecular-scale speciation of Zn and Ni in soil ferromanganese nodules from loess soils of the Mississippi Basin. *Environ. Sci. Technol.* 2003, 37, 75-80.

[37] Manceau, A.; Marcus, M. A.; Tamura, N.; Proux, O.; Geoffroy, N.; Lanson, B., Natural speciation of Zn at the micrometer scale in a clayey soil using X-ray fluorescence, absorption, and diffraction. *Geochim. Cosmochim. Acta* 2004, 68, 2467-2483.

[38] Manceau, A.; Tommaseo, C.; Rihs, S.; Geoffroy, N.; Chateigner, D.; Schlegel, M. L.; Tisserand, D.; Marcus, M. A.; Tamura, N.; Zueng-Sang, C., Natural speciation of Mn, Ni, and Zn at the micrometer scale in a clayey paddy soil using X-ray fluorescence, absorption, and diffraction. *Geochim. Cosmochim. Acta* 2005, 60, 4007-3034.

[39] Scheinost, A. C.; Kretzschmar, R.; Pfister, S.; Roberts, D. R., Combining selective sequential extractions, X-ray absorption spectroscopy, and principal component analysis for quantitative zinc speciation in soil. *Environ. Sci. Technol.* 2002, 36, 5021-5028.

[40] Odnevall Wallinder, I.; Leygraf, C.; Karlèn, C.; Heijerick, D. G.; Janssen, C. R., Atmospheric corrosion of zinc-based materials runoff rates, chemical speciation and ecotoxicity effects. *Corros. Sci.* 2001, 43, 809-816.

2. Formation of Zn-rich phyllosilicate, Zn-layered double hydroxide and hydrozincite in contaminated calcareous soils

Abstract

Recent studies demonstrated that Zn-phyllosilicate- and Zn-layered double hydroxide-type (Zn-LDH) precipitates may form in contaminated soils. However, the influence of soil properties and Zn content on the quantity and type of precipitate forming has not been studied in detail so far. In this work, we determined the speciation of Zn in six carbonate-rich surface soils (pH 6.2 to 7.5) contaminated by aqueous Zn in the runoff from galvanized power line towers (1322 to 30090 mg/kg Zn). Based on 12 bulk and 23 micro-focused extended X-ray absorption fine structure (EXAFS) spectra, the number, type and proportion of Zn species were derived using principal component analysis, target testing, and linear combination fitting. Nearly pure Zn-rich phyllosilicate and Zn-LDH were identified at different locations within a single soil horizon, suggesting that the local availabilities of Al and Si controlled the type of precipitate forming. Hydrozincite was identified on the surfaces of limestone particles that were not in direct contact with the soil clay matrix. With increasing Zn loading of the soils, the percentage of precipitated Zn increased from ~20% to ~80%, while the precipitate type shifted from Zn-phyllosilicate and/or Zn-LDH at the lowest studied soil Zn contents over predominantly Zn-LDH at intermediate loadings to hydrozincite in extremely contaminated soils. These trends were in agreement with the solubility of Zn in equilibrium with these phases. Sequential extractions showed that large fractions of soil Zn (~30% to ~80%) as well as of synthetic Zn-kerolite, Zn-LDH, and hydrozincite spiked into uncontaminated soil were readily extracted by unbuffered 1 M NH_4NO_3 followed by 1 M NH_4-acetate buffered to pH 6.0. Even though the formation of Zn precipitates allows for the retention of Zn in excess to the adsorption capacity of calcareous soils, the long-term immobilization potential of these precipitates is limited.

Published as: Jacquat, O., Voegelin, A., Villard, A., Marcus, M.A., Kretzschmar, R., Formation of Zn-rich phyllosilicate, Zn-layered double hydroxide and hydrozincite in contaminated calcareous soils. Geochim. Cosmochim. Acta 2008, 72, 5037-5054.

2.1. Introduction

Anthropogenic emissions from industrial activities, traffic, and agriculture lead to the accumulation of heavy metals in soils worldwide. Among the heavy metals, zinc is one of the most extensively used. High Zn concentrations in soils may inhibit microbial activity and cause phytotoxicity. This may lead to reduced soil fertility and crop yields and, in severe cases, to soil degradation and erosion [1]. The bioavailability and mobility of Zn in soils are controlled by its chemical speciation, i.e., by adsorption and precipitation reactions. In acidic soils, Zn predominantly adsorbs by cation exchange. With increasing soil pH, specific Zn adsorption to soil organic matter, clay minerals, oxides and carbonates becomes more relevant. In addition, Zn may also precipitate in high pH soils [1, 2]. Based on thermodynamic data, Zn hydroxide ($Zn(OH)_2$), smithsonite ($ZnCO_3$) or hydrozincite ($Zn_5(OH)_6(CO_3)_2$) have been postulated to control Zn solubility in contaminated neutral and calcareous soils [3-5]. Spectroscopic work indicated that Zn may also substitute for Ca in the calcite structure [6]. To date, however, the formation of hydrozincite, smithsonite or Zn-substituted calcite in contaminated calcareous soils has not been unequivocally confirmed [7-10].

On the other hand, numerous extended X-ray absorption fine structure (EXAFS) spectroscopy studies have shown that the formation of Zn-phyllosilicate or Zn-layered double hydroxide (Zn-LDH) may be quantitatively relevant in slightly acidic to neutral soils contaminated by mining and smelting emissions [10-14]. Similar results were also reported for contaminated calcareous soils [7-11]. Spectroscopic studies on pristine and contaminated acidic soils demonstrated the incorporation of Zn into the gibbsitic sheets of Al-hydroxy interlayered clay minerals (Zn-HIM) [15-17] and the phyllomanganate lithiophorite [15, 16, 18]. All these recently identified Zn species are layered minerals containing Zn in octahedral sheets.

The formation of layered Zn-bearing precipitates has been documented for soils with variable composition and different source of Zn input. For the assessment of the behavior of Zn in the soil environment, however, more detailed quantitative knowledge about the occurrence and behavior of these Zn species is needed. Firstly, it is essential to understand how soil properties and soil Zn content affect the types and amounts of precipitates forming in a given soil. Secondly, it needs to be established how differences in Zn speciation affect Zn mobility and bioavailability in soil. In order to reliably determine these relations, observations on a larger number of soils are needed. Spectroscopic studies so far considered soils contaminated by mining, smelting or foundry emissions [10-14, 17], deposition of dredged sediments [7, 9, 19], or sewage irrigation [8]. In these soils, introduced and soil-formed Zn species could be successfully

identified by spatially resolved microfocused (μ-) EXAFS spectroscopy. For the determination of the quantitative abundance of soil-formed Zn-bearing precipitates, on the other hand, bulk EXAFS data need to be analyzed following a linear combination fit (LCF) approach [10]. In the presence of substantial fractions of introduced Zn species, especially in the case of species with a pronounced EXAFS from high-Z backscatterers such as many primary Zn-bearing minerals, however, the EXAFS of whole soil samples may be dominated by introduced Zn species, and the sensitivity and accuracy of LCF analysis regarding the distinction and quantification of different soil-formed Zn species may be limited [10].

In this work, we investigated the speciation and lability of Zn in six calcareous soils, which had been contaminated over several decades with Zn in the runoff water of galvanized power line towers. As these runoff waters contain aqueous Zn^{2+} [20], the distinction and quantification of different soil-formed Zn species can be more reliably achieved than in soils polluted with Zn-bearing contaminants. Focusing on calcareous soils spanning a relatively narrow range in soil pH, we were able to address the effect of Zn loading on Zn speciation in more detail. To determine the speciation of soil Zn, we used bulk- and μ-EXAFS spectroscopy. The fractionation of Zn was determined by single and sequential extractions.

2.2. Materials and Methods

2.2.1. Soil sampling and bulk soil properties

The soil sampling sites were located in Switzerland between 390 and 1900 m above sea level and varied in exposition and local climatic conditions. Five soils (GLO, TAL, BAS, LAUS, SIS) had developed from limestone (Jura mountain range) and one (LUC2) from dolomite (Swiss Alps). The soils had been contaminated by runoff water from 30 to 55 years old galvanized power line towers. Corrosion of the Zn coating led to soil contamination with aqueous Zn. About 1 kg of topsoil (0-5 cm) was collected close to the foundation of each tower, where contamination was expected to be highest. The soils were air-dried at room temperature, manually broken into small aggregates, homogenized in an agate mortar, sieved to <2 mm aggregate size and stored in plastic containers at room temperature in the dark. Powdered subsamples <50 μm were prepared by grinding the soil material <2 mm using an agate mill.

The soil pH was determined with a glass electrode in 10 mM $CaCl_2$ (solution-to-soil ratio 10 mL/g). Before analysis, the suspension was shaken for 10 minutes and equilibrated for at least 30 minutes. Total metal contents were quantified by analyzing pressed pellets (4 g soil and 0.9 g Licowax C®) with energy dispersive

X-ray fluorescence (XRF) spectrometry (Spectro X-lab 2000). Total carbon (TC) was measured on powdered soil samples using a CHNS analyzer (CHNS-32, LECO). Total inorganic carbon (TIC) was determined by reacting 0.3-0.9 g of soil with 1 M sulfuric acid (H_2SO_4) under heating. The evolving CO_2 was trapped on NaOH-coated support and was quantified gravimetrically. Total organic carbon (TOC) was calculated by subtracting the TIC from the TC content. After the removal of soil organic matter with H_2O_2, the sand content (50-2000 μm) was quantified by wet sieving, the clay content (<2 μm) by the pipette method [21], and the silt content was calculated. The effective cation exchange capacity (ECEC) was determined by extracting 7 g of soil with 210 mL of 0.1 M $BaCl_2$ for 2 h [22]. After centrifugation, solutions were filtered (0.2 μm, nylon), acidified with 1% (v/v) 30% HNO_3, and analyzed by inductively coupled plasma – optical emission spectrometry (ICP-OES, Varian Vista-MPX). The ECEC was calculated from the extracted amounts of Ca, Mg, K, Na, Al and Mn.

From the soil material >2 mm of SIS, LAUS and BAS, white (WP) and reddish-brown limestone particles (RP) were manually separated. These particles were covered by crusts visible in the light microscope. These crusts were manually isolated for analysis (SIS-WPC, SIS-RPC, LAUS-WPC, and LAUS-RPC; WPC = white particle crust, RPC = reddish-brown particle crust). Even though white limestone particles from BAS were not covered with distinct crusts, surface material was also isolated for analysis (BAS-WPC). From the soils LUC2, GLO, and TAL, white limestone particles were isolated from the soil material <2 mm (LUC2-WP, GLO-WP, and TAL-WP). All samples were ball-milled to <50 μm for analysis by XRF, X-ray diffraction (XRD) and/or EXAFS spectroscopy. XRD patterns were recorded on a Bruker D4 diffractometer (Cu anode, energy dispersive solid state detector; continuous scans from 10° to 40° 2θ with variable slits, 0.02° steps; 18 s/step).

2.2.2. Sequential extraction of soils and reference compounds

The fractionation of Zn in the soils was determined using the 7-step sequential extraction procedure (SEP) of Zeien and Brümmer [23]. Experimental details are provided in Voegelin et al. [24]. Briefly, the extraction consisted of the following steps yielding fractions F1 to F7 (solution-to-soil ratio (SSR) in mL/g; reaction time; hypothetical interpretation according to Zeien and Brümmer [23]): F1: 1 M NH_4NO_3 (SSR = 25; 24 h; readily soluble and exchangeable); F2: 1 M NH_4-acetate, pH 6.0 (SSR=25; 24 h; specifically adsorbed, $CaCO_3$ bound, and other weakly bound species); F3: 0.1 M NH_2OH-HCl plus 1 M NH_4-acetate, pH 6.0 (SSR=25; 30 min; bound to Mn-oxides); F4: 0.025 M NH_4-EDTA, pH 4.6 (SSR=25; 90 min; bound to organic substances); F5: 0.2 M NH_4-oxalate, pH 3.25, in dark (SSR=25; 2h; bound to amorphous

and poorly crystalline Fe oxides); F6: 0.1 M ascorbic acid in 0.2 M NH_4-oxalate, pH 3.25, in boiling water (SSR=25; 2 h; bound to crystalline Fe oxides); F7: XRF analysis (residual fraction). All soils were extracted in duplicates and extracts were analyzed twice using ICP-OES (Varian Vista-MPX).

The sequential extraction was also performed with an uncontaminated non-calcareous topsoil (pH-value 6.5, 15 g/kg TIC, 150 g/kg clay [14]) and with quartz powder (Fluka®, Nr. 83340) spiked to 2000 mg/kg Zn using synthetic Zn phases (hydrozincite, Zn-LDH, Zn-kerolite – see next paragraph for details on these minerals). Prior to extraction, the Zn-phases were mixed for 24 h with the dry soil or quartz powder using an overhead shaker.

2.2.3. Reference samples for EXAFS spectroscopy

A series of kerolite-type phyllosilicates containing Zn and Mg in their octahedral sheets were synthesized as described by Decarreau [25]. Briefly, 100 mL of 0.3 M ($ZnCl_2$ + $MgCl_2$) at Zn/(Zn+Mg) ratios of 1, 0.75, 0.5, 0.25, and 0.03 and 20 mL of 1 M HCl were added to 400 mL of 0.1 M $Na_2SiO_4 \cdot 5H_2O$ under vigorous stirring. The resulting gels were washed and centrifuged three times, before dispersion in 500 mL doubly deionized water (DDI water, 18.2 MΩ·cm, Milli-Q® Element, Millipore). The suspensions were aged for two weeks at 75 °C. Subsequently, they were centrifuged and washed (DDI water) five times, frozen in liquid N_2 (LN) and freeze-dried. XRF analysis indicated Zn/(Zn+Mg) ratios of 1, 0.8, 0.6, 0.34, and 0.06 for the products ("Zn-kerolite", "$Zn_{0.8}Mg_{0.2}$-kerolite", "$Zn_{0.6}Mg_{0.4}$-kerolite", "$Zn_{0.34}Mg_{0.66}$-kerolite", and "$Zn_{0.06}Mg_{0.94}$-kerolite", respectively), i.e, preferential incorporation of Zn over Mg into the precipitate structure. A layered double hydroxide containing Zn and Al in a ratio of 2:1 ("Zn-LDH") was synthesized according to Taylor [26]. Hydroxy-Al interlayered montmorillonite (HIM) was prepared by slowly titrating a suspension of 20 g/L montmorillonite (SWy-2, Clay Mineral Society) and 40 mmol/L $AlCl_3$ to pH 4.5 [27]. After equilibration for 15 h, the precipitate was washed four times, frozen in LN and freeze-dried. Zn in HIM ("Zn-HIM", 6900 mg/kg Zn) was obtained by suspending 1 g of HIM in a 500 mL 2 mM $ZnCl_2$ plus 10 mM $CaCl_2$ solution for 15 h at pH 5.0. The product was washed, frozen using LN and freeze-dried. Natural Zn-containing lithiophorite ("Zn-lithiophorite") from Cornwall, Great Britain, was kindly provided by Beda Hofmann (Natural History Museum Berne, Switzerland).

Amorphous $Zn(OH)_2$ ("$Zn(OH)_2$") was prepared by adding 66 ml 25% NH_3 to 500 mL 1 M $Zn(NO_3)_2$ [28]. The solution was vigorously stirred and purged with N_2. After 2 h, the precipitate was centrifuged and washed five times in DDI water, frozen in LN and freeze-dried. For the synthesis of Zn-substituted calcite ("Zn-calcite"), vaterite was first

produced by adding 500 mL 0.4 M $CaCl_2$ to 500 mL 0.4 M Na_2CO_3, using N_2-saturated DDI water [29]. The vaterite was obtained by filtration of the suspension. Four g of wet vaterite were reacted with 200 mL of 460 µM $ZnCl_2$ during 5 d at room temperature, resulting in Zn-substituted calcite of composition $Zn_{0.003}Ca_{0.997}CO_3$ ("Zn-calcite"). The precipitate was washed, frozen and freeze-dried. $Zn_5(OH)_6(CO_3)_2$ ("hydrozincite", Alfa Aesar, Nr. 33398) and $Zn_3(PO_4)_2$ (anhydrous "Zn-phosphate", Alfa Aesar, Nr. 13013) were used without further treatment. Natural $ZnCO_3$ ("smithsonite") from Namibia was kindly provided by André Puschnig (Natural History Museum Basel, Switzerland).

For the preparation of birnessite with high and low Zn content, Na-buserite was first synthesized by mixing cooled (<5°C) 200 mL 0.5 M $Mn(NO_3)_2$ into 250 mL DDI water containing 55 g NaOH under vigorous stirring [30, 31]. After oxidation for 5 h with bubbling O_2, the precipitate was separated by centrifugation, washed with DDI water until the pH was close to 9, and stored wet. Eight g of wet Na-buserite were dispersed in 1 L Ar-saturated 0.1 M $NaNO_3$ in the dark. Sorption of Zn at Zn/Mn ratios of 0.088 ("high Zn birnessite") and 0.003 ("low Zn birnessite") was achieved by adding appropriate amounts of $Zn(NO_3)_2$ keeping the suspension at pH 4 using a pH-stat apparatus (Titrando, Metrohm®) [32]. After equilibration for 3 h, the samples were filtered, frozen using LN and freeze-dried. Zn complexed by phytate ("Zn-phytate") was prepared by adding 1.2 mmol $Zn(NO_3)_2$ and 200 µL of triethylamine to a mixed solution of 20 mL DDI water and 20 mL methanol containing 0.27 mmol of inositol hexaphosphoric acid [33]. The solution was stirred for 3 h at 60°C. The product was then filtered, frozen and freeze-dried. Zn was adsorbed to ferrihydrite ("Zn-sorbed Fh") by reacting 0.8 g of freeze-dried ferrihydrite with 800 mL 1 mM $Zn(NO_3)_2$ and 100 mM $NaNO_3$ at pH 6.5 during 24 h [34], resulting in a Zn content of 28600 mg/kg Zn. The sample was then separated by centrifugation, frozen in LN and freeze dried. Aqueous Zn ("aqueous Zn") was analyzed as a 0.5 M $ZnNO_3$ solution. An EXAFS spectrum of Zn adsorbed to calcite ("Zn-sorbed Cc", 1200 mg/kg Zn) was kindly provided by Evert Elzinga (Rutgers University). The sample had been prepared by spiking a solution of 0.45 g/L calcite with 10 µM $ZnCl_2$ [35].

The structure of synthetic Zn-bearing precipitates (ZnMg-kerolites, Zn-LDH, Zn-HIM, Zn-calcite, amorphous $Zn(OH)_2$), Zn sorbent phases (birnessite, ferrihydrite), natural specimens (lithiophorite, smithsonite), and purchased chemicals (hydrozincite, Zn-phosphate) was confirmed by X-ray diffraction analysis.

2.2.4. Acquisition of bulk Zn K-edge EXAFS spectra

Bulk Zn K-edge (9659 eV) EXAFS spectra at room temperature were collected at the beamline X11A at the National Synchrotron Light Source (NSLS, Brookhaven,

USA) and at the XAS beamline at the Angströmquelle Karlsruhe (ANKA, Karlsruhe, Germany). Powdered soil samples and reference materials were mixed with polyethylene or Licowax C® and pressed into 13-mm pellets for analysis in fluorescence or transmission mode. The energy was calibrated using a metallic Zn foil (first maximum of the first derivative of the adsorption edge at 9659 eV). At NSLS, the Si(111) monochromator was manually detuned to 75% of maximum intensity. Fluorescence spectra were recorded using a Stern-Heald-type detector filled with Ar gas and a Cu filter (edge jump $\Delta\mu t=3$) to reduce the intensity of scattered radiation. At ANKA, the Si(111) monochromator was detuned to 65% using a software-controlled monochromator stabilization. Fluorescence spectra were collected with a 5-element Ge solid state detector. Zn-lithiophorite was analyzed at the Dutch Belgian Beamline (DUBBLE) at the European Synchrotron Radiation Facility (Grenoble, France) using a similar setup as at the XAS beamline (ANKA).

2.2.5. µ-XRF and µ-EXAFS analysis on soil thin sections

Freeze-dried soil aggregates of soils GLO, SIS and LUC2 were embedded in high purity resin (Epofix Struers or Araldit 2020). Polished thin sections (30-45 µm thick) were prepared on glass slides. From LUC2, also a free standing section (30 µm thick) was prepared. The thin sections were analyzed at the beamline 10.3.2 at the Advanced Light Source (ALS, Berkeley, USA) [36]. The sections were mounted at 45° to the incident beam and the fluorescence signal was recorded at 90° using a 7-element Ge solid state detector. Element distribution maps were obtained at incident photon energies of 10 keV and 7.012 keV (100 eV below Fe K-edge) with resolutions (step sizes) of 20×20 or 5×5 μm^2 and dwell times of 100, 150 or 200 ms/point. At selected points of interest (POI), fluorescence spectra (10 keV) and Zn K-edge EXAFS spectra were recorded using a beam size between 5×5 and 16×7 μm^2, depending on local Zn concentration and the size of the feature of interest.

2.2.6. EXAFS spectra extraction and analysis by PCA, TT, and LCF

EXAFS spectra were extracted using the software code Athena [37, 38]. The first maximum of the first derivative of the absorption edge was used to set E_0. Normalized absorption spectra were obtained by subtracting a first order polynomial fitted to the pre-edge data (-150 to -30 eV relative to E_0) and subsequently dividing through a second order polynomial fitted to the post-edge data (+150 eV up to 100 eV before end of spectrum). EXAFS spectra were extracted by fitting the post-edge data (0.5 to 12 $Å^{-1}$) with a cubic spline function and minimizing the amplitude of the Fourier transform at radial distances <0.9 Å (Autobk algorithm, k-weight = 3; R_{bkg} = 0.9 Å).

Principal component analysis (PCA) and target transform testing (TT) were carried out using Sixpack [39]. All k^3-weighted bulk- and micro-EXAFS spectra were analyzed over the k-range 2 to 10 $Å^{-1}$. The number of components required to reproduce the entire set of spectra without experimental noise was determined by PCA based on the empirical indicator function (IND) [40]. TT based on the significant components was then used to determine the suitability of reference spectra to describe the experimental data. This assessment was based on the empirical SPOIL value [41] and the normalized sum of squared residual (NSSR) of the target transforms [8, 9, 19, 42].

Using the selected reference spectra, the experimental spectra were analyzed by linear combination fitting (LCF) using the approach and software developed by Manceau and coworkers [10, 43]. The LCF analysis was carried out by calculating all possible 1-component to 4-component fits based on all reference spectra selected from PCA and TT. Starting from the best 1-component fit as judged by the lowest NSSR (NSSR = $(\Sigma_i(k^3\chi_{exp}-k^3\chi_{fit})^2)/\Sigma_i(k^3\chi_{exp}{}^2)$), additional references were considered in the fit as long as they resulted in a decrease in NSSR by at least 10 %. The overall precision of LCF with respect to fitted fractions of individual reference spectra has previously been estimated to 10% of the total Zn [19]. However, the detection limit, precision, and accuracy of LCF analyses depend on the EXAFS of individual species of interest, structural and spectral similarities between different phases in mixtures, and the availability of a database including all relevant reference spectra [10].

2.2.7. Calculation of Zn solubility in equilibrium with Zn-containing precipitates

The solubility of Zn was calculated in equilibrium with different Zn-bearing phases (composition; ion activity product (IAP); log solubility product ($\log K_{so}$)): Amorphous Zn hydroxide ($Zn(OH)_2$; $(Zn^{2+})(H_2O)^2(H^+)^{-2}$; 12.47), zincite (ZnO; $(Zn^{2+})(H_2O)^2(H^+)^{-2}$; 11.19), smithsonite ($ZnCO_3$; $(Zn^{2+})(CO_3^{2-})$; -10.0), hydrozincite ($Zn_5(CO_3)_2(OH)_6$; $(Zn^{2+})^5(CO_3^{2-})^2(H_2O)^6(H^+)^{-6}$; 8.7, [44]), Zn-LDH ($Zn_2Al(OH)_6(CO_3)_{0.5}$; $(Zn^{2+})^2(Al^{3+})(H_2O)^6(CO_3^{2-})^{0.5}(H^+)^{-6}$; 11.19, [45]), Zn-kerolite ($Zn_3Si_4O_{10}(OH)_2$; $(Zn^{2+})^3(H_4SiO_4)^4(H_2O)^{-4}(H+)^{-6}$; 6.7, calculated from predicted $\Delta G^0_{f,298K}$ [46]), Zn-chlorite ($(Zn_5Al)(Si_3Al)O_{10}(OH)_8$); $(Zn^{2+})^5(Al^{3+})^2(H_4SiO_4)^3(H_2O)^6(H^+)^{-16}$; 37.6, calculated from predicted $\Delta G^0_{f,298K}$ [46]). Activity corrections and complexation of aqueous Zn were not included. Zn solubility was calculated for atmospheric (pCO_2 = 3.2×10^{-4} atm, "low CO_2") and hundredfold atmospheric CO_2 partial pressure ("high CO_2"). "Low Al" and "high Al" scenarios were calculated for Al^{3+} in equilibrium with gibbsite and amorphous Al-hydroxide, respectively ($Al(OH)_3$; $(Al^{3+})(H_2O)^3(H^+)^{-3}$; 8.11 and 10.8). For "low Si" and "high Si" calculations, silicic acid was assumed to be in equilibrium with quartz and amorphous silica, respectively (SiO_2; $(H_4SiO_4)(H_2O)^{-2}$; -2.74 and -4.0). Unless otherwise

stated, equilibrium constants were taken from the MinteqA2 V4 database [47].

2.3. Results

2.3.1. Bulk soil characteristics

Selected properties of the soil samples are reported in Table 2.1. The 6 soils had pH values between 6.2 and 7.5 and covered a wide range in TIC (1 to 89 g/kg), clay content (90 to 450 g/kg), and ECEC (99 to 410 $mmol_c/kg$). Contamination with aqueous Zn from corroding power line towers over 30 to 55 years had led to the accumulation of 1322 to 30090 mg/kg Zn in the topsoil layers. In Switzerland, 150 mg/kg Zn represents an upper level for typical geogenic Zn contents and soils with more than 2000 mg/kg Zn are considered to be heavily contaminated [48]. In Table 2.1, the soils are arranged by increasing total Zn content divided by clay content (Zn/clay).

Table 2.1. Physical and chemical properties and Zn content of the studied soil materials.

Soil	Geology	pH	TOC	TIC	Texture (g/kg)			ECEC[a]	Tower age[b]	Total Zn	Zn/clay[c]	Exch. Zn[d]
		($CaCl_2$)	(g/kg)	(g/kg)	Clay	Silt	Sand	($mmol_c/kg$)	(years)	(mg/kg)	(mg/kg)	(mg/kg)
GLO	Limestone	6.6	49	1.2	451	319	230	406	30	1322	2900	194
LUC2	Dolomite	7.3	33	87	88	131	781	181	55	1398	15900	12
BAS	Limestone	6.4	74	4.4	382	434	184	263	30	12170	31900	2548
LAUS	Limestone	6.2	44	6.5	406	348	246	164	39	13810	34000	2838
TAL	Limestone	7.5	14	89	108	244	648	99	39	6055	56100	20
SIS	Limestone	6.5	59	17	309	288	403	371	39	30090	97400	3052

[a]Effective cation exchange capacity. [b]Indicating duration of soil contamination. [c]Total Zn content divided by clay content (i.e., concentration in clay fraction if clay fraction contained all Zn). [d]Exchangeable Zn in 0.1 M $BaCl_2$ at solution-soil-ratio of 30 mL/g.

2.3.2. Principal component analysis and target transform testing

Before considering the speciation of Zn in individual soils, we performed a principal component analysis (PCA) with all 35 EXAFS spectra (bulk soils (6 spectra), limestone crusts/particles (6), μ-EXAFS spectra from GLO (5), LUC2 (9), and SIS (9)) to determine the number of distinguishable spectral components. The parameters of the first 8 components obtained by PCA are given in Table 2.2. The IND function reached a minimum for 5 spectral components. The first 5 components explained 70% of the total experimental variance and provided a good reconstruction of all 35 EXAFS spectra (NSSR 0.5 to 6.8%).

Table 2.2. Results of the principal component analysis of 12 bulk- and 23 μ-EXAFS spectra.

Component	Eigenvalue	Variance	Cum. Var.[a]	IND[b]
1	179.4	0.441	0.441	0.01042
2	60.6	0.149	0.591	0.00567
3	16.6	0.040	0.632	0.00541
4	12.9	0.031	0.663	0.00535
5	11.4	0.028	0.691	0.00532
6	9.9	0.024	0.716	0.00537
7	8.7	0.021	0.737	0.00547
8	8.0	0.019	0.757	0.00560

[a] Cumulative variance. [b] Indicator function.

We therefore used the first 5 components from PCA for the assessment of reference spectra by target transform testing (TT) (Table 2.3), considering references with SPOIL values below 6 in subsequent LCF analysis of experimental data (see footnote of Table 2.3 for classification of SPOIL values). Among all tested references, aqueous Zn had the lowest SPOIL value. TT also returned a low SPOIL for hydrozincite, Zn-rich kerolites, and $Zn(OH)_2$, while the SPOIL of Zn-LDH was slightly higher. Also Zn-sorbed ferrihydrite and calcite and Zn-phytate were classified as good references based on their SPOIL values. The SPOIL of Zn in kerolite phases increased with decreasing Zn/(Zn+Mg) ratio, paralleled by an increase in the NSSR of the respective target transform. SPOIL values of low Zn-birnessite, smithsonite, Zn-calcite, and high Zn-birnessite classified these references as good to fair. However, the high NSSR of their target transform, i.e., the deviation between the experimental and the reconstructed spectra shown in Figure 2.1, suggested that these Zn species were not dominant in the samples. The high SPOIL (>6) and NSSR of Zn-HIM and Zn-lithiophorite containing Zn in octahedral sheets surrounded exclusively by light Al atoms indicated that this type of coordination environment was not relevant in the studied soils. These two latter references were therefore not considered for LCF. Overall, PCA combined with TT indicated that reference spectra of ZnMg-kerolite, Zn-LDH, hydrozincite, smithsonite, $Zn(OH)_2$ and adsorbed/complexed Zn species in octahedral and tetrahedral coordination (aqueous Zn, Zn-phytate, Zn-sorbed calcite, Zn-sorbed ferrihydrite, Zn-phosphate, low- and high Zn-birnessite) were suitable to describe the experimental EXAFS spectra by LCF. A more detailed structural characterization of selected reference spectra based on shell fitting is provided in the appendix 1.

Table 2.3. Target testing of reference spectra using the first five components obtained by PCA (Table 2.2).

References	SPOIL[a]	NSSR (%)
aqueous Zn	1.2	4.0
hydrozincite	1.5	4.4
Zn-kerolite	1.6	2.5
$Zn_{0.8}Mg_{0.2}$-kerolite	1.9	2.1
$Zn(OH)_2$	2.0	8.3
Zn-phytate	2.4	4.4
Zn-LDH	2.5	1.7
$Zn_{0.6}Mg_{0.4}$-kerolite	2.6	2.7
low Zn-birnessite	2.7	13.9
Zn-sorbed calcite	2.8	3.6
$Zn_{0.34}Mg_{0.66}$-kerolite	2.8	7.5
smithsonite	2.9	32.9
Zn-sorbed ferrihydrite	3.0	4.4
$Zn_{0.06}Mg_{0.94}$-kerolite	3.2	12.8
Zn-phosphate	3.2	6.0
Zn-calcite	3.7	34.9
high Zn-birnessite	4.4	29.4
Zn-HIM	6.3	41.7
Zn-lithiophorite	10.3	38.1

[a]SPOIL classification: 0-1.5 excellent; 1.5-3 good; 3-4.5 fair; 4.5-6 acceptable; >6 unacceptable reference [41].

The number of suitable reference spectra identified by TT was higher than the number of principal components from PCA. This may be related to the occurrence of species uniformly distributed throughout the samples [49] or to spectral similarities between different reference spectra [42]. Furthermore, the principal components identified by PCA may also reflect the dominant backscattering signals occurring in variable proportions in different Zn species. In Zn-LDH and all Zn-kerolite phases, octahedrally coordinated Zn is contained in octahedral sheets surrounded by variable amounts of Zn and Mg/Al/Si in the second shell (Zn/Mg/Al in octahedral sheet, Si in adjacent tetrahedral sheet, see appendix 1 for further details). In Zn-phosphate, Zn-sorbed calcite, Zn-sorbed ferrihydrite, and Zn-phytate, on the other hand, Zn is tetrahedrally coordinated. The EXAFS spectra of tetrahedral Zn in sorbed or complexed form are dominated by the first-shell Zn-O signal and are therefore relatively similar (Fig. 2.1).

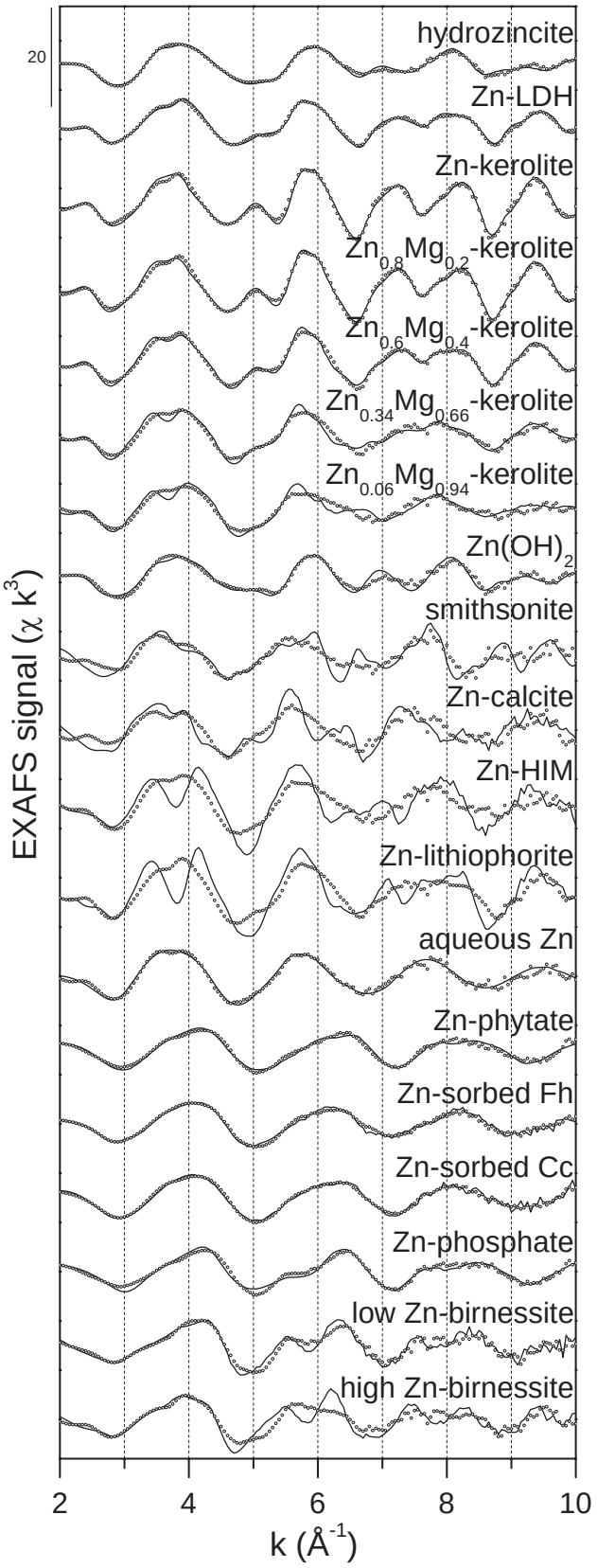

Figure 2.1. Zn K-edge EXAFS spectra of selected Zn references (solid lines) and target transforms (dots) calculated with the first five components from principal component analysis (Tables 2.2 and 2.3).

This complicated the distinction of these species in experimental spectra with several spectral contributions. In LCF, we therefore quantified tetrahedrally coordinated sorbed Zn ("sorbed ^{IV}Zn") without differentiating using the reference providing the lowest NSSR. Similarly, the spectrum of aqueous Zn was used as the only proxy for octahedrally coordinated Zn bound as an outer-sphere sorption complex or as an inner-sphere complex with weak backscattering from atoms in the sorbent phase.

2.3.3. Microscale speciation of Zn in soil GLO

Light microscope images from a thin-section of soil GLO together with Zn, Ca, Fe, and Mn distribution maps are shown in Figure 2.2. High Zn concentrations occured in FeMn-nodules present throughout the soil section. At lower concentrations, Zn was also present within the clayey soil matrix. EXAFS spectra collected on selected POI are shown in Figure 2.3. LCF parameters are provided in Table 2.4.

Two μ-EXAFS spectra (GLO-4 and GLO-5) were recorded within a large FeMn-nodule shown in more detail in Figure 2.2C. Higher Zn concentrations were observed in Mn-rich than in Fe-rich zones of the nodule. The spectrum of the Mn-rich interior of the nodule (GLO-5) exhibited a splitting of the second EXAFS oscillation near 6 $Å^{-1}$ (Fig. 2.3). This splitting, though more pronounced, is typical for Zn adsorbed to birnessite at low surface coverage (Fig. 2.1). The relative height of the Kα fluorescence lines of Mn, Fe, and Zn (Mn/Fe/Zn ≈ 1.4/1/1) suggested that Zn may be associated with both Mn- and Fe-(hydr)oxides. Based on these observations, the LCF of GLO-5 (Table 2.4, Fig. 2.3) was based on low Zn-birnessite and Zn-sorbed ferrihydrite (NSSR 12.1%), even though a better fit (NSSR 7.1%) would have been obtained with 42% low Zn-birnessite and 64% Zn-phytate. Zn-birnessite has previously been identified in a marine FeMn-nodule [50] as well as in natural [7, 18] and contaminated soils [7, 10, 14]. The spectrum from the Fe-rich zone of the nodule (GLO-4) did not exhibit the splitting at ~6 $Å^{-1}$ observed for GLO-5 and was best described by a 1-component fit using the spectrum of Zn-sorbed ferrihydrite (Table 2.4). This suggested that Fe-(hydr)oxides were likely the main sorbent for Zn, in line with the relative heights of the Kα fluorescence lines (Mn/Fe/Zn ≈ 2/10/1) indicating a much higher Fe/Mn ratio than in the Mn-rich zone of the nodule. The spectrum GLO-2 closely resembled the Zn-phytate reference (Figs. 2.1 and 2.3, Table 2.4), suggesting that Zn at this location was mainly tetrahedrally coordinated and complexed by organic phosphate groups [42]. The spectrum GLO-1 exhibited the spectral features of Zn-LDH (Fig. 2.1 and 2.3), as reflected by the results from LCF (Table 2.4).

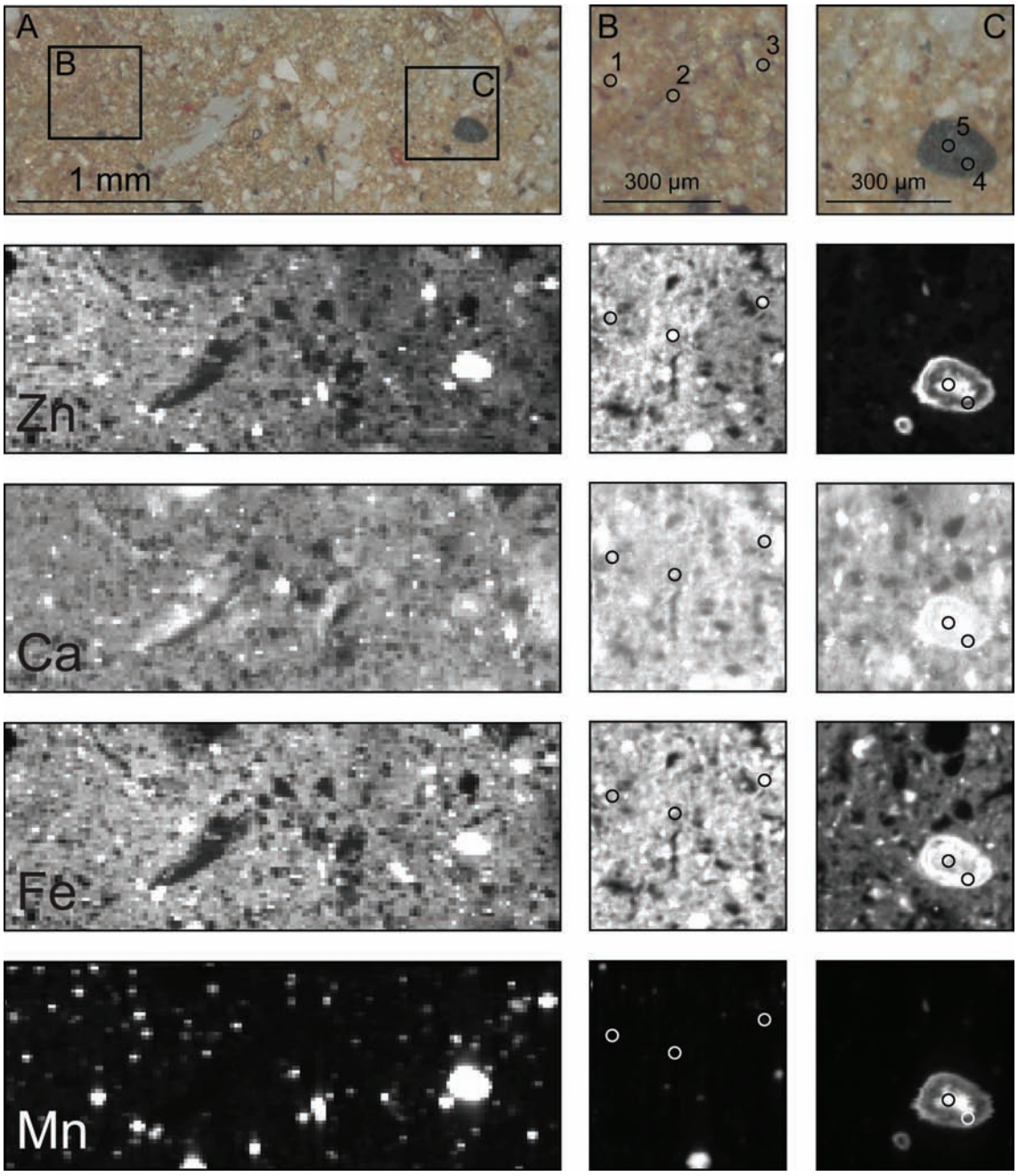

Figure 2.2. Light microscope images of the GLO soil thin section and corresponding µ-XRF maps (black: lowest intensity; white: 90% of highest recorded intensity in map). (A) Coarse map of a 3000×1150 µm^2 area (20×20 µm^2 resolution, 100 ms dwell time). (B) and (C) Fine maps of 470×500 µm^2 area (5×5 µm^2 resolution, 100 ms dwell time).

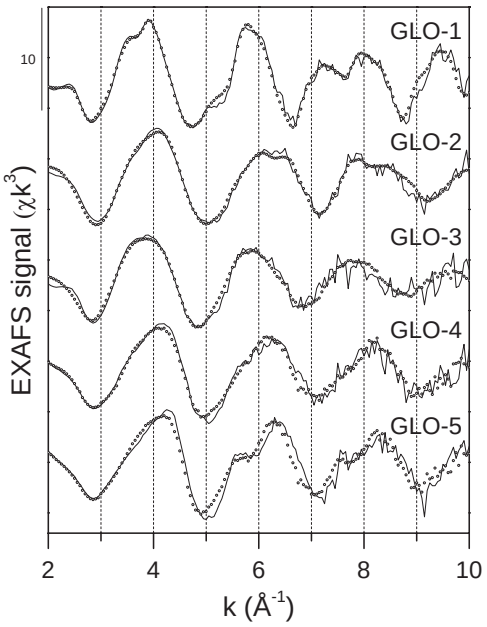

Figure 2.3. μ-EXAFS spectra from the GLO soil thin section (solid lines) and LCF spectra (dots). LCF results are provided in Table 2.4.

Table 2.4. Linear combination fits of the μ-EXAFS from thin-section of the soil GLO.

Spectrum	Zn-LDH	sorbed $^{IV}Zn^{a}$	aqueous Zn	low Zn-birnessite	Sum	NSSR
	(%)	(%)	(%)	(%)	(%)	(%)
GLO-1	93	———	17	———	110	3.9
GLO-2	———	90 (Ph)	22	———	112	4.0
GLO-3	———	39 (Fh)	54	———	93	9.9
GLO-4	———	99 (Fh)	———	———	99	8.7
GLO-5	———	65 (Fh)	———	37	102	12.2

[a](Ph): Zn-phytate, (Fh): Zn-sorbed ferrihydrite.

2.3.4. Microscale speciation of Zn in soil LUC2

The distribution of Ca in the soil thin section of soil LUC2 reflected the high content of mostly dolomite sand (781 g/kg) in this soil (Fig. 2.4). The Zn distribution indicated localized Zn rich zones and Zn at lower concentrations associated with organic material. Except for a prominent FeMn-nodule, the distribution of Zn was not closely related with Fe and Mn. While the POI LUC2-1 to LUC2-7 were located on the thin section shown in Figure 2.4, LUC2-8 and LUC2-9 were analyzed on a second thin section. The EXAFS spectra for LUC2-1 to LUC2-9 together with LCF spectra are shown in Figure 2.5. LCF parameters are listed in Table 2.5.

The EXAFS spectrum collected on an organic fragment (LUC2-1) closely matched the Zn-phytate reference (Figs. 2.1 and 2.5), indicating the presence of organically complexed tetrahedral Zn [42]. In contrast, LCF of the spectra LUC2-2 and LUC2-7 located next to dolomite grains returned substantial fractions of Zn-sorbed calcite as best proxy for tetrahedrally coordinated sorbed Zn. The spectrum LUC2-4 collected on a Zn-rich spot of ~25 μm diameter perfectly matched the reference spectrum of $Zn_{0.8}Mg_{0.2}$-kerolite (Fig. 2.5, Table 2.5). The spectrum LUC2-8 collected on another Zn-rich spot, however, revealed the typical features of Zn-LDH (Fig. 2.5). The best LCF was achieved with a mixture of 103% Zn-LDH and 18% $Zn_{0.8}Mg_{0.2}$-kerolite (Table 2.5). The deviation of the sum of fitted fractions from 100 % may be related to slight differences in the mineral structure and crystallinity of the sample and reference material [10]. Inspection of the Fourier-transformed EXAFS spectra LUC2-4 and LUC2-8 and their LCF (Fig. A1.2, appendix 1) further confirmed that the spectrum LUC2-4 was nearly identical to the spectrum of $Zn_{0.8}Mg_{0.2}$-kerolite and that the spectrum LUC2-8 was best described by Zn-LDH and a minor fraction of $Zn_{0.8}Mg_{0.2}$-kerolite. In addition to Zn-kerolite (spectrum LUC2-4) and Zn-LDH (spectrum LUC2-8), the LCF of the spectra LUC2-6 and LUC2-7 further suggested that also hydrozincite may locally form within the same soil environment.

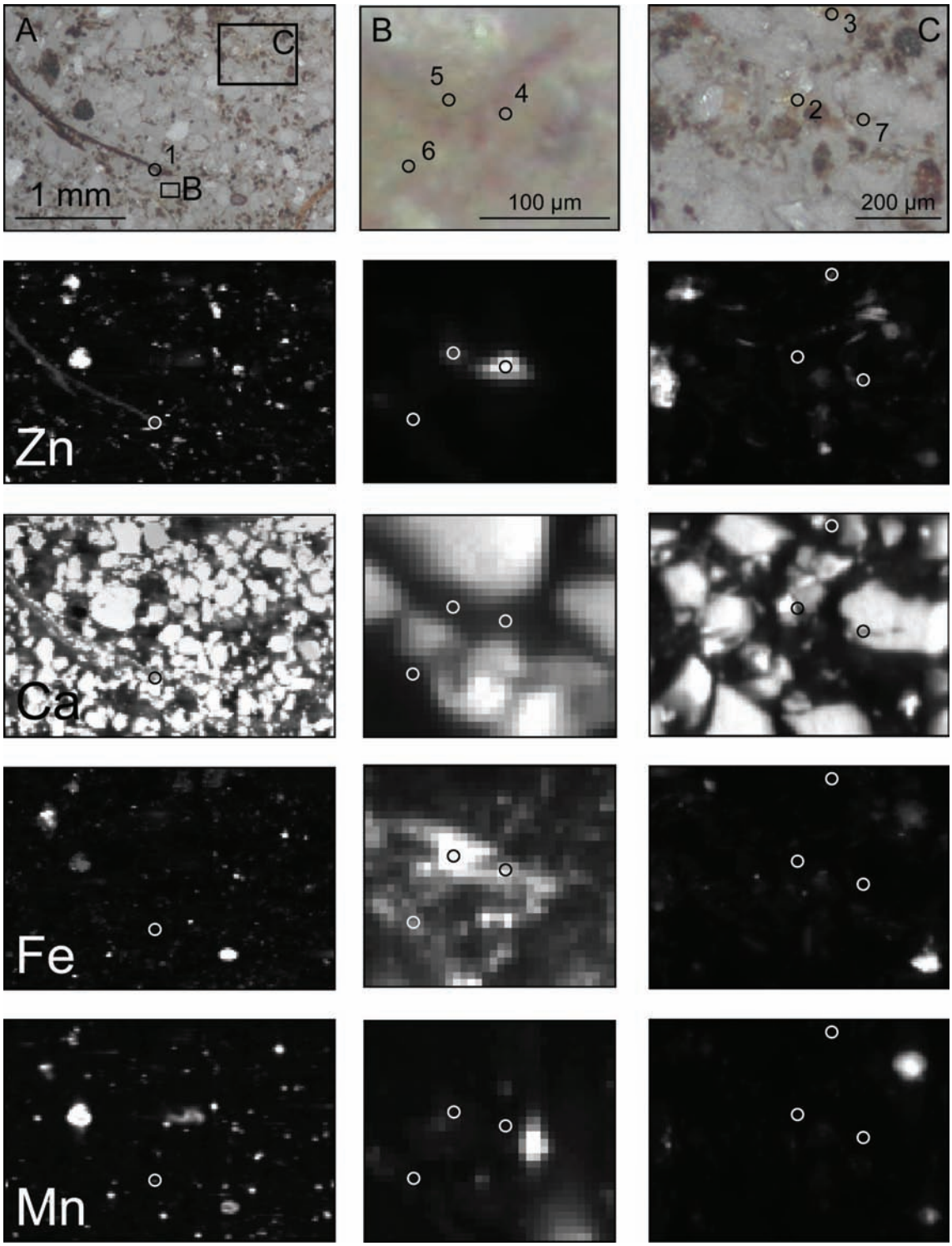

Figure 2.4. Light microscope images of the LUC2 soil thin section and corresponding µ-XRF maps for Zn, Ca, Fe and Mn (black: lowest intensity; white: 90% of highest recorded intensity in map). (A) Coarse map of a 3000×2000 µm² area (20×20 µm² resolution, 100 ms dwell time). (B) Fine map of a 200×150 µm² area and (C) fine map of a 700×500 µm² area (5×5 µm² resolution, 100 ms dwell time).

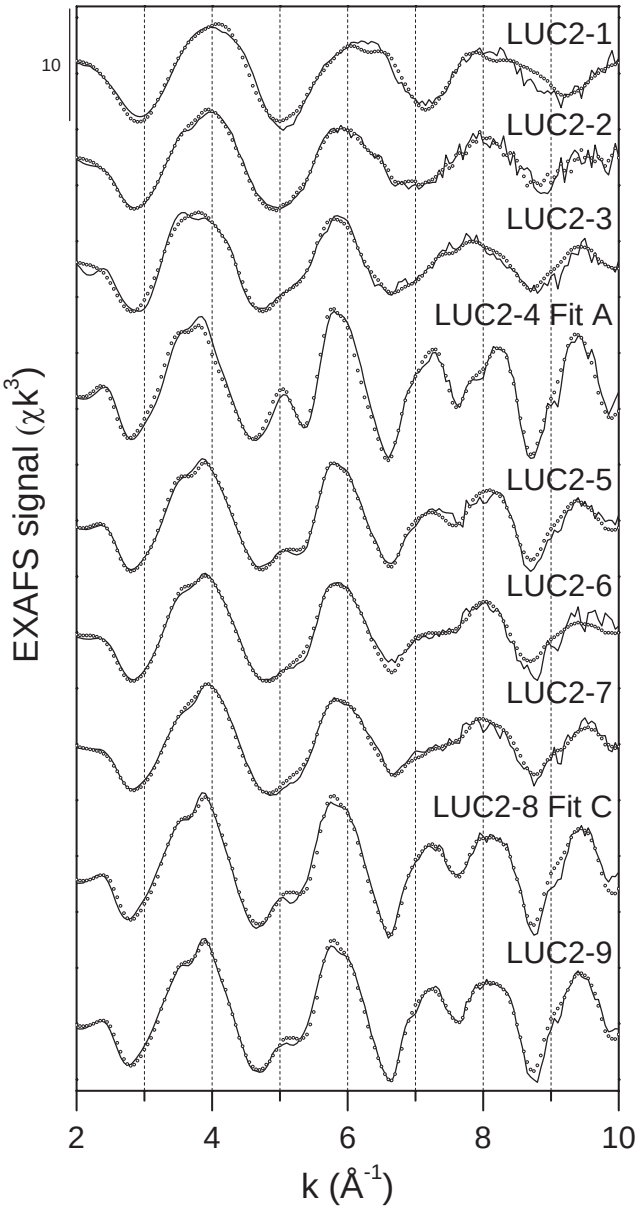

Figure 2.5. μ-EXAFS spectra from thin sections of soil LUC2 (solid lines) and LCF spectra (dots). LCF results are provided in Table 2.5.

Table 2.5. Linear combination fits of μ-EXAFS spectra from the thin-sections of the soil LUC2 (Fig. 2.5).

Spectrum	hydrozincite	Zn-LDH	Zn-kerolite[a]	sorbed ^{IV}Zn[b]	aqueous Zn	Sum	NSSR
	(%)	(%)	(%)	(%)	(%)	(%)	(%)
LUC2-1	———	———	———	84 (Ph)	23	107	5.5
LUC2-2	———	32	———	54 (Cc)	15	101	4.9
LUC2-3	———	———	22 (80Zn)	36 (Cc)	51	109	4.2
LUC2-4 Fit A	———	———	93 (80Zn)	———	———	93	3.5
LUC2-4 Fit B	———	126	———	———	———	126	10.4
LUC2-5	40	32	35 (60Zn)	———	———	107	2.6
LUC2-6	51	36	———	———	21	108	4.8
LUC2-7	———	60	———	36 (Cc)	13	109	3.8
LUC2-8 Fit A	———	———	87 (80Zn)	———	———	87	10.5
LUC2-8 Fit B	———	127	———	———	———	127	3.3
LUC2-8 Fit C	———	103	18 (80Zn)	———	———	121	2.8
LUC2-9	———	103	19 (80Zn)	———	———	122	1.9

[a](80Zn): $Zn_{0.8}Mg_{0.2}$-kerolite, (60Zn): $Zn_{0.6}Mg_{0.4}$-kerolite, [b](Ph): Zn-phytate, (Cc): Zn-sorbed calcite.

2.3.5. Microscale speciation of Zn in soil SIS

Distribution maps of Zn, Ca, and Fe in a thin section from soil SIS are shown in Figure 2.6. The maps indicated the presence of limestone particles embedded in a clayey soil matrix rich in Zn and Fe. As in the soils LUC2 and GLO, Mn was present in discrete FeMn-nodules. The entire soil matrix was rich in Zn, reflecting the extremely high Zn content of soil SIS (Table 2.1). Due to the high Zn contents throughout the soil matrix, no enrichment of Zn was observed in FeMn-nodules.

Micro-EXAFS and corresponding LCF spectra of 9 POI (SIS-1 to SIS-9) are shown in Figure 2.7. LCF parameters are provided in Table 2.6. The spectra SIS-1, SIS-2, SIS-3 did not exhibit pronounced high frequency features and LCF returned a high fraction of tetrahedrally coordinated Zn (Zn-sorbed calcite) at these locations. The μ-EXAFS spectra SIS-4 to SIS-9 (except SIS-6) were best fitted with Zn-LDH and minor contributions of Zn-phyllosilicate ($Zn_{0.8}Mg_{0.2}$-kerolite) and sorbed ^{IV}Zn. None of the analyzed POI indicated the presence of hydrozincite.

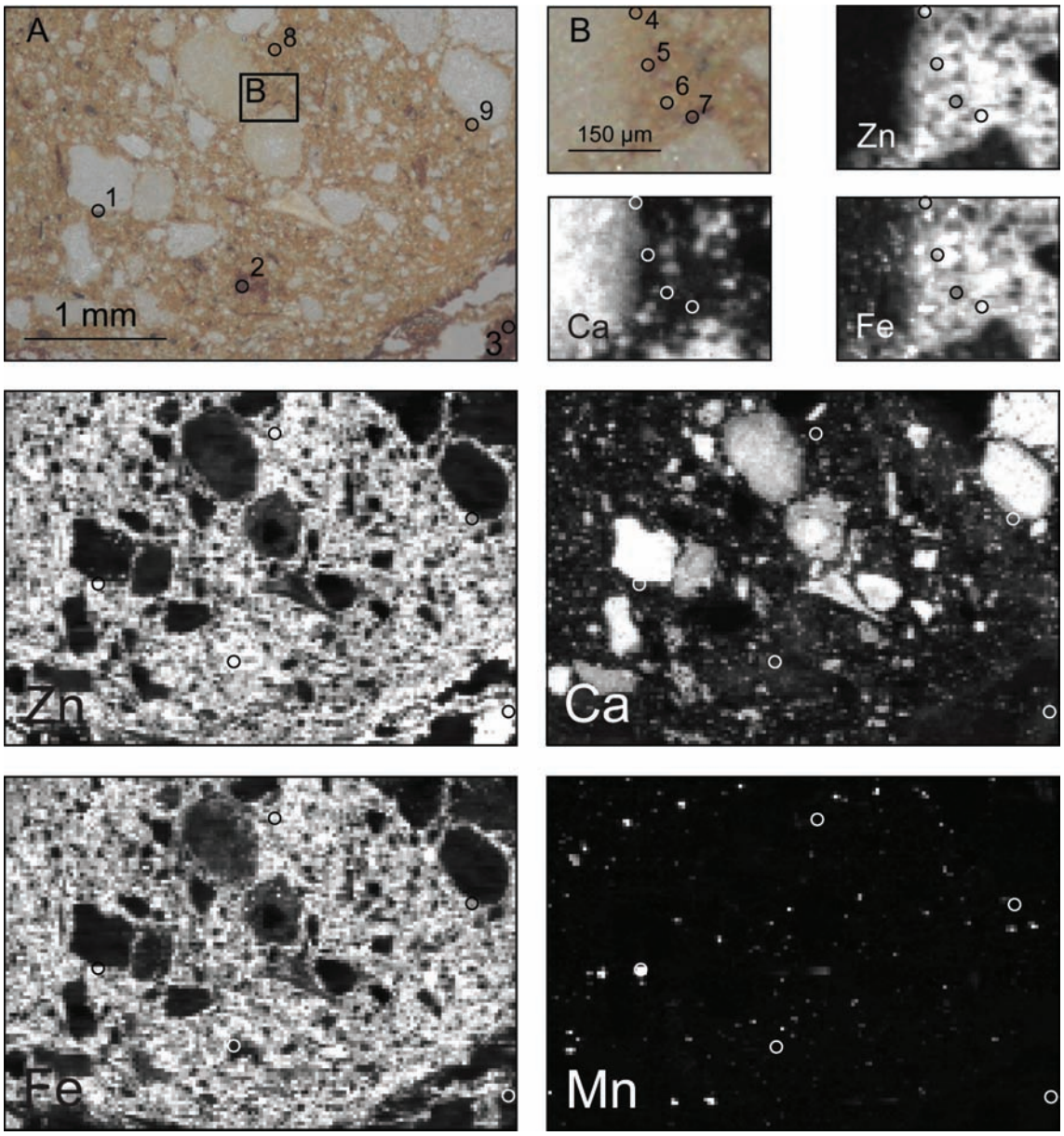

Figure 2.6. Light microscope images of the SIS soil thin section and corresponding µ-XRF maps (black: lowest intensity; white: 90% of highest recorded intensity in map). (A) Coarse map of a 3600×2400 µm² area (20×20 µm² resolution, 200 ms dwell time). (B) Fine map of a 360×240 µm² area (5×5 µm² resolution, 150 ms dwell time).

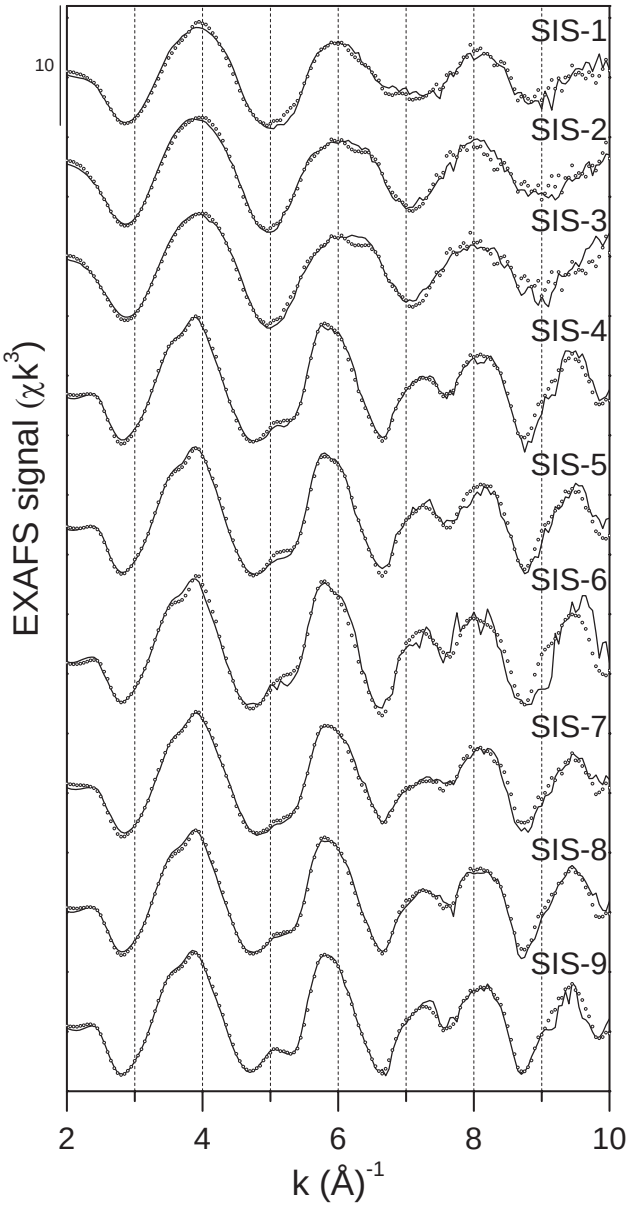

Figure 2.7. μ-EXAFS spectra collected on the SIS soil thin section (solid lines) and LCF spectra (dots). LCF results are provided in Table 2.6.

Table 2.6. Linear combination fits of the μ-EXAFS spectra from the thin-section of the soil SIS (Fig. 2.7).

Spectrum	Zn-LDH	$Zn_{0.8}Mg_{0.2}$-kerolite	sorbed $^{IV}Zn^{a}$	aqueous Zn	Sum	NSSR
	(%)	(%)	(%)	(%)	(%)	(%)
SIS-1	37	———	61 (Cc)	———	98	5.0
SIS-2	———	———	73 (Cc)	31	104	3.9
SIS-3	———	———	76 (Cc)	26	102	6.2
SIS-4	75	19	25 (Cc)	———	119	2.2
SIS-5	79	15	27 (Fh)	———	121	2.5
SIS-6	118	———	———	———	118	9.8
SIS-7	67	13	39 (Cc)	———	119	2.2
SIS-8	78	17	22 (Cc)	———	117	1.7
SIS-9	56	36	23 (Cc)	———	112	1.9

[a](Cc): Zn-sorbed calcite, (Fh): Zn-sorbed ferrihydrite.

2.3.6. Speciation of Zn associated with limestone particles

In addition to the aggregated matrix, all soils also contained isolated white limestone particles. White limestone particles from soils SIS and LAUS were covered with massive up to 0.5 mm thick crusts (light microscope images shown in Fig. A1.4). The XRD pattern showed that the crust material from soil SIS consisted mainly of hydrozincite (Fig. A1.5). XRD patterns of crusts from soils BAS and LAUS also indicated traces of hydrozincite, but were dominated by calcite and quartz (Fig. A1.5). EXAFS analysis (Fig. 2.8, Table 2.7) confirmed that hydrozincite was the only Zn-bearing phase in the sample SIS-WPC. No crusts were observed on limestone particles from the soils TAL, GLO, and LUC2, and XRD patterns of powdered limestone samples did not show any diffraction peaks of hydrozincite (not shown). However, EXAFS spectra revealed that a significant fraction of Zn associated with limestone particles from LUC2 and TAL was hydrozincite (Fig. 2.8, Table 2.7). For the soil GLO with lowest Zn content, LCF indicated that most Zn on limestone particles was adsorbed to the calcite surface.

Soils SIS and LAUS also contained reddish-brown limestone particles consisting mainly of calcite and quartz. These particles were covered with thin crusts of black, brown and red color (Fig. A1.4). XRD patterns of these crusts indicated the presence of clay minerals, quartz, calcite, feldspars and goethite, but hydrozincite was not detected (not shown). EXAFS spectroscopy showed that about two thirds of Zn in these crusts was sorbed ^{IV}Zn and Zn-rich kerolite, and that only about one third was contained in hydrozincite (Fig. 2.8, Table 2.7).

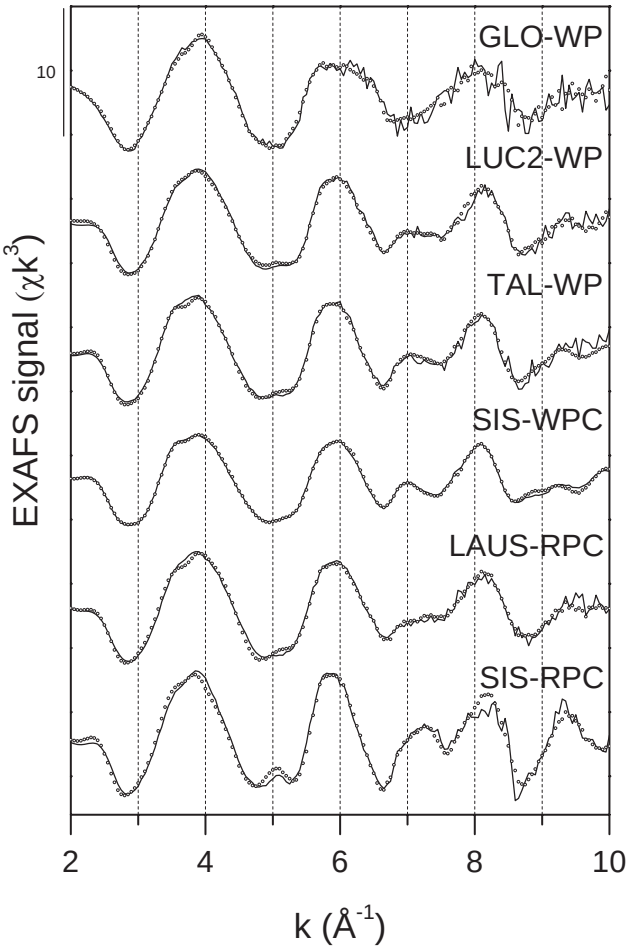

Figure 2.8. EXAFS spectra collected from white limestone particles (WP), white limestone particle crusts (WPC) and red limestone particle crusts (RPC) (solid lines) and LCF spectra (dots). LCF results are provided in Table 2.7.

Table 2.7. Linear combination fits of Zn K-edge EXAFS spectra from limestone particles and crusts and limestone particles (Fig. 2.8).

Spectrum[a]	hydrozincite (%)	Zn-LDH (%)	Zn-kerolite[b] (%)	sorbed ^{IV}Zn[c] (%)	Zn-calcite (%)	Sum (%)	NSSR (%)
GLO-WP	———	30	———	62 (Cc)	13	105	9.5
LUC2-WP	47	———	20 (80Zn)	27 (Cc)	———	94	2.8
TAL-WP	78	———	19 (60Zn)	———	———	97	2.9
SIS-WPC	85	———	———	———	———	85	0.4
LAUS-RPC	38	———	27 (60Zn)	36 (Fh)	———	101	2.2
SIS-RPC	33	———	47 (80Zn)	25 (Fh)	———	105	3.8

[a]WP=white limestone particles, WPC=white limestone particle crust, RPC=red limestone particle crust. [b](80Zn): $Zn_{0.8}Mg_{0.2}$-kerolite, (60Zn): $Zn_{0.6}Mg_{0.4}$-kerolite, [c](Cc): Zn-sorbed calcite, (Fh): Zn-sorbed ferrihydrite.

2.3.7. Speciation of Zn in whole soils by bulk EXAFS spectroscopy

The EXAFS spectra of the bulk soil samples and corresponding LCF spectra are shown in Figure 2.9. LCF results are provided in Table 2.8. The sum of the fitted fractions of Zn-rich kerolite ($Zn_{0.8}Mg_{0.2}$-kerolite or $Zn_{0.6}Mg_{0.4}$-kerolite), Zn-LDH, and hydrozincite (Σppt) indicates the total fraction of Zn contained in precipitates, and the sum of sorbed ^{IV}Zn and aqueous Zn (Σsorbed) represents the percentage of adsorbed and complexed Zn in tetrahedral and octahedral coordination. The percentage of precipitated Zn increased with increasing Zn/clay content (total Zn normalized over clay content, Table 2.1), showing that the speciation of Zn systematically shifted with Zn loading of the soils.

The low percentages of precipitates in soils GLO and LUC2 complicated the differentiation between Zn-LDH and ZnMg-kerolite. Using either Zn-LDH or $Zn_{0.8}Mg_{0.2}$-kerolite as proxy for precipitated Zn resulted in LCF with similar NSSR (see Fig. A1.3 and Table A1.2 in appendix 1 for details). Since only Zn-LDH was detected in the soil thin section of soil GLO, the fit based on Zn-LDH was listed in Table 2.8. For soil LUC2, the LCF based on $Zn_{0.8}Mg_{0.2}$-kerolite provided a visually better match to the Fourier-transformed EXAFS signal in the region of the second-shell (Fig. A1.3). Furthermore, pure $Zn_{0.8}Mg_{0.2}$-kerolite was identified in the soil thin section (Fig. 2.5 and Table 2.5). Therefore, the LCF based on $Zn_{0.8}Mg_{0.2}$-kerolite was reported in Table 2.8. In the higher contaminated soils BAS and LAUS, about half of the total Zn was associated with neoformed precipitates (Table 2.8). LCF based on Zn-LDH and minor fractions of sorbed ^{IV}Zn and aqueous Zn satisfactorily reproduced the experimental spectra (Fig. A1.3). However, adding $Zn_{0.8}Mg_{0.2}$-kerolite to the LCF led to a further decrease in the NSSR (Table A1.2) and improved the quality of the fit in the region of the second shell (Fig. A1.3, Table A1.2), suggesting that a minor fraction of a ZnMg-kerolite-type precipitate may have formed in addition to Zn-LDH. Only slightly higher NSSR were obtained if Zn-kerolite or $Zn_{0.6}Mg_{0.4}$-kerolite instead of $Zn_{0.8}Mg_{0.2}$-kerolite were used for LCF, due to the similarity in the respective reference spectra. Thus, the LCF of individual spectra was not sensitive to the exact Zn/(Zn+Mg) ratio of Zn-rich phyllosilicates. The similar LCF results for soils BAS and LAUS supported the assumption that comparable soil physicochemical conditions and Zn content result in similar Zn speciation. For the soils TAL and SIS with extreme Zn/clay contents (Table 2.1), LCF indicated that about half of the total soil Zn was bound in hydrozincite (Table 2.8). This finding was in agreement with the identification of hydrozincite crusts on limestone particles from both soils (Table 2.7, Fig. A1.5).

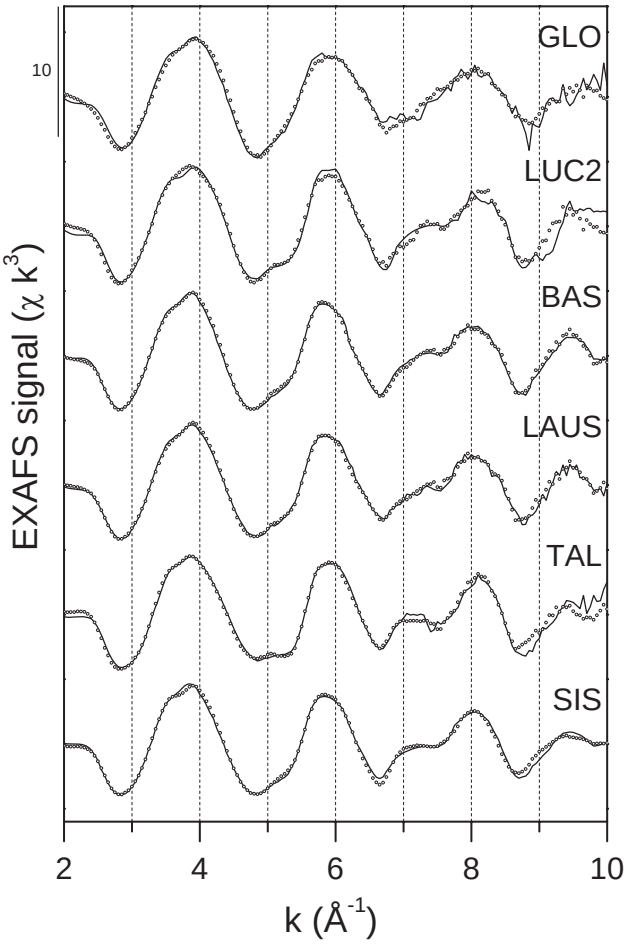

Figure 2.9. EXAFS spectra of the bulk soil samples (solid lines) and LCF spectra (dots). LCF results are provided in Table 2.8.

Table 2.8. Linear combination fits of the EXAFS spectra of the bulk soil samples (Fig. 2.9).

Spectrum	hydrozincite	Zn-LDH	Zn-kerolite[a]	sorbed ^{IV}Zn[b]	aqueous Zn	Sum	NSSR	Σppt[c]	Σsorbed[d]
	(%)	(%)	(%)	(%)	(%)	(%)	(%)	(%)	(%)
GLO	———	20	———	50 (Fh)	31	101	5.0	20	81
LUC2	———	———	29 (80Zn)	56 (Fh)	21	106	4.9	29	77
BAS	———	40	13 (80Zn)	26 (Cc)	22	101	0.8	53	48
LAUS	———	36	13 (80Zn)	34 (Cc)	17	100	1.3	49	51
TAL	52	———	25 (80Zn)	24 (Cc)	———	101	3.6	77	24
SIS	51	30	———	———	16	97	1.1	81	16

[a](80Zn): $Zn_{0.8}Mg_{0.2}$-kerolite, (60Zn): $Zn_{0.6}Mg_{0.4}$-kerolite, [b](Cc): Zn-sorbed calcite, (Fh): Zn-sorbed ferrihydrite, [c]sum of precipitate species (hydrozincite, Zn-LDH, and Zn-kerolite), [d]Sum of sorbed species (sorbed ^{IV}Zn and aqueous Zn).

2.3.8. Sequential extraction of Zn from spiked and contaminated soils

Sequential extraction results are presented in Figure 2.10 (absolute amounts of extracted Zn, Fe, and Mn are reported in the appendix 1, Table A1.3). The extractability of synthetic references spiked into a neutral non-calcareous soil increased in the order Zn-kerolite, Zn-LDH, hydrozincite. Sequential extractions with spiked quartz powder indicated the same sequence of extractability. Comparison between spiked soil and spiked quartz powder demonstrated that sequential extraction results for spiked soil were greatly affected by readsorption or reprecipitation [51]. Considering that the fractions F1 and F2 are intended to release mobile and easily mobilizable Zn [23], respectively, all 3 Zn species were readily extractable at slightly acidic pH of 6.0 in the presence of a complexing ligand (acetate). Rapid dissolution of Zn-LDH has also been observed at more acidic pH of 3.0 [52].

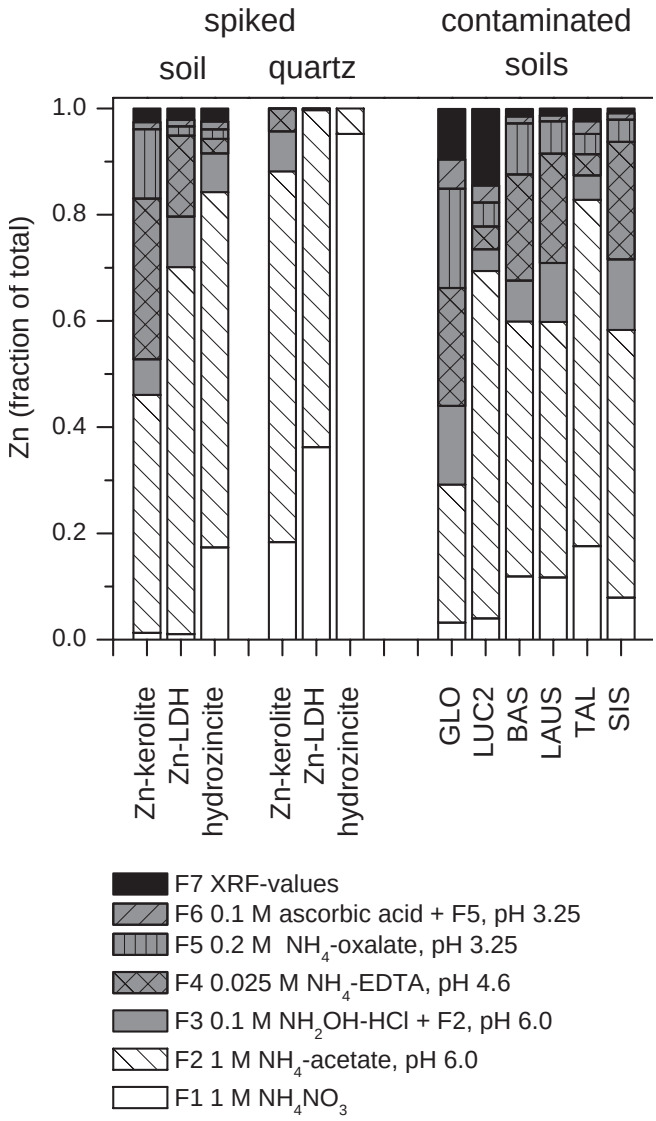

Figure 2.10. Fractionation of Zn by sequential extraction. Results for uncontaminated soil and quartz powder spiked with Zn-kerolite, Zn-LDH, and hydrozincite and for contaminated soil samples.

The lowest mobilizable percentage of total Zn (29% in F1+F2) was found for soil GLO, which contained the lowest fraction of precipitated Zn (Table 2.8). In contrast, between 59 and 83% of total Zn in the other soils was extracted in F1+F2, indicating that most Zn was present in labile form. Although hydrozincite represented about half of the total Zn in these soils, sequential extraction results from soil TAL were in much better agreement with the fractionation behaviour of hydrozincite than results from soil SIS. This observation can be related to the higher clay content, organic carbon content, and Zn content of soil SIS; factors favoring readsorption and reprecipitation during sequential extraction [53, 54].

2.3.9. Solubility of Zn in thermodynamic equilibrium with Zn-bearing precipitates

Solubility calculations for Zn in equilibrium with a series of Zn-bearing mineral phases are shown in Figure 2.11.

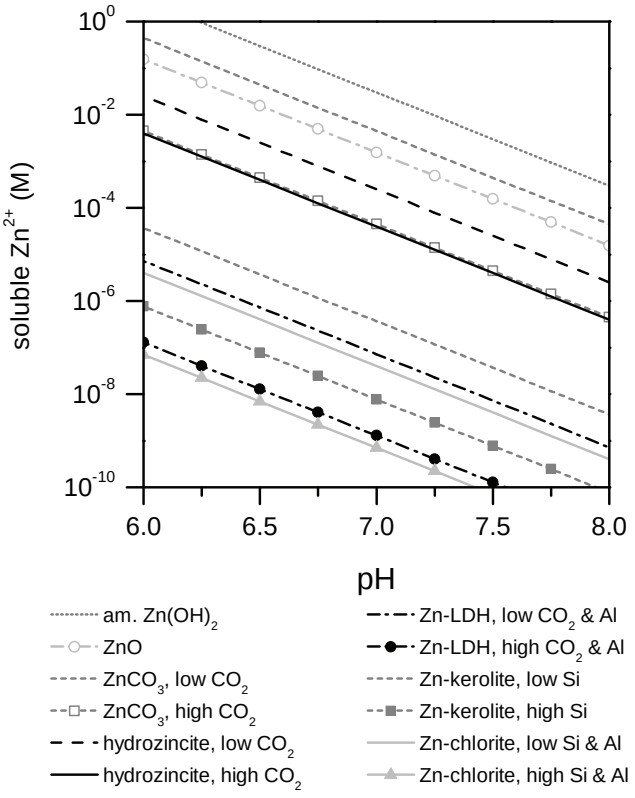

Figure 2.11. Solubility of Zn^{2+} in equilibrium with selected Zn-bearing phases. "low CO_2" and "high CO_2" denote calculations at atmospheric (3.2×10^{-4} atm) and hundredfold atmospheric CO_2 partial pressure. "low Al" and "high Al" denote calculations with Al^{3+} in equilibrium with gibbsite and amorphous $Al(OH)_3$, respectively. "low Si" and "high Si" calculations consider silicic acid in equilibrium with quartz ("low Si") and amorphous SiO_2 ("high Si").

Amongst the Zn (hydr)oxides and Zn (hydroxy)carbonates, hydrozincite is the thermodynamically most stable phase at typical soil pCO_2 levels. Formation of Zn (hydr) oxides might only occur at unrealistically low soil pCO_2. At high CO_2 partial pressure, smithsonite and hydrozincite result in similar Zn solubility. However, formation of smithsonite is limited by its slow precipitation kinetics relative to hydrozincite [5]. Even if low Si and Al concentrations in equilibrium with quartz and gibbsite are considered, Zn-phyllosilicates and Zn-LDH result in much lower Zn solubilities than hydrozincite, smithsonite, and Zn (hydr)oxides. Higher concentrations of Si and Al in equilibrium with amorphous SiO_2 and $Al(OH)_3$ and high pCO_2 even further decrease the solubility of Zn in equilibrium with Zn-phyllosilicates and Zn-LDH. With respect to Zn-phyllosilicates and Zn-LDH, the calculations indicate that the availabilities of Si and Al and the pCO_2 are critical in the control of the least soluble phase. In previous studies [9, 14], the solubility of Zn in the presence of Zn-LDH was estimated from a $logK_{so}$ of 19.94. This value had been derived from dissolution equilibria [55]. Here, we used a considerably lower $logK_{so}$ of 11.19 determined by calorimetry [45]. Based on this $logK_{so}$, the solubility of Zn in equilibrium with Zn-LDH varies in a similar range as in equilibrium with Zn-phyllosilicates. Depending on the concentrations of dissolved Al, Si, and CO_2, formation of Zn-LDH may even be thermodynamically favored over the formation of Zn-phyllosilicates, in contrast to trends previously estimated on the basis of the higher $logK_{so}$ from Johnson et al. [55].

2.4. Discussion

2.4.1. Changes in speciation with Zn loading and soil properties

Within the studied set of calcareous soils, increasing Zn loading (as indicated by Zn content divided by the clay size mass fraction) resulted in increasing precipitate formation and in a shift in precipitate type (Tables 2.1 and 2.8). These observations can be interpreted as a sequence of increasing Zn input into soil. Initially, Zn uptake is dominated by adsorption mechanisms. Adsorbed/complexed Zn species identified in soil thin sections included tetrahedrally coordinated Zn complexed by organic functional groups, adsorbed to Fe- and Mn-(hydr)oxides, and to calcite as well as octahedrally coordinated adsorbed Zn (outer-sphere or inner-sphere). With increasing saturation of adsorption sites, dissolved Zn concentrations increase and at some point exceed the solubility limits of Zn-bearing precipitates. In the soils GLO and LUC2, which had the lowest Zn contents within the studied set of soils, Zn-LDH and/or Zn-phyllosilicate formed, but represented minor fractions of the total Zn (Table 2.8). Depletion of readily available Si at higher Zn loadings may explain the predominant formation of LDH-

type precipitates in soils BAS and LAUS. Finally, extreme Zn input may deplete the readily available pools of both Si and Al, leading to the formation of hydrozincite. This was observed for the soil SIS and TAL with highest Zn loadings relative to their clay contents as well as locally on calcite particles from all soils except GLO. Overall, the observed trends in the extent and type of Zn precipitate formation with increasing Zn loading can be rationalized based on the availability of adsorption sites, Si and Al. In the present study, no clear relation between precipitate formation and soil pH was found. This can be attributed to the relatively narrow pH-range (pH 6.2 to 7.5) of the investigated carbonate-buffered soils.

2.4.2. Changes in Zn extractability with Zn loading and soil properties

Increasing Zn loading resulted in increasing precipitate formation and in a shift to precipitates which were found to be more readily released by sequential extraction when spiked into uncontaminated soils. The sequential extraction data from contaminated soils only partly reflected these trends, due to readsorption and reprecipitation phenomena that depend on Zn loading. However, the lower percentage of Zn extracted in F1+F2 from soil GLO than from soils with higher percentages of precipitated Zn clearly demonstrate that the incorporation of Zn into these precipitates does not correspond to a reduction in the extractability of Zn.

In contrast to Zn speciation inferred from EXAFS spectroscopy, which mainly varied with Zn loading, Ba-exchangeable fractions of Zn substantially varied with the availability of adsorption sites (ECEC, organic carbon content, clay content) and with adsorption affinity (controlled by soil pH) (Table 2.1). Although soil GLO contained ~5 times less Zn than soil TAL, its exchangeable Zn content was ~10 times higher. This reflected the much higher ECEC, clay and organic carbon content and the lower pH of soil GLO. Comparison of the soils LUC2 and LAUS, on the other hand, showed that higher Zn content at similar ECEC resulted in a higher exchangeable Zn content.

2.4.3. Formation and structure of layered Zn-precipitates

Previous studies demonstrated the formation of Zn-rich phyllosilicate and Zn-LDH in contaminated soils under field conditions [9, 11, 12, 14]. In the soil LUC2, we identified both types of precipitates in nearly pure form at different locations (Fig. 2.5, Table 2.5), likely as a consequence of differences in local chemical conditions.

Regarding the formation of Zn-phyllosilicate, the LCF of bulk- and μ-EXAFS spectra based on the reference spectra of Zn-rich kerolites were consistently better than fits based on the spectrum of pure Zn-kerolite. This observation is in agreement with previous EXAFS studies on the speciation of Zn in contaminated calcareous soils

[8, 10] and suggests that the formation of Zn-rich phyllosilicates is favored over the formation of the pure Zn-phyllosilicate endmember in the soil environment.

For many μ-EXAFS spectra for which LCF indicated the presence of Zn-LDH, the fits were significantly improved by including a minor fraction of Zn-rich kerolite (on average 14% of the sum of Zn-LDH and Zn-kerolite considering all μ-EXAFS for which LCF indicated Zn-LDH (n=14), Tables 2.4, 2.5 and 2.6). Similarly, Zn-kerolite accounted for about 25% of the precipitate fraction (Zn-LDH + Zn-kerolite) in the EXAFS spectra of BAS and LAUS (Table 2.8). The same Zn-LDH over Zn-kerolite ratio was obtained in a previous study on the speciation of Zn in a soil contaminated by ZnO [14]. There are at least five possible processes which could explain these observations: 1) The formation of mainly Zn-LDH and a minor fraction of Zn-phyllosilicate is related to the kinetics of precipitate formation and the supply of Si and Al [14]. 2) Rapid formation of Zn-LDH is followed by silicate incorporation into the interlayer and transformation of Zn-LDH into Zn-phyllosilicate [56, 57]. 3) Formation of Zn-phyllosilicate is followed by Zn-LDH formation after depletion of readily available Si. 4) Precipitates with phyllosilicate- and LDH-type structural features are forming. 5) A substantial fraction of total Zn is adsorbed at the edges of clay minerals.

Concerning the second possibility, experimental evidence for the transformation of Zn-LDH into Zn-phyllosilicate is still lacking. However, hexagonal zaccagnaite crystals (Zn-LDH mineral) in calcite veins in marble were found to be covered with a thin crust of fraipontite (Zn-phyllosilicate) [58], which may have formed from zaccagnaite in contact with Si-rich water. On the other hand, Zn speciation in a non-calcarous soil (pH 6.5, 15 g/kg org. C, 150 g/kg clay, 2800 mg/kg Zn) stabilized within 9 months after contamination with ZnO and about half of the Zn was incorporated into precipitates which were fit by ~75% Zn-LDH and ~25% Zn-phyllosilicate [14]. Almost the same Zn speciation was found for soils BAS and LAUS with similar soil characteristics after 3 decades of soil contamination. This suggests that transformation of Zn-LDH into Zn-phyllosilicate has not occurred to a major extent within this period of time. Regarding the third possibility - initial Zn-phyllosilicate formation followed by Zn-LDH precipitation at increasing Zn loading - it is worth noting that this interpretation is in line with the trend in precipitate type observed in our bulk soils. Concerning the fourth possibility, examples for layered Zn species with structural features of both Zn-kerolite and Zn-LDH include Zn-chlorite ($(Zn_5Al)(Si_3Al)O_{10}(OH)_8$, baileychlore [59]) and fraipontite ($(Zn, Al)_3(Si, Al)_2O_5(OH)_4$ [60]). Note that the thermodynamic calculations indicated a lower solubility of Zn in the presence of Zn-chlorite than in equilibrium with Zn-kerolite or Zn-LDH. Based on the average local coordination of Zn in Zn-chlorite (LDH-type and phyllosilicate-type layers in Zn-chlorite) and fraipontite (octahedral sheet with LDH-like composition

and only one adjacent tetrahedral sheet), we assume that the EXAFS spectra of these species would resemble a mixture of Zn-kerolite and Zn-LDH. As a fifth possibility, small fractions of Zn-kerolite in LCF dominated by Zn-LDH might serve as a proxy for Zn inner-spherically adsorbed at the edges of clay minerals. The EXAFS of this type of Zn sorption complex is characterized by the cancellation of second shell contributions from light atoms in the octahedral sheet and nearest Si neighbors in the tetrahedral sheets and the presence of a signal from next-nearest Si neighbors [61, 62]. The signal from next-nearest Si is also prominent in ZnMg-kerolite reference spectra [61]. Thus, small fractions of ZnMg-kerolite fit in addition to a major fraction of Zn-LDH might partly account for Zn adsorbed at the edges of clay minerals.

2.4.4. Formation of hydrozincite in soils

In the soils SIS and TAL with highest Zn loadings, around half of the Zn was contained in hydrozincite (Table 2.8, Fig. 2.9). However, none of the μ-EXAFS spectra from the clayey matrix of soil SIS indicated any hydrozincite, even if collected close to the surface of calcareous particles. In contrast, pure hydrozincite crusts were observed on isolated limestone particles without direct contact with the clayey matrix (Table 2.7, Fig. 2.8). This observation is in agreement with a laboratory study showing that Al and Si in solution promote Zn-phyllosilicate formation at the expense of hydrozincite precipitation [63] and with our thermodynamic calculations of Zn solubility in equilibrium with Zn-bearing phases, showing that Zn-kerolite and Zn-LDH are thermodynamically more stable than hydrozincite if Si and Al are present (Fig. 2.11). Microbially mediated precipitation of hydrozincite at nearly neutral pH has previously been documented in a stream contaminated by discharge from mine tailings [64]. Based on a first-shell Zn-O distance obtained from EXAFS shell fitting, Hansel and coworkers [65] postulated that hydrozincite had formed on the roots of wetland plants grown at a contaminated site. Furthermore, hydrozincite formation in calcareous soils has been postulated based on thermodynamic data [5]. However, this is the first study in which neoformed hydrozincite has been unequivocally identified in soil.

2.5. Conclusions

In contaminated calcareous soils, precipitation of Zn-phyllosilicate, Zn-LDH, and hydrozincite allows accumulation of increasing amounts of Zn exceeding the capacity for Zn uptake by adsorption, thereby limiting the leaching of Zn to deeper soil horizons and groundwater. The fraction of Zn in precipitates strongly depends on total Zn content and the availability of adsorption sites. Bulk and local Zn speciation inferred from EXAFS spectroscopy are in line with thermodynamic calculations on the solubility of

Zn in the presence of various Zn-bearing phases and indicate that Zn-LDH and Zn-phyllosilicate are preferably formed over hydrozincite in the presence of Al and Si. Because these precipitates only form at increasing saturation of adsorption sites, their attenuating effect on the short-term bioavailability of Zn is likely limited. In addition, accumulated Zn precipitates are readily mobilizable in the presence of complexing agents or under acidifying conditions. Thus, changes in soil chemical conditions might cause the release of previously accumulated Zn. This study focused on soils contaminated by aqueous Zn in the runoff water from galvanized power line towers. However, the same trends in Zn speciation are expected to apply to increasing amounts of Zn released from the weathering of Zn bearing contaminants or the decomposition of Zn-containing sewage sludge.

Acknowledgements

Jakob Frommer (ETH Zurich) is acknowledged for fruitful discussions regarding the analysis of XAS data. We thank Gerome Tokpa (ETH Zurich) for performing the sequential extraction of the soil samples and Kurt Barmettler (ETH Zurich) for help in the laboratory. Jon Chorover (Arizona University) and Evert Elzinga (Rutgers University) provided valuable feedback on earlier versions of this manuscript. The spectrum of Zn-sorbed calcite was kindly provided by Evert Elzinga. We thank André Puschnig (Natural History Museum Basel) and Beda Hofmann (Natural History Museum Bern) for providing smithonite and lithophorite, respectively. Stefan Mangold (XAS, ANKA, Germany) and Kumi Pandya (X11A, NSLS, USA) are acknowledged for their help with data acquisition. Robert Ford, Maarten Nachtegaal and an anonymous reviewer are thanked for their constructive comments on an earlier version of this manuscript. The Angströmquelle Karlsruhe GmbH (ANKA, Karlsruhe, Germany) and the Advanced Light Source (ALS, Berkeley, USA) are acknowledged for providing beamtime. The ALS is supported by the Director, Office of Science, Office of Basic Energy Sciences, Material Sciences Division, of the U.S. Departement of Energy under Contract No. DE-AC03-76SF00098 at Lawrence Berkeley National Laboratory. This project was financially supported by the Swiss National Science Foundation under contracts no. 200021-101876 and 200020-116592.

References

[1] Alloway, B. J., *Heavy Metals in Soils*. Chapman & Hall: London, 1995.

[2] Adriano, D. C., *Trace Elements in Terrestrial Environments: Biogeochemistry, Bioavailability, and Risks of Metals.* 2nd ed.; Springer: New York, 2001.

[3] Saeed, M.; Fox, R. L., Relations between suspension pH and zinc solubility in

acid and calcareous soils. *Soil Sci.* 1977, 124, 199-204.

[4] Sharpless, R. G.; Wallihan, E. F.; Peterson, F. F., Retention of zinc by some arid zone soil materials treated with zinc sulfate. *Soil Sci. Soc. Am. P.* 1969, 33, 901-904.

[5] Schindler, P.; Reinert, M.; Gamsjäger, H., Löslichkeitskonstanten und freie Bildungsenthlapien von $ZnCO_3$ und $Zn_5(OH)_6(CO_3)_2$ bei 25°C. *Helvetica Chimica Acta* 1969, 52, 2327-2332.

[6] Reeder, R. J.; Lamble, G. M.; Northrup, P. A., XAFS study of the coordination and local relaxation around Co^{2+}, Zn^{2+}, Pb^{2+}, and Ba^{2+} trace elements. *Am. Mineral.* 1999, 84, 1049-1060.

[7] Isaure, M.-P.; Manceau, A.; Geoffroy, N.; Laboudigue, A.; Tamura, N.; Marcus, M. A., Zinc mobility and speciation in soil covered by contaminated dredged sediment using micrometer-scale and bulk-averaging X-ray fluorescence, absorption and diffraction techniques. *Geochim. Cosmochim. Acta* 2005, 69, 1173-1198.

[8] Kirpichtchikova, T. A.; Manceau, A.; Spadini, L.; Panfili, F.; Marcus, M. A.; Jacquet, T., Speciation and solubility of heavy metals in contaminated soil using X-ray microfluorescence, EXAFS spectroscopy, chemical extraction, and thermodynamic modeling. *Geochim. Cosmochim. Acta* 2006, 70, 2163-2190.

[9] Panfili, F. R.; Manceau, A.; Sarret, G.; Spadini, L.; Kirpichtchikova, T.; Bert, V.; Laboudigue, A.; Marcus, M. A.; Ahamdach, N.; Libert, M. F., The effect of phytostabilization on Zn speciation in a dredged contaminated sediment using scanning electron microscopy, X-ray fluorescence, EXAFS spectroscopy, and principal components analysis. *Geochim. Cosmochim. Acta* 2005, 69, 2265-2284.

[10] Manceau, A.; Lanson, B.; Schlegel, M. L.; Harge, J. C.; Musso, M.; Eybert-Berard, L.; Hazemann, J. L.; Chateigner, D.; Lamble, G. M., Quantitative Zn speciation in smelter-contaminated soils by EXAFS spectroscopy. *Am. J. Sci.* 2000, 300, 289-343.

[11] Juillot, F.; Morin, G.; Ildefonse, P.; Trainor, T. P.; Benedetti, M.; Galoisy, L.; Calas, G.; Brown, G. E., Occurrence of Zn/Al hydrotalcite in smelter-impacted soils from northern France: Evidence from EXAFS spectroscopy and chemical extractions. *Am. Mineral.* 2003, 88, 509-526.

[12] Nachtegaal, M.; Marcus, M. A.; Sonke, J. E.; Vangronsveld, J.; Livi, K. J. T.; Van der Lelie, D.; Sparks, D. L., Effects of in situ remediation on the speciation and bioavailability of zinc in a smelter contaminated soil. *Geochim. Cosmochim. Acta* 2005, 69, 4649-4664.

[13] Schuwirth, N.; Voegelin, A.; Kretzschmar, R.; Hofmann, T., Vertical distribution and speciation of trace metals in weathering flotation residues of a zinc/lead sulfide mine. *J. Environ. Qual.* 2007, 36, 61-69.

[14] Voegelin, A.; Pfister, S.; Scheinost, A. C.; Marcus, M. A.; Kretzschmar, R., Changes in zinc speciation in field soil after contamination with zinc oxide. *Environ. Sci. Technol.* 2005, 39, 6616-6623.

[15] Manceau, A.; Marcus, M. A.; Tamura, N.; Proux, O.; Geoffroy, N.; Lanson, B., Natural speciation of Zn at the micrometer scale in a clayey soil using X-ray fluorescence, absorption, and diffraction. *Geochim. Cosmochim. Acta* 2004, 68, 2467-2483.

[16] Manceau, A.; Tommaseo, C.; Rihs, S.; Geoffroy, N.; Chateigner, D.; Schlegel, M. L.; Tisserand, D.; Marcus, M. A.; Tamura, N.; Zueng-Sang, C., Natural speciation of Mn, Ni, and Zn at the micrometer scale in a clayey paddy soil using X-ray fluorescence, absorption, and diffraction. *Geochim. Cosmochim. Acta* 2005, 60, 4007-3034.

[17] Scheinost, A. C.; Kretzschmar, R.; Pfister, S.; Roberts, D. R., Combining selective sequential extractions, X-ray absorption spectroscopy, and principal component analysis for quantitative zinc speciation in soil. *Environ. Sci. Technol.* 2002, 36, 5021-5028.

[18] Manceau, A.; Tamura, N.; Celestre, R. S.; MacDowell, A. A.; Geoffroy, N.; Sposito, G.; Padmore, H. A., Molecular-scale speciation of Zn and Ni in soil ferromanganese nodules from loess soils of the Mississippi Basin. *Environ. Sci. Technol.* 2003, 37, 75-80.

[19] Isaure, M.-P.; Laboudigue, A.; Manceau, A.; Sarret, G.; Tiffrau, C.; Trocellier, P.; Lamble, G. M.; Hazemann, J. L.; Chateigner, D., Quantitative Zn speciation in a contaminated dredged sediment by μ-PIXE, μ-SXRF, EXAFS spectroscopy and principal component analysis. *Geochim. Cosmochim. Acta* 2002, 66, 1549-1567.

[20] Bertling, S.; Wallinder, I. O.; Leygraf, C.; Kleja, D. B., Occurrence and fate of corrosion-induced zinc in runoff water from external structures. *Sci. Total Environ.* 2006, 367, 908-923.

[21] Gee, G.; Or, D., Particle size analysis. In *Methods of Soil Analysis. Part4. Physical Methods*, Dane, J. H.; Topp, C. C., Eds. Soil Science Society of America, Madison, USA: 2002; pp 255-293.

[22] Hendershot, W. H.; Duquette, M., A simple chloride method for determining cation exchange capacity and exchangeable cations. *Soil Sci. Soc. Am. J.* 1986, 50, 605-608.

[23] Zeien, H.; Brümmer, G. W., Chemische Extraktionen zur Bestimmung von Schwermetallbindungsformen in Böden. *Mitt. Dtsch. Bodenkundl. Ges.* 1989, 59, 505-510.

[24] Voegelin, A.; Tokpa, G.; Jacquat, O.; Barmettler, K.; Kretzschmar, R., Zinc fractionation in contaminated soils by sequential and single extractions: Influence of soil properties and zinc content. *J. Environ. Qual.* 2008, 37, 1190-1200.

[25] Decarreau, A., Cristallogène expérimentale des smectites magnésiennes: hectorite, stévensite. *Bull. Mineral.* 1980, 103, 570-590.

[26] Taylor, R. M., The rapid formation of crystalline double hydroxy salts and other compounds by controlled hydrolysis. *Clay Miner.* 1984, 19, 591-603.

[27] Lothenbach, B.; Furrer, G.; Schulin, R., Immobilization of heavy metals by polynuclear aluminium and montmorillonite compounds. *Environ. Sci. Technol.* 1997, 31, 1452-1462.

[28] Genin, P.; Delahayevidal, A.; Portemer, F.; Tekaiaelhsissen, K.; Figlarz, M., Preparation and characterization of alpha-type nickel hydroxides obtained by chemical precipitation - study of the anionic species. *Eur. J. Solid State Inorg. Chem.* 1991, 28, 505-518.

[29] Schosseler, P. M.; Wehrli, B.; Schweiger, A., Uptake of Cu^{2+} by the calcium carbonates vaterite and calcite as studied by continuous wave (CW) and pulse electron paramagnetic resonance. *Geochim. Cosmochim. Acta* 1999, 63, 1955-1967.

[30] Feng, X. H.; Liu, F.; Tan, W. E.; Liu, X. W., Synthesis of birnessite form the oxidation of Mn^{2+} by O_2 in alkali medium: effects of synthesis conditions. *Clay Miner.* 2004, 52, 240-250.

[31] Giovanoli, R.; Stähli, E.; Feitknecht, W., Über Oxidhydroxide des vierwertigen Mangans mit Schichtengitter. *Helv. Chim. Acta* 1970, 27, 209-220.

[32] Lanson, B.; Drits, V. A.; Gaillot, A.-C.; Silvester, E.; Plançon, A.; Manceau, A., Structure of heavy-metal sorbed birnessite: Part 1. Results from X-ray diffraction. *Am. Mineral.* 2002, 87, 1631-1645.

[33] Rodrigues-Filho, U. P.; Vaz Jr., S.; Felicissimo, M. P.; Scarpellini, M.; Cardoso, D. R.; Vinhas, R. C. J.; Landrers, R.; Schneider, J. F.; McGarvey, B. R.; Andersen, M. L.; Skibsted, L. H., Heterometallic manganese/zinc-phytate complex as model compound for metal storage in wheat grains. *J. Inorg. Biochem.* 2005, 99, 1973-1982.

[34] Waychunas, G. A.; Fuller, C. C.; Davis, J. A., Surface complexation and precipitate geometry for aqueous Zn(II) sorption on ferrihydrite: I. X-ray

absorption extended fine structure spectroscopy analysis. *Geochim. Cosmochim. Acta* 2002, 66, 1119-1137.

[35] Elzinga, E. J.; Reeder, R. J., X-ray absorption spectroscopy study of Cu^{2+} and Zn^{2+} adsorption complexes at the calcite surface: Implications for site-specific metal incorporation preferences during calcite crystal growth. *Geochim. Cosmochim. Acta* 2002, 66, 3943-3954.

[36] Marcus, M. A.; MacDowell, A. A.; Celestre, R. S.; Manceau, A.; Miler, T.; Padmore, H. A.; Sublett, R. E., Beamline 10.3.2 at ALS: a hard X-ray microprobe for environmental and materials science. *J. Synchrotron Rad.* 2002, 11, 239-247.

[37] Newville, M., IFEFFIT: interactive XAFS analysis and FEFF fitting. *J. Synchrotron Rad.* 2001, 8, 322-324.

[38] Ravel, B.; Newville, M., Athena, Artemis, Hephaestus: data analysis for X-ray absorption spectroscopy using IFEFFIT. *J. Synchrotron Rad.* 2005, 12, 537-541.

[39] Webb, S. M., SIXPack: a graphical user interface for XAS analysis using IFEFFIT. *Phys. Scr.* 2005, T115, 1011-1014.

[40] Malinowski, E. R., Determination of the number of factors and the experimental error in a data matrix. *Anal. Chem.* 1977, 49.

[41] Malinowski, E. R., Theory of error for target factor analysis with applications to mass spectrometry and nuclear magnetic resonance spectrometry. *Anal. Chim. Acta* 1978, 103, 339-354.

[42] Sarret, G.; Balesdent, J.; Bouziri, L.; Garnier, J. M.; Marcus, M. A.; Geoffroy, N.; Panfili, F.; Manceau, A., Zn speciation in the organic horizon of a contaminated soil by micro-x-ray fluorescence, micro- and powder-EXAFS spectroscopy, and isotopic dilution. *Environ. Sci. Technol.* 2004, 38, 2792-2801.

[43] Manceau, A.; Boisset, M. C.; Sarret, G.; Hazemann, R. L.; Mench, M.; Cambier, P.; Prost, R., Direct determination of lead speciation in contaminated soils by EXAFS spectroscopy. *Environ. Sci. Technol.* 1996, 30, 1540-1552.

[44] Preis, W.; Gamsjager, H., (Solid plus solute) phase equilibria in aqueous solution. XIII. Thermodynamic properties of hydrozincite and predominance diagrams for (Zn^{2+}+H_2O+CO_2). *J. Chem. Thermodyn.* 2001, 33, 803-819.

[45] Allada, R. K.; Peltier, E.; Navrotsky, A.; Casey, W. H.; Johnson, C. A.; Berbeco, H. T.; Sparks, D. L., Calorimetric determination of the enthalpies of formation of hydrotalcite-like solids and their use in the geochemical modeling of metals in natural waters. *Clays Clay Miner.* 2006, 54, 409-417.

[46] Vieillard, P., New method for the prediction of Gibbs free energies of formation

of phyllosilicates (10 Å and 14 Å) based on the electronegativity scale. *Clays Clay Miner.* 2002, 50, 352-363.

[47] Allison, J. D.; Brown, D. S.; Novo-Gradac, K. J., MINTEQA2/PRODEFA2, a geochemical assessment model for environmental systems. *U.S. Environemtal Protection Agency* 1991.

[48] VBBo, Verordnung über Belastungen des Bodens (Swiss Ordinance relating to Impacts on Soil). *SR 814.12, Eidgenössische Drucksachen und Materialzentrale, Bern, Switzerland.* 1998.

[49] Manceau, A.; Marcus, M. A.; Tamura, N., Quantitative speciation of heavy metals in soils and sediments by synchrotron X-ray techniques. In *Application of synchrotron radiation in low-temperature geochemistry and environmental science*, Fenter, P. A.; Rivers, M. L.; Sturchio, N. C.; Sutton, S. R., Eds. Mineralogical Society of America, Washington, DC: 2002; Vol. 49.

[50] Marcus, M. A.; Manceau, A.; Kersten, M., Mn, Fe, Zn and As speciation in a fast-growing ferromanganese marine nodule. *Geochim. Cosmochim. Acta* 2004, 68, 3125-3136.

[51] Gleyzes, C.; Tellier, S.; Astruc, M., Fractionation studies of trace elements in contaminated soils and sediments: a review of sequential extraction procedures. *Trac-Trend Anal. Chem.* 2002, 21, 451-467.

[52] Voegelin, A.; Kretzschmar, R., Formation and dissolution of single and mixed Zn and Ni precipitates in soil: Evidence from column experiments and extended X-ray absorption fine structure spectroscopy. *Environ. Sci. Technol.* 2005, 39, 5311-5318.

[53] Kheboian, C.; Bauer, C. F., Accuracy of selective extraction procedures for metal speciation in model aquatic sediments. *Anal. Chem.* 1987, 59, 1417-1423.

[54] Shan, X. Q.; Bin, C., Evaluation of sequential extraction for speciation of trace-metals in model soil containing natural minerals and humic acid. *Anal. Chem.* 1993, 65, 802-807.

[55] Johnson, C.A.; Glasser, F.P., Hydrotalcite-like minerals ($M_2Al(OH)_6(CO_3)_{0.5}\cdot XH_20$, where M = Mg, Zn, Co, Ni) in the environment: synthesis, characterization and thermodynamic stability. *Clays Clay Miner.* 2003, 51, 357-357.

[56] Depège, C.; El Metoui, F.-Z.; Forano, C.; De Roy, A.; Dupuis, J.; Besse, J.-P., Polymerization of silicates in layered double hydroxides. *Chem. Mater.* 1996, 8, 952-960.

[57] Ford, R. G.; Sparks, D. L., The nature of Zn precipitates formed in the presence of pyrophyllite. *Environ. Sci. Technol.* 2000, 34, 2479-2483.

[58] Merlino, S.; Orlandi, P., Carraraite and zaccagnaite, two new minerals from the

Carrara marble quarries: their chemical compositions, physical properties, and structural features. *Am. Mineral.* 2001, 86, 1293-1301.

[59] Rule, A. C.; Radke, F., Baileychlore, the Zn end member of the trioctahedral chlorite series. *Am. Mineral.* 1988, 73, 135-139.

[60] Cesàro, G., Sur la fraipontite, silicate basique hydraté de zinc et d'alumine. *Anal. Soc. Geol. Be.* 1927, 50, B106-111.

[61] Schlegel, M. L.; Manceau, A.; Charlet, L.; Hazemann, J. L., Adsorption mechanisms of Zn on hectorite as a function of time, pH, and ionic strength. *Am. J. Sci.* 2001, 301, 798-830.

[62] Schlegel, M. L.; Manceau, A., Evidence for the nucleation and epitaxial growth of Zn phyllosilicate on montmorillonite. *Geochim. Cosmochim. Acta* 2006, 70, 901-917.

[63] Tiller, K. G.; Pickering, J. G., Synthesis of zinc silicates at 20°C and atmospheric pressure. *Clays Clay Miner.* 1974, 22, 409-416.

[64] Podda, F.; Zuddas, P.; Minacci, A.; Pepi, M.; Baldi, F., Heavy metal coprecipitation with hydrozincite [$Zn_5(CO_3)_2(OH)_6$] from mine waters caused by photosynthetic microorganisms. *Appl. Environ. Microbiol.* 2000, 66, 5092-5098.

[65] Hansel, C. M.; Fendorf, S.; Sutton, S.; Newville, M., Characterization of Fe plaque and associated metals on the roots of mine-waste impacted aquatic plants. *Environ. Sci. Technol.* 2001, 35, 3863-3868.

3. Local coordination of Zn in hydroxy-interlayered minerals and implications for Zn retention in soils

Abstract

The objective of this study was to determine the local coordination of Zn in hydroxy-interlayered smectite (HIS) as a function of Zn loading and synthesis conditions and to assess the importance of hydroxy-interlayered minerals (HIM) for Zn retention in contaminated soils. Published and newly collected extended X-ray absorption fine structure (EXAFS) spectra of HIS reacted with Zn at molar Zn/hydroxy-Al ratios from 0.013 to 0.087 (corresponding to final Zn contents of 1615-8600 mg/kg Zn) were evaluated by shell fitting. In Zn-HIS, Zn was octahedrally coordinated to oxygen at 2.06-2.08 Å and surrounded by Al atoms at 3.03-3.06 Å in the second-shell. With increasing molar Zn/hydroxy-Al ratio, the coordination number of second-shell Al decreased from 6.6 to 2.1. These results were interpreted as a progressive shift from Zn incorporation in the vacancies of gibbsitic Al-polymers to Zn adsorption to incomplete Al-polymers and finally uptake by cation exchange in the polymer-free interlayer space of HIS with increasing Zn loadings. In a second part, we determined the speciation of Zn in eight contaminated soils (251-1039 mg/kg Zn) with acidic to neutral pH (pH 4.1-6.9) using EXAFS spectroscopy. All soils contained hydroxy-Al interlayered vermiculite (HIV). The analysis of EXAFS spectra by linear combination fitting (LCF) showed that a substantial fraction of total Zn (29-84%) was contained in HIM with high Zn loading. The remaining Zn was adsorbed to organic and inorganic soil components and incorporated into phyllosilicates. In sequential extractions of Zn-HIS spiked into quartz powder and the Zn contaminated soils, Zn was mainly released in the two most resistant fractions, in qualitative agreement with the findings from LCF. Our results suggest that formation of Zn-HIM may strongly retain Zn in pristine and moderately contaminated acidic to neutral soils. Due to their limited sorption capacity, however, HIM do not allow for the accumulation of high levels of Zn in response to continued Zn input into soils.

Published as: Jacquat, O., Voegelin, A., Kretzschmar, R., Local coordination of Zn in hydroxy-interlayered minerals and implications for Zn retention in soils. Geochim. Cosmochim. Acta 2009, 73, 348-363.

3.1. Introduction

Hydroxy-interlayered minerals (HIM) are phyllosilicates containing hydroxy-polymers in their interlayer. They can form as a weathering product of chlorite or by the formation of hydroxy-polymers within the interlayers of smectite (HIS) and vermiculite (HIV) [1]. The positively charged hydroxy-polymers in the interlayer are either dioctahedral (gibbsitic) or trioctahedral (brucitic) island-type structures depending on the composing cations [2, 3]. Dioctahedral hydroxy-Al is the principal component of the non-exchangeable interlayer material in acidic soils, whereas trioctahedral hydroxy-Mg interlayering may be significant in marine sediments and alkaline soils [3]. Moderately acidic soil pH, low organic matter content, oxidizing conditions and frequent wetting and drying are considered to favor the pedogenic formation of hydroxy-Al interlayered phyllosilicates [3].

The formation of hydroxy-Al interlayers in smectites or vermiculites strongly reduces the cation exchange capacity (CEC) and affects the ion sorption properties of the clay minerals [1, 4, 5]. Laboratory studies have shown that Cu, Cd, Ni, Pb, and Zn sorb strongly to hydroxy-Al interlayered montmorillonite under acidic conditions, while adsorption to pure montmorillonite at acidic pH is dominated by cation exchange [4, 6, 7]. Furthermore, hydroxy-Al polymers bound to a clay surface have a higher affinity for metal sorption than pure Al hydroxides [8]. Recent studies on Zn sorption to hydroxy-interlayered minerals using extended X-ray absorption fine structure (EXAFS) spectroscopy confirmed the uptake of Ni and Zn into the vacant octahedral sites of gibbsitic hydroxy-Al interlayers in montmorillonite [9, 10]. Uptake of Zn into the vacant sites of gibbsitic sheets has also been documented for the phyllomanganate lithiophorite [11, 12]. In contrast, uptake of tetrahedrally or octahedrally coordinated Zn by pure gibbsite is mainly due to the formation of mononuclear bidentate sorption complexes [10, 13].

The incorporation of Zn into the hydroxy-Al interlayers of HIM by specific adsorption may have a substantial impact on Zn bioavailability and mobility in acidic soils, where adsorption is otherwise mainly due to cation exchange [4, 14]. Using bulk- and μ-EXAFS spectroscopy, Zn incorporated into HIM (Zn-HIM) has so far been detected in one contaminated [14] and two uncontaminated acidic soils [12, 15].

To date, the influence of the mode of Zn uptake (adsorption/coprecipitation) and of Zn loading on the local coordination of Zn in Zn-HIM has not been studied. Furthermore, data on the abundance of Zn-HIM in soils as a function of their physicochemical properties and on the importance of Zn-HIM for immobilization of Zn in soils is still lacking. The first objective of this study was to characterize the local coordination of Zn

in a series of synthetic Zn-HIS in relation to synthesis conditions and Zn content. Based on these findings, the second objective was to determine the abundance and Zn-loading of Zn-HIM in a series of HIM-containing soils with different soil characteristics and variable level of Zn contamination using EXAFS spectroscopy. Finally, we aimed at relating Zn reactivity as inferred from batch and sequential extractions to molecular-level Zn speciation. For the purpose of this study, soils were sampled near galvanized power line towers. The soils differed in composition, but were all contaminated by aqueous Zn in the runoff water from the towers. This allows studying the effect of soil properties and Zn concentration on the formation of pedogenic Zn species without interference from primary Zn-bearing contaminants.

3.2. Experimental Section

3.2.1. Soil samples and bulk soil properties

Eight topsoils (GER, MOM, SAR, CHI1, BUN, GRÜ, BIB2, HAU) developed from different parent materials were sampled across Switzerland close to the foundations of galvanized power line towers (Table 3.1). Runoff water containing aqueous Zn from the corrosion of the galvanized steel surfaces [16] has led to local Zn contamination. The soils have developed from metamorphic (SAR), igneous (MOM, CHI) and sedimentary bedrocks (GER, BUN, GRÜ, BIB2, HAU). About 1 kg of the upper soil layer (0-5 cm) was collected at each site, air-dried at 25°C, homogenized using an agate mortar and sieved to <2 mm. The dry samples were stored in plastic containers in the dark at room temperature.

Table 3.1. Physicochemical properties and Zn contents of the soil samples.

Soil	Geology	pH	TOC	TIC	Texture			ECEC[a]	Total Zn	Exch. Zn[b]
		$CaCl_2$			Clay	Silt	Sand			(mg/kg)
			(g/kg)	(g/kg)	——	(g/kg)	——	($mmol_c$/kg)	(mg/kg)	(%)
GER	Alluvium	4.1	27	-	48	348	604	40	403	104 (26)
MOM	Paragneiss	4.6	37	-	77	302	621	25	1039	286 (28)
SAR	Schist	4.6	52	-	105	700	195	78	251	35 (14)
CHI1	Orthogneiss	4.9	14	-	42	149	809	4	971	118 (12)
BUN	Conglomerate	5.5	44	-	215	455	330	149	852	139 (16)
GRÜ	Glacial till	6.0	36	0.3	253	363	384	146	852	99 (12)
BIB2	Conglomerate	6.1	36	1.1	324	344	332	232	861	21 (2)
HAU	Limestone	6.9	42	0.2	227	320	453	102	276	<1 (<0.3)

[a]Effective cation exchange capacity. [b]Exchangeable Zn in 0.1 M $BaCl_2$ (SSR 30 mL/g; in parentheses percentage of total Zn).

For analyses requiring powdered and homogenized material, an agate disc swing mill was used to prepare <50 µm powdered subsamples from the <2 mm soil material.
The soil pH was determined with a glass electrode in a suspension of 1 g of soil in 10 mL of 0.01 M $CaCl_2$ solution. Prior to measurement, the soil suspension was shaken for 10 minutes and equilibrated for at least 30 minutes. Total metal contents were quantified by analyzing pressed pellets (4 g powdered soil <50 µm and 0.9 g Licowax C®) with energy dispersive X-ray fluorescence (XRF) spectrometry (Spectro X-lab 2000). The exchangeable contents of Na, Mg, Al, K, Ca, Mn, and Fe were determined in duplicates by extracting 7 g of soil with 0.1 M $BaCl_2$ (prepared from doubly deionized water (DDI), 18.2 MΩ·cm, Milli-Q® Element, Millipore) at a solution-to-solid ratio (SSR) of 30 mL/g [17]. After centrifugation, the solutions were filtered (0.45 µm nylon filter, WICOM®) and acidified (1 % (v/v) 30 % HNO_3). The extracts were analyzed by inductively coupled plasma – optical emission spectrometry (ICP-OES, Varian Vista-MPX). The effective cation exchange capacity (ECEC) was calculated from the charge equivalents of the extracted amounts of Na^+, Mg^{2+}, Al^{3+}, K^+, Ca^{2+}, and Mn^{2+}. Total carbon contents (TC) of powdered samples (<50 µm) were determined using a CHNS element analyzer (LECO CHNS-932). Total inorganic contents (TIC) of soils with pH>5.9 were determined by reacting 0.3-0.9 g of powdered soil <50 µm with 1 M H_2SO_4 in a reaction flask. The evolving CO_2 was trapped in a Nesbitt bulb containing NaOH-coated pellets and quantified gravimetrically. Total organic carbon contents were determined by subtracting the respective TIC content form the TC content. After pretreatment of the soil material <2 mm with H_2O_2 for removal of organic matter, the sand content (50-2000 µm) was quantified by wet sieving and the clay content (<2 µm) was determined using the pipette method [18]. The silt content (2-50 µm) of the soil samples was calculated to be the difference between the total soil weight and the sum of the sand and clay content [18].

3.2.2. Clay extraction and analysis

To isolate the <2 µm size (clay) fraction, 20 g of soil were dispersed in 800 mL of 0.5 M NaCl. The suspension was subsequently sonified for 1 minute and passed through a 50 µm sieve. The sieved fraction >50 µm was twice resuspended in DI water and sieved again to collect more fine material. The three bottles containing the filtrate were subsequentlyy centrifuged, the water decanted, and the sediment <50 µm resuspended and merged. After vigorous mixing of the suspension in a plastic bottle and allowing the settling of material >2 µm (time calculated from Stoke's law), the top 10 cm of the 14 cm high water column were siphoned off. This procedure was repeated twice with fresh DI water to collect more clay [19]. The three clay suspensions were flocculated by $MgCl_2$ addition and merged. Excess salt was removed by three washing steps with DDI

water until the supernatant was free of chloride ($AgNO_3$ test). The Mg-saturated clay was frozen in liquid N_2 (LN) and freeze-dried. K-saturated clay was prepared by exchanging 30 mg of Mg-saturated clay with 10 mL of 1 M KCl [20]. For complete exchange of the interlayer cations, the KCl solution was renewed twice. Excess salt was removed by three washing and centrifugation steps (5 min, 3400 g) using DDI water. Oriented specimens of the Mg- and K-saturated clay fractions were prepared by air-drying 30 mg of clay onto glass slides of 2.5 cm diameter. Ethylene glycol (EG) and glycerol (Gly) solvation was obtained by leaving an oriented Mg-saturated mount on the shelf of an EG or Gly-containing desiccator for 6 h at 60 °C and for 12 h at 110°C, respectively [21, 22]. Oriented specimens of the citrate-extracted soil clay fraction (see section 2.8 for details) were similarly prepared and analyzed. The K-saturated samples were placed for at least 1 h in a preheated muffle furnace at 100°, 300° and 550 °C and measured by X-ray diffraction (XRD) after each heat treatment. X-ray diffraction patterns of the clay fractions were recorded on a Bruker D4 diffractometer equipped with a Cu anode and an energy dispersive SOL-X Si(Li) detector. Patterns were measured in continuous scan mode from 3° to 37° 2-theta using variable slits, step size of 0.02° and a counting time of 4 s per step.

3.2.3. Reference compounds for EXAFS spectroscopy

In this study, we evaluated published and newly collected reference spectra for Zn-containing HIS, which differed in synthesis conditions (Table 3.2). All samples had in common that HIS was prepared by reacting Al with smectite (montmorillonite) at a ratio of 2 mmol/g. However, they differed in the duration of HIS aging (before/after Zn addition), mode of Zn incorporation (either coprecipitation during Al hydrolysis or sorption to preformed HIS), molar ratio of reacted Zn over hydroxy-Al ("Zn/Al ratio") and pH during Zn uptake (Table 3.2). Published EXAFS spectra for Zn-HIS synthesized by adsorbing Zn to preformed HIS at low Zn/Al ratios and near-neutral pH [10] were kindly provided by Michel Schlegel (Commissariat à l'Énergie Atomique (CEA), Saclay, France). Briefly, HIS was synthesized from MX-80 montmorillonite (Clay Spur bed, Wyoming, USA; N_2-BET surface area of 31.3 m^2/g [23]). At pH 6.0 and 7.0, Zn-HIS was obtained by reacting 2 g/L of the HIS with 50 or 200 µM $ZnCl_2$, corresponding to Zn/Al ratios of 0.0125 and 0.05, respectively. After 1 d, the Zn-HIS were isolated ("Zn-HIS-1.6-pH6", "Zn-HIS-1.6-pH7", and "Zn-HIS-6.5-pH7" in Table 3.2). Reference materials for Zn coprecipitated with Al during HIS formation were prepared in our laboratory at Zn/Al ratios of 0.2 and 0.5 at pH 4.5 and over a reaction period of 15 d ("Zn-HIS-7.6-CPT" and "Zn-HIS-7.7-CPT", respectively, in Table 3.2), as described in Scheinost et al. [14]. Also over a reaction time of 15 d, Zn was sorbed to

preformed HIS at a Zn/Al ratio of 0.5 at pH 5.0 (“Zn-HIS-5.7-pH5” in Table 3.2).

Table 3.2. Synthesis conditions of Zn-HIS phases, product compostion, and results from LCF.

	Synthesis conditions				Product composition		LCF results			
Sample name	pH	Initial[d] Zn/Al	Time[e] (d)	Uptake Mode[f]	Zn (mg/kg)	Final Zn/Al	Zn-6Al[h] (%)	Zn-2Al[i] (%)	Zn-OS[j] (%)	NSSR (%)
Zn-HIS-1.6-pH6[a]	6.0	0.013	1	Ads	1615	0.013	——	——	——	——
Zn-HIS-1.6-pH7[a]	7.0	0.013	1	Ads	1625	0.013	100	——	——	0.5
Zn- HIS-6.5-pH7[a]	7.0	0.05	1	Ads	6500	0.05	97	——	——	0.6
Zn-HIS-7.6-CPT[b]	4.5	0.2	15	Cpt	7600	0.067[g]	78	——	15	2.9
Zn-HIS-7.7-CPT[b]	4.5	0.5	15	Cpt	7750	0.069[g]	71	——	21	2.5
Zn-HIS-2.1-pH5	5.0	1.0	0.63	Ads	2100	0.019[g]	73	——	19	2.4
Zn-HIS-2.9-pH5	5.0	2.5	0.63	Ads	2900	0.026[g]	51	37	10	1.1
Zn-HIS-4.0-pH5	5.0	5	0.63	Ads	4000	0.035[g]	41	61	——	1.1
Zn-HIS-5.7-pH5[b]	5.0	0.5	15	Ads	5700	0.050[g]	34	49	17	2.0
Zn-HIS-6.9-pH5	5.0	10	0.63	Ads	6900	0.061[g]	23	60	16	1.6
Zn-HIS-8.6-pH5	5.0	25	0.63	Ads	8600	0.087[g]	19	57	24	3.4
Zn-sorb. gibbsite-4.0	6.0	——	——	Ads	4000	——	5	80	8	1.7
Zn-sorb. gibbsite-1.9[c]	6.0	——	——	Ads	1950	——	——	——	——	——

[a]Spectra from Schlegel and Manceau [10]. [b]Phases described in Scheinost et al. [14]. [c]Spectrum from Roberts et al. [13].[d]Initial Zn/hydroxy-Al ratio during Zn uptake. [e]Reaction time allowed for Zn uptake. [f]Ads: Adsorption of Zn to preformed HIS, CPT: Coprecipitation of Zn during HIS synthesis. [g]Final Zn/Al ratio in solid calculated from the total Zn content and assuming that all added Al was incorporated into HIS during synthesis. [h]Zn coordinated to 6 second-neighbor Al (reference Zn-HIS-1.6-pH6). [i]Zn coordinated by 2 second-neighbor Al (reference Zn-sorbed gibbsite-1.9). [j]Outer-spherically sorbed Zn (reference aqueous Zn).

In order to prepare hydroxy-Al interlayered smectites with higher Zn/Al ratios (Zn/Al ratio between 1 to 25), a suspension of 20 g/L montmorillonite (SWy-2, Newcastle formation, Wyoming, USA, Clay Mineral Society Source Clays; N_2-BET surface area 31.8 m^2/g [24]) and 40 mmol/L $AlCl_3$ was slowly titrated to pH 4.5 with 0.1 M NaOH [6]. After equilibration for 15 h, the precipitate was washed four times with DDI water, frozen in LN and freeze-dried. Different loadings of Zn in HIS were obtained by suspending 1 g of HIS in 500 mL 10 mM $CaCl_2$ containing 2, 5, 10, 20 and 50 mM $ZnCl_2$, resulting in Zn/Al ratios of 1, 2.5, 5, 10, and 25, respectively (Table 3.2). The suspensions were aged during 15 h at pH 5.0. The final products were repeatedly washed with DDI water, frozen using LN and freeze-dried. The elemental composition determined by XRF showed that the fraction of Zn uptake decreased with increasing initial Zn/Al ratio, resulting in Zn contents of 2100 (“Zn-HIS-2.1-pH5”), 2900 (“Zn-

HIS-2.9-pH5"), 4000 ("Zn-HIS-4.0-pH5"), 6900 ("Zn-HIS-6.9-pH5") and 8600 mg/kg ("Zn-HIS-8.6-pH5"). X-ray diffraction on oriented mounts of K-saturated Zn-HIS at increasing temperatures confirmed the formation of HIS.

Natural Zn-containing kaolinite ("natural Zn-kaolinite", 180 mg/kg Zn) from Decazeville, France and synthetic Zn-kaolinite ("synthetic Zn-kaolinite") were kindly provided by Farid Juillot (Institut de Minéralogie et de Physique des Milieux Condensés, Université Paris Diderot, Paris, France). The synthetic Zn-kaolinite was prepared as described in Petit et al. [25]. Briefly, 20 mL of 0.2 M ($Al(NO_3)_3$ + $Zn(NO_3)_2$) at Zn/Al ratio of 0.05 were added to 20 ml of 0.2 M $Na_2SiO_4 \cdot 5H_20$ and 20 ml 0.2 M NaOH under vigorous stirring during 1 h. The resulting gel was washed and centrifuged 3 times before drying at 80°C during 48 h. 210 mg of the dried gel was dispersed in 30 mL DDI water and the suspension was aged in a closed vessel for 14 days at 230°C. Subsequently, the precipitate was washed 3 times and air-dried. The synthetic Zn-kaolinite had a Zn/Al ratio of 0.0006 (270 mg/kg Zn), indicating only limited Zn uptake into the kaolinite structure. Natural Zn-containing lithiophorite ("Zn-lithiophorite", 180 mg/kg Zn) from Cornwall, Great Britain, was kindly provided by Beda Hofmann (Natural History Museum Bern, Switzerland). Lithiophorite (free of Zn) was synthesized according to Feng et al. [26]. The structures of the kaolinites and lithiophorites were confirmed by XRD.

Gibbsite was synthesized as described in Kyle et al. [27]. Zn was adsorbed to gibbsite by reacting 1 g of gibbsite with 1 L of 0.1 M $NaNO_3$ containing 1 mM $Zn(NO_3)_2$ (24 h, pH 6.0). The Zn-sorbed gibbsite was filtered, washed, frozen in LN and freeze-dried. The final product contained 4000 mg/kg ("Zn-sorbed gibbsite-4.0"). An EXAFS spectrum of a similarly synthesized Zn-sorbed gibbsite containing 1900 mg/kg Zn ("Zn-sorbed gibbsite-1.9") was kindly provided by Darryl Roberts [13]. Zn adsorbed to goethite was prepared by adding 800 mL solution of 1 mM $Zn(NO_3)_2 \cdot 4H_2O$ and 0.1 M $NaNO_3$ to 0.8 g of goethite [28]. The suspension was titrated to pH 7.0 and reacted during 62 h, resulting in a Zn content of 2900 mg/kg. Preparation of Zn-sorbed birnessite at low surface coverage (Zn/Mn =0.003, "low Zn-birnessite") has been described elsewhere [29].

3.2.4. EXAFS spectra acquisition

Bulk Zn K-edge EXAFS spectra were recorded at the XAS beamline at the Angströmquelle Karlsruhe (ANKA, Karlsruhe, Germany). The Si (111) monochromator was detuned by 35% using a software-controlled monochromator stabilization to reduce higher harmonics. The monochromator was calibrated by assigning the first maximum of the first derivative of the absorption edge of metallic Zn to 9659 eV. Powdered soil

and reference samples were pressed into pellets with polyethylene or Licowax C®. They were analyzed at room temperature in fluorescence (5-element Ge solid state detector) or in transmission mode, depending on Zn concentration. Microspectroscopic analyses on a polished thin section of embedded aggregates of soil GRÜ were performed at the beamline 10.3.2 [30] at the Advanced Light Source (ALS, Berkeley, USA). After the analysis of element distributions by μ-XRF spectrometry (see appendix 2 for details), one Zn K-edge EXAFS spectrum was recorded using a beam size of 16 x 7 μm^2.

3.2.5. EXAFS data extraction and analysis

Extraction of the EXAFS spectra from the raw data was performed using the software code Athena [31]. The E_0 was set to the maximum of the first derivative of the absorption edge. The spectra were normalized by subtracting a first order polynomial fit to the data before the edge (-150 to -30 eV relative to E_0) and subsequently dividing through a second order polynomial fit to the post-edge data (+150 eV up to 100 eV before end of spectrum). The EXAFS signal was extracted using a cubic spline function and the Autobk algorithm implemented in Athena (Rbkg = 0.9 Å, k-weight = 3, spline k-range from 0.5 to 12 $Å^{-1}$). The EXAFS spectra were Fourier-transformed over the k-range 2-10 $Å^{-1}$, using a Kaiser-Bessel apodization window (window parameter = 2.5).

Linear combination fits (LCF) were calculated following an approach and software developed by Manceau and coworkers [30, 32, 33]. Reference spectra for LCF were selected from an extensive database including crystalline Zn phases, Zn adsorbed to different mineral surfaces, and Zn complexed by organic molecules. Spectra were either recorded on own reference materials [14, 29, 34] or were provided by other researchers. In addition to the reference compounds described in section 3.2.3, spectra considered for this study included Zn-layered double hydroxide (Zn-LDH), ZnMg-kerolite at various Zn/Mg ratios (Zn-kerolite, $Zn_{0.8}Mg_{0.2}$-kerolite, $Zn_{0.6}Mg_{0.4}$-kerolite, $Zn_{0.34}Mg_{0.66}$-kerolite, $Zn_{0.03}Mg_{0.97}$-kerolite), amorphous $Zn(OH)_2$, Zn adsorbed to goethite, Zn bearing birnessite with high (Zn/Mn ratio of 0.088) and low (Zn/Mn ratio of 0.003) coverage, Zn sorbed to ferrihydrite, Zn sorbed to calcite, Zn-phytate and aqueous Zn (0.5 M $ZnNO_3$, pH 6.0) (see appendix 2 for details). The LCF analysis of the experimental spectra was carried out by calculating 1-component to 4-components fits. Starting from the best 1-component fit as judged by the lowest NSSR ($NSSR = (\Sigma_i(k^3\chi_{exp}-k^3\chi_{fit})^2)/\Sigma_i(k^3\chi_{exp})^2$), additional components were considered to substantially improve the fit as long as the NSSR decreased by at least 10% relative to the previous fit. The approximate precision of LCF with respect to the fractions of individual reference spectra has previously been estimated to 10% of the total Zn [35]. However, the detection limit, precision, and accuracy of LCF depend on the EXAFS amplitude of the species of interest, structural

and spectral similarities between different species in mixtures, and the availability of a database including all relevant reference spectra [33].

The EXAFS spectra of selected synthetic and natural reference materials were analyzed by shell fitting in *r*-space. Theoretical scattering paths were calculated with FEFF 8.40 [36]. Shell-fitting of Zn-HIS, Zn-sorbed gibbsite and aqueous Zn spectra was performed using Zn-O and Zn-Al paths calculated from the structure of gibbsite [37], by placing one Zn atom into a dioctahedral vacancy. For the analysis of Zn-kaolinite spectra, Zn-O, Zn-Al and Zn-Si single scattering paths were obtained by substituting one Al atom by Zn in the structure of kaolinite [38]. Shell fits were calculated over the *r*-range 1-3 Å (or 1-2.1 Å for aqueous Zn) using the software code Artemis [31]. Path parameters were optimized by minimizing the normalized sum of squared residuals ($NSSR = (\Sigma_i(k^3\chi_{exp}-k^3\chi_{fit})^2)/\Sigma_i(k^3\chi_{exp})^2$). The amplitude reduction factor S_0 was fixed to 0.85 [39] and the energy shift was constrained to be the same for all shells within individual fits.

3.2.6. Simulation of Zn K-edge EXAFS spectra for gibbsitic model clusters

Simulations of Zn K-edge EXAFS spectra were carried out for three different gibbsitic model clusters. Structural representations of the three clusters are provided in the appendix 2 (Fig. A2.4 to A2.6). Using ATOMS [40], the basic structure of all clusters was derived from the structure of talc [41]. After removing all Si atoms and replacing Mg by Al, three different gibbsitic clusters were constructed: (1) Gibbsitic cluster with one central Zn atom placed in the dioctahedral vacancy, all other vacancies unfilled ("unfilled gibbsitic cluster"). (2) Gibbsitic cluster with a central Zn atom placed in the dioctahedral vacancy, all other vacancies filled with Zn ("filled gibbsitic cluster"). (3) Gibbsitic cluster with one central Zn substituting for one Al atom ("substituted gibbsitic cluster"). Using FEFF 8.40 [36], Zn K-edge EXAFS spectra were calculated for all thee gibbsitic clusters over different cluster sizes around the central Zn atom, limiting the maximum half-path distance to 8 Å and including either only single scattering ("SS") or all single and multiple scattering paths with up to six legs ("SS+MS"). Based on shell-fits of experimental Zn-HIS spectra, the Debye-Waller parameter was fixed to 0.008 $Å^2$ for the first-shell single scattering Zn-O path and to 0.004 $Å^2$ for the second-shell Zn-Al and next nearest Zn-O (at ~3.28 Å) paths. For all other single- and multiple-scattering paths, the Debye Waller parameter was fixed to 0.008 $Å^2$. An energy shift of -7 eV was assigned to all paths (based on shell-fits of experimental Zn-HIS spectra).

3.2.7. Sequential extraction procedure

In order to assess the fractionation of Zn in the contaminated soils, the 7-step sequential extraction procedure (SEP) of Zeien and Brümmer [42] was used. Experimental details are provided in Voegelin et al. [43]. Briefly, each soil was extracted in duplicates (2 g of soil each) according to the following sequence (with hypothetical interpretation according to Zeien and Brümmer [42] in parentheses): Fraction F1: 1M NH_4NO_3 (readily soluble and exchangeable); Fraction F2: 1M NH_4-acetate, pH 6.0 (mobilizable and $CaCO_3$ bound); Fraction F3: 0.1 M NH_2OH-HCl + 1 M NH_4-acetate, pH 6.0 (Mn oxides); Fraction F4: 0.025 M NH_4-EDTA, pH 4.6 (bound to organic substances); Fraction F5: 0.2 M NH_4-oxalate, pH 3.25 (bound to amorphous and poorly crystalline Fe oxides); Fraction F6: 0.1 M ascorbic acid + 0.2 M NH_4-oxalate, pH 3.25 (bound to crystalline Fe oxides). All extraction steps were performed with a solution-to-soil ratio of 25 mL/g. The solutions from the extraction steps F1 to F6 were analyzed by ICP-OES. The residual fraction F7 was determined by XRF spectrometry.

Different synthetic Zn-bearing phases (Zn-HIS-6.9-pH5, Zn-gibbsite-4.0, low Zn-birnessite and lithiophorite–see paragraph 3.2.3 for details on reference materials) were spiked into 2 g of quartz powder (Fluka®, Nr. 83340) to achieve contamination levels of 200, 250, 400 mg/kg Zn, and 3000 mg/kg Mn, respectively. The spiked quartz powders were homogenized for 24 h on an overhead shaker prior to sequential extraction.

3.2.8. Na-citrate extraction

In order to dissolve the hydroxy-Al interlayers of phyllosilicate minerals, the residual soil or quartz from the SEP (i.e., the residual material after step F6) was extracted using the method of Tamura [44]. The same extraction was also performed with pure reference materials (Zn-HIS-6.9-pH5, Zn-HIS-2.1-pH5, and synthetic Zn-kaolinite, see paragraph 3.2.3 for details on reference materials) as well as with the <2 μm size fraction of the soils. The extractions were performed in duplicates using either 50 or 250 mg of material at a SSR of 200 ml/g. The samples were extracted for 1 h in boiling 0.3 M Na-citrate solution adjusted to pH 7.3. Subsequently, the extracts were separated by centrifugation (5 min, 3200 g), passed through nylon filters (0.45 μm) and acidified (1 % v/v 30 % HNO_3). After repeating this treatment two times, the three extracts were quantitatively merged and the Zn content analyzed by ICP-OES. The citrate-extracted soil clay fractions were Mg-saturated and analyzed by X-ray diffraction as described in section 3.2.2.

3.3. Results

3.3.1. Soil properties and mineralogy

Physical and chemical properties and Zn contents of the soil samples are provided in Table 3.1. The soils were contaminated with 251 and 1039 mg/kg Zn due to the input of aqueous Zn with the runoff water from power line towers that have been constructed 35 to 74 years ago. Upper levels of normal geogenic soil Zn contents in Switzerland are 57, 88, 95, 116, and 132 mg/kg for soils with pH ($CaCl_2$) of <4.3, 4.3-5.0, 5.1-6.1, 6.2-6.7, and 6.8-7.6, respectively [45]. The Zn contents of all soils except SAR and HAU exceeded these levels 7-12 fold, indicating substantial contamination from the power line towers. The Zn contents of the soils SAR and HAU exceeded the upper levels of normal geogenic soil Zn 2-3 fold, suggesting that these soils were also slightly contaminated with Zn.

XRD patterns of oriented mounts of the <2 μm size fraction of the soils GER, GRÜ and HAU are shown in Figure 3.1. The mineralogy was dominated by hydroxy-interlayered minerals, kaolinite, illite and quartz. The 14.2 Å (6.2° 2θ Cu Kα) peak observed for all Mg-saturated slides did not collapse upon K-saturation and heating to 100°C, but shifted to ~11.2 Å after heating to 550°C, indicating that the interlayer space of the 14.2 Å mineral was filled with hydroxy-polymers [1, 46]. The 14 Å peak observed after heating the K-saturated clay fraction to 550°C confirmed the presence of chlorite. Also after the removal of hydroxy-Al interlayers from soil clay minerals by Na-citrate extraction, ethylene glycol (EG) and glycerol (Gly) solvation did not cause a shift of the 14.2 Å peak to higher d-spacings (Fig. A2.9), indicating that it originated mainly from hydroxy-interlayered vermiculite (HIV) rather than hydroxy-interlayered smectite (HIS). Accessory minerals observed included K-feldspar, plagioclase and goethite. Interstratified illite-vermiculite was also detected in the GER soil. XRD patterns collected on the clay fractions of the soils MOM, SAR, CHI, BUN and BIB2 are provided in the appendix 2 (Figs. A2.7 and A2.8). The clay mineralogy of these soils were similar to the soils GER, GRÜ and HAU and were also characterized by a substantial fraction of HIV.

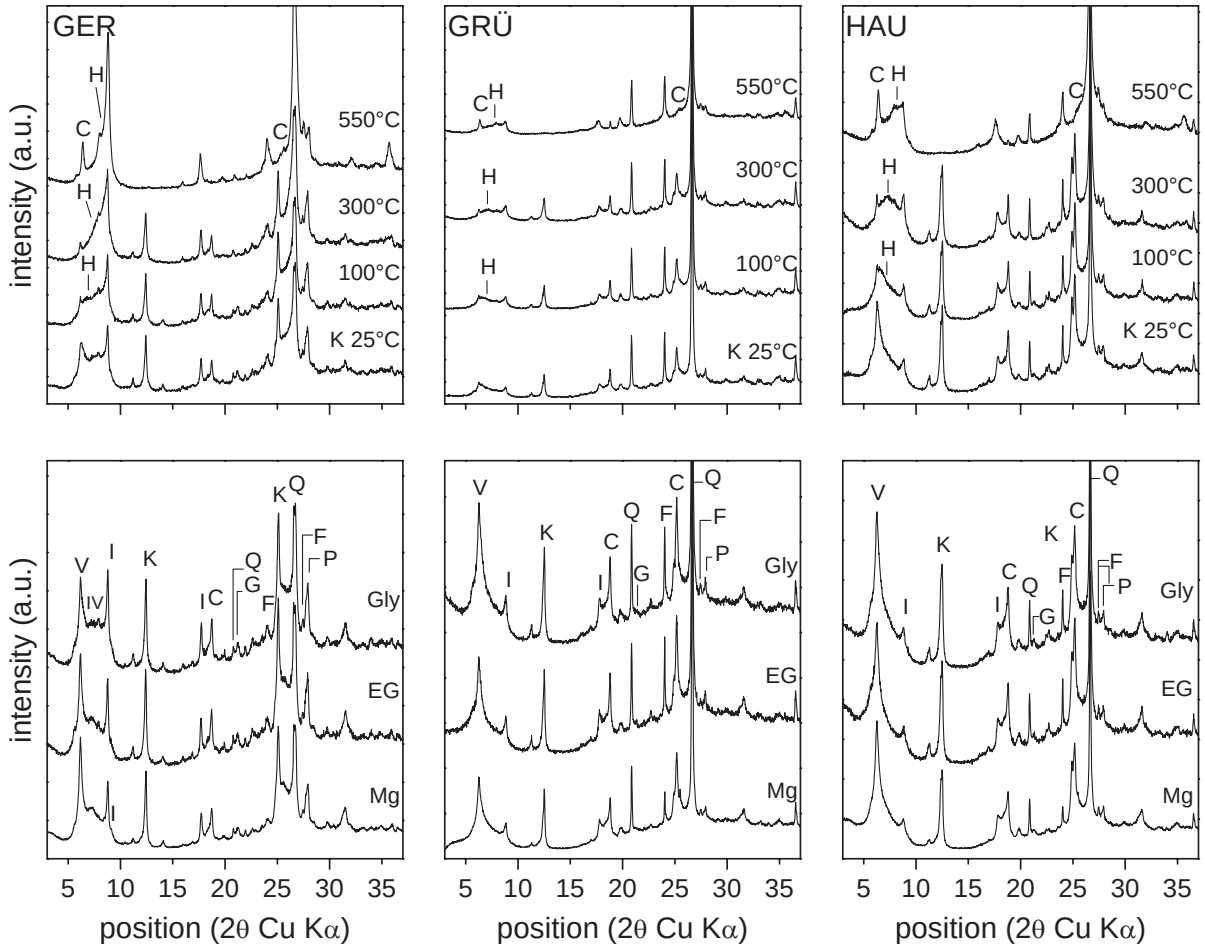

Figure 3.1. X-ray diffraction patterns of oriented mounts of the <2 µm size soil fraction. Lower panels: Mg-saturated slides in air-dried state (Mg) and after ethylene glycol (EG) and glycerol solvation (Gly). Upper panels: K-saturated slides (K) after ex situ thermal treatment. C: chlorite; F: K-feldspars; G: goethite; H: hydroxy-interlayered vermiculite; I: illite; IV: interstratified mica-vermiculite; K: kaolinite; P: plagioclase; Q: quartz; V: vermiculite.

3.3.2. Uptake of Zn into HIS and local coordination from EXAFS spectroscopy

The Zn contents and final Zn/Al ratios of the synthetic Zn-HIS phases are listed in Table 3.2. Depending on synthesis pH, initial Zn/Al ratio, reaction time, and mode of Zn uptake, final Zn contents varied between 1615 and 8600 mg/kg (25 to 132 mmol/kg). These contents correspond to molar Zn/Al ratios of 0.013 to 0.087, indicating that only a minor fraction of total Zn had been incorporated at higher initial Zn/Al ratios. In addition to higher pH, factors that seemed to favored Zn incorporation were Zn coprecipitation rather than adsorption and increased equilibration time.

The EXAFS spectra and corresponding Fourier transforms of the Zn-HIS and Zn-sorbed gibbsite references are presented in Figure 3.2. Results from shell fitting are provided in Table 3.3.

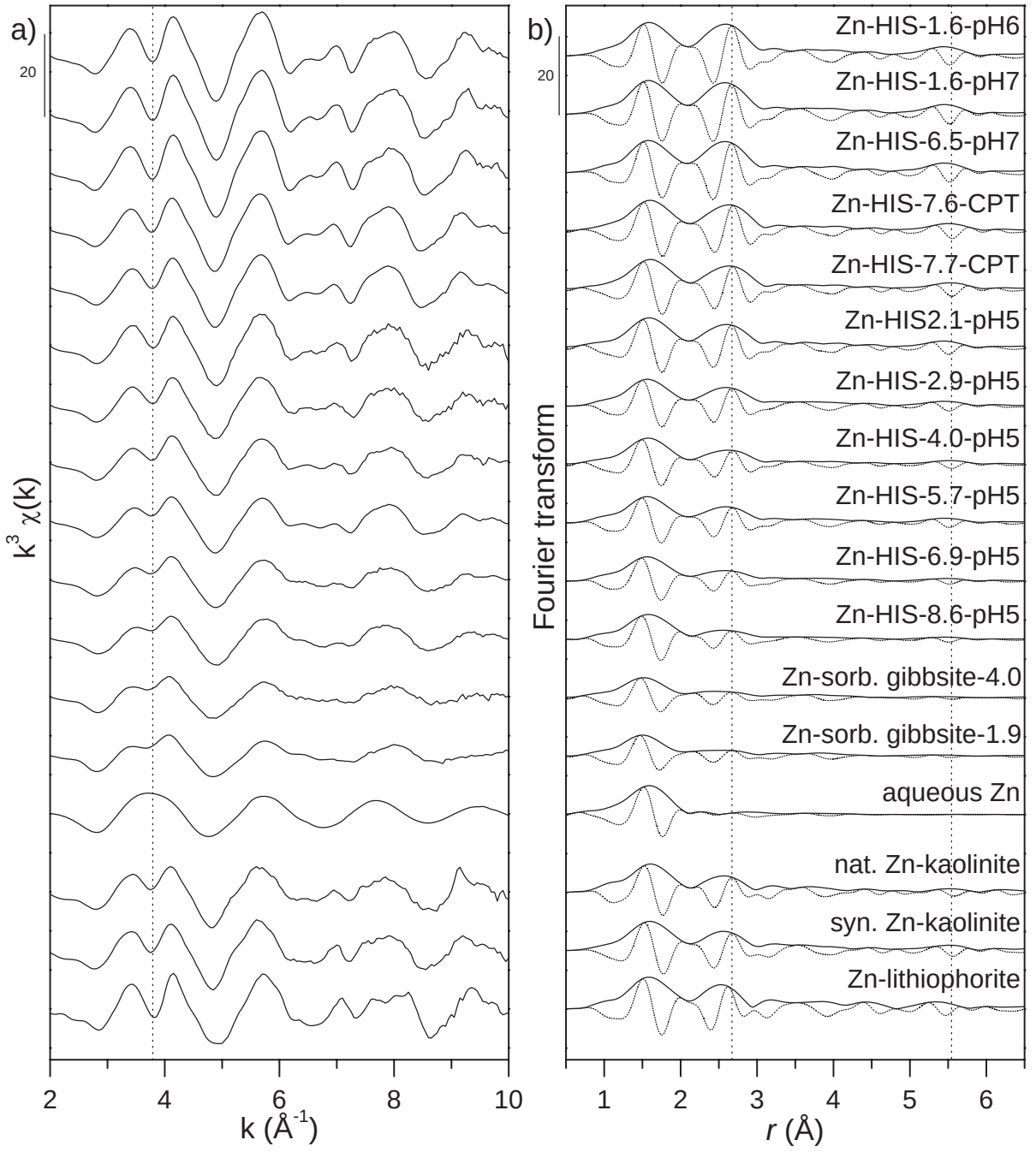

Figure 3.2. EXAFS spectra (a) and Fourier transform magnitudes and imaginary parts (b) of Zn-HIS, Zn-sorbed gibbsite, Zn-kaolinite and Zn-lithiophorite. Vertical dashed lines are located at 3.79 Å^{-1} (a) and 2.67 Å and 5.54 Å (b). Parameters from shell fits are reported in Table 3.2.

Table 3.3. Results from shell fits to the reference spectra shown in Fig. 3.2 (*r*-range 1 to 3 Å)

	Zn-O shell			Zn-Al shell			Zn-X shell					
Samples	R_{Zn-O}[a]	CN[b]	σ^2 (Å^2)[c]	R_{Zn-Al}[a]	CN[b]	σ^2 (Å^2)[c]	X	R_{Zn-X}[a]	CN[b]	σ^2 (Å^2)[c]	ΔE_0 (eV)[d]	NSSR (%)[e]
Zn-HIS-1.6-pH6	2.08	6.9	0.008	3.04	6.6[f]	0.004[g]	O	3.28	6.6[f]	0.004[g]	7.4	0.9
Zn-HIS-1.6-pH7	2.08	6.8	0.007	3.04	6.6[f]	0.004[g]	O	3.28	6.6[f]	0.004[g]	7.1	1.0
Zn- HIS-6.5-pH7	2.08	6.8	0.008	3.03	6.7[f]	0.005[g]	O	3.28	6.7[f]	0.005[g]	6.9	0.9
Zn-HIS-7.6-CPT	2.08	6.3	0.008	3.06	5.4[f]	0.005[g]	O	3.27	5.4[f]	0.005[g]	7.5	0.7
Zn-HIS-7.7-CPT	2.08	6.1	0.008	3.06	4.7[f]	0.004[g]	O	3.28	4.7[f]	0.004[g]	7.9	0.8
Zn-HIS-2.1-pH5	2.08	6.1	0.008	3.04	4.6[f]	0.004[g]	O	3.27	4.6[f]	0.004[g]	7.4	0.8
Zn-HIS-2.9-pH5	2.07	6.3	0.010	3.04	3.9[f]	0.004[g]	O	3.28	3.9[f]	0.004[g]	6.9	0.9
Zn-HIS-4.0-pH5	2.07	6.1	0.010	3.04	3.6[f]	0.005[g]	O	3.28	3.6[f]	0.005[g]	6.9	0.8
Zn-HIS-5.7-pH5	2.07	5.8	0.009	3.05	3.1[f]	0.004[g]	O	3.27	3.1[f]	0.004[g]	7.2	0.7
Zn-HIS-6.9-pH5	2.06	5.8	0.010	3.04	2.6[f]	0.005[g]	O	3.29	2.6[f]	0.005[g]	6.9	0.8
Zn-HIS-8.6-pH5	2.06	5.3	0.008	3.04	2.1[f]	0.004[g]	O	3.30	2.1[f]	0.004[g]	8.0	1.0
Zn-sorb. gibbsite-4.0	2.04	5.8	0.013	3.01	1.7[f]	0.005[g]	O	3.28	1.7[f]	0.005[g]	4.6	0.9
Zn-sorb. gibbsite-1.9	2.03	5.8	0.012	3.01	1.7[f]	0.005[g]	O	3.26	1.7[f]	0.005[g]	3.6	0.9
aqueous Zn	2.08	6.3	0.008	——	—	——	—	——	—	——	6.1	0.2
nat. Zn-kaolinite	2.09	5.9	0.008	3.05	4.3	0.004[g]	Si	3.16	1.4[h]	0.004[g]	7.1	1.1
syn. Zn-kaolinite	2.10	6.5	0.008	3.05	6.9	0.009[g]	Si	3.13	2.3[h]	0.009[g]	7.2	1.1
Zn-lithiophorite	2.07	6.3	0.007	2.99	4.5[f]	0.002	O	3.27	4.5[f]	0.004	7.3	0.7

[a]Radial distance; uncertainties are ~ 0.01 Å for Zn-O, 0.01-0.03 for Zn-Al and 0.04-0.2 for Zn-X shells. [b]Coordination numbers; uncertainties are 0.8-1.5 for Zn-O and 0.7-2.2 for Zn- Al/X shells. [c]Debye Waller parameters; uncertainties are ~0.002 Å^2 for Zn-O. [d]Energy shift; set equal for all shells in a fit, uncertainties are 0.1-2.5 eV. [e]Normalized sum of the squared residuals (NSSR=$\Sigma(data_i\text{-}fit_i)^2/\ \Sigma(data_i)^2$). [f,g]Set equal for Zn-Al and Zn-X path within individual fit. [h]CN of Si constrained to 1/3 of CN of Al during fit.

A direct comparison of the spectra of Zn-HIS-1.6-pH6 and Zn-sorbed gibbsite-1.9 in k- and *r*-space is shown in Figure 3.3. Zn-HIS samples synthesized at the lowest Zn/Al ratio and pH 6.0-7.0 (Zn-HIS-1.6-pH6, Zn-HIS-1.6-pH7, and Zn-HIS-6.5-pH7) as well as samples prepared by Zn coprecipitation (Zn-HIS-7.6-CPT and Zn-HIS-7.7-CPT) exhibited first-shell Zn-O distances of 2.06-2.08 Å and coordination numbers of 6.1-6.9. Second-shell Zn-Al distances varied between 3.03-3.06 Å and coordination numbers between 4.7 and 6.6. These data suggest that octahedrally coordinated Zn was predominantly incorporated in the dioctahedral vacancies of gibbsitic hydroxy-Al polymers, i.e., as a hexadentate complex surrounded by 6 second-neighbor Al atoms (see Figures A2.4 and A2.5 in the appendix 2). In the spectra, this was phenomenologically reflected in the splitting of the first EXAFS oscillation at 3.8 Å^{-1} and in the coincidence

of the maxima of the Fourier transform magnitude and imaginary part of the second shell [10, 14, 15].

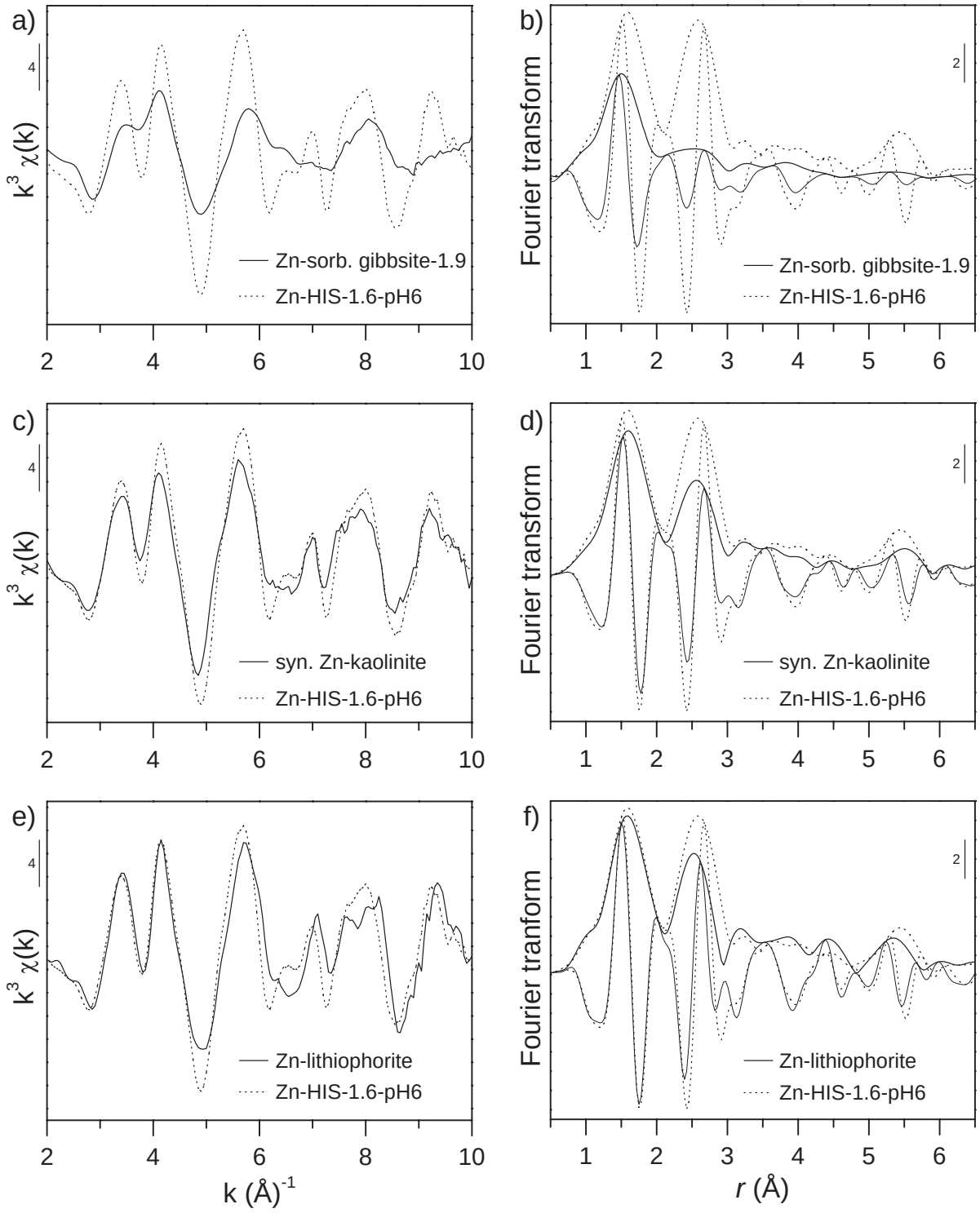

Figure 3.3. Comparison of the EXAFS spectra of Zn-HIS-1.6-pH6.0 with: Zn-sorbed gibbsite-1.9 (a, b), synthetic Zn-kaolinite (b, d) and Zn-lithophorite (e, f) in k-space and in *r*-space, respectively.

Shell fits to the spectra of Zn adsorbed to gibbsite returned a second-shell Zn-Al distance of 3.01 Å and a coordination number of 1.7. In *r*-space, the magnitude of the first shell of the spectrum of Zn-sorbed gibbsite-1.9 was clearly lower than for Zn-HIS-1.6-pH6 and the imaginary part was shifted to slightly lower *r* (Fig. 3.3). In the fits, these differences were reflected in a lower first-shell Zn-O distance (2.03 versus 2.08 Å), a lower coordination number (5.8 versus 6.9), and a higher Debye-Waller parameter (0.012 versus 0.008 $Å^2$) for Zn-sorbed gibbsite-1.9 than Zn-HIS-1.6-pH6 (Table 3.3). In agreement with previous studies [10, 13], these fitting results suggest that Zn sorbed to gibbsite was mainly octahedrally and to a lesser extent tetrahedrally coordinated with O, forming mainly mononuclear bidentate (i.e., edge-sharing) sorption complexes with Al octahedra at the surface of gibbsite. Aqueous Zn is shown in Figure 3.2 as a proxy for Zn sorbed as an outer-sphere complex. The Zn-O coordination number and distance obtained from shell fitting confirm the octahedral coordination of hydrated Zn^{2+}.

The EXAFS spectra of Zn-HIS phases synthesized at pH 5.0 by adsorption of Zn to preformed HIS show a gradual transition from the first group of spectra (octahedral Zn in the vacancy of gibbsitic hydroxy-Al polymers) to Zn-sorbed gibbsite (mainly octahedrally coordinated Zn forming bidentate edge-sharing sorption complexes) and/or aqueous Zn (exchangeable Zn) (Fig. 3.2). This trend was reflected by shell fits indicating a gradual decrease in second-shell Zn-Al coordination number with increasing Zn-loading of the HIS (Tables 3.2 and 3.3). LCF analysis confirmed that all Zn-HIS spectra could be well reproduced by one- to three component fits using the spectra Zn-HIS-1.6-pH6, Zn-sorbed gibbsite-1.9, and aqueous Zn (Table 3.2, LCF shown in Fig. A2.2 in the appendix). The fractions of Zn-HIS-6.9-pH5 returned by LCF varied systematically with Zn-HIS composition and were nearly independent on whether only Zn-sorbed gibbsite-1.9, only aqueous Zn, or both spectra were present in the fit. On the other hand, the relative fractions of Zn-sorbed gibbsite-1.9 and aqueous Zn varied considerably (Table 3.2), which may have been due to the spectral similarity of these references. Nevertheless, both Zn-sorbed gibbsite-1.9 and aqueous Zn were needed for good LCF, especially for the spectra of Zn-HIS prepared by adsorption of Zn at pH 5.0. Overall, the LCF results indicated that the dominant factor favoring the sorption of Zn in the vacancies of hydroxy-Al polymers was the molar ratio Zn/Al during synthesis. Under otherwise identical conditions, increasing Zn loading of HIS resulted in the sorption of Zn to Al-polymer sites with decreasing Al coordination as well as to cation exchange sites. In addition to low Zn/Al ratios in the Zn-HIS, other factors that favored Zn incorporation into hydroxy-Al vacancies included higher pH and coprecipitation of Zn during HIS synthesis instead of Zn adsorption to preformed HIS (Table 3.2). The Zn-HIS samples synthesized by Zn adsorption at pH 5.0 were washed with DI water

prior to drying, which may have removed some exchangeable Zn. Thus, the measured Zn contents and the fractions of exchangeable Zn estimated from LCF fits may be somewhat lower than during contact of the HIS with the Zn-containing solution.

3.3.3. EXAFS simulations for gibbsitic model clusters: Effect of Zn location and loading

In order to extend our preceding EXAFS interpretation by shell-fitting and to assess the effect of Zn incorporation in various positions within gibbsitic structures on the EXAFS signal, we performed a series of EXAFS simulations for gibbsitic model clusters (structures depicted in Figures A2.4-A2.6, appendix 2). Simulation results in k- and *r*-space are presented in Figure 3.4. First, we considered a gibbsitic cluster containing one Zn atom located in a dioctahedral vacancy, with all other vacancies unfilled ("Unfilled"). Calculations for increasing cluster sizes up to 8 Å based on single scattering ("SS") or including multiple scattering ("SS+MS") (with maximum half path lengths of 8 Å) did not properly reproduce the splitting of the first EXAFS oscillation at 3.8 $Å^{-1}$ (Fig. 3.2a). The comparison of the Fourier-transformed EXAFS spectrum of Zn-HIS-1.6-pH6 backtransformed over increasing *r*-ranges (Fig. A2.3, appendix 2) indicated that this splitting mainly originated from scattering in the *r*-range 3.1-5.0 Å (not phase-shifted), which includes single-scattering from O atoms as well as multiple-scattering paths involving O and Al. Correct simulation of this splitting would thus require the 3-dimensional refinement of the gibbsitic structure around the central Zn atom, which was beyond the scope of this study. However, the simulations over a cluster size of 8 Å without and with multiple scattering clearly indicated that the peak at 5.5 Å in the Fourier transform resulted mainly from focused multiple scattering along the 6 collinear Zn-Al-Al axes (Fig. A2.4), as typically observed in octahedral sheets [47-49].

A simulation over a radius of 8.0 Å including single and multiple scattering was also performed with a gibbsitic cluster whose dioctahedral vacancies were all filled with Zn ("Filled", Fig. 3.4). Compared to the unfilled gibbsitic cluster, the presence of 6 Zn atoms at a distance of 5.3 Å from the central Zn atom resulted in an additional peak in the Fourier transform at 4.9 Å (Fig. 3.4). This peak is not observed in the experimental spectra of Zn-HIS (Fig. 3.2), suggesting that Zn atoms do not occupy adjacent vacancies in gibbsitic hydroxy-Al polymers of HIS. This compares with the low final Zn/Al ratio of all Zn-HIS references (Table 3.2), indicating that individual Zn atoms in the hydroxy-Al polymers were separated from each other. The lack of detectable next-nearest cationic Zn-Zn pairing in hydroxy-Al polymers may be due to charge repulsion, due to the structural distortion invoked by filling octahedral vacancies with Zn, or due to the limited size of the gibbsitic clusters in HIM.

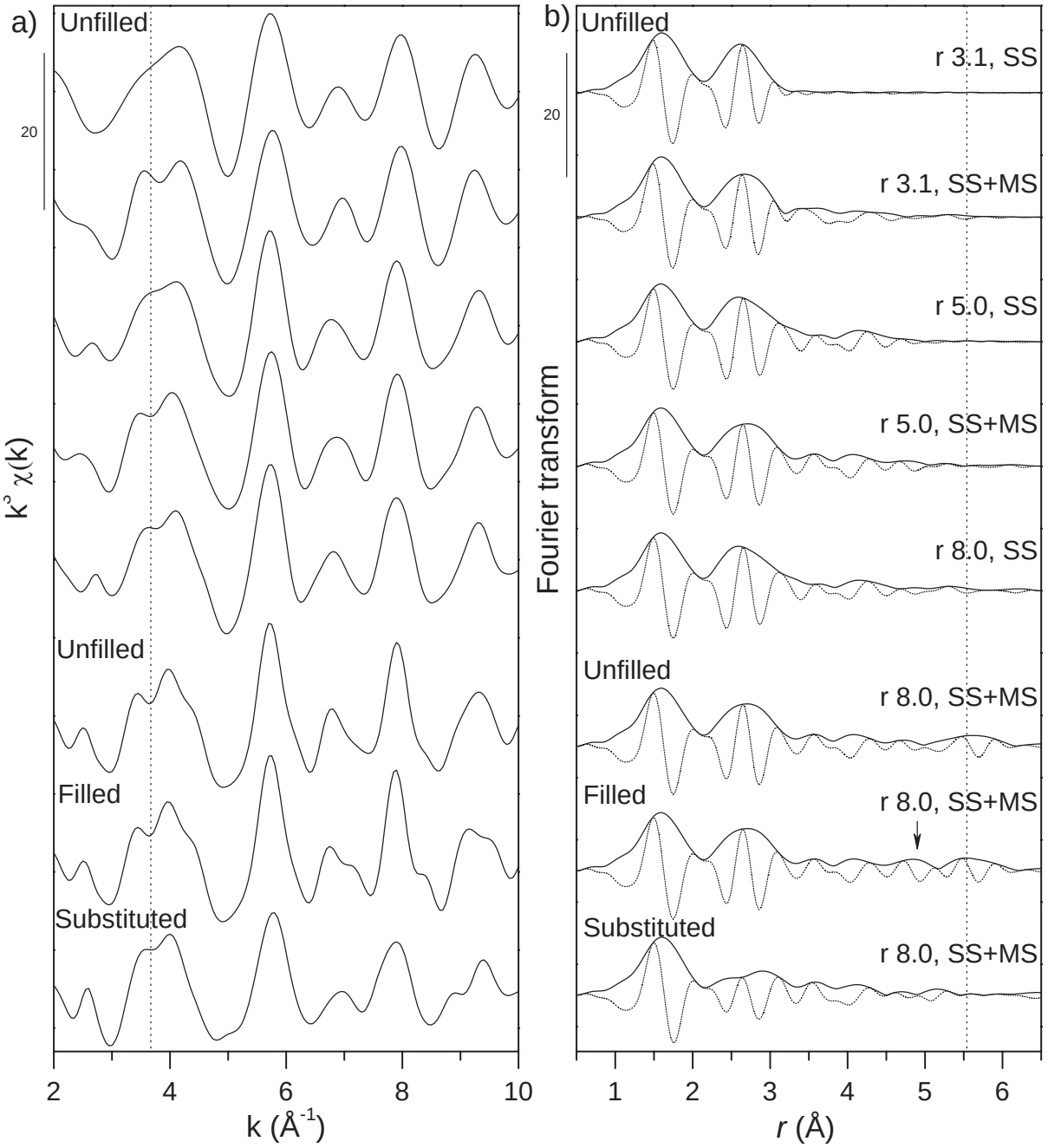

Figure 3.4. Simulated EXAFS spectra for Zn in gibbsitic model clusters. Simulations were carried out over increasing distances (*r* in Å) and included single scattering (SS) or single and multiple scattering (SS+MS) paths. Unfilled: Zn atom in octahedral vacancy of gibbsitic Al-cluster. Filled: All dioctahedral vacancies filled with Zn (arrow indicates 4.9 Å shell from Zn-Zn contributions). Substituted: Zn substituting for Al in gibbsite structure. Structures are shown in the appendix (Figs. A2.4-A2.6). Vertical dashed lines are located at 3.67 $Å^{-1}$ (a) and 5.54 Å (b).

The last simulation was performed for a gibbsitic cluster in which Zn substitutes for an Al atom ("Substituted", Fig. 3.4). In this cluster, Zn is surrounded by 3 Al atoms at 3.05 Å, 6 Al atoms at 5.3 Å and 3 Al atoms at 6.1 Å. Compared to the gibbsitic clusters with Zn incorporated into the dioctahedral vacancy, the substituted cluster has a lower

number of Al atoms coordinated at a distance of 6.1 Å and does not exhibit any collinear Zn-Al-Al arrangement. Therefore, no peak is observed in the Fourier transform at 5.5 Å. Considering Zn-HIS synthesized at near neutral pH and low initial Zn/Al ratio, the presence of a pronounced peak at 5.5 Å in the Fourier transformed spectra (Fig. 3.2) in combination with the high second shell Zn-Al coordination numbers obtained from shell fits (Table 3.3) thus unequivocally show that Zn has been taken up into the vacancies of the gibbsitic structures.

3.3.4. Local coordination of Zn in Zn-kaolinite and Zn-lithiophorite

The EXAFS spectra of Zn-kaolinite and Zn-lithiophorite resemble the spectra of Zn-HIS (Fig. 3.2), reflecting the similarity in the local coordination of Zn. First-shell Zn-O distances (2.09-2.10 Å) and coordination numbers (5.9-6.5) obtained for Zn-kaolinite indicate that Zn was octahedrally coordinated (Table 3.3). Compared to the Zn-HIS reference, the EXAFS oscillations of synthetic (and natural) Zn-containing kaolinite were shifted to slightly lower k-values and the left side of the second oscillation in k-space showed a curvature at 5.2 $Å^{-1}$ which was absent in the Zn-HIS-1.6-pH6 reference spectrum (Fig. 3.3c). Compared to the Zn-HIS-1.6-pH6 spectrum, synthetic Zn-kaolinite exhibited a much lower second shell amplitude (Fig. 3.3d). This could partly be due to destructive interference with backscattering contributions from Si [12, 47, 50]. However, also the peak at 5.5 Å resulting from single and multiple focused scattering along collinear Zn-Al-Al arrangements is much lower (Fig. 3.3). Considering the simulations of EXAFS spectra of gibbsitic model clusters (Fig. 3.4), these differences suggest that Zn uptake into kaolinite may have partly been due to incorporation into vacant dioctahedral sites and partly due to substitution for Al.

The EXAFS oscillations of Zn-lithiophorite show a shift to higher k-values with respect to the ones of Zn-HIS-1.6-pH6 (Fig. 3.3e). In *r*-space, the imaginary part of the second shell of lithiophorite was shifted to lower *r* (Fig. 3.3f), consistent with a shorter Zn-Al distance (2.99 versus 3.04 Å, Table 3.3), as reported in previous work [12].

3.3.5. Analysis of the soil EXAFS spectra by LCF

The EXAFS spectra of all soil samples, the clay fractions of soils GRÜ and HAU, and a μ-EXAFS spectrum from soil GRÜ are shown in Figure 3.5. For the soil GRÜ, nearly identical spectra were observed for the bulk soil, the clay fraction (GRÜ-clay) and the clayey matrix in a soil thin section (GRÜ-μ), in which Zn was evenly distributed within the clayey soil matrix (Fig. A2.10). Also for soil HAU, nearly identical spectra were obtained from the bulk soil and the clay size fraction.

The first EXAFS oscillation of all spectra is split at 3.8 $Å^{-1}$, similarly as in the Zn-

HIS, Zn-sorbed gibbsite, Zn-kaolinite and Zn-lithiophorite reference spectra (Figs. 3.2 and 3.5). Consequently, we selected these reference spectra for the analysis of the soil spectra by LCF. Adsorbed/complexed Zn species and Zn-bearing precipitates such as Zn-LDH or ZnMg-kerolite phases with 3% to 100% Zn/(Zn+Mg) content were also included in the LCF analysis. In the EXAFS spectra of adsorbed/complexed Zn species, the first shell Zn-O contribution may dominate the overall shape of the EXAFS signal due to weak backscattering contributions from second shell neighbors caused by low coordination numbers, disorder, or cancellation effects. As a result, clear distinction between different adsorbed/complexed species is complicated in soil spectra with several contributions. In LCF, we therefore only referred to octahedrally coordinated sorbed Zn ("sorbed ^{VI}Zn") and tetrahedrally coordinated sorbed Zn ("sorbed ^{IV}Zn") using the reference providing the lowest NSSR. While sorbed ^{VI}Zn may either be specifically or electrostatically bound, sorbed ^{IV}Zn only occurs as inner-sphere complex. For LCF, we used Zn-sorbed goethite (octahedrally coordinated Zn forming inner-sphere sorption complex [28]) and aqueous Zn as proxies for sorbed ^{VI}Zn. For sorbed ^{IV}Zn, we used reference spectra of Zn-phytate (proxy for Zn bound to organic phosphate groups [51]) and Zn-sorbed birnessite at low surface coverage. In addition, Zn-sorbed calcite (tetrahedral Zn, [52]) was included in LCF of soils with pH >5, but never occurred in the best LCF.

Overall, LCF indicated that Zn-HIM, Zn-containing phyllosilicates (ZnMg-kerolite phases) and adsorbed Zn are the major Zn species in the studied soils (Fig. 3.5. and Table 3.4). No Zn-LDH was detected by LCF in any of the studied soils. Since only HIV but no HIS was detected in the studied soils, we assume the fitted Zn-HIS fractions to correspond to Zn-HIV. While all Zn-HIS references depicted in Figure 3.2 were used for LCF, best fits were consistently achieved with the reference Zn-HIS-6.9-pH5. This suggests that uptake of Zn into HIM tends to result in relatively similar local Zn coordination in HIM in all soils. For most soils, LCF results also indicated the presence of Zn in phyllosilicates with intermediate to high Zn/Mg ratio (represented by ZnMg-kerolite as structural proxies). However, except for soil CHI1, the fractions of Zn-HIM always exceeded the ZnMg-kerolite fraction. While LCF returned no sorbed Zn for the soils HAU and SAR with lowest Zn contents, the highest fractions of sorbed Zn were found for the two most acidic soils GER (60%) and MOM (65%). LCF returned similar results for the soils BUN, GRÜ and BIB2, likely reflecting their comparable soil physicochemical properties and Zn contents (Table 3.1). For the clay fraction of soil HAU, the best two-component fit was achieved with Zn-HIS-4.0-pH5 and $Zn_{0.6}Mg_{0.4}$-kerolite (71 % and 31 %, respectively, NSSR 2.34%). Adding synthetic Zn-kaolinite as a third reference reduced NSSR by more than 40% and visually improved the fit

in the region of Zn-Si backscattering (3 to 4.5 Å in *r*-space, data not shown). For the validation of this result, however, direct identification of Zn-kaolinite within the soil matrix would be needed, e.g., using spatially resolved µ-EXAFS spectroscopy.

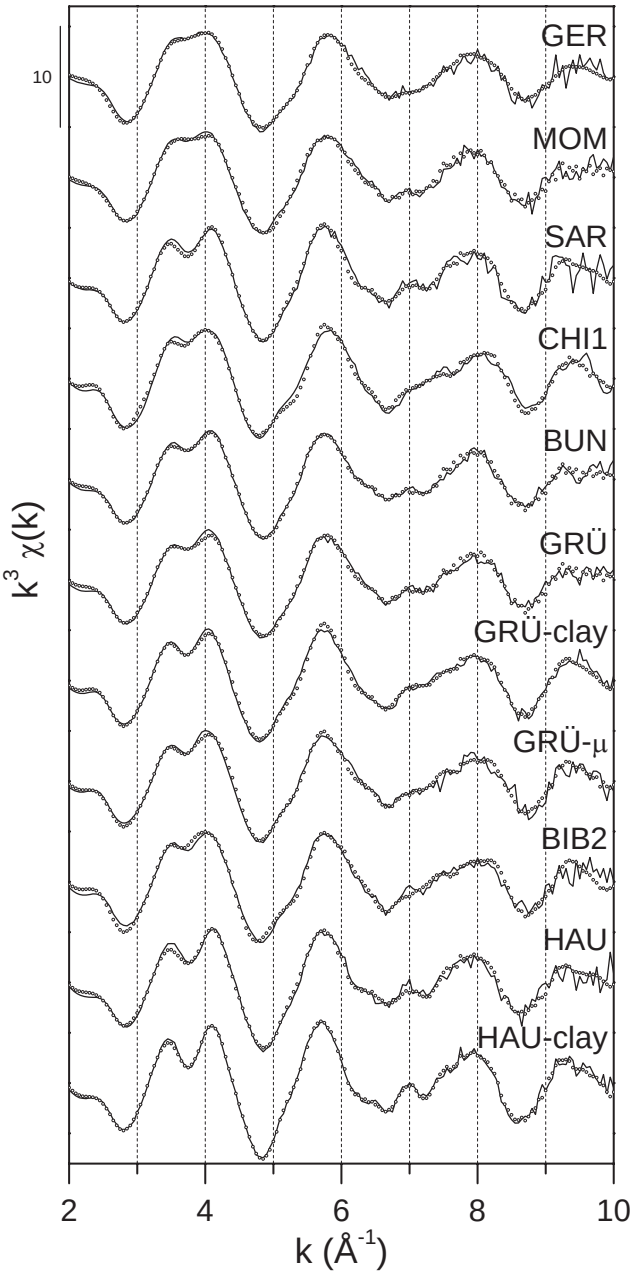

Figure 3.5. EXAFS spectra of bulk soils, soil clay fractions and clayey matrix in a thin section of soil GRÜ (solid lines) and LCF spectra (open dots). LCF results are provided in Table 3.4.

Table 3.4. Linear combination fits of EXAFS spectra from bulk soils, the soil clay fractions, and a thin section of soil GRÜ.

Spectrum	Zn-HIS-6.9-pH5	Zn-kerolite[a]	sorbed ^{VI}Zn[b]	sorbed ^{IV}Zn[c]	Sum	NSSR
	(%)	(%)	(%)	(%)	(%)	(%)
GER	29	18 (80Zn)	31 (Aq)	29 (Ph)	107	3.87
MOM	36	———	22 (Aq) + 43 (Go)	———	101	3.78
SAR	75	24 (60Zn)	———	———	99	5.05
CHI	34	48 (60Zn)	———	16 (Ph) + 16 (Bi)	114	2.32
BUN	54	15 (34Zn)	33 (Go)	———	102	2.16
GRÜ	52	13 (60Zn)	36 (Go)	———	101	2.50
GRÜ-clay	61	39 (60Zn)	———	———	100	2.08
GRÜ-µ	48	38 (60Zn)	———	16 (Bi)	102	3.52
BIB2	50	24 (60Zn)	29 (Go)	———	103	3.56
HAU	84	15 (60Zn)	———	———	99	4.50
HAU-clay	53	21 (60Zn) + 29 (Ka)	———	———	103	1.37

[a](80Zn): $Zn_{0.8}Mg_{0.2}$-kerolite, (60Zn): $Zn_{0.6}Mg_{0.4}$-kerolite, (34Zn): $Zn_{0.34}Mg_{0.66}$-kerolite, (Ka) synthetic Zn-kaolinite. [b](Aq): aqueous Zn, (Go): Zn-sorbed goethite. [c](Ph): Zn-phytate, (Bi): low Zn-birnessite (Zn/Mn=0.003).

3.3.6. Sequential and Na-citrate extractions

Sequential extraction results are presented in Figure 3.6. The percentage of exchangeable Zn (fraction F1) systematically decreased with increasing soil pH, from >30% in the acidic soils GER and MOM to <1% in the soils BIB2 and HAU with pH >6. Regardless of soil pH, between 49 to 66% of the total Zn was found in the last two fractions (F6+F7), indicating that most Zn was present in stable form. The additional Na-citrate extraction step mobilized large fractions (40-80%) of the residual Zn after the extraction step F6.

From Zn-HIS-6.9-pH5 spiked into quartz powder, about 30% of the Zn was extracted in the first extraction step, showing that this reference contained also exchangeable Zn. The remainder of the Zn was fractionated into F5-F7. The stepwise dissolution of Zn-HIS using oxalate solutions is consistent with the study of Farmer et al. [53] showing that the release of oxalate-soluble Al in podzolic soils is related to the extraction of pedogenic hydroxy-Al interlayers of HIV. Na-citrate treatment almost completely removed the Zn remaining after F6. Similarly, extraction of pure Zn-HIS-6.9-pH5 and Zn-HIS-2.1-pH5 with Na-citrate released >78% of the total Zn (results not shown). In contrast, Na-citrate treatment only released 15% of the total Zn from synthetic Zn-kaolinite, confirming the high selectivity of citrate for hydroxy-Al polymers. From Zn-sorbed gibbsite spiked into quartz powder, about 60% of the total soil Zn were extracted

in the first two steps of the SEP. In comparison with the data for Zn-HIS-6.9-pH5, this indicates that Zn sorbed to hydroxy-Al polymers in clays is more strongly retained than Zn-sorbed to gibbsite, in agreement with previous work [8]. The SEP results thus suggest that Zn sorption to aluminium (hydr)oxides was not dominant in the studied soils. The hydroxylamine hydrochloride (NH_2OH-HCl) solution used in F3 selectively dissolved birnessite and lithiophorite, as previously reported [54]. In the soils, little Zn was extracted in F3 (2-9 % of total Zn), suggesting that only a minor fraction of Zn was sorbed to or incorporated into Mn-bearing minerals.

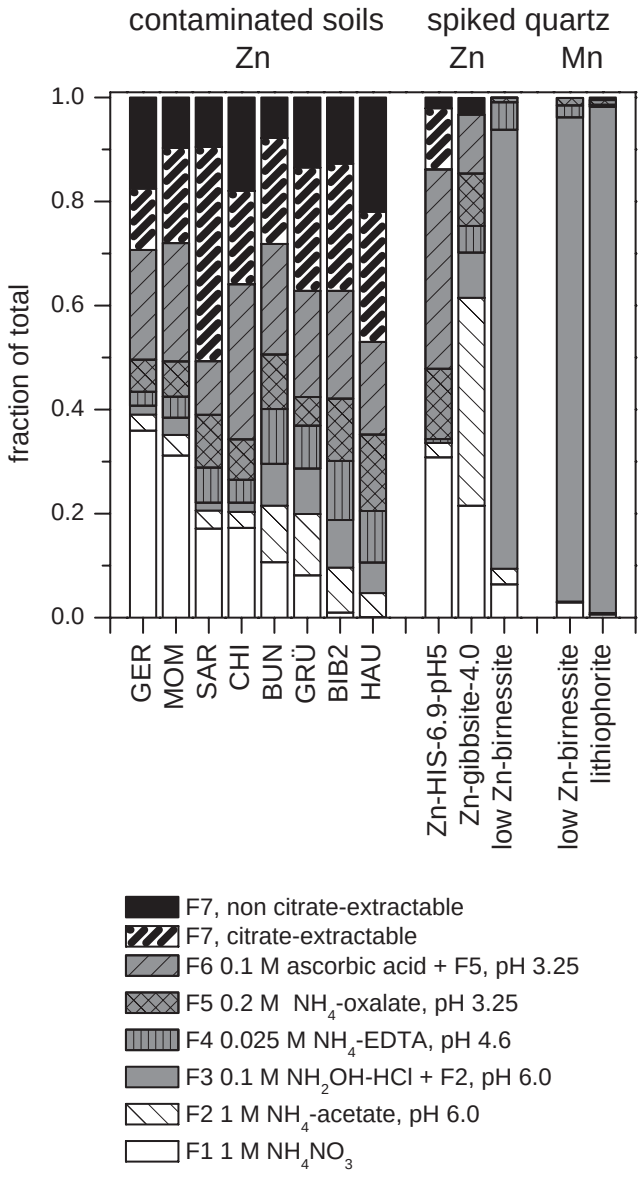

Figure 3.6. Sequential extraction results for contaminated soil samples (Zn) and for quartz powder spiked with Zn-HIS-6.9-pH5 (Zn), Zn-gibbsite-4.0 (Zn), low Zn-birnessite (Zn+Mn) and lithiophorite (Mn). Note: The citrate extraction of the residual fraction F7 was only performed for soils and Zn-HIS-6.9-pH5 spiked quartz.

3.4. Discussion

3.4.1. Sorption of Zn in hydroxy-interlayered minerals

The sorption of Zn to HIS as a function of hydroxy-Al loading, solution pH, and Zn concentration has previously been studied by Janssen and coworkers [4, 55]. They found that the formation of hydroxy-Al interlayers reduces the cation exchange capacity, but provides high-affinity sorption sites for Zn. Thus, sorption of Zn to HIS could be modeled as a combination of high-affinity sorption of Zn to Al-polymers and cation exchange to the interlayer-free portions of the HIS. The extent of specific Zn sorption increased with Al-loading and solution pH. These results were obtained from experiments with Wyoming Clay Spur montmorillonite. The same type of clay material was also used by Schlegel and Manceau [10]. It has a N_2-BET surface area of ~31 m^2/g similar to the Wyoming montmorillonite SWy-2 [23, 24], which has been used in the current study and the work by Scheinost et al. [14]. Thus, the results from Zn uptake studies by Janssen et al. [4] can be compared to the local coordination of Zn derived from EXAFS data obtained with a similar clay mineral.

The analysis of the EXAFS spectra (Fig. 3.2, Table 3.3) demonstrated that the local coordination of Zn sorbed to Al-polymers depends on solution pH, initial Zn/Al ratio, mode of Zn uptake, and reaction time. In general, higher pH, lower initial Zn/Al ratio, and Zn coprecipitation instead of adsorption seems to favor the bonding of Zn as a hexadentate complex in the vacancies of gibbsitic Al-polymers. As the Zn loading of the Zn-HIS phases increased with high Zn/Al ratio or longer incubation time, uptake shifted to sorption at sites with decreasing Al coordination and to uptake by cation exchange (Table 3.2). Differentiation between these two trends by LCF was complicated, because they both had similar effects on the shape of the EXAFS spectra (reduced second shell and higher shell signals compared to Zn incorporated into dioctahedral vacancies). According to Janssen et al. [4], uptake of Zn by cation exchange only becomes relevant once sorption to Al-polymers approaches its maximum.

At a hydroxy-Al loading of 2 mol/kg, i.e., the same as for to the HIS phases studied in this work, sorption at pH 5.0 was reported to reach a maximum of 80 mmol/kg specifically sorbed and 80 mmol/kg exchangeable Zn [4]. At pH 6.6, maximum uptake reached 250 mmol/kg specifically sorbed and 130 mmol/kg exchangeable Zn [4]. Thus, the Zn-HIS samples synthesized at pH 6.0 and 7.0 at low Zn/Al ratio were loaded with Zn at levels far below the maximum for high-affinity uptake, as reflected in the high coordination numbers. In Zn-HIS synthesized by adsorption of Zn to HIS at pH 5.0, however, the samples with highest loadings exceeded the maximum for specific

sorption (80 mmol/kg, 5200 mg/kg) indicated by Janssen et al. [4]. Based on this limit for specific Zn uptake, 23% of the Zn in the sample Zn-HIS-6.9-pH5 would be expected to be exchangeably adsorbed. This compares to a fitted fraction of outer-sphere aqueous Zn of 16% (Table 3.2) and an exchangeable (F1) fraction of ~30% released by sequential extraction (Fig. 3.6). However, some exchangeable Zn may have been lost from these samples (Zn-HIS with Zn adsorbed at pH 5.0 at high initial Zn/Al ratios) as they were washed with DI water after reaction with Zn-containing solution, possibly causing a reduction in the sorbed amount of Zn and the fraction of exchangeable Zn relative to the HIS in contact with the Zn-containing solution.

The shift in Zn speciation with Zn-loading reflects that hydroxy-Al polymers form island-like structures rather than complete gibbsitic interlayer sheets [1, 5], in which Zn could only be incorporated into the dioctahedral vacancies. Complete hydroxy-Al interlayers cannot form in HIM because, as the degree of Al-polymerization increases, the positive charge of the interlayer becomes negligible and the negative charge of the 2:1 layers cannot be balanced [5]. Based on the stoichiometry of the montmorillonite SWy-2 ($[Al_{3.02}Fe_{0.41}Mn_{0.01}Mg_{0.54}Ti_{0.02}][Si_{7.98}\ Al_{0.02}]O_{20}(OH)_4$) and assuming a maximum of 4 Al atoms in the hydroxy-interlayer per unit cell, the filling of the interlayers of the synthetic HIS with hydroxy-Al (2 mmol/g montmorillonite) reached 37 % of a complete gibbsite sheet. An average filling of 78% has been reported from the analysis of HIM contained in 12 Alabama soils [56]. These hydroxy-Al polymers may be arranged as polymer chains and partial cyclic polymers [5], offering a variety of sorption sites for Zn with different degree of Al coordination. The EXAFS results suggest that Zn occupies these sites in the order of decreasing Al coordination. Interestingly, the coprecipitation of Zn with hydroxy-Al led to a higher final Zn/Al ratio and higher Zn-Al coordination than sorption of Zn to preformed HIS under otherwise comparable conditions (Zn-HIS-7.7-CPT versus Zn-HIS-5.7-pH5, Tables 3.2 and 3.3). This could indicate that the incorporation of Zn^{2+} into the gibbsitic polymers during HIS formation partly compensated the loss of positive charge due to Al polymerisation, enhancing the formation of cyclic Zn-containing hydroxy-Al polymers.

3.4.2. Retention of Zn in hydroxy-interlayered phyllosilicates in soils

Analysis of the soil EXAFS spectra by LCF indicated that Zn in all soils was to a substantial extent sequestered into Zn-HIM (Table 3.4, proxy Zn-HIS-6.9-pH5). Since only HIV, but no HIS was detected in the studied soils, we assume Zn-HIM in these soils to mainly correspond to Zn-HIV. The highest percentages of Zn-HIM (75-84%) were detected in the soils HAU and SAR which had the lowest Zn contents (Table 3.1). In the soils BUN, GRÜ and BIB2, which all had an intermediate soil pH and similar

organic C, clay and Zn contents, about half (50-54%) of the total Zn was present as Zn-HIM. The lowest fractions of Zn-HIM (29-34%) were found in the soils GER, MOM, and CHI1 with low pH and clay contents. The percentages of Zn sorbed to other soil components than HIM decreased from the soils GER and MOM (60-65%) with lowest pH and clay contents over the soils CHI, BUN, GRÜ and BIB2 (29-36%) with acidic to intermediate pH to the soils HAU and SAR (0%) with lowest Zn contents. The results from LCF qualitatively matched the trends in Zn fractionation by sequential extraction (Fig. 3.6). While the exchangeable fraction F1 decreased with increasing soil pH, all soils contained a substantial percentage of Zn in the fractions F6+F7, which was highest in the soils HAU and SAR.

Even though all Zn-HIS references were included in the LCF analysis, the best fits were consistently obtained with the reference spectrum Zn-HIS-6.9-pH5. This reference is characterized by a relatively high Zn loading (Table 3.2) and a rather low Zn-Al coordination number (Table 3.3). Thus, the speciation of Zn within soil HIM was similar in all soils and indicative for a loading close to HIM sorption capacity. This interpretation is supported by estimates of the maximum amounts of soil Zn that can be retained by specific uptake into HIM (based on specific Zn adsorption maxima for HIS of 80 mmol/kg at pH 5.0 and 250 mmol/kg at pH 6.6, [4]). In a soil with pH 5.0 and a low clay content of 100 g/kg (assumed to consist of 25% HIM), the maximum soil Zn content sequestered into Zn-HIM would equal 131 mg/kg Zn, while 1020 mg/kg Zn could be specifically sorbed in HIM in a soil with pH 6.6 and 250 g/kg clay (assumed to consist of 25% HIM). Considering the Zn contents of the studied soils (Table 3.1), it is therefore likely that the HIM in most soils were loaded with Zn close to their sorption maximum.

Except for soil MOM, LCF also returned substantial fractions (13-48%) of Zn incorporated into phyllosilicates (using ZnMg-kerolites as proxies, Table 3.4). The fitted amounts of ZnMg-kerolite (fractions × soil Zn content) exceeded the upper limits for normal geogenic Zn contents in most soils. This suggests that the Zn-phyllosilicate formed in response to Zn input rather than being of geogenic origin, highlighting the relevance of these phases for Zn uptake in soils over wide pH ranges [33, 34, 57].

Previous studies reported the formation of Zn-HIM in contaminated and uncontaminated soils with pH 3.9-5.6 [12, 14, 15]. In the present study, we identified Zn-HIM in a range of soils including soils with acidic pH as well as soils with slightly acidic to near-neutral pH containing inorganic C (GRÜ, BIB2, and HAU). These results demonstrate that formation of Zn-HIM is not restricted to acidic soil environments. Even though soil HAU had a neutral pH and contained substantial amounts of organic C, the major fraction of total Zn was associated with HIM, indicating the high stability

of Zn-HIM even in environments where other Zn phases could form. In natural soils or soils contaminated with moderate amounts of Zn, incorporation of Zn into HIM may be a dominant sequestration pathway. However, the sorption capacity of HIM is limited. If continued Zn input into acidic soils leads to the accumulation of Zn to the sorption limits of HIM, further Zn will readily leach to deeper soil layers. In slightly acidic to neutral soils, on the other hand, saturation of HIM with Zn will result in Zn retention via alternative mechanisms such as enhanced Zn adsorption to soil organic matter or formation of Zn bearing precipitates of the LDH- or phyllosilicate-type [29, 34].

3.5. Conclusions

Zn sorption to Al-polymers in HIM at low loadings occurs in the dioctahedral vacancies of cyclic gibbsitic clusters. With increasing Zn loading, Zn sorption shifts to sites with decreasing Al coordination. Zn sorbed to the hydroxy-Al polymers in HIM are stable even under acidic conditions where other specific uptake mechanisms for Zn are less relevant. However, the sorption capacity of HIM is limited. Therefore, HIM may strongly affect the speciation of Zn in pristine soils or soils at moderate contamination levels, but do not allow to immobilize and accumulate continued input of high levels of Zn into soils.

Acknowledgements

Michel Schlegel and Darryl Roberts are acknowledged for providing several EXAFS spectra of reference compounds used in this study. We thank Farid Juillot for providing Zn-kaolinite samples, Beda Hofmann for providing natural Zn containing lithiophorite, Jakob Frommer for preparation of gibbsite, Gerome Tokpa for performing sequential extractions of soil samples, André Villard for thin section preparation and Kurt Barmettler and Charlotte Ganter for support in the laboratory. Three anonymous reviewers are thanked for their constructive comments on an earlier version of this manuscript. Stefan Mangold (XAS, ANKA, Germany) and Matthew Marcus (10.3.2, ALS, USA) are acknowledged for their help with data acquisition. The Angströmquelle Karlsruhe GmbH (ANKA, Karlsruhe, Germany) and the Advanced Light Source (ALS, Berkeley, USA) are acknowledged for providing beamtime. The ALS is supported by the Director, Office of Science, Office of Basic Energy Sciences, Material Sciences Division, of the U.S. Departement of Energy under Contract No. DE-AC03-76SF00098 at Lawrence Berkeley National Laboratory. This project was financially supported by the Swiss Science Foundation under Contract No. 200021-101876 and 200020-116592.

References

[1] Barnhisel, R. I.; Bertsch, P. M., Chlorites and hydroxy-interlayered vermiculite and smectite. In *Minerals in Soil Environments*, Dixon, J. B.; Weed, S. B., Eds. Soil Science Society of America: Madison, 1989.

[2] Dixon, J. B.; Jackson, M. L., Properties of intergradient chlorite-expansible layer silicates of soil. *Soil Sci. Soc. Am. Proc.* 1962, 26, 356-382.

[3] Rich, C. I., Hydroxy interlayers in expansible layer silicates. *Clays Clay Miner.* 1968, 16, 15-30.

[4] Janssen, R. P. T.; Bruggenwert, M. G. M.; van Riemsdijk, W. H., Zinc ion adsorption on montmorillonite-Al hydroxide polymer systems. *Eur. J. Soil Sci.* 2003, 54, 347-355.

[5] Meunier, A., Soil hydroxy-interlayered minerals: A re-interpretation of their crystallochemical properties. *Clays Clay Miner.* 2007, 55, 380-388.

[6] Lothenbach, B.; Furrer, G.; Schulin, R., Immobilization of heavy metals by polynuclear aluminium and montmorillonite compounds. *Environ. Sci. Technol.* 1997, 31, 1452-1462.

[7] Saha, U. K.; Taniguchi, S.; Sakurai, K., Adsorption behavior of cadmium, zinc, and lead on hydroxyaluminum– and hydroxyaluminosilicate–montmorillonite complexes. *Soil Sci. Soc. Am. J.* 2001, 65, 694-703.

[8] Keizer, M. G.; Bruggenwert, M. G. M., Adsorption of heavy metals by clay-aluminium hydroxide complexes. In *Interactions at the Soils Colloid-Soil Solution Interface*, Bolt, G. H.; De Boodt, M. F.; Hayes, M. H. B.; McBride, M. B., Eds. Kluwer Academic Publishers: Dordrecht, 1991; pp 177-203.

[9] Nachtegaal, M.; Scheidegger, A. M.; Dahn, R.; Chateigner, D.; Furrer, G., Immobilization of Ni by Al-modified montmorillonite: A novel uptake mechanism. *Geochim. Cosmochim. Acta* 2005, 69, 4211-4225.

[10] Schlegel, M. L.; Manceau, A., Zn incorporation in hydroxy-Al- and Keggin Al-13-intercalated montmorillonite: A powder and polarized EXAFS study. *Environ. Sci. Technol.* 2007, 41, 1942-1948.

[11] Manceau, A.; Tamura, N.; Celestre, R. S.; MacDowell, A. A.; Geoffroy, N.; Sposito, G.; Padmore, H. A., Molecular-scale speciation of Zn and Ni in soil ferromanganese nodules from loess soils of the Mississippi Basin. *Environ. Sci. Technol.* 2003, 37, 75-80.

[12] Manceau, A.; Tommaseo, C.; Rihs, S.; Geoffroy, N.; Chateigner, D.; Schlegel, M. L.; Tisserand, D.; Marcus, M. A.; Tamura, N.; Zueng-Sang, C., Natural speciation of Mn, Ni, and Zn at the micrometer scale in a clayey paddy soil

using X-ray fluorescence, absorption, and diffraction. *Geochim. Cosmochim. Acta* 2005, 60, 4007-3034.

[13] Roberts, D. R.; Ford, R. G.; Sparks, D. L., Kinetics and mechanisms of Zn complexation on metal oxides using EXAFS spectroscopy. *J. Colloid Interface Sci.* 2003, 263, 364-376.

[14] Scheinost, A. C.; Kretzschmar, R.; Pfister, S.; Roberts, D. R., Combining selective sequential extractions, X-ray absorption spectroscopy, and principal component analysis for quantitative zinc speciation in soil. *Environ. Sci. Technol.* 2002, 36, 5021-5028.

[15] Manceau, A.; Marcus, M. A.; Tamura, N.; Proux, O.; Geoffroy, N.; Lanson, B., Natural speciation of Zn at the micrometer scale in a clayey soil using X-ray fluorescence, absorption, and diffraction. *Geochim. Cosmochim. Acta* 2004, 68, 2467-2483.

[16] Odnevall Wallinder, I.; Leygraf, C.; Karlèn, C.; Heijerick, D. G.; Janssen, C. R., Atmospheric corrosion of zinc-based materials runoff rates, chemical speciation and ecotoxicity effects. *Corros. Sci.* 2001, 43, 809-816.

[17] Hendershot, W. H.; Duquette, M., A simple chloride method for determining cation exchange capacity and exchangeable cations. *Soil Sci. Soc. Am. J.* 1986, 50, 605-608.

[18] Gee, G.; Or, D., Particle size analysis. In *Methods of Soil Analysis. Part 4. Physical Methods*, Dane, J. H.; Topp, C. C., Eds. Soil Science Society of America, Madison, USA: 2002; pp 255-293.

[19] Kimpe, C. R., Soil separation for mineralogical analysis. In *Soil Sampling and Methods of Analysis*, Carter, M. R., Ed. Lewis Publishers: Boca Raton, 1993.

[20] Kimpe, C. R., Clay and silt analysis. In *Soil Sampling and Methods of Analysis*, Carter, M. R., Ed. Lewis Publishers: Boca Raton, 1993.

[21] Brown, G.; Farrow, R., Introduction of glycerol into flakes aggregates by vapour pressure. *Clay Miner. Bull.* 1956, 3, 44-45.

[22] Brunton, G., Vapor pressure glycolation of oriented clay minerals. *Am. Mineral.* 1955, 40, 124-126.

[23] Bradbury, M. H.; Baeyens, B., N_2-BET surface area measurements on crushed and intact minerals and rocks: A proposal for estimating sorption transfer factors. *Nucl. Technol.* 1998, 122, 250-253.

[24] van Olphen, H.; Fripiat, J. J., *Data Handbook for Clay Minerals and Other Non-Metallic Minerals*. Pergamon Press: Oxford, 1979.

[25] Petit, S.; Decarreau, A.; Mosser, C.; Ehret, G.; Grauby, O., Hydrothermal synthesis (250°C) of copper-substituted kaolinites. *Clays Clay Miner.* 1995, 43,

482-494.

[26] Feng, Q.; Honbu, C.; Yanagisawa, K.; Yamasaki, N., Hydrothermal soft chemical reaction for formation of sandwich layered manganese oxide. *Chem. Mater.* 1999, 11, 2444-2450.

[27] Kyle, J. H.; Posner, A. M.; Quirk, J. P., Kinetics of isotopic exchange of phosphate adsorbed on gibbsite. *J. Soil Sci.* 1975, 26, 32-43.

[28] Schlegel, M. L.; Manceau, A.; Charlet, L., EXAFS study of Zn and ZnEDTA sorption at the goethite (alpha-FeOOH)/water interface. *J. Phys. IV* 1997, 7, 823-824.

[29] Jacquat, O.; Voegelin, A.; Villard, A.; Marcus, M. A.; Kretzschmar, R., Formation of Zn-rich phyllosilicates, Zn-layered double hydroxide and hydrozincite in contaminated calcareous soils. *Geochim. Cosmochim. Acta* 2002, 72, 5037-5054.

[30] Marcus, M. A.; MacDowell, A. A.; Celestre, R. S.; Manceau, A.; Miler, T.; Padmore, H. A.; Sublett, R. E., Beamline 10.3.2 at ALS: a hard X-ray microprobe for environmental and materials science. *J. Synchrotron Rad.* 2004, 11, 239-247.

[31] Ravel, B.; Newville, M., Athena, Artemis, Hephaestus: data analysis for X-ray absorption spectroscopy using IFEFFIT. *J. Synchrotron Rad.* 2005, 12, 537-541.

[32] Manceau, A.; Boisset, M. C.; Sarret, G.; Hazemann, R. L.; Mench, M.; Cambier, P.; Prost, R., Direct determination of lead speciation in contaminated soils by EXAFS spectroscopy. *Environ. Sci. Technol.* 1996, 30, 1540-1552.

[33] Manceau, A.; Lanson, B.; Schlegel, M. L.; Harge, J. C.; Musso, M.; Eybert-Berard, L.; Hazemann, J. L.; Chateigner, D.; Lamble, G. M., Quantitative Zn speciation in smelter-contaminated soils by EXAFS spectroscopy. *Am. J. Sci.* 2000, 300, 289-343.

[34] Voegelin, A.; Pfister, S.; Scheinost, A. C.; Marcus, M. A.; Kretzschmar, R., Changes in zinc speciation in field soil after contamination with zinc oxide. *Environ. Sci. Technol.* 2005, 39, 6616-6623.

[35] Isaure, M.-P.; Laboudigue, A.; Manceau, A.; Sarret, G.; Tiffrau, C.; Trocellier, P.; Lamble, G. M.; Hazemann, J. L.; Chateigner, D., Quantitative Zn speciation in a contaminated dredged sediment by μ-PIXE, μ-SXRF, EXAFS spectroscopy and principal component analysis. *Geochim. Cosmochim. Acta* 2002, 66, 1549-1567.

[36] Ankudinov, A. L.; Ravel, B.; Rehr, J. J.; Conradson, S. D., Real-space multiple-scattering calculation and interpretation of x-ray-absorption near-edge structure.

Phys. Rev. B 1998, 58, 7565-7576.

[37] Saalfeld, H.; Wedde, M., Refinement of crystal-structure of gibbsite, $Al(OH)_3$. *Z. Kristallogr.* 1974, 139, 129-135.

[38] Bish, D. L.; Vondreele, R. B., Rietveld refinement of non-hydrogen atomic positions in kaolinite. *Clays Clay Miner.* 1989, 37, 289-296.

[39] Teo, B. K., *EXAFS: Basic Principles and Data Analysis*. Springer: Berlin, 1986.

[40] Ravel, B., ATOMS: crystallography for the X-ray absorption spectroscopist. *J. Synchrotron Rad.* 2001, 8, 314-316.

[41] Perdikatsis, B.; Burzlaff, H., Structural refinement of talc $Mg_3[(OH)_2Si_4O_{10}]$. *Z. Kristallogr.* 1981, 156, 177-186.

[42] Zeien, H.; Brümmer, G. W., Chemische Extraktionen zur Bestimmung von Schwermetallbindungsformen in Böden. *Mitt. Dtsch. Bodenkundl. Ges.* 1989, 59, 505-510.

[43] Voegelin, A.; Tokpa, G.; Jacquat, O.; Barmettler, K.; Kretzschmar, R., Zinc fractionation in contaminated soils by sequential and single extractions: Influence of soil properties and zinc content. *J. Environ. Qual.* 2008, 37, 1190-1200.

[44] Tamura, T., Identification of clay minerals from acid soils. *J. Soil Sci.* 1958, 9, 141-147.

[45] Keller, T.; Desaules, A., Böden der Schweiz: Schadstoffgehalte und Orientierungswerte. *Umwelt Materialen 139, Bundesamt für Umwelt, Wald and Lanschaft, Bern, Switzerland.* 2001.

[46] Douglas, L. A., Vermiculites. In *Minerals in Soil Environments*, Dixon, J. B.; Weed, S. B., Eds. Soil science society of America: Madison, 1989; pp 635-728.

[47] Juillot, F.; Morin, G.; Ildefonse, P.; Calas, G.; Brown, G. E., EXAFS signature of structural Zn at trace levels in natural and synthetic trioctahedral 2 : 1 phyllosilicates. *Am. Mineral.* 2006, 91, 1432-1441.

[48] O'Day, P.; Rehr, J. J.; Zabinsky, S. I.; Brown, G. E. J., Extended X-ray absorption fine structure (EXAFS) analysis of disorder and multiple-scattering in complex crystalline solids. *J. Am. Chem. Soc.* 1994, 116, 2938-2949.

[49] Schlegel, M. L.; Manceau, A., Evidence for the nucleation and epitaxial growth of Zn phyllosilicate on montmorillonite. *Geochim. Cosmochim. Acta* 2006, 70, 901-917.

[50] Manceau, A.; Calas, G., Nickel-bearing clay-minerals. 2. Intracrystalline distribution of nickel - an X-ray absorption study. *Clay Miner.* 1986, 21, 341-360.

[51] Sarret, G.; Saumitou-Laprade, P.; Bert, V.; Proux, O.; Hazemann, J. L.; Traverse, A.; Marcus, M. A.; Manceau, A., Forms of zinc accumulated in the hyperaccumulator Arabidopsis halleri. *Plant Physiol.* 2002, 130, 1815-1826.

[52] Elzinga, E. J.; Reeder, R. J., X-ray absorption spectroscopy study of Cu^{2+} and Zn^{2+} adsorption complexes at the calcite surface: Implications for site-specific metal incorporation preferences during calcite crystal growth. *Geochim. Cosmochim. Acta* 2002, 66, 3943-3954.

[53] Farmer, V. C.; Smith, B. F. L.; Wilson, M. J.; Loveland, P. J.; Payton, R. W., Readily-extractable hydroxyaluminium interlayers in clay- and silt-sized vermiculite. *Clay Miner.* 1988, 23, 271-277.

[54] Chao, T. T., Selective dissolution of manganese oxides from soils and sediments with acidified hydroxylamine hydrochloride. *Soil Sci. Soc. Am. Proc.* 1972, 36, 764-768.

[55] Janssen, R. P. T.; Bruggenwert, M. G. M.; van Riemsdijk, W. H., Effect of Al hydroxide polymers on cation exchange of montmorillonite. *Eur. J. Soil Sci.* 2003, 54, 335-345.

[56] Kirkland, D. L.; Hajek, B. F., Formula derivation of Al-interlayered vermiculite in selected soil clays. *Soil Sci.* 1972, 114, 317-322.

[57] Nachtegaal, M.; Marcus, M. A.; Sonke, J. E.; Vangronsveld, J.; Livi, K. J. T.; Van der Lelie, D.; Sparks, D. L., Effects of in situ remediation on the speciation and bioavailability of zinc in a smelter contaminated soil. *Geochim. Cosmochim. Acta* 2005, 69, 4649-4664.

4. Soil properties controlling Zn speciation and fractionation in contaminated soils

Abstract

We determined the speciation of Zn in 49 soils differing widely in pH (4.1 to 7.7) and total Zn content (251-30090 mg/kg) using extended X-ray absorption fine structure (EXAFS) spectroscopy. All soils had been contaminated since several decades by inputs of aqueous Zn with runoff-water from galvanized power line towers. Pedogenic Zn species identified by EXAFS included octahedrally- and tetrahedrally coordinated sorbed or complexed Zn, Zn in hydroxy-interlayered minerals (Zn-HIM), Zn-rich phyllosilicates, Zn-layered double hydroxides (Zn-LDH), and hydrozincite. Zn-HIM was only observed in (mostly acidic) soils containing less than 2000 mg/kg of Zn, reflecting the high affinity but limited sorption capacity of HIM. Zn-bearing precipitates, such as Zn-LDH and Zn-rich phyllosilicates, became more dominant with increasing pH and increasing total Zn content relative to the total concentration of adsorption sites. Zn-LDH was the most abundant Zn-precipitate and was detected in soils with pH >5.2. Zn-rich phyllosilicates were detected even at lower soil pH, but they were generally less abundant than Zn-LDH. Hydrozincite was only identified in two soils with extremely high Zn contents. When the soils were grouped according to their Zn speciation inferred from EXAFS, clear differences in Zn fractionation by sequential extraction were identified. From Zn-HIM containing soils, most of the total Zn was recovered in the exchangeable and the most recalcitrant fractions. In contrast, from soils containing the highest percentage of Zn-precipitates, Zn was mainly extracted in the intermediate extraction steps. The results of this study demonstrate that soil pH and Zn contamination level relative to the concentration of adsorption sites are the most important factors controlling the formation of pedogenic Zn species, and hence, Zn fractionation by sequential extraction.

Submitted to Geochimica Cosmochimica Acta as: Jacquat, O., Voegelin, A., Kretzschmar, R., Soil properties controlling Zn speciation and fractionation in contaminated soils.

4.1. Introduction

Soil contamination with zinc (Zn) is widespread and in many regions still increasing due to emissions from mining, smelting, chemical and processing industries, agriculture, and sewage sludge application. Elevated Zn concentrations in soils can pose long-term risks for soil fertility and ecosystem health, e.g., by affecting soil microbial activity or causing phytotoxicity. The speciation of Zn exerts a strong influence on the mobility, bioavailability and toxicity of Zn in contaminated soils. In acidic soils, adsorption of Zn is mostly governed by cation exchange on negatively charged surfaces of clay minerals and soil organic matter, leaving adsorbed Zn relatively labile. At near-neutral to alkaline soil pH, specific adsorption of Zn to Fe- and Mn-(hydr)oxides, clay minerals, and organic matter, as well as precipitation of Zn-rich mineral phases become predominant [1, 2].

Metal fractionation in soils is commonly assessed by single or sequential extractions [3-6]. Due to the limited selectivity of extraction procedures [6, 7], however, the types and concentrations of different Zn species cannot be inferred from extraction data [8-10]. In contrast, synchrotron-based extended X-ray absorption fine structure (EXAFS) spectroscopy allows for the in-situ identification and quantification of the dominant metal species [8, 9]. Over the past two decades, EXAFS spectroscopy greatly contributed to advances in elucidating the fate of heavy metals in contaminated soils and sediments [11-15]. Based on the interpretation of bulk and micro-focused soil EXAFS spectra by linear combination fits (LCF) of reference spectra, Manceau and coworkers [16] first identified and quantified different Zn species present in the clay and silt fractions of contaminated soils. Besides Zn-bearing minerals from smelter emissions, several pedogenic (soil-formed) Zn species were identified, including Zn-bearing phyllosilicate-type precipitates, Zn in the structure of goethite, and Zn sorbed to Fe and Mn oxides [16]. Further studies on the forms of Zn in soils contaminated by mining, smelting, or foundry emissions, deposition of dredged sediments or sewage irrigation confirmed the formation and quantitative relevance of Zn-bearing precipitates and sorbed/complexed Zn species upon weathering of the Zn-bearing phases emitted by the respective contamination source [8, 17-25] (Table 4.1). Pedogenic Zn precipitates identified in these slightly acidic to neutral soils included Zn-layered double hydroxides (Zn-LDH) and Zn-phyllosilicates. In an acidic contaminated soil, Zn was shown to be strongly retained by incorporation into the Al-hydroxy-interlayer of hydroxy-interlayered minerals (HIM) [9]. The formation of Zn-HIM, as well as the uptake of Zn into the gibbsitic sheets of the phyllomanganate lithiophorite, have also been reported for pristine soils [26-28].

Table 4.1. Soil characteristics and nature and proportion of Zn species identified by bulk EXAFS spectroscopy in upland contaminated soils (chronological order).

Sample Material	Contamination[a]	Soil properties			LCF results	Ref.[f]
		pH	Zn[b]	TOC[c]		
Sandy horizon <2µm fraction Mortagne du Nord	Smelter	6.5 – 7.5	3140	NA	63% $Zn_{0.25}Mg_{0.75}$-kerolite 19% Zn-sorbed Fe hydroxides 20% Zn-sorbed birnessite	[16]
Tilled soil <2µm fraction Evin-Malmaison	Smelter	5.6 – 6.7	3816	NA	42% Zn containing goethite 68% $Zn_{0.2}Mg_{0.8}$-kerolite	[16]
Sandy soil <40 µm fraction Maatheide	Smelter	NA	59220	NA	47% $Zn_{0.25}Mg_{0.75}$-kerolite 14% hemimorphite 12% willemite 12% Zn-sorbed birnessite	[16]
Dredged sediment	Smelter	NA	6600	NA	73% sphalerite 40% Zn-sorbed ferrihydrite	[17]
Organic soil[d]	Smelter	3.2	6200	NA	66% franklinite 34% sphalerite	[22]
Stony loam[e]	Smelter	3.9	890	NA	Zn sorbed to Al-groups Fe and Mn hydroxides organic matter or aqueous Zn	[22]
Organic soil[d]	Smelter	3.2	6200	320	60% franklinite 30% sphalerite 10% aqueous Zn	[9]
Silty loam[e]	Smelter	3.9	890	50	55% aqueous Zn 45% Zn hydroxy-interlayer phyllosilicate	[9]
Luvisol Tilled Evin-Malmaison	Smelter	7.5	571	15	25% Zn bound to organic matter or goethite <35% Zn-phyllosilicates Zn-LDH	[19]
Luvisol Wooded Evin-Malmaison	Smelter	5.5	1380	64	41% Zn bound to organic matter or goethite <26% Zn-phyllosilicates 15% aqueous Zn Zn-LDH	[19]

[a]Contamination source. [b]Total Zn content (mg/kg). [c]Total organic carbon (g/kg), NA : not available. [d, e]Same soils, respectively. [f]Reference (chronological order).

To date, about a dozen studies (summarized in Table 4.1) have addressed the speciation of Zn in contaminated upland soils using EXAFS spectroscopy, mostly considering soils contaminated by emissions from mining and smelting. In these soils, Zn-bearing phases stemming from the emission source may still dominate the Zn speciation, thereby, lowering the sensitivity and accuracy of bulk EXAFS spectroscopy with respect to the identification and quantification of pedogenic Zn species [16]. Furthermore, due to the limited range of soils investigated by EXAFS spectroscopy so far, comprehensive data on the effects of soil properties and Zn content on the occurrence and abundance of various pedogenic Zn species is still lacking. In order to assess the environmental fate and ecotoxicological effects of Zn in contaminated soils, a better understanding of the formation of pedogenic Zn species as influenced by soil properties and Zn contamination level is needed.

Table 4.1. Continued

Sample Material	Contamination[a]	Soil properties			LCF results	Ref.[f]
		pH	Zn[b]	TOC[c]		
Organic soil	Smelter	6.2	21078	376	45% Zn bound to organic matter 20% aqueous Zn 15% franklinite 10% Zn-sorbed apatite/Zn-phytate 10% Zn-sorbed ferrihydrite	[23]
Non-calcareous loam	Brass foundry	6.5	2800	15	37% Zn-LDH 14% $Zn_{0.8}Mg_{0.2}$-kerolite 30% Zn-phytate 18% aqueous Zn <10% Zn-sorbed Mn and Fe hydroxides	[25]
Luvisol	Dredged sediment	8.2	6600	NA	60% sphalerite 20-30% Zn-sorbed Fe hydroxides 20-30% Zn-sorbed hectorite	[18]
Dregded sediment	Smelter	7.8	4700	7.2	50% Sphalerite 40% Zn-sorbed ferrihydrite 10-20% Zn-LDH and $Zn_{0.7}Mg_{0.3}$-kerolite	[21]
Sandy soil Non-remediated	Smelter	6.4	20476	NA	46% Zn-LDH 42% hemimorphite 11% gahnite	[20]
Sandy soil Remediated	Smelter	6.7	13144	NA	24% Zn-kerolite 39% hemimorphite 40% Zn-sorbed kaolinite (i.e. Zn-LDH)	[20]
Sandy loam	Sewage irrigation	6.5 - 7.0	1103	33	30% Zn-sorbed ferrihydrite 28% Zn phosphate dihydrate 24% $Zn_{0.45}Mg_{0.55}$-kerolite 11% willemite <10% gahnite	[8]
Mine tailings 4-6 cm depth	Mine tailings	5.5	650	24	53% Zn-sorbed montmorillonite 38% $Zn_{0.25}Mg_{0.75}$-kerolite	[24]

[a]Contamination source. [b]Total Zn content (mg/kg). [c]Total organic carbon (g/kg), NA : not available. [d, e]Same soils, respectively. [f]Reference (chronological order).

In a previous study, we investigated the fractionation of Zn in 49 contaminated soils spanning a wide range in soil properties and Zn loading using single and sequential extractions [10]. The soils had been contaminated by inputs of aqueous Zn with runoff-water from galvanized power line towers, thus, allowing us to investigate the influence of soil properties on the fractionation of Zn by sequential extraction excluding any interference by Zn-bearing phases stemming from the contamination source. Trends in the Zn fractionation data suggested that soil pH and soil Zn loading are the main factors influencing the fractionation of Zn [10]. In two subsequent studies, we investigated the speciation of Zn in six calcareous and eight mostly acidic HIM-containing soils in detail using bulk and micro-focused EXAFS spectroscopy [29, 30]. We demonstrated that the amount and type of Zn-precipitates forming in calcareous soils was mainly influenced by Zn contamination level and that formation of Zn-precipitates had resulted

in substantial accumulation of Zn in excess of the soil's capacity for Zn adsorption [30]. Furthermore, we showed that HIM represent an important sorbent for Zn in (mostly acidic) HIM-containing soils at low to intermediate Zn loadings [29]. The objectives of the current work were (i) to investigate the speciation of Zn in 49 contaminated soils by bulk EXAFS spectroscopy, analyzing all spectra by principle component analysis (PCA), target transform testing (TT), and linear combination fitting (LCF) using a large set of Zn reference spectra, (ii) to relate Zn speciation (inferred from EXAFS spectroscopy) to soil properties and Zn contamination level, and (iii) to discuss how differences in Zn speciation are reflected in Zn fractionation by sequential extractions as an indicator of Zn reactivity in soils.

4.2. Materials and Methods

4.2.1. Soil sampling and soil properties

Forty-nine topsoils (0-5 cm) were collected underneath 17 to 74 years-old galvanized power line towers across different geologic and climatic regions of Switzerland. The samples were air-dried, sieved to <2mm size, and homogenized by mixing. Powdered subsamples <50 μm were prepared from the <2mm fraction using an agate rotary mill. Soil pH was determined after equilibration of 1 g soil with 10 mL 0.01 M $CaCl_2$. Pressed pellets made of powdered soil material were analyzed for total element concentrations using an energy-dispersive X-ray fluorescence (XRF) spectrometer (Spectro X-Lab 2000). Total carbon (TC) content of the soils was determined on powdered samples using a CHNS elemental analyzer (CHNS-932, LECO). Total inorganic carbon (TIC) content of soils with pH >5.9 was quantified gravimetrically, following the method described by Loeppert et al. [31]. Total organic carbon (TOC) content was determined by subtracting the TIC from the respective TC content. After pretreatment of the soils with H_2O_2 for oxidation of organic matter, the sand content (50-200 μm) was quantified gravimetrically by wet sieving, the clay content (<2 μm) was determined by the pipette method [32], and the silt content was calculated. The contents of exchangeable Na, K, Mg, Ca, Al, Mn, Fe and Zn were determined in duplicate by extracting 7 g of soil with 210 mL 0.1 M $BaCl_2$ [33] and analyzing the cation concentrations by inductively coupled plasma-optical emission spectrometry (ICP-OES, Varian Vista MPX). Effective cation exchange capacity (ECEC) was calculated as the sum of charge equivalents of the extracted amounts of Na^+, K^+, Mg^{2+}, Ca^{2+}, Al^{3+}, Mn^{2+}, Fe^{2+} and Zn^{2+} per mass of soil.

4.2.2. EXAFS measurements and data extraction

EXAFS spectra of soil and reference samples at the Zn K-edge (9659 eV) were measured on the XAS beamline at ANKA (Angströmquelle Karlsruhe, Karlsruhe, Germany), the Swiss-Norwegian Beamline at ESRF (European Synchrotron Radiation Facility, Grenoble, France), and beamline X-11A at NSLS (National Synchrotron Light Source, Brookhaven, USA). Powdered soil samples and reference materials were measured in fluorescence or transmission mode at room temperature. Beam energy was calibrated by setting the first maximum of the first derivative of the absorption edge of metallic Zn to 9659 eV. The EXAFS spectra were extracted from the raw data using the software code Athena [34, 35]. The first inflection point of the absorption edge was used to set E_0. Absorption spectra were normalized using a first-order polynomial in the pre-edge region (-150 to -30 eV relative to E_0) and a second-order polynomial in the post-edge region (+150 eV up to 100 eV before end of spectrum). The EXAFS spectra were extracted using a cubic spline function adjusted by minimizing the amplitude of the Fourier transform at radial distances <0.9 Å (Autobk algorithm implemented in Athena, k-weight 3). Fourier transformed EXAFS spectra were extracted over the k-range 2 to 10 $Å^{-1}$, using a Kaiser-Bessel apodization window (window parameter = 2.5).

4.2.3. EXAFS reference spectra

An extensive database of Zn K-edge EXAFS spectra of reference samples was compiled and included primary Zn minerals (sphalerite, zincite, chalcophanite, gahnite, hemimorphite, willemite), secondary minerals and precipitates (ZnMg-kerolites with Zn/(Mg+Zn) ratios of 100 % (Zn-kerolite), 80% ($Zn_{0.8}Mg_{0.2}$-kerolite), 60% ($Zn_{0.6}Mg_{0.4}$-kerolite), 34% ($Zn_{0.34}Mg_{0.66}$-kerolite), and 6% ($Zn_{0.06}Mg_{0.94}$-kerolite), Zn-LDH, Zn-lithiophorite, amorphous $Zn(OH)_2$, Zn-goethite, Zn-ferrihydrite, Zn-phosphate), carbonates (Zn substituted calcite, hydrozincite, smithsonite), sorbed/complexed Zn at different loadings (Zn-sorbed birnessite, calcite, ferrihydrite, goethite, gibbsite, talc, Al-hydroxy interlayered montmorillonite (Zn-HIS)) and organic Zn species (Zn-phytate, Zn-oxalate dihydrate, Zn-citrate dihydrate, Zn-acetate dihydrate, Zn-malate). Details on most synthesis procedures have previously been reported [9, 25, 29, 30]. Zn-sorbed talc was prepared by mixing 200 mg talc (Sigma-Aldrich, Nr. 243604) with 50 mL of 20 µM $Zn(NO_3)_2$, 300 mM $NaNO_3$, 50 mM 2-(N-morpholino)ethanesulfonic acid and 35 mM NaOH. After reaction for 17 h at pH 6.6, the reacted talc was separated by centrifugation, frozen in liquid nitrogen, and freeze-dried. The final product contained 254 mg/kg Zn. The spectrum of Zn-sorbed calcite was kindly provided by Evert Elzinga [36].

4.2.4. EXAFS data analysis

Principal component analysis (PCA) and target transform testing (TT) were carried out on k^3-weighted bulk EXAFS spectra (k-range 2 to 10 $Å^{-1}$, interpolated to 0.05 $Å^{-1}$ grid) using SIXPack [37]. The number of relevant principal components was evaluated based on the empirical indicator function (IND) [38]. Including the relevant principal components, target transform testing was performed to identify suitable references for the analysis of soil EXAFS spectra by linear combination fitting (LCF). This assessment was based on the empirical SPOIL value [39] and the normalized sum of the squared residuals ($NSSR = \Sigma_i(k^3\chi_{exp}-k^3\chi_{fit})^2/\Sigma_i(k^3\chi_{exp})^2$) of the target transform [8, 17, 21, 23]. Subsequently, LCF analysis was carried out by calculating all possible single-component to five-component fits using the approach developed by Manceau and coworkers [16, 40]. Starting from the single-component (n=1) fit with the lowest NSSR, the number of components n was stepwise increased as long as the NSSR of the best n+1-component fit was at least 10% below the NSSR of the best n-component fit. The detection limit and precision of LCF has previously been estimated to be around 10% of the total Zn [17]. However, the sensitivity and accuracy of LCF ultimately depend on the spectral characteristics of all individual components present in the sample, and systematic errors result if a relevant reference is missing in the database used for LCF [16].

4.2.5. Sequential extraction

The fractionation of Zn in all soils except PER and LAU was previously determined using the sequential extraction procedure of Zeien and Brümmer [5] consisting of seven extraction steps [10]. Briefly, each soil was extracted in duplicates (2 g of soil each) according to the following sequence (with hypothetical interpretation according to Zeien and Brümmer [5] in parentheses): Fraction F1: 1 M NH_4NO_3 (readily soluble and exchangeable); Fraction F2: 1 M NH_4-acetate, pH 6.0 (mobilizable and $CaCO_3$ bound); Fraction F3: 0.1 M NH_2OH-HCl + 1 M NH_4-acetate, pH 6.0 (Mn oxides); Fraction F4: 0.025 M NH_4-EDTA, pH 4.6 (organically bound); Fraction F5: 0.2 M NH_4-oxalate, pH 3.25 (bound to amorphous and poorly crystalline Fe oxides); Fraction F6: 0.1 M ascorbic acid + 0.2 M NH_4-oxalate, pH 3.25 (bound to crystalline Fe oxides). All extraction steps were performed with a solution-to-soil ration of 25 mL/g. The solutions from the extraction steps F1 to F6 were analyzed by ICP-OES. The residual fraction F7 was determined by XRF spectrometry.

4.3. Results

4.3.1. Soil properties

Selected physical and chemical properties and the Zn contents of the 49 soils are summarized in Table 4.2. The data for all individual soils are provided in the appendix information (Tables A3.1 to A3.4). The soils differed strongly in pH, ranging from acidic to weakly alkaline (pH 4.1 to 7.7), and covered a wide range in TOC (9 to 102 g/kg), TIC (0 to 89 g/kg), texture (clay: 38 to 451 g/kg, silt: 111 to 700 g/kg, sand: 184 to 781 g/kg), and ECEC (8 to 464 mmolc/kg). The total Zn contents ranged from 251 to 30090 mg/kg, with an average of 4937 mg/kg.

Table 4.2. Summarized soil properties and Zn content, and normalized LCF results of all studied soils and soils containing Zn-HIM, <30%, 30-60%, and >60% of Zn-precipitates, respectively. For each group, minimum, average, and maximum values are provided.

		Soil properties							LCF results					
Group[a]		pH	TOC	Clay	ECEC[b]	Zn	Exch. Zn[c]	Zn_{eq}/ PCEC[d]	Zn-HIM	Zn-LDH	Zn-phyl.[e]	Hyd.[f]	^{VI}Zn[g]	^{IV}Zn[h]
			—(g/kg)—		($mmol_c$/kg)	–(mg/kg)–		——	(%)	(%)	(%)	(%)	(%)	(%)
All soils	min.	4.1	9	38	8	251	0	0.02	0	0	0	0	0	0
n = 49	avg.	6.0	48	176	174	4937	888	0.54	11	29	10	2	18	30
	max.	7.7	102	451	464	30090	3745	2.25	85	78	42	0	64	63
Zn-HIM	min.	4.1	9	48	8	251	<1	0.02	17	0	0	0	0	0
n = 12	avg.	5.2	41	150	92	786	176	0.12	43	2	16	0	25	13
	max.	6.9	97	334	232	1634	676	0.31	85	29	42	0	64	41
Zn-precipitates	min.	5.1	33	77	120	1322	<1	0.09	0	0	0	0	20	37
<30 %	avg.	6.0	60	175	225	4124	1379	0.39	0	6	14	0	31	50
n = 8	max.	7.3	95	451	411	9136	2834	0.84	0	29	27	0	44	63
Zn-precipitates	min.	5.3	21	71	84	1649	124	0.12	0	31	0	0	0	16
30-60%	avg.	6.1	54	208	201	6380	1216	0.64	0	41	8	0	15	36
n = 18	max.	6.9	102	406	362	13780	2838	1.89	0	59	21	0	28	60
Zn-precipitates	min.	5.6	14	38	71	1046	<1	0.13	0	0	0	0	0	0
>60 %	avg.	6.6	37	151	182	7694	922	0.94	0	53	6	9	6	25
n = 11	max.	7.7	78	309	464	30090	3745	2.25	0	78	25	53	31	40

[a]n: number of soils, [b]Effective cation exchange capacity, [c]Exchangeable Zn in 0.1 M $BaCl_2$ at solution-soil-ratio of 30 ml/g, [d]Total Zn content in charge equivalence divided by potential cation exchange capacity (PCEC) calculated according to Curtin and Rostad [55]. [e]Zn-phyllosilicate, [f]Hydrozincite, [g]Sorbed ^{VI}Zn, [h]Sorbed ^{VI}Zn.

The total Zn contents of all soils exceeded the upper limits of normal geogenic Zn concentrations of Swiss soils, which range from 57 mg/kg in acidic soils to 132 mg/kg Zn in neutral soils [41]. Thirty of 49 soils contained more than 2000 mg/kg Zn. Above this level, landuse restriction or soil remediation has to be undertaken in Switzerland

[42]. For the purpose of this study, we refer to soils with less than 2000 mg/kg as moderately contaminated, to soils from 2000 to 5000 mg/kg as strongly contaminated, and to soils with more than 5000 mg/kg as extremely contaminated.

4.3.2. PCA-TT analysis of bulk EXAFS spectra

The entire set of 49 soil EXAFS spectra is shown in Figure 4.1. In order to determine the number of statistically significant spectral components, the soil EXAFS spectra were evaluated by principal component analysis (PCA). The parameters of the first nine components obtained by PCA are given in Table 4.3. The empirical IND function reached a minimum for six spectral components, indicating that six spectral components were needed to reproduce the entire set of 49 soil EXAFS spectra [38]. The first six components explained 70% of the variance in the soil EXAFS data and satisfactorily reproduced all 49 soil EXAFS spectra (NSSR 0.4 to 3.0%).

The suitability of Zn reference spectra for LCF was subsequently identified by target transform testing (TT) using the first six components from PCA. This assessment was based on the classification of reference spectra using the empirical SPOIL value [39]: 0-1.5 excellent; 1.5-3 good; 3-4.5 fair; 4.5-6 acceptable; >6 unacceptable reference spectrum. Among all tested references, adsorbed, complexed, and mineral Zn species in tetrahedral coordination with low backscattering from second-neighbor atoms (Zn-phosphate, Zn-phytate, Zn-sorbed ferrihydrite and Zn-sorbed calcite) were assigned the lowest SPOIL values (Table 4.4). Target transform testing also returned a low SPOIL value for octahedrally coordinated aqueous Zn, whereas the SPOIL value of Zn-sorbed talc and Zn-sorbed goethite, which also contain Zn in octahedral coordination, categorized these reference spectra as fair. Among the ZnMg-kerolites available in our database, the best target transform was obtained for the pure Zn-kerolite. With increasing fraction of Mg in the octahedral layer, the SPOIL value increased. Zn-LDH, $Zn(OH)_2$ and hydrozincite were classified as good references, with similar SPOIL values as the Zn-rich kerolite phases. The spectra of Zn-LDH and Zn-rich kerolites exhibit split oscillations at 3.8 $Å^{-1}$ and 7.5 $Å^{-1}$ and an upward oscillation at 5 $Å^{-1}$ (Fig. 4.1). In Zn-rich phyllosilicates, backscattering of tetrahedral Si cations causes the upward oscillation at 5 $Å^{-1}$ to be prominent [43, 44]. In contrast, a shoulder instead of a well resolved peak is observed around 5 $Å^{-1}$ in the spectrum of Zn-LDH (Fig. 4.1). Furthermore, the absence of tetrahedral Si sheets in Zn-LDH leads to an oscillation maximum around 8.0 $Å^{-1}$, whereas in Zn-phyllosilicates, the respective oscillation peaks at 8.5 $Å^{-1}$ [45, 46]. Overall, many of the soil EXAFS spectra had spectral features closely resembling those of Zn-LDH (Fig 4.1. groups B, C, D), though further spectral components and noise added to their shape.

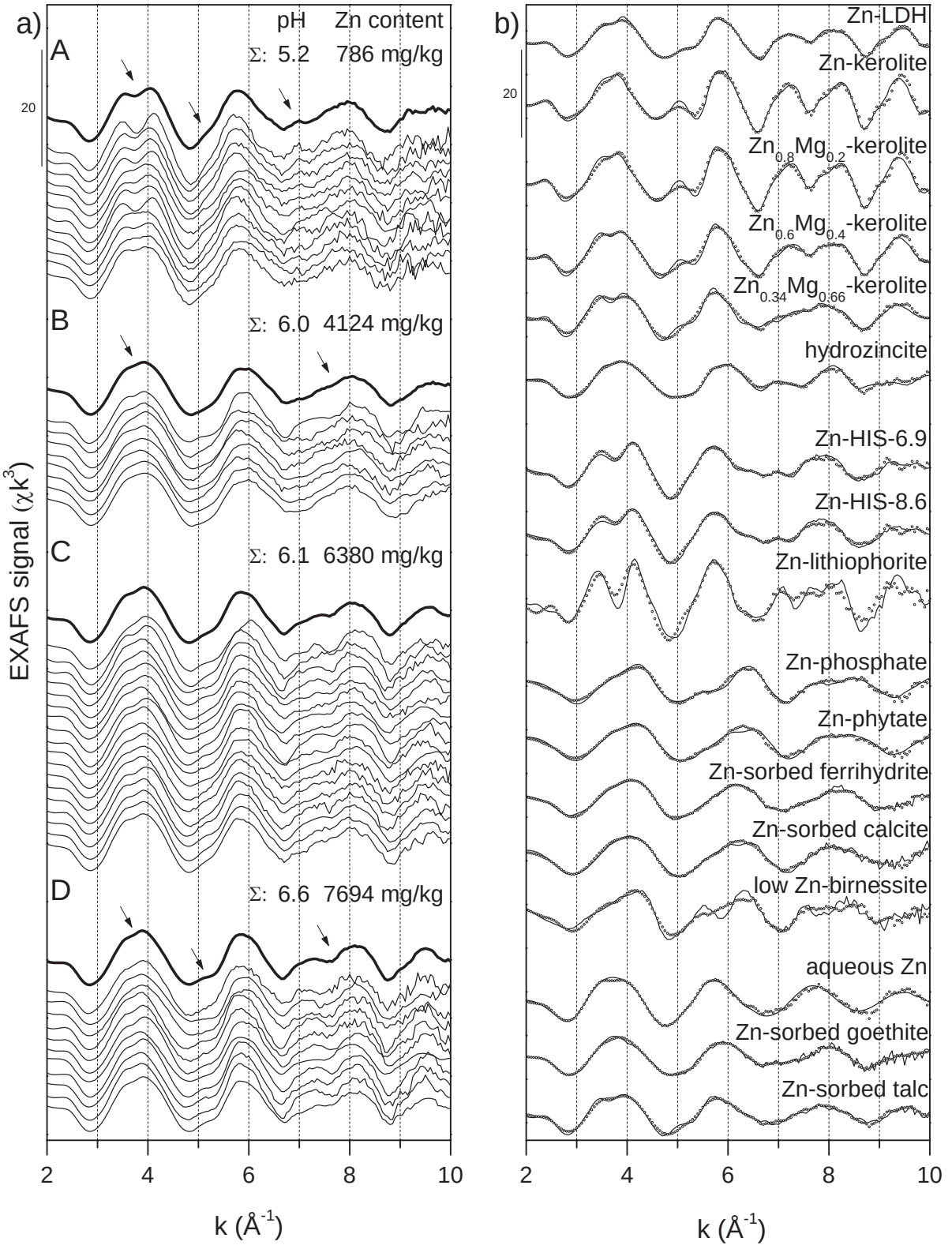

Figure 4.1. (a) Zn K-edge EXAFS spectra of soil samples grouped according to LCF results (Table 4.2). For the four defined groups, an average spectrum (Σ, thick lines) was calculated, highlighting the spectral characteristics of each group. (b) Zn K-edge EXAFS spectra for selected Zn compounds and sorbed/complexed reference compounds (solid lines) and target transforms (dotted lines, Table 4.4) calculated with the first 6 components of the principal component analysis (Table 4.3 and 4.4).

Table 4.3. Results of the principal component analysis on 49 EXAFS spectra.

Component	Eigenvalue	Variance	Cum. Var.[a]	IND[b]
1	218.7	0.496	0.496	0.00312
2	31.8	0.072	0.568	0.00254
3	23.8	0.054	0.622	0.00210
4	11.7	0.026	0.649	0.00205
5	10.8	0.024	0.673	0.00200
6	9.0	0.020	0.694	0.00198
7	7.9	0.017	0.711	0.00199
8	7.4	0.016	0.728	0.00199
9	7.2	0.016	0.745	0.00200

[a]Cumulative variance. [b]Indicator function.

The best proxies for Zn-HIM as indicated by TT were hydroxy-Al interlayered smectite (HIS) with high Zn loadings (Zn-HIS-6.9: 6900 mg/kg Zn, Zn-HIS-4.0: 4000 mg/kg Zn, Zn-HIS-8.6: 8600 mg/kg Zn). The spectra show a distinct splitting at 3.8 $Å^{-1}$ and lack the shoulder at 5 $Å^{-1}$ as well as the split oscillation observed in spectra of Zn-LDH or Zn-phyllosilicates (Fig. 4.1). In HIM with low Zn loadings, Zn is mainly incorporated in the dioctahedral vacancies of Al-hydroxy-polymers (with 6 Al atoms in the second shell), giving rise to a pronounced splitting of the first oscillation at 3.8 $Å^{-1}$ [9, 29, 47]. With increasing Zn-loading of HIM, the splitting becomes less marked, reflecting increasing Zn sorption to sites on hydroxy-polymers with lower Al coordination and uptake by cation exchange [29]. The suitable Zn-HIS reference compounds returned by PCA are characterized by high Zn loading, indicative of HIS close to maximum Zn sorption capacity [29]. Several soil spectra showed identical spectral features as Zn-HIS with high Zn loadings (Fig. 4.1, group A).

The SPOIL value of Zn sorbed to birnessite (low and high Zn loadings) and Zn-lithiophorite classified these references as fair to acceptable, but the high NSSR and visual mismatch of their target transforms suggested that these Zn species were not dominant in the soil samples (Table 4.4). The best spectral match as judged by NSSR was obtained for the spectrum of Zn-LDH, followed by octahedrally coordinated aqueous Zn and tetrahedrally coordinated Zn sorbed to ferrihydrite (Table 4.4, Fig. 4.1).

As discussed above, PCA indicated that six spectral components were needed to reproduce the entire set of soil EXAFS spectra. However, a much larger number of reference spectra was found suitable for LCF based on TT. This has previously been attributed to the occurrence of several species in constant proportions in all analyzed spectra [14]. We expect this effect to be negligible in the present study, because the 49

soils cover wide ranges in soil properties and Zn contamination level. Alternatively, the low number of principal components may also reflect the similarity in the spectral features of different reference compounds with similar local Zn coordination [23]. Consequently, considering the similarities of reference spectra (Fig. 4.1), the following three groups of species were introduced for further discussion of the results of LCF of the soil EXAFS spectra: (i) ZnMg-kerolites ("Zn-kerolite", including $Zn_{0.8}Mg_{0.2}$-kerolite, $Zn_{0.6}Mg_{0.4}$-kerolite, and $Zn_{0.34}Mg_{0.66}$-kerolite), (ii) sorbed or complexed Zn species in tetrahedral coordination with low second-shell signal (“sorbed ^{IV}Zn”, including Zn-phosphate, Zn-phytate, Zn-sorbed ferrihydrite, Zn-sorbed calcite, and low Zn birnessite), and (iii) octahedrally coordinated sorbed or complexed Zn species with low second-shell signal (“sorbed ^{VI}Zn”, including aqueous Zn, Zn-sorbed goethite and Zn-sorbed talc).

Table 4.4. Target testing of selected reference spectra using the first six components obtained by PCA (Table 4.3) and their occurrence in subsequent LCF.

References	SPOIL[a]	NSSR (%)	LCF[b]
Zn-phosphate	1.1	4.4	1
Zn-phytate	1.2	4.4	3
Zn-sorbed ferrihydrite	1.5	3.1	27
aqueous Zn	1.7	3.1	26
Zn-kerolite	1.7	4.2	0
Zn-LDH	1.7	1.4	31
Zn-sorbed calcite	1.7	4.8	10
$Zn_{0.8}Mg_{0.2}$-kerolite	1.8	3.7	14
$Zn(OH)_2$	1.8	8.1	0
hydrozincite	1.9	3.5	2
$Zn_{0.6}Mg_{0.4}$-kerolite	2.3	3.3	9
Zn-HIS-6.9	2.8	3.2	9
Zn-HIS-4.0	3.1	5.3	0
low Zn-birnessite	3.2	17.5	1
$Zn_{0.34}Mg_{0.66}$-kerolite	3.5	4.5	6
Zn-lithiophorite	3.7	13.3	0
Zn-HIS-8.6	3.8	4.2	3
Zn-sorbed talc	4.4	4.8	0
$Zn_{0.06}Mg_{0.94}$-kerolite	4.4	6.4	0
Zn-sorbed goethite	4.5	5.5	8
high Zn-birnessite	5.7	29.4	0

[a]SPOIL classification: 0-1.5 excellent; 1.5-3 good; 3-4.5 fair; 4.5-6 acceptable; >6 unacceptable reference [39]. [b]Number of occurrence in LCF.

4.3.3. LCF analysis of soil EXAFS spectra

In Figure 4.2, the LCF results are summarized for all soils sorted by increasing pH from left to right. For comparison of relative Zn speciation (Fig. 4.2b), all LCF fits were normalized to 100%. Absolute fractions of different Zn species were obtained by multiplying the normalized fractions with total soil Zn content (Fig. 4.2a). Detailed LCF results for the 49 soil EXAFS spectra are provided in the appendix 3 (Tables A3.5 to A3.8). The sum of the fitted fractions ranged from 97% to 122%. Deviations from 100% may be due to reduced amplitudes in soil or reference spectra (as a consequence of overabsorption in fluorescence data or pinhole effects in transmission data) or arise from slight differences in the structure of Zn species present in soil samples and EXAFS reference materials [14].

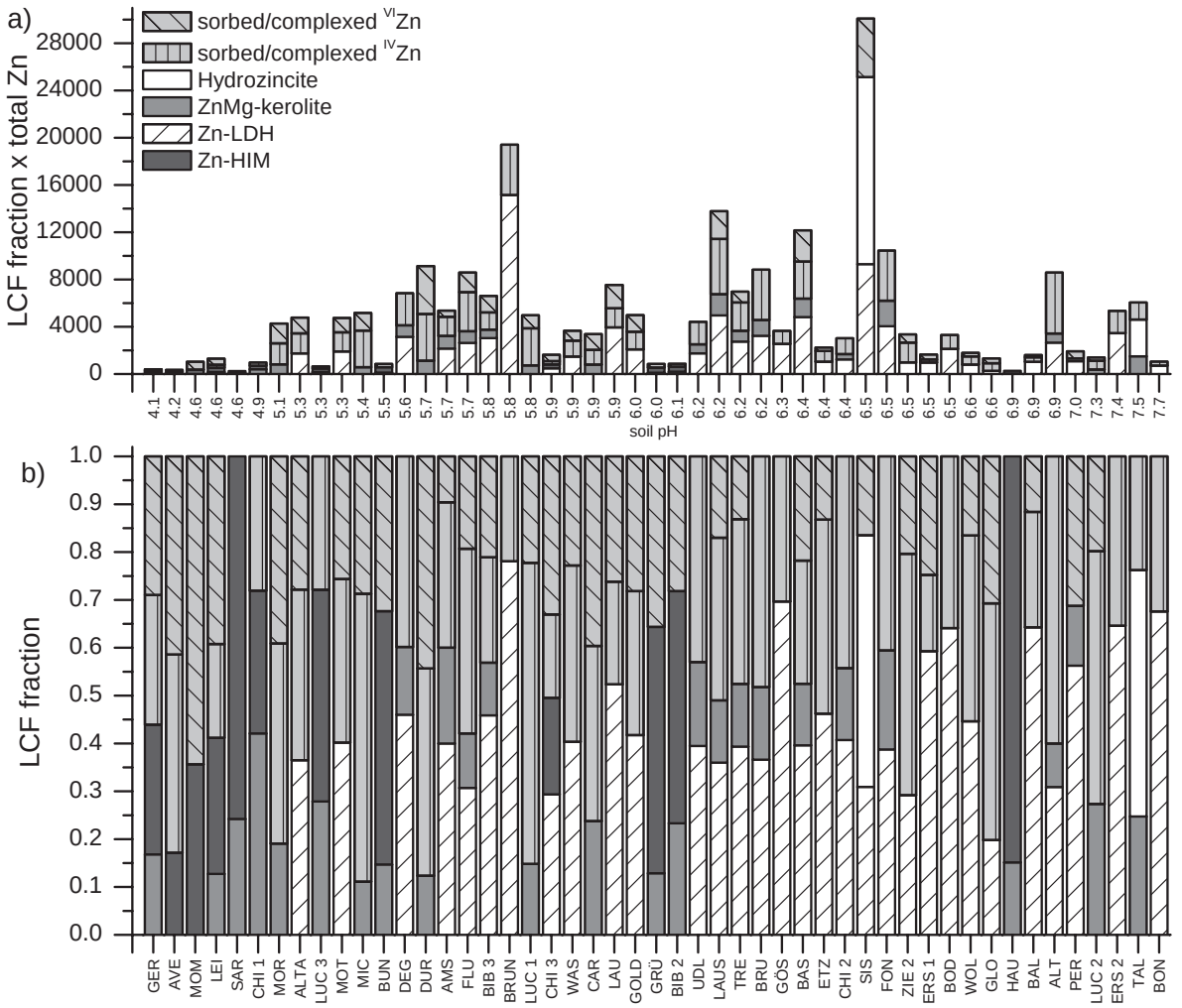

Figure 4.2. Results from the LCF analysis of 49 contaminated soils. Normalized fraction of Zn-HIM, Zn-LDH, Zn-phyllosilicate, hydrozincite, sorbed/complexed Zn in tetrahedral coordination and sorbed/complexed Zn in octahedral coordination (panel b) and normalized fractions multiplied by the respective total Zn content (panel a). Soils are arranged by increasing soil pH from left to right.

The number of times individual Zn species occurred in best LCF fits is indicated in Table 4.4. From the 21 references included in the LCF analysis of the 49 soil EXAFS spectra, only 14 occurred in the best LCF (Fig. 4.2, Tables A3.5-A3.8). Seven reference spectra occurred more than 8 times and five more than 9 times (18%) in the best LCF, which qualitatively compared to the six relevant spectral components identified by PCA. From the nine references with SPOIL >3 (fair, acceptable), 5 were not used in any of the best LCF. In contrast, only 2 of the 12 references with SPOIL <3 (excellent, good) did not occur in any of the best LCF. Thus, references with a lower SPOIL were more likely to contribute to the best LCF. On the other hand, Zn-phosphate (proxy for sorbed ^{IV}Zn) had the lowest SPOIL of all tested references (Table 4.4), but only appeared in one best LCF. This comparison of PCA and TT results with the occurrence of individual reference spectra in LCF indicated that the IND and SPOIL values need to be considered with care with respect to the selection and relevance of individual reference spectra for LCF.

Zn-HIM was identified in 12 soils with relatively low total Zn contents. In the majority of soils with pH above 5.2, Zn-LDH was a dominant Zn species. Zn-kerolites were identified over a wide soil pH range, but generally accounted only for minor fractions of total Zn. To facilitate further data analysis and discussion, four groups of soils were distinguished based on these LCF results: (A) soils containing Zn-HIM, (B) soils containing <30% of total Zn in Zn-precipitates (i.e., Zn-LDH, Zn-phyllosilicates, hydrozincite) and no Zn-HIM, (C) soils containing 30 to 60% Zn-precipitates and no Zn-HIM, and (D) soils containing >60% Zn-precipitates and no Zn-HIM. The average LCF results for groups A to D are provided in Table 4.2 and averaged spectra are plotted in Figure 4.1 (thick lines).

All 12 soils with Zn-HIM (group A) contained less than 2000 mg/kg Zn (Fig. 4.2, Table 4.2 and Tables A3.1 and A3.4). From the Zn-HIS references in our database, those containing Zn close to maximum sorption capacity (Zn-HIS-6.9 and Zn-HIS-8.6) provided the best fits. Eight of the 12 soils containing Zn-HIM were previously investigated in greater detail and substantial amounts of hydroxy-interlayered vermiculites (HIV) were identified in their clay fractions, suggesting that the fitted Zn-HIS fractions represented Zn contained in HIV [29]. In the other four soils, additional information on soil clay mineralogy would be needed to determine whether Zn-HIM mainly represents Zn-HIV or Zn-HIS. Apart from Zn-HIM, LCF indicated mainly sorbed/complexed Zn in predominantly octahedral coordination and only minor fractions of precipitated Zn (Table 4.2). Despite the spectral similarities of Zn-lithiophorite and Zn-HIS at low Zn loadings [29], the best LCF never included Zn-lithiophorite, in agreement with the poor TT reconstruction of Zn-lithiophorite (Table 4.4, Fig. 4.1).

In the eight soils containing less than 30% of total Zn in Zn-precipitates and no Zn-HIM (group B), sorbed/complexed Zn in tetrahedral and octahedral coordination dominated according to LCF. Mostly Zn-kerolites accounted for the minor precipitate fractions (Tables 4.2 and A3.6). In the remaining 29 soils with Zn-precipitate fractions of 30 to 60% (group C, 18 soils) or >60% (group D, 11 soils), Zn-LDH was the dominant Zn precipitate and the major Zn species in 12 soils (Fig. 4.2, Tables A3.7 and A3.8). Hydrozincite was identified in two calcareous soils (TAL, SIS) with >60% Zn-precipitates. These two soils had previously been studied in detail [30]. Crusts of hydrozincite were identified on limestone particles, accounting for about half of the total Zn (Table A3.4). Despite the similar low SPOIL value of $Zn(OH)_2$ and hydrozincite, making them good references for LCF analysis, $Zn(OH)_2$ was never detected by LCF. This is attributed to the much higher solubility of $Zn(OH)_2$ (and hydrozincite) than of Zn-LDH and Zn-phyllosilicates under soil chemical conditions [21, 30, 48].

4.3.4. Distinction between Zn-LDH, Zn-phyllosilicates and Zn-sorbed talc by LCF

Both Zn-LDH and ZnMg-kerolites contain Zn in trioctahedral sheets, in which octahedral Zn is coordinated by Zn and light atoms (Al, Mg) in the second-shell [25, 43]. In addition, tetrahedral Si-sheets linked to the trioctahedral sheet contribute to the local coordination of Zn in ZnMg-kerolites [43, 49, 50]. These differences in local coordination are reflected in the different EXAFS of Zn-LDH and Zn-rich kerolite, in k- as well as in *r*-space (Figs. 4.3ad). The second-shell peak in the Fourier-transformed EXAFS spectra is affected by destructive interferences between the backscattering contributions from second-shell Zn and Al/Mg as well as from second-shell Si and Al/Mg [43, 49, 50]. Backscattering from more distant O and next-nearest Si in ZnMg-kerolites gives rise to a characteristic EXAFS signal in the *r*-range 3.4-4.3 Å [43, 49, 50], which is absent in Zn-LDH. Similar to the ZnMg-kerolites, a signal from next-nearest Si is also observed in the spectrum of Zn adsorbed at the edges of talc (Fig. 4.3d, Zn-sorbed talc), whereas the destructively interfering signals from second-shell Si and Mg nearly cancel out [51]. As evident from Fig. 4.3ad, the spectra of Zn-LDH, Zn-rich kerolite, and Zn-sorbed talc reveal characteristic features. These features unequivocally allow determining dominant Zn speciation in cases where one of these species accounts for the major fraction of Zn. Due to the similar structural features present in these species, however, two types of spectral interferences might have affected the LCF of bulk soil samples (Fig. 4.2, Tables A3.5-A3.8): (i) In soils with low total precipitate fractions (group B), distinction between Zn-LDH, Zn-phyllosilicate, and Zn-sorbed talc might have been hampered. (ii) In soils containing a substantial fraction of Zn-LDH,

the minor fractions of Zn-kerolite returned by LCF might have erroneously resulted from the presence of Zn-LDH and Zn-sorbed talc. These potential interferences were tested for all soil spectra and are exemplarily discussed for the soils LUC1 and FON.

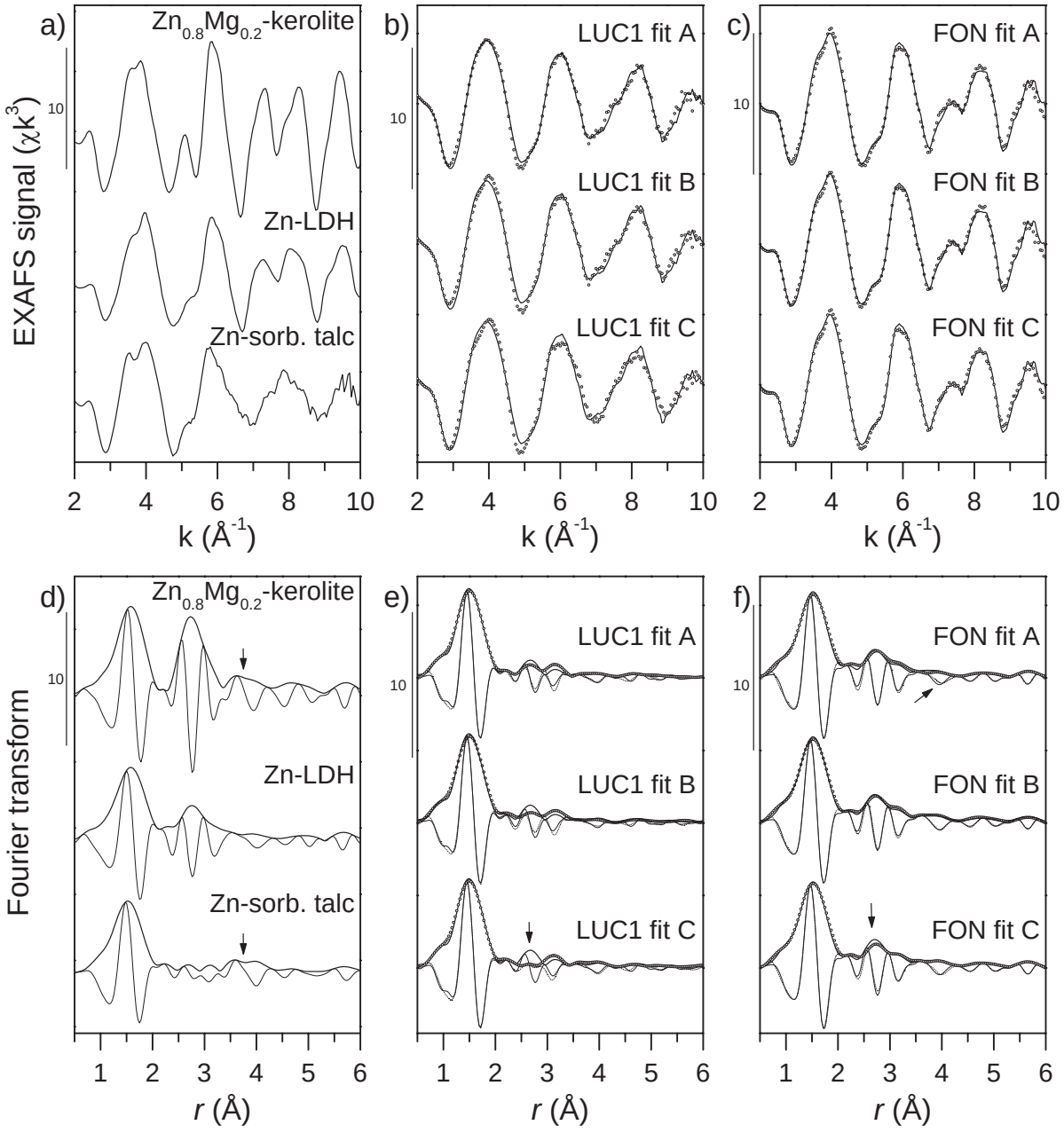

Figure 4.3. Bulk EXAFS spectra and Fourier transformed spectra of $Zn_{0.8}Mg_{0.2}$-kerolite , Zn-LDH and Zn-sorbed talc (a, d) and soils LUC1 (b, e) and FON (c, f) with LCF reconstruction (dots). LUC1; fit A with $Zn_{0.8}Mg_{0.2}$-kerolite; fit B: with Zn-LDH; fit C: with Zn-sorbed talc. FON; fit A with Zn-LDH; fit B: with Zn-LDH and $Zn_{0.6}Mg_{0.4}$-kerolite; FON; fit C: with Zn-LDH and Zn-sorbed talc. LCF results in Table 4.5.

In soils, where the fractions of Zn-precipitates was low (<30 %), using either Zn-LDH or ZnMg-kerolite as a proxy for precipitated Zn resulted in LCF with similar NSSR. As illustrated for soil LUC1 (Fig. 4.3e fits A and B, Table 4.5), neither much

difference in NSSR nor in the LCF spectrum were observed. Use of the Zn-sorbed talc reference resulted in slightly poorer fits and reconstructions of the second FT peak (Fig. 4.3e, Table 4.5). Except for soil GLO, where μ-EXAFS spectra from a soil thin section provided additional information on Zn speciation [30], the best LCF with lowest NSSR were reported. These fits consistently included a ZnMg-kerolite reference (rather than Zn-LDH or Zn-sorbed talc), suggesting that ZnMg-kerolite indeed accounted for a minor fraction of total Zn in these soils. Due to potential interference from Zn-LDH or Zn-sorbed talc, the fitted fractions should however be considered upper limits of Zn-rich phyllosilicates in these soils. In 29 soils, the sum of the fitted precipitate fractions exceeded 30%. For 14 of these soils, the best LCF indicated predominant formation of Zn-LDH, but also included a minor ZnMg-kerolite fraction. This ZnMg-kerolite fraction not only decreased the NSSR by more than 10%, but also visually improved the Fourier-transformed LCF in the region of second-shell contributions (2.4 to 3.4 Å) and of next-nearest Si backscattering (3.4 to 4.3 Å), as shown for soil FON (Fig. 4.3f).

Table 4.5. Linear combination fits for soils LUC1, FON and DUR. Comparison for multiple components fits using either Zn-kerolite or Zn-sorbed talc.

Spectrum	Zn-kerolite[a]	Zn-LDH	Zn-sorbed talc	sorbed ^{IV}Zn[b]	sorbed ^{VI}Zn[c]	Sum	NSSR
	(%)	(%)	(%)	(%)	(%)	(%)	(%)
LUC1 fit A	16 (80Zn)	———	———	68 (Fh)	24	108	1.78
LUC1 fit B	———	30	———	62 (Fh)	19	111	2.10
LUC1 fit C	———	———	38	56 (Fh)	16	110	3.53
FON fit A	———	72	———	41 (Fh)	———	113	1.74
FON fit B	23 (60Zn)	43	———	45 (Fh)	———	111	1.36
FON fit C	———	61	16	36 (Fh)	———	114	1.38

[a](80Zn): $Zn_{0.8}Mg_{0.2}$-kerolite, (60Zn): $Zn_{0.6}Mg_{0.4}$-kerolite, [b](Fh): Zn-sorbed ferrihydrite, [c]Aqueous Zn.

Fits with similar NSSR were obtained if Zn-sorbed talc instead of ZnMg-kerolite was used (Table 4.5). However, adding Zn-sorbed talc improved the LCF in the region of next-nearest Si contributions, but did not properly resolve the second-shell signal (Fig. 4.3f). This trend was observed for all soils dominated by Zn-LDH, supporting the presence of minor fractions of Zn-rich phyllosilicates. Furthermore, the preference of ZnMg-kerolite over Zn-sorbed talc in LCF fits is in agreement with the better match of the TT of the ZnMg-kerolite phases than Zn-sorbed talc (Fig. 4.1, Table 4.4) and the higher SPOIL of the Zn-sorbed talc reference spectrum (Table 4.4). However, spectral contributions of Zn adsorbed at the edges of clay minerals cannot conclusively be ruled

out and the fractions of ZnMg-kerolite obtained by LCF must therefore be taken as uppermost values.

In most fits involving ZnMg-kerolite, the best LCF was obtained with $Zn_{0.8}Mg_{0.2}$-kerolite (Tables A3.5-A3.8). However, fits of similar quality were also obtained using pure Zn-kerolite or $Zn_{0.6}Mg_{0.4}$-kerolite instead. This reflects the similarity of the EXAFS spectra of the Zn-rich kerolites and indicates that LCF of experimental spectra consisting of several spectral components is not sensitive to the exact Zn/(Zn+Mg) ratio of Zn-rich phyllosilicates [30]. Nevertheless, the consistent preference of Zn-rich kerolites over pure Zn-kerolite in the best LCF suggests that soil formed trioctahedral Zn-phyllosilicates typically contain minor fractions of Mg.

4.4. Discussion

4.4.1. Effect of soil properties and Zn loading on Zn speciation

We studied the speciation of Zn in a large set of contaminated soils by EXAFS spectroscopy in order to identify major factors controlling Zn speciation and fractionation. First, the physical and chemical properties of the soils, grouped based on LCF results, were compared to examine if changes in soil conditions resulted in systematic differences in Zn speciation. The results of this evaluation are summarized in Table 4.2 and showed that the occurrence and abundance of Zn-HIM, and Zn-precipitates (Zn-LDH, Zn-phyllosilicate, hydrozincite), and sorbed/complexed Zn species, was related to soil properties and Zn contamination level.

Zn in hydroxy-interlayered minerals (Zn-HIM) was identified as a major species in 12 of 49 soils (group A). Most of these soils were strongly to slightly acidic (average soil pH 5.2) and all had moderate Zn contamination levels (<2000 mg/kg Zn, Fig. 4.2 and Table 4.2 and Tables A3.1 and A3.4). The relatively low average ECEC of these soils (92 mmolc/kg) can be explained by their mostly low pH as well as their modest organic carbon (41 g/kg) and clay contents (150 g/kg). Such soil conditions are known to favor the formation of pedogenic HIM [52]. For all soils containing Zn-HIM, the best LCF results were achieved with Zn-HIS references with high Zn-loading close to maximum sorption capacity. This suggests that soil HIM were highly loaded with Zn. Additional Zn inputs may therefore not be converted into Zn-HIM, thus favoring the formation of other Zn species or Zn leaching to deeper soil horizons with further increases of Zn contamination. In batch experiments, the extent of specific sorption of Zn to HIM was shown to increase with increasing pH [53, 54]. However, the limited number of specific sorption sites for Zn in HIM and the limited abundance of HIM in soils pose limits to the amounts of Zn that can be bound as Zn-HIM [29]. Thus, Zn-

HIM can only be expected as a dominant Zn species in uncontaminated to moderately contaminated soils.

The soils without detectable Zn-HIM (groups B-D) exhibited markedly higher average soil pH and Zn contents than soils containing Zn-HIM. From soils with <30% of total Zn in Zn-precipitates (group B) to soils with >60% Zn-precipitates (group D), average soil pH and average Zn contents increased, whereas TOC decreased (Table 4.2). However, the observed ranges of pH, total Zn, and TOC exhibited substantial overlap among groups B to D (Table 4.2, Fig. A3.1). The trends for clay content, ECEC, and exchangeable Zn were less evident (Table 4.2, Fig. A3.1), although average ECEC values decreased from group B to C to D (Table 4.2). Zn-LDH was detected as the most abundant Zn-bearing precipitate, occurring in 31 soils containing 1046 to 30090 mg/kg Zn, with pH between 7.7 and 5.3 (Fig. 4.2 and Tables A3.1-A3.8). These results are consistent with previous field studies, reporting the formation of Zn-LDH in contaminated soils with pH between 5.5 and 7.8 and Zn contents ranging from 571 to 20476 mg/kg (Table 4.1) [19-21, 25]. In contrast to Zn-LDH (or Zn-HIM), Zn-phyllosilicates accounted for a minor fraction of Zn-bearing minerals in moderately to extremely contaminated soils (251-19410 mg/kg Zn) with soil pH varying from 4.1 to 7.5 (Fig. 4.2 and Table A3.1-A3.8). Though Zn-LDH or Zn-sorbed talc may partially account for the fraction of Zn-phyllosilicates, our results indicate that Zn-phyllosilicates may form over a large pH range and Zn content in soils, in agreement with previous work [8, 16, 17, 19-21, 24], but suggest that Zn-phyllosilicates are rather a minor Zn species in contaminated soils. Except for a study on the Zn speciation in the clay- and silt-size fractions of a smelter-impacted soil [16], Zn-phyllosilicates so far were not reported to account for the major fraction of Zn in contaminated soils (Table 4.1). Hydrozincite was only detected in two extremely contaminated calcareous soils (pH 6.5 and 7.5, 6055 and 30090 mg/kg Zn, respectively, Table A3.4), corroborating that its formation is limited to environments with extremely high Zn levels and relatively low Al and Si availability [30].

Sorbed/complexed Zn species in octahedral coordination were on average more abundant in acidic soils (i.e., soils containing Zn-HIM, group A), whereas sorbed/complexed Zn species in tetrahedral coordination were prevailing in near-neutral to neutral soils (soils without detectable Zn-HIM, groups B-D)(Table 4.2). The average fraction of sorbed or complexed Zn detected by LCF in soils B to D decreased from 81 to 31 % (sum of ^{VI}Zn and ^{IV}Zn in Table 4.2), paralleling a decrease in the percentage of octahedrally coordinated sorbed or complexed Zn (from 31 to 6%). Considering that outer-spherically or electrostatically sorbed Zn is octahedrally coordinated, whereas inner-spherically bound Zn may either occur in tetrahedral or octahedral coordination, these trends indicate a decreasing fraction of Zn retained by cation exchange with

increasing pH and/or Zn loading. In agreement with this interpretation, the highest percentage of sorbed/complexed ^{VI}Zn (65% of total Zn) was found for soil MOM characterized by low pH and low Zn loading (Table 4.2, and Table A3.1).

4.4.2. Relation between Zn speciation and Zn fractionation

The fractionation of Zn in 47 out of the 49 soils studied here has been determined in an earlier study [10], using the 7-step sequential extraction procedure of Zeien and Brümmer [5]. Trends in Zn extraction data suggested that soil pH and Zn content were the dominant factors affecting Zn fractionation. This trend was in agreement with the results of the current study indicating that soil pH and Zn loading were also the dominant factors controlling Zn speciation (Figs. 4.1 and A3.1). Based on the 4 groups of soils derived from LCF analysis (Table 4.2), we examined whether trends in Zn speciation were reflected in systematic differences in Zn fractionation patterns (Fig. 4.4).

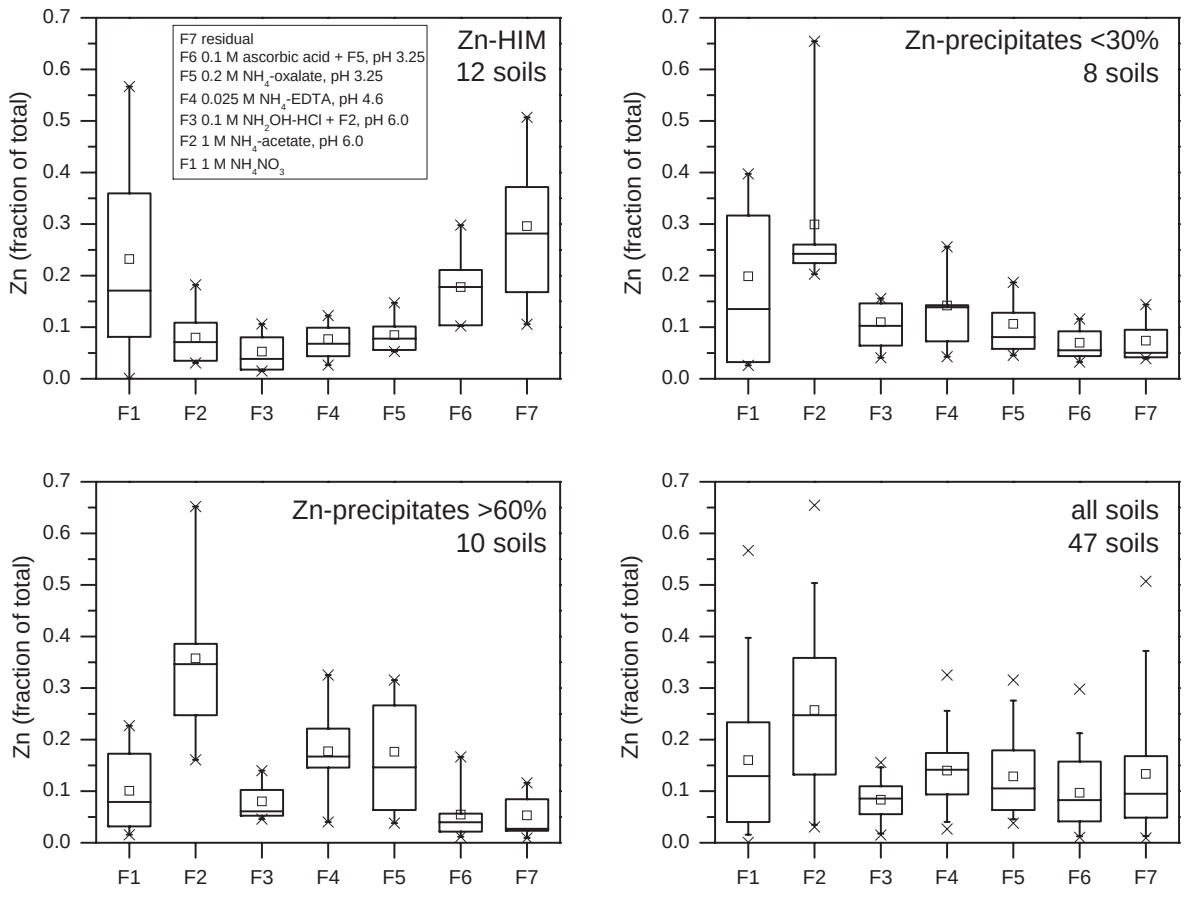

Figure 4.4. Summarizing results of the sequentially extracted fractions of Zn in soils containing Zn-HIM, LCF fraction of Zn-precipitates lower than 30%, LCF fraction of Zn-precipitates higher than 60% and results for all 47 soils extracted. Boxes cover the 25-75 percentile range (including the median (lines dividing boxes) and the arithmetic mean (squares)), bars cover the 5-95 percentile range, and crosses indicated the maximum and minimum values. Sequential extractions data from Voegelin et al. [10]. Detailed LCF fit results are provided in the appendix 3.

In the 12 soils containing Zn-HIM, Zn was mainly present in the exchangeable (F1) and the most recalcitrant fractions (F6, F7). Similar results were previously reported for an acidic, smelter-contaminated soil containing 45% Zn-HIM [9]. Using the same extraction procedure, we previously demonstrated that synthetic Zn-HIS spiked into quartz is mainly recovered in F1 and the last two fractions (F6 and F7) [29]. Thus, the predominant occurrence of Zn in the fractions F6 and F7 in the Zn-HIM containing soils was likely due to Zn incorporated into Zn-HIM. This interpretation is supported by earlier linear regression results suggesting that the fraction of Zn extracted in F6 was related to the amount of Al extracted in F6 [10] as well as by previous reports demonstrating oxalate to mobilize Al-polymers from pedogenic HIM [55]. The large variation in exchangeable Zn (F1) observed for the 12 soils from group A was related to their pH ranging from 4.1 to 6.9 (Table A3.1, Fig. 4.2). In the soils from group A, on average 43% of the total Zn was identified as Zn-HIM and 47% of the total Zn was extracted in fractions F6 and F7. Furthermore. the fraction of Zn in F6+F7 was weakly correlated with the fraction of Zn-HIM from LCF (r=0.61, Fig. A3.2). Thus, the EXAFS speciation results of Zn-HIM containing soils were to some extent reflected in the sequential extraction data. The high molar Zn/Mn ratio obtained in the fraction F3 designed for the removal of Mn-oxides suggested Mn-oxides (e.g., lithiophorite, birnessite) to be of minor relevance for Zn retention in the studied soils, in agreement with EXAFS speciation results.

In soils containing <30% of total Zn in Zn-precipitates (group B, Table 4.2, Fig. 4.2), i.e., dominated by adsorbed/complexed Zn species, about half of the total Zn was on average extracted in the mobile (F1, 20%) and easily mobilizable (F2, 30%) fractions, the other half being distributed over F3 to F5 and, somewhat less, F6 and F7 (Fig. 4.4). In soils containing >60% of Zn-precipitates (group D), less Zn was on average extracted in F1 (10%) and more in F2 (36%). Markedly higher fractions of Zn were also extracted in F4 and F5 compared to soil of group B (Fig. 4.4). When mixed into soil, synthetic Zn-LDH and pure Zn-kerolite were mainly extracted in fraction F2 and to a lesser extent in fraction F4 [30]. Thus, the occurrence of Zn in F4 and F5 in the contaminated soils was likely due to the presence of specifically adsorbed Zn and potential Zn redistribution arising from the dissolution of Zn-precipitates in F2. In contrast to soils containing Zn-HIM, much less Zn was extracted in the last two fractions F6 and F7. Overall, these results show that Zn in soil-formed precipitates is readily mobilizable at pH 6.0 in the presence of a weakly complexing ligand. Thus, Zn accumulated into precipitates is only conditionally immobilized.

4.4.3. Zn speciation and fractionation in relation to soil pH and Zn loading

The present study demonstrated that Zn-HIM, Zn-LDH, Zn-phyllosilicates and hydrozincite are quantitatively important Zn species in a wide range of soils contaminated with Zn over years to decades and that the occurrence and abundance of these species is mainly related to soil pH and total Zn content. Even though the effects of ECEC, clay content and organic clay content were not as marked, the observed trends (Table 4.2, Fig. A3.1) suggested that the availability of sorption sites also influenced Zn speciation. As an estimate for the concentration of available sorption sites, we calculated the potential cation exchange capacity (PCEC) of the studied soils as a function of soil organic carbon and clay content according to a relation derived from the analysis of 1600 Canadian soils [56]: PCEC (in mmolc/kg) = $3.97 \times f_{oc} + 0.57 \times f_{cl}$, where 3.97 and 0.57 are the concentrations of sorption sites on organic carbon and clay (in mmolc/kg at pH 8.2) and f_{oc} and f_{cl} are the mass fractions of soil organic carbon and clay (e.g., kg/kg), respectively. In Figure 4.5, total soil Zn in charge equivalents (Zn_{eq}) normalized by the PCEC is plotted versus soil pH, indicating that the maximum Zn loading of the studied soils markedly increased with increasing soil pH, in some soils even exceeding the PCEC.

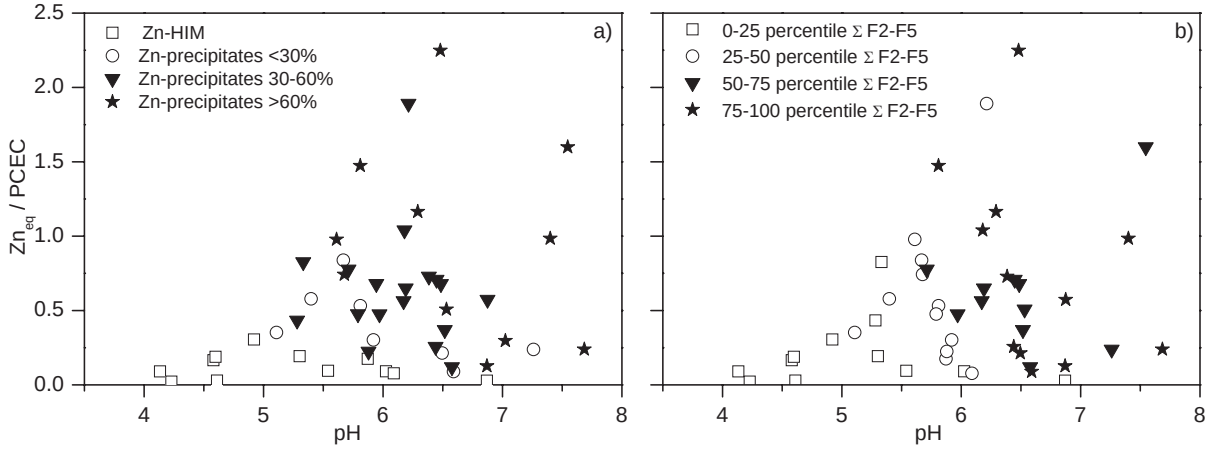

Figure 4.5. Total soil Zn in charge equivalents (mmolc/kg) divided by calculated potential cation exchange capacity (mmolc/kg, estimated from soil organic C and clay content) as a function of soil pH. (a) Soils grouped according to Zn speciation from LCF. (b) Soils grouped based on fractionation data (soils grouped by percentile ranges based on the amount of Zn extracted in F2 to F5).

In Figure 4.5a, the soils were grouped according to speciation results from LCF (Fig. 4.2, Tables A3.5-A3.8). For a given soil pH, Zn speciation tended to shift from soils containing Zn-HIM to soils bearing >60 % of Zn-precipitates as the ratio of total Zn_{eq}/PCEC increased (Fig. 4.5a). However, distinct limits could not be drawn due to the wide and often overlapping range in soil properties and Zn content within each of

the four groups of soils (Table 4.2). Similar trends were observed at fixed Zn_{eq}/PCEC over increasing soil pH. This suggests that the speciation of Zn gradually shifts with saturation of sorption sites and soil pH. Thus, for soils with high availability of sorption sites (i.e., low Zn content and/or high organic matter and/or clay content), Zn uptake is dominated by adsorption mechanisms on organic and mineral soil components and by retention in HIM (if present). With increasing saturation of sorption sites and of HIM, dissolved Zn concentrations increase and at some point exceed the solubility limits of Zn-precipitates. Similar trends are observed with an increase in soil pH (Fig. 4.5). Consequently, at elevated pH and/or high Zn contamination level, Zn-precipitates are the major Zn species forming.

Soils grouped according to the fraction of Zn extracted in the steps F2 to F5 of the sequential extraction procedure are shown in Figure 4.5b. Similar to the trends in Zn speciation (Fig. 4.5a), the soil groups are partly separated along increasing soil pH and Zn_{eq}/PCEC, although with some overlap. Higher fractions of Zn tended to be fractionated into F2-F5 at higher Zn_{eq}/PECEC and/or higher soil pH (Fig. 4.5b), in agreement with the trends in Zn fractionation between the different groups of soils obtained from LCF (Fig. 4.4) and an increase in the fraction of Zn extracted in F2-F5 with increasing precipitate fraction (Fig. A3.3). The good agreement between sequential extraction data and LCF results reflects that soil pH and Zn loading (relative to available sorption sites) are not only the dominant factors controlling Zn speciation but also fractionation and indicates that Zn fractionation is controlled by Zn speciation.

4.5. Conclusions

In contaminated soils, soil pH and Zn loading relative to the availability for sorption sites are the most important parameters influencing Zn speciation. Formation of Zn-HIM is restricted to moderately contaminated HIM-containing soils. Zn-phyllosilicates form over a wide range of soil pH, but are quantitatively less relevant than Zn-LDH, which is the dominant Zn-precipitate at higher soil pH and/or Zn loading. The fractionation of Zn as observed by sequential extraction depends on Zn speciation and is therefore also related to soil pH and Zn loading. This study considered soils contaminated by inputs of aqueous Zn. Similar trends in Zn speciation may be expected for aqueous Zn released from Zn-bearing contaminants such as sewage sludge or smelter slag, though local chemical conditions around weathering or decomposing contaminant phases may also affect Zn speciation. The current study indicates the soil chemical conditions under which different types of Zn species occur in soils that mainly formed under temperate climate conditions. Further studies are needed to explore the speciation and fractionation of Zn in other types of soils such as periodically anoxic soils or soils from boreal or

tropical zones. The results from this study are also relevant for other elements such as Ni and Co, which partially exhibit similar geochemical behavior as Zn.

Acknowledgements

Evert Elzinga (Rutgers University) kindly provided the EXAFS spectra of Zn-sorbed calcite. Kurt Barmettler (ETH Zurich) is acknowledged for technical support in the laboratory. We thank Stefan Mangold from the XAS beamline at ANKA (Germany), the staff from the SNBL beamline at the ESRF (France) and Kumi Pandya from the beamline X11A at NSLS (USA) for their help with EXAFS data acquisition. The ANKA (Germany) and SNBL at the ESRF (France) are acknowledged for the provision of beamtime. This project was financially supported by the Swiss National Science Foundation under contracts no. 200021-101876 and 200020-116592.

References

[1] Adriano, D. C., *Trace Elements in Terrestrial Environments: Biogeochemistry, Bioavailability, and Risks of Metals.* 2nd ed.; Springer: New York, 2001.

[2] Alloway, B. J., *Heavy Metals in Soils*. Chapman & Hall: London, 1995.

[3] Shuman, L. M., Fractionation method for soil microelements. *Soil Sci.* 1985, 140, 11-22.

[4] Tessier, A.; Campbell, P. G. C.; Bisson, M., Sequential extraction procedure for the speciation of particulate trace metals. *Anal. Chem.* 1979, 51, 844-851.

[5] Zeien, H.; Brümmer, G. W., Chemische Extraktionen zur Bestimmung von Schwermetallbindungsformen in Böden. *Mitt. Dtsch. Bodenkundl. Ges.* 1989, 59, 505-510.

[6] Young, S. D.; Zhang, H.; Tye, A. M.; Maxted, A.; Thums, C.; Thornton, I., Characterizing the availability of metals in contaminated soils. I. The solid phase: sequential extraction and isotopic dilution. *Soil Use Manag.* 2005, 21, 450-458.

[7] Gleyzes, C.; Tellier, S.; Astruc, M., Fractionation studies of trace elements in contaminated soils and sediments: a review of sequential extraction procedures. *Trac-Trend Anal. Chem.* 2002, 21, 451-467.

[8] Kirpichtchikova, T. A.; Manceau, A.; Spadini, L.; Panfili, F.; Marcus, M. A.; Jacquet, T., Speciation and solubility of heavy metals in contaminated soil using X-ray microfluorescence, EXAFS spectroscopy, chemical extraction, and thermodynamic modeling. *Geochim. Cosmochim. Acta* 2006, 70, 2163-2190.

[9] Scheinost, A. C.; Kretzschmar, R.; Pfister, S.; Roberts, D. R., Combining selective sequential extractions, X-ray absorption spectroscopy, and principal

component analysis for quantitative zinc speciation in soil. *Environ. Sci. Technol.* 2002, 36, 5021-5028.

[10] Voegelin, A.; Tokpa, G.; Jacquat, O.; Barmettler, K.; Kretzschmar, R., Zinc fractionation in contaminated soils by sequential and single extractions: Influence of soil properties and zinc content. *J. Environ. Qual.* 2008, 37, 1190-1200.

[11] Brown, G. E. J.; Calas, G.; Waychunas, G. A.; Petiau, J., X-ray absorption spectroscopy and its applications in mineralogy and geochemistry. In *Spectroscopic Methods in Mineralogy and Geology, Reviews in Mineralogy*, Ribbe, P. H., Ed. Mineralogy Society of America: Washington, DC, 1988; Vol. 431-512, pp 1-115.

[12] Fendorf, S. E.; Sparks, D. L.; Lamble, G. M.; Kelley, M. J., Applications of X-ray absorption fine-structure spectroscopy to soils. *Soil Sci. Soc. Am. J.* 1994, 58, 1583-1595.

[13] Schulze, D. G.; Bertsch, P. M., Synchrotron X-ray techniques in soil, plant, and environmental research. In *Advances in Agronomy, 55*, Sparks, D. L., Ed. Academic Press, 1-66: 1995; Vol. 55, pp 1-66.

[14] Manceau, A.; Marcus, M. A.; Tamura, N., Quantitative speciation of heavy metals in soils and sediments by synchrotron X-ray techniques. In *Application of synchrotron radiation in low-temperature geochemistry and environmental science*, Fenter, P. A.; Rivers, M. L.; Sturchio, N. C.; Sutton, S. R., Eds. Mineralogical Society of America, Washington, DC: 2002; Vol. 49.

[15] O'Day, P. A., Molecular environmental geochemistry. *Rev. Geophys.* 1999, 37, 249-274.

[16] Manceau, A.; Lanson, B.; Schlegel, M. L.; Harge, J. C.; Musso, M.; Eybert-Berard, L.; Hazemann, J. L.; Chateigner, D.; Lamble, G. M., Quantitative Zn speciation in smelter-contaminated soils by EXAFS spectroscopy. *Am. J. Sci.* 2000, 300, 289-343.

[17] Isaure, M.-P.; Laboudigue, A.; Manceau, A.; Sarret, G.; Tiffrau, C.; Trocellier, P.; Lamble, G. M.; Hazemann, J. L.; Chateigner, D., Quantitative Zn speciation in a contaminated dredged sediment by μ-PIXE, μ-SXRF, EXAFS spectroscopy and principal component analysis. *Geochim. Cosmochim. Acta* 2002, 66, 1549-1567.

[18] Isaure, M.-P.; Manceau, A.; Geoffroy, N.; Laboudigue, A.; Tamura, N.; Marcus, M. A., Zinc mobility and speciation in soil covered by contaminated dredged sediment using micrometer-scale and bulk-averaging X-ray fluorescence, absorption and diffraction techniques. *Geochim. Cosmochim. Acta* 2005, 69,

1173-1198.

[19] Juillot, F.; Morin, G.; Ildefonse, P.; Trainor, T. P.; Benedetti, M.; Galoisy, L.; Calas, G.; Brown, G. E., Occurrence of Zn/Al hydrotalcite in smelter-impacted soils from northern France: Evidence from EXAFS spectroscopy and chemical extractions. *Am. Mineral.* 2003, 88, 509-526.

[20] Nachtegaal, M.; Marcus, M. A.; Sonke, J. E.; Vangronsveld, J.; Livi, K. J. T.; Van der Lelie, D.; Sparks, D. L., Effects of in situ remediation on the speciation and bioavailability of zinc in a smelter contaminated soil. *Geochim. Cosmochim. Acta* 2005, 69, 4649-4664.

[21] Panfili, F. R.; Manceau, A.; Sarret, G.; Spadini, L.; Kirpichtchikova, T.; Bert, V.; Laboudigue, A.; Marcus, M. A.; Ahamdach, N.; Libert, M. F., The effect of phytostabilization on Zn speciation in a dredged contaminated sediment using scanning electron microscopy, X-ray fluorescence, EXAFS spectroscopy, and principal components analysis. *Geochim. Cosmochim. Acta* 2005, 69, 2265-2284.

[22] Roberts, D. R.; Scheinost, A. C.; Sparks, D. L., Zinc speciation in a smelter-contaminated soil profile using bulk and microspectroscopic techniques. *Environ. Sci. Technol.* 2002, 36, 1742-1750.

[23] Sarret, G.; Balesdent, J.; Bouziri, L.; Garnier, J. M.; Marcus, M. A.; Geoffroy, N.; Panfili, F.; Manceau, A., Zn speciation in the organic horizon of a contaminated soil by micro-x-ray fluorescence, micro- and powder-EXAFS spectroscopy, and isotopic dilution. *Environ. Sci. Technol.* 2004, 38, 2792-2801.

[24] Schuwirth, N.; Voegelin, A.; Kretzschmar, R.; Hofmann, T., Vertical distribution and speciation of trace metals in weathering flotation residues of a zinc/lead sulfide mine. *J. Environ. Qual.* 2007, 36, 61-69.

[25] Voegelin, A.; Pfister, S.; Scheinost, A. C.; Marcus, M. A.; Kretzschmar, R., Changes in zinc speciation in field soil after contamination with zinc oxide. *Environ. Sci. Technol.* 2005, 39, 6616-6623.

[26] Manceau, A.; Tamura, N.; Celestre, R. S.; MacDowell, A. A.; Geoffroy, N.; Sposito, G.; Padmore, H. A., Molecular-scale speciation of Zn and Ni in soil ferromanganese nodules from loess soils of the Mississippi Basin. *Environ. Sci. Technol.* 2003, 37, 75-80.

[27] Manceau, A.; Marcus, M. A.; Tamura, N.; Proux, O.; Geoffroy, N.; Lanson, B., Natural speciation of Zn at the micrometer scale in a clayey soil using X-ray fluorescence, absorption, and diffraction. *Geochim. Cosmochim. Acta* 2004, 68, 2467-2483.

[28] Manceau, A.; Tommaseo, C.; Rihs, S.; Geoffroy, N.; Chateigner, D.; Schlegel,

M. L.; Tisserand, D.; Marcus, M. A.; Tamura, N.; Zueng-Sang, C., Natural speciation of Mn, Ni, and Zn at the micrometer scale in a clayey paddy soil using X-ray fluorescence, absorption, and diffraction. *Geochim. Cosmochim. Acta* 2005, 60, 4007-3034.

[29] Jacquat, O.; Voegelin, A.; Kretzschmar, R., Local coordination of Zn in hydroxy-interlayered minerals and implications for Zn retention in soils. *Geochim. Cosmochim. Acta* 2009, 73, 348-363.

[30] Jacquat, O.; Voegelin, A.; Villard, A.; Marcus, M. A.; Kretzschmar, R., Formation of Zn-rich phyllosilicates, Zn-layered double hydroxide and hydrozincite in contaminated calcareous soils. *Geochim. Cosmochim. Acta* 2008, 72, 5034-5057.

[31] Loeppert, R. H.; Suarez, D. L., Carbonate and Gypsum. In *Methods of Soil Analysis. Part 3. Chemical Methods*, Soil Science Society of America: Madison, 1996.

[32] Gee, G.; Or, D., Particle size analysis. In *Methods of Soil Analysis. Part 4. Physical Methods*, Dane, J. H.; Topp, C. C., Eds. Soil Science Society of America, Madison, USA: 2002; pp 255-293.

[33] Hendershot, W. H.; Duquette, M., A simple chloride method for determining cation exchange capacity and exchangeable cations. *Soil Sci. Soc. Am. J.* 1986, 50, 605-608.

[34] Newville, M., IFEFFIT: interactive XAFS analysis and FEFF fitting. *J. Synchrotron Rad.* 2001, 8, 322-324.

[35] Ravel, B.; Newville, M., Athena, Artemis, Hephaestus: data analysis for X-ray absorption spectroscopy using IFEFFIT. *J. Synchrotron Rad.* 2005, 12, 537-541.

[36] Elzinga, E. J.; Reeder, R. J., X-ray absorption spectroscopy study of Cu^{2+} and Zn^{2+} adsorption complexes at the calcite surface: Implications for site-specific metal incorporation preferences during calcite crystal growth. *Geochim. Cosmochim. Acta* 2002, 66, 3943-3954.

[37] Webb, S. M., SIXPack: a graphical user interface for XAS analysis using IFEFFIT. *Phys. Scr.* 2005, T115, 1011-1014.

[38] Malinowski, E. R., Determination of the number of factors and the experimental error in a data matrix. *Anal. Chem.* 1977, 49.

[39] Malinowski, E. R., Theory of error for target factor analysis with applications to mass spectrometry and nuclear magnetic resonance spectrometry. *Anal. Chim. Acta* 1978, 103, 339-354.

[40] Manceau, A.; Boisset, M. C.; Sarret, G.; Hazemann, R. L.; Mench, M.; Cambier,

P.; Prost, R., Direct determination of lead speciation in contaminated soils by EXAFS spectroscopy. *Environ. Sci. Technol.* 1996, 30, 1540-1552.

[41] Keller, T.; Desaules, A., Böden der Schweiz: Schadstoffgehalte und Orientierungswerte. *Umwelt Materialen 139, Bundesamt für Umwelt, Wald and Lanschaft, Bern, Switzerland.* 2001.

[42] VBBo, Verordnung über Belastungen des Bodens (Swiss Ordinance relating to Impacts on Soil). *SR 814.12, Eidgenössische Drucksachen und Materialzentrale, Bern, Switzerland.* 1998.

[43] Schlegel, M. L.; Manceau, A.; Charlet, L.; Chateigner, D.; Hazemann, J.-L., Sorption of metal ions on clay minerals III. Nucleation and epitaxial growth of Zn phyllosilicate on the edges of hectorite. *Geochim. Cosmochim. Acta* 2001, 65, 4155-4170.

[44] Schlegel, M. L.; Manceau, A., Evidence for the nucleation and epitaxial growth of Zn phyllosilicate on montmorillonite. *Geochim. Cosmochim. Acta* 2006, 70, 901-917.

[45] Scheinost, A. C.; Sparks, D. L., Formation of layered single- and double-metal hydroxide precipitates at the mineral/water interface: A multiple-scattering XAFS analysis. *J. Colloid Interface Sci.* 2000, 223, 167-178.

[46] Voegelin, A.; Kretzschmar, R., Formation and dissolution of single and mixed Zn and Ni precipitates in soil: Evidence from column experiments and extended X-ray absorption fine structure spectroscopy. *Environ. Sci. Technol.* 2005, 39, 5311-5318.

[47] Schlegel, M. L.; Manceau, A., Zn incorporation in hydroxy-Al- and Keggin Al-13-intercalated montmorillonite: A powder and polarized EXAFS study. *Environ. Sci. Technol.* 2007, 41, 1942-1948.

[48] Ford, R. G.; Sparks, D. L., The nature of Zn precipitates formed in the presence of pyrophyllite. *Environ. Sci. Technol.* 2000, 34, 2479-2483.

[49] Juillot, F.; Morin, G.; Ildefonse, P.; Calas, G.; Brown, G. E., EXAFS signature of structural Zn at trace levels in natural and synthetic trioctahedral 2 : 1 phyllosilicates. *Am. Mineral.* 2006, 91, 1432-1441.

[50] Manceau, A.; Calas, G., Nickel-bearing clay-minerals. 2. Intracrystalline distribution of nickel - an X-ray absorption study. *Clay Miner.* 1986, 21, 341-360.

[51] Schlegel, M. L.; Manceau, A.; Charlet, L.; Hazemann, J. L., Adsorption mechanisms of Zn on hectorite as a function of time, pH, and ionic strength. *Am. J. Sci.* 2001, 301, 798-830.

[52] Rich, C. I., Hydroxy interlayers in expansible layer silicates. *Clays Clay Miner.*

1968, 16, 15-30.

[53] Janssen, R. P. T.; Bruggenwert, M. G. M.; van Riemsdijk, W. H., Zinc ion adsorption on montmorillonite-Al hydroxide polymer systems. *Eur. J. Soil Sci.* 2003, 54, 347-355.

[54] Lothenbach, B.; Furrer, G.; Schulin, R., Immobilization of heavy metals by polynuclear aluminium and montmorillonite compounds. *Environ. Sci. Technol.* 1997, 31, 1452-1462.

[55] Farmer, V. C.; Smith, B. F. L.; Wilson, M. J.; Loveland, P. J.; Payton, R. W., Readily-extractable hydroxyaluminium interlayers in clay- and silt-sized vermiculite. *Clay Miner.* 1988, 23, 271-277.

[56] Curtin, D.; Rostad, H. P. W., Cation exchange and buffer potential of Saskatchewan soils estimated from texture, organic matter and pH. *Can. J. Soil Sci.* 1997, 77, 621-626.

5. Changes in Zn speciation during soil formation from Zn-rich limestones

Abstract

In order to better understand the long-term speciation and fractionation of Zn in soils, we investigated three soils naturally enriched in Zn (237-864 mg/kg Zn) from the weathering of Zn-rich limestones (40-207 mg/kg Zn) using extended X-ray absorption fine structure (EXAFS) spectroscopy and sequential extractions. The analysis of bulk EXAFS spectra by linear combination fitting (LCF) indicated that Zn in the oolitic limestones was mainly present as Zn-containing calcite (Dornach), Zn-containing goethite (Gurnigel) and Zn-containing goethite and sphalerite (Liestal). Correspondingly, extraction of the powdered rocks with 1 M NH_4-acetate at pH 6.0 mobilized only minor fractions of Zn from the Gurnigel and Liestal limestones (<30%), but most Zn from the Dornach rock (81%). In the Dornach soil, part of the Zn released from the dissolving limestone was subsequently incorporated into pedogenic hydroxy-interlayered vermiculite (Zn-HIV, ~30%) and Zn-containing kaolinite (~30%) and adsorbed or complexed by soil organic and inorganic components (~40%). The Gurnigel and Liestal soils contained substantial amounts of Zn-containing goethite (~50%) stemming from the parent rock and smaller amounts of Zn-containing kaolinite (~20%) and adsorbed or complexed Zn species (~30%). In the soil from Liestal, sphalerite was only found in trace amounts, indicating its dissolution during soil formation. In sequential extractions, large percentages of Zn (~55 to 85%) were extracted in recalcitrant extraction steps, confirming that Zn-HIV, Zn-containing kaolinite and Zn-containing goethite are highly resistant to weathering. These Zn-bearing phases thus represent long-term hosts for Zn in soils over thousands of years. The capability of these phases to immobilize Zn in heavily contaminated soils may however be limited by their uptake capacity (especially HIV and kaolinite) or their abundance in soil.

Submitted to Geochimica Cosmochimica Acta as: Jacquat, O., Voegelin, A., Juillot, F., Kretzschmar, R., Changes in Zn speciation during soil formation from Zn-rich limestones.

5.1. Introduction

Zinc is an essential micronutrient for plants and animals. At elevated concentrations, however, Zn may exert toxic effects on plants and microorganisms, thereby leading to a decrease in soil fertility and crop yield [1]. The bioavailability and mobility of Zn in soils depend to a large degree on its chemical form or speciation. Studies on the sorption and speciation of Zn in metal oxide and clay mineral suspensions demonstrated its versatile reactivity and suggested that the formation of layered precipitates such as hydroxides, layered double hydroxides (LDH) or phyllosilicates may be an important sequestration mechanism in contaminated soils at near-neutral to alkaline pH [2-4]. Spectroscopic studies on the speciation of Zn in soils contaminated over years to decades confirmed the formation and relevance of Zn-phyllosilicate- and Zn-LDH-type precipitates under field conditions [5-10]. In calcareous soils, both Zn-LDH and Zn-phyllosilicate were identified, with Zn-LDH dominating at higher Zn loadings and extreme Zn levels leading to the formation of hydrozincite [11]. In contrast, specific sorption of Zn in the Al-hydroxy interlayers of hydroxy-interlayered minerals (HIM) was found to be an important Zn uptake mechanism in (mostly acidic) HIM-containing soils at low to moderate contamination levels [12, 13]. Thus, several recently identified layered Zn phases are quantitatively relevant in contaminated soils, their occurrence depending on soil pH, the level of Zn contamination, and the abundance of organic and mineral sorbent phases [14].

The aforementioned studies showed that Zn-LDH, Zn-phyllosilicates and Zn-HIM may occur in soil environments after years to decades of Zn contamination, but little is still known about the stability of these Zn phases over thousands of years and their impact on the fate of Zn over geologic timescales. Studying the speciation of Zn in pristine soils may provide valuable information about the long-term fate of Zn in a weathering soil environment and also support the optimization of remediation strategies for contaminated soils. In saprolite developed from metalliferous mafic rocks and in weathered Zn-bearing ore deposits, several Zn-rich layered precipitates were identified, including fraipontite (Zn-serpentine), sauconite (Zn-smectite), baileychlore (Zn-chlorite) and zaccaganite (Zn-LDH) [15-19]. Both Zn-HIM and Zn-phyllosilicates (as Zn-kerolite) have been identified in pristine acidic soils [20-22].

In this study, we investigated three soils with geogenically elevated Zn contents which developed over the recent Quaternary period from Zn-rich Jurassic limestones. Our objectives were (i) to determine the chemical forms of Zn in three soil-forming limestone rocks and the associated naturally Zn-enriched soils and (ii) to assess the reactivity of Zn due to changing soil chemical conditions during weathering. The

speciation of Zn was determined by bulk- and microfocused EXAFS (μ-EXAFS) spectroscopy. The reactivity of Zn in the limestone rocks and soil materials was inferred from single and sequential extractions.

5.2. Materials and Methods

5.2.1. Sampling sites

The studied soils are located in the northwestern part of Switzerland and developed from Zn-rich Jurassic limestones of the Jura mountain range. The soils developed since the last glacial maximum [23, 24] and are therefore estimated to be ~10000 years old. At all three sites, the soils were well-drained and unaffected by groundwater.

The first soil (DOR) is located 1 km south of the village of Dornach (47° 28'N, 7° 37'E). Soil samples were collected from five distinct horizons. The soil profile consisted of a 5 cm thick black hemic organic layer with a very thin base of sapric material (Oe), a dark-brown organo-mineral horizon (Ah, 0-7 cm, 10YR 3 3), and two clayey horizons varying in color from light brown (Bw, 7-17 cm, 10YR 4 6) to yellowish brown (BwC, 17-35 cm, 10YR 5 6). The hard saprolitic horizon of oolitic micritic limestone (R) of Oxfordian age (~160 Ma) was sampled at depths of 32 to 42 cm. The soil profile has previously been described in detail [25, 26] and was classified as Haplic Cambisol according to the World Reference Base for Soil Resources [27].

Both the second (GUR) and third soil (LIE) were classified as Rendzic Leptosol according to the World Reference Base for Soil Resources [27]. The soil GUR was sampled 2 km east of the pass of la Vue des Alpes (Le Gurnigel, 47° 05'N, 6° 54'E). It had formed on oolitic limestone of late Bajocian age (~168 Ma) and consisted of an organic-rich layer containing limestone particles (Aca, 0-10 cm, 10YR 3 3) covering the unweathered limestone (R, sampled at 10-14 cm depth). The soil LIE, was located on the south-west rolling footslope of the Schleifenberg hill (47° 29'N, 7° 44'E) near Liestal. Both the limestone-rich soil horizon (Aca, 0-8 cm, 10YR 3 3) and the underlying bedrock (R) consisting of oolitic limestone of early Bajocian age (~170 Ma), were sampled.

5.2.2. Sample preparation and bulk soil properties

The soil samples were air-dried at 25°C, manually broken into small aggregates, gently homogenized in an agate mortar and sieved to <2mm. Powdered samples <50 μm of soil and limestone samples were prepared using a vibratory agate disc mill. The soil pH was measured in 10 mM $CaCl_2$ using a glass electrode. Wax pellets were prepared from the powdered samples (4 g of material and 0.9 g of Licowax©) and analyzed for

total element contents by energy-dispersive X-ray fluorescence spectrometry (Spectro X-Lab 2000). Total carbon contents (TC) were determined on powdered samples using a CHNS Analyzer (CHNS-32, LECO). Total inorganic carbon (TIC) contents were determined by reacting 0.3-0.9 g of soil material with 1 M sulfuric acid (H_2SO_4) under heating. The evolving CO_2 was adsorbed in a Nesbitt bulb containing NaOH-coated sorbent and was quantified gravimetrically [28]. TC and TIC analyses were performed in duplicates. Total organic carbon (TOC) was calculated by subtracting the TIC from the TC content. After pretreatment of the soils with H_2O_2 for removal of organic matter, the sand content (50-2000 μm) was quantified by wet sieving and the clay content (<2 μm) using the pipette method [29]. The silt content (2-50 μm) was calculated as the difference to total soil weight.

5.2.3. Clay extraction and analysis

The clay fraction (<2 μm size fraction) was isolated by wet sieving and sedimentation. About 20 g of the <2 mm soil material was dispersed in 800 mL 0.5 M NaCl prepared from doubly deionized water (DDI, 18.2 MΩ·cm, Milli-Q® Element, Millipore), sonified for 1 minute and passed through a 50 μm sieve. The residue was twice resuspended in 800 mL DDI water, sonified, and sieved. The three filtrates were merged, resuspended, and siphoned off after the appropriate sedimentation time calculated by Stoke's law. The sedimentation procedure was repeated twice with fresh DDI water [30]. The three clay suspensions were flocculated with $MgCl_2$, merged, and washed free of chloride ($AgNO_3$ test) using DDI water. The Mg-saturated clay fraction was frozen in liquid N_2 (LN) and freeze-dried. The K-saturated clay samples were prepared by exchanging 30 mg of Mg-saturated clay with 10 mL of 1.0 M KCl [31]. The KCl solution was renewed twice to ensure complete exchange of the interlayer cations. Excess salt was removed in three washing (DDI water) and centrifugation cycles (5 min, 3400 g). Oriented specimens of the Mg- and K-saturated clays were prepared by settling a suspension of 30 mg of clay onto glass slides (2.5 cm in diameter) and drying at room temperature. Ethylene glycol (EG) and glycerol (Gly) solvation was performed by leaving an oriented Mg-saturated slide on the shelf of an EG- or Gly-containing desiccator (6 h at 60 °C or 12 h at 110 °C, respectively) [32, 33]. For thermal treatment, the oriented slides of the K-saturated clay fraction were heated for at least 1 h in a preheated muffle furnace at 100, 300 and 550°C (all treatments in sequence on same slide). The X-ray diffraction (XRD) patterns were recorded using a Cu anode and an energy dispersive solid state detector (Bruker D4 diffractometer, Bruker AXS, Germany). Patterns were measured from 3° to 37° 2-theta using variable slits, a step size of 0.02° in continuous scan mode, and a counting time of 4 s per step. Oriented mounts of the citrate-extracted soil clay fractions (see

section 5.2.9 for details) were analyzed in analogy after Mg-saturation and EG and Gly solvation.

5.2.4. Reference compounds for EXAFS spectroscopy

For the preparation of reference samples of Zn coprecipitated with ferrihydrite and goethite, a method for the synthesis of goethite [34] was adapted. About 135 mL of 1 M KOH were added to 75 mL of 0.3 M ($Fe(NO_3)_3 \cdot 9H_2O$ + $Zn(NO_3)_2 \cdot 4H_2O$) at a molar Zn/(Zn+Fe) ratio of 0.015. After vigorous stirring, the fresh precipitate was centrifuged and the supernatant decanted. The resulting Zn-containing ferrihydrite ("Zn-ferrihydrite") was washed and centrifuged five times with DDI water. Subsequently, the sample was frozen in LN and freeze-dried. In a second vessel, the synthesis was repeated. After dilution in 1.5 L DDI water, the fresh Zn-ferrihydrite precipitate was aged during 67 h at 70 °C to achieve transformation to goethite. The suspension was centrifuged and washed five times with 0.2 M oxalic acid in the dark to remove amorphous Fe oxides. The Zn-containing goethite ("Zn-goethite") was washed three times with DDI water, frozen in LN and freeze-dried. The structure of Zn-ferrihydrite and Zn-goethite was confirmed by XRD. Final Zn contents determined by XRF spectrometry were 14000 mg/kg for Zn-ferrihydrite and 16500 mg/kg for Zn-goethite. Sphalerite ("ZnS", Alfa Aesar, Nr. 040091) was used without further treatment. Zn-containing calcite ($Zn_{0.003}Ca_{0.997}CO_3$, "Zn-calcite") was synthesized by reacting 4 g of vaterite with 200 mL of 460 µM $ZnCl_2$ for 5 d [11]. The reference database also included natural and synthetic Zn-containing kaolinite ("nat. Zn-kaolinite" and "syn. Zn-kaolinite") with Zn contents of 180 and 270 mg/kg as well as a series of hydroxy-Al interlayered smectites (HIS) with increasing Zn contents ("Zn-HIS-2.1", "Zn-HIS-2.9", Zn-HIS-4.0" and "Zn-HIS-6.9" with Zn contents of 2100, 2900, 4000, and 6900 mg/kg, respectively). These references were discussed in detail in an earlier study [12]. A series of ZnMg-kerolites with variable Zn and Mg contents included "Zn-kerolite", "$Zn_{0.8}Mg_{0.2}$-kerolite", "$Zn_{0.6}Mg_{0.4}$-kerolite", "$Zn_{0.34}Mg_{0.66}$-kerolite", and "$Zn_{0.06}Mg_{0.94}$-kerolite") [11]. References for adsorbed and complexed Zn species included, amongst others, "Zn-phytate", "Zn-sorbed calcite", "Zn-sorbed ferrihydrite", "low Zn-birnessite" and "Zn-sorbed talc" for which details have been provided in earlier studies [11, 14].

5.2.5. Bulk Zn K-edge EXAFS spectra acquisition

Zinc K-edge EXAFS spectra were measured at the XAS beamline at the Angströmquelle Karlsruhe (ANKA, Karlsruhe, Germany) and the Swiss Norwegian beamline SNBL at the European Synchrotron Radiation Facility (ESRF, Grenoble, France). At both beamlines, the monochromator was calibrated by assigning the first

inflection point of the K-edge absorption spectrum of metallic Zn to 9659 eV. Powdered soil and rock samples and reference materials were mixed with polyethylene or Licowax© and pressed into 13-mm pellets for analysis. The pellets were analyzed at room temperature in fluorescence mode using a 5-element (ANKA) or a 13-element (SNBL) Ge solid state detector or in transmission mode (ionization chambers), depending on Zn concentration.

5.2.6. μ-XRF and μ-EXAFS analyses on soil thin sections

For μ-XRF and μ-EXAFS analyses, undisturbed soil aggregates from the horizons DOR-BwC, GUR-Aca and LIE-Aca were impregnated with a high purity resin (Epofix Struers or Araldit 2020) and prepared as polished sections of 50, 150 and 200 μm thickness, respectively. The sections were analyzed at beamline 10.3.2 at the Advanced Light Source (ALS, Berkeley, USA) [35]. Soil thin-sections were placed at an angle of 45° to the incident beam and the fluorescence signal was recorded at an angle of 90° using a 7-element Ge solid state detector. The μ-XRF maps were obtained by scanning the samples with step sizes of 20×20, 10×10, or 5×5 μm^2 and dwell times of 200 or 100 ms/point at an incident photon energy of 10 keV. For the distribution of Mn in the DOR-BwC horizon, an additional map was collected at an incident photon energy of 7012 eV (100 eV below Fe K-edge). For the other two sections GUR-Aca and LIE-Aca, the Mn Kα intensity was decontaminated from leakage of Fe Kα fluorescence into the Mn channel by subtracting a constant fraction of the recorded Fe signal (determined graphically from the scatter plot of the Mn intensity versus the Fe intensity). Zn K-edge EXAFS spectra were recorded at points of interest (POI) using a beam size between 5×5 and 16×7 μm^2 depending on the size of the relevant feature. The black-white scale of the XRF maps was defined to cover the range between the minim pixel value (black) and the 99 percentile of all pixel values (white).

5.2.7. EXAFS data extraction and analysis

EXAFS data extraction was performed using the software code Athena [36]. All spectra were normalized by fitting a first order polynomial to the pre-edge data (-150 to -30 eV relative to E_0) and a second order polynomial to the post-edge region (+150 up to -100 eV before end of spectrum). The energy was converted to photoelectron wave vector units ($Å^{-1}$, k-space) by setting E_0 to the first maximum of the first derivative of the absorption edge. EXAFS spectra were extracted by fitting the post-edge data with a cubic spline function using the Autobk algorithm implemented in Athena (Rbkg = 0.9 Å, k-weight = 3, spline k-range from 0.5 to 12 $Å^{-1}$).

The soil EXAFS spectra were evaluated by principal component analysis (PCA) and

target transform testing (TT) using SIXPack [37]. Considering all k^3-weighted bulk- and micro-EXAFS spectra (k-range 2 to 10 $Å^{-1}$), the number of spectral components required to reproduce the entire data set without experimental noise was determined by PCA based on the empirical indicator (IND) function [38, 39]. To identify suitable reference spectra for data analysis by linear combination fitting (LCF), TT was then performed on a large database of reference spectra, which included, among others, synthetic (syn.) and natural (nat.) minerals and precipitates (syn. Zn-kaolinite, nat. Zn-kaolinite, syn. Zn-containing kerolite at various Zn/Mg ratios (pure Zn-kerolite, $Zn_{0.8}Mg_{0.2}$-kerolite, $Zn_{0.6}Mg_{0.4}$-kerolite, $Zn_{0.34}Mg_{0.66}$-kerolite, $Zn_{0.06}Mg_{0.94}$-kerolite), Zn-LDH, Zn-lithiophorite), carbonates (Zn-calcite, hydrozincite, smithsonite), Zn incorporated into hydroxy-interlayered smectite (Zn-HIS) at various loadings (Zn-HIS-6.9 (6900 mg/kg Zn), Zn-HIS-4.0 (4000 mg/kg), Zn-HIS-2.9 (2900 mg/kg) and Zn-HIS-2.1 (2100 mg/kg)), and adsorbed/complexed Zn species (Zn-phytate, Zn-sorbed ferrihydrite, Zn-sorbed calcite, Zn-sorbed goethite, aqueous Zn) [11, 12, 14]. The empirical SPOIL value [40] and the normalized sum of squared residual (NSSR) of the target transforms [6, 9, 41, 42] were used to judge the suitability of reference spectra for LCF.

The spectra of the soil and rock samples were analyzed by linear combination fitting (LCF) using the approach and software developed by Manceau and coworkers [7, 43]. All possible one-component to 4-component fits were optimized by minimizing NSSR ($NSSR = (\Sigma_i(k^3\chi_{exp}-k^3\chi_{fit})^2)/\Sigma_i(k^3\chi_{exp})^2$). Starting from the best one-component fit, the best fit with n+1 components was considered to be significantly better than the best n-component fit, if its NSSR was at least 10% lower than the NSSR of the best n-component fit. The precision of fractions obtained from LCF has previously been estimated to be around 10% of the total Zn [41], but strongly depends on the spectral characteristics of all Zn species present in the sample [7].

5.2.8. Batch extraction of limestone samples

The calcite fraction of the limestone samples (R horizons) was dissolved in 1 M NH_4-acetate solution buffered at pH 6.0 in order to obtain an estimate for the fraction of Zn contained in carbonates. Ten grams of powdered rock were suspended in 800 mL 1 M NH_4-acetate solution. After mixing for 1 h, the suspensions were slowly titrated with about 200 mL 1 M HCl. The exact volume of 1 M HCl needed to dissolve all carbonates was calculated assuming that all Ca in the limestones (determined by XRF spectrometry) was contained in $CaCO_3$. The solution pH remained constant (pH 6.0 ± 0.1) during the entire extraction time. After centrifugation, the supernatants were filtered (0.45 µm, nylon) and acidified with 1% (v/v) 30% HNO_3 for subsequent analysis of released Zn by inductively coupled plasma – optical emission spectrometry (ICP-OES,

Varian Vista-MPX).

5.2.9. Extractions of soils and reference compounds

The soil samples were sequentially extracted following the extraction procedure of Zeien and Brümmer [44]. Experimental details have been provided previously [45]. Briefly, each soil was extracted in duplicates (2 g of soil per extraction) according to the following sequence (with hypothetical interpretation according to Zeien and Brümmer [44] in parentheses): Fraction F1: 1M NH_4NO_3 (readily soluble and exchangeable); Fraction F2: 1M NH_4-acetate, pH 6.0 (titrated to pH 6.0 using HCl to dissolve carbonates; mobilizable and $CaCO_3$ bound); Fraction F3: 0.1 M NH_2OH-HCl + 1 M NH_4-acetate, pH 6.0 (Mn oxides); Fraction F4: 0.025 M NH_4-EDTA, pH 4.6 (bound to organic substances); Fraction F5: 0.2 M NH_4-oxalate, pH 3.25 (bound to amorphous and poorly crystalline Fe oxides); Fraction F6: 0.1 M ascorbic acid + 0.2 M NH_4-oxalate, pH 3.25 (bound to crystalline Fe oxides). All extraction steps were performed with a solution-to-soil ratio of 25 mL/g. The solutions from the extraction steps F1 to F6 were analyzed by ICP-OES. The residual fraction F7 was determined by XRF spectrometry.

Zn-goethite, Zn-ferrihydrite and ZnS (see paragraph 5.2.4 for details on reference materials) and Zn-HIS-6.9 [12] were mixed with 2 g of quartz powder (Fluka®, Nr. 83340) or 2 g of a non-calcareous topsoil (pH of 6.5, 15 g/kg org. C, 150 g/kg clay, [10]) to achieve Zn contents of 1900, 2500, 2000 and 200 mg/kg, respectively. After mixing for 24 h using an overhead shaker, the spiked samples were sequentially extracted as described for the soils.

An additional step to remove Al-hydroxy-polymers from HIM was performed following the method of Tamura [46] for the residual material from the sequential extraction (i.e., the residual material after step F6) of the soil samples DOR-Ah, DOR-Bw and DOR-BwC and the reference Zn-HIS-6.9 spiked into quartz powder. The same extraction was also performed with the pure reference materials Zn-HIS-6.9 and syn. Zn-kaolinite as well as with the <2 μm size fraction of the soils. The extractions were performed in duplicates using either 50 or 250 mg of material at a solution-to-material ratio of 200 mL/g. The samples were extracted three times in boiling 0.3 M Na-citrate solution adjusted to pH 7.3. The three extracts were quantitatively merged and Zn concentrations analyzed by ICP-OES.

5.3. Results

5.3.1. Physical and chemical properties and mineralogy of studied soil materials

Physical and chemical properties and Zn contents of the different soil materials are listed in Table 5.1. Total element contents and molar Zn/element ratios are provided in Table A4.1 in the appendix. The soil-forming oolitic limestones (horizons R in Table 5.1), contained between 43 and 207 mg/kg Zn. These concentrations are close to or higher than the 90-percentile level (n=37) of 48 mg/kg Zn reported for limestones from Switzerland [47], indicating an elevated Zn content in the limestones from all three locations.

Table 5.1. Physicochemical properties and Zn content of the different soil horizons.

Soil	Horizon	Depth (cm)	pH ($CaCl_2$)	TOC (g/kg)	TIC (g/kg)	Clay (g/kg)	Silt (g/kg)	Sand (g/kg)	Total Zn (mg/kg)
DOR	Oe	+5 - 0	4.5	415	0.7	——	——	——	318
	Ah	0 - 7	5.3	44	0.4	522	363	115	783
	Bw	7 - 17	6.6	31	2.7	591	300	109	734
	BwC	17 - 38	7.2	17	12	615	218	167	476
	R	38 - 42	———	——	——	——	——	——	207
GUR	Aca	0 - 10	6.8	194	3	639	293	68	864
	R	10 - 14	———	——	——	——	——	——	43
LIE	Aca	0 – 8	7.3	142	26	693	141	166	237
	R	8 - 15	———	——	——	——	——	——	92

In the DOR soil profile, clay content and pH decreased from the BwC (7.2, 615 g/kg, respectively) to the Ah horizon (5.3, 522 g/kg, respectively), paralleled by an increase in Zn content from 476 mg/kg in the BwC to 783 mg/kg in the Ah horizon. Substantial amounts of Zn (318 mg/kg) were also contained in the acidic Oe horizon. The Aca horizons of the soils GUR and LIE, which were in direct contact with the bedrock, had a neutral pH, a high clay content (>600 g/kg), and high Zn concentrations (864 and 237 mg/kg, respectively). In Switzerland, the upper limits for normal geogenic Zn contents in soils with pH 5.1-6.1, 6.2-6.7 and 6.8-7.6 are 95, 116 and 132 mg/kg, respectively [48]. The Zn content of all three soils exceeded these limits by 2-6 times. For the surface horizons of soil DOR (Oe, Ah), at most 100 mg/kg Zn have previously been estimated to originate from atmospheric emissions of a brass foundry located one kilometer away from the sampling site [25] (corresponding to <31 and <13% of the

total Zn content of the Oe and the Ah horizon, respectively). At Gurnigel and Liestal, significant anthropogenic Zn inputs can be excluded [49-51].

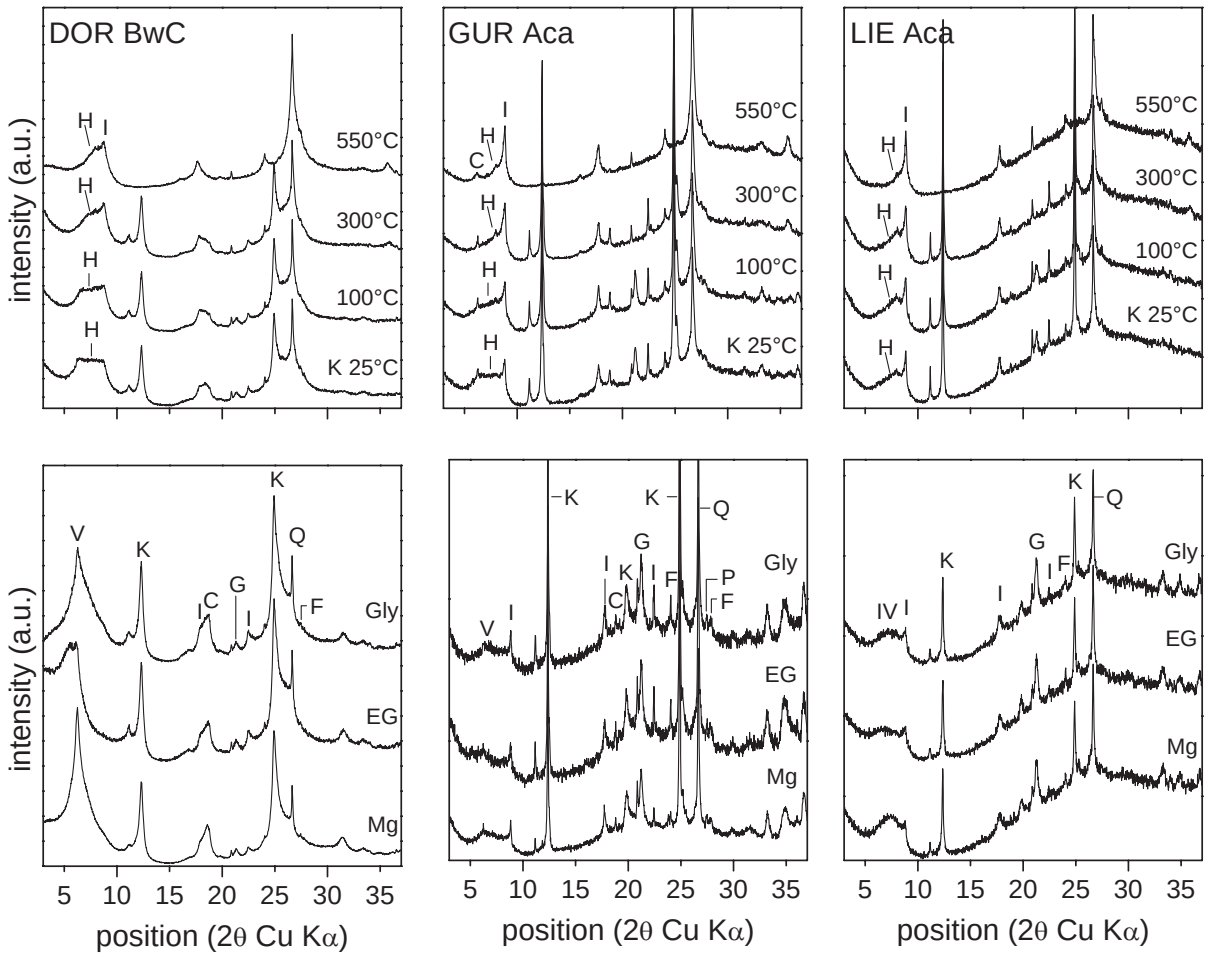

Figure 5.1. X-ray diffraction patterns of oriented mounts of the <2 μm size soil fraction. Lower panels Mg-saturated slides in air-dried state (Mg) and after ethylene glycol (EG) and glycerol solvation (Gly). Upper panels: K-saturated slides (K) after ex situ thermal treatment. C: chlorite; F: K-feldspars; G: goethite; H: hydroxy-interlayered vermiculite; I: illite; IV: interstratified illite-vermiculite; K: kaolinite; P: plagioclase; Q: quartz; V: vermiculite.

XRD patterns of oriented mounts of the <2 μm size fraction of the soil samples from DOR-BwC, GUR-Aca and LIE-Aca are shown in Figure 5.1. The clay mineralogy was dominated by kaolinite, vermiculite, illite and quartz. Goethite was present as a major accessory mineral. The 14.2 Å peak (6.2° 2θ Cu Kα) observed in the air-dried Mg-saturated slides of DOR-BwC and GUR-Aca was partially shifted to higher d-spacings after treatment with ethylene glycol (EG), whereas no shift was observed under glycerol (Gly) solvation. After K-saturation and gentle heat treatment (100°C), the 14.2 Å peak did not collapse to 10 Å. Instead, it remained expanded and collapsed to ~11.2 Å after heating to 550°C. These trends indicated that the interlayer space of the 14.2 Å mineral was filled with hydroxy-polymers [52, 53]. Also after the removal of hydroxy-Al

interlayers from soil clay minerals by Na-citrate extraction, ethylene glycol (EG) and glycerol (Gly) solvation did not cause a shift of the 14.2 Å peak to higher d-spacings (Fig. A4.1), indicating that it originated mainly from hydroxy-interlayered vermiculite (HIV) rather than hydroxy-interlayered smectite (HIS). The 12 Å peak (7.3° 2θ Cu Kα) of the interstratified illite-vermiculite mineral identified in the Mg-saturated slide of LIE-Aca showed similar response to Gly and EG solvation and heat treatment. Thus, like the vermiculite minerals identified in DOR-BwC and GUR-Aca, also the vermiculite layers of interstratified clay minerals in the sample LIE-Aca contained hydroxy-polymers. Changes in the XRD patterns of heat-treated mounts confirmed the presence of goethite (transforming to hematite between 100°C and 300°C) and kaolinite (dehydroxylating during 1 h heating at 550°C). The samples DOR-Ah and DOR-Bw had a similar clay mineralogy as the sample DOR-BwC (Fig. A4.2).

5.3.2. Speciation of Zn in limestones

The EXAFS spectra of the limestones (DOR-R, GUR-R, LIE-R) and corresponding linear combination fits are presented in Figure 5.2. LCF results are given in Table 5.2. The spectra of the three limestones are clearly distinct, indicating that the local coordination of Zn is different in each rock. The spectrum DOR-R was best reconstructed with Zn-containing calcite (Zn-calcite). The fitted fraction was only 88%, which may be due to minor differences in the crystallinity or Zn-content of the Zn-calcite in DOR-R and the synthetic Zn-calcite reference, the presence of other metal cations in the calcite of DOR-R, or spectral contributions from minor Zn species that were not detected by LCF. In the limestone from Gurnigel (GUR-R), Zn-calcite was not detected. Instead, LCF indicated that Zn-containing goethite (Zn-goethite) was the major Zn species. In the limestone from LIE (spectrum LIE-R), mainly sphalerite (ZnS) and a minor fraction of Zn-goethite were detected.

The extraction results of the limestone samples were in qualitative agreement with the speciation inferred from EXAFS spectroscopy: From DOR-R, 81% of the total Zn was extracted during carbonate dissolution, in line with EXAFS data showing Zn to mainly substitute for Ca in the calcite structure. In contrast, only minor fractions of the total Zn were extracted from the limestones GUR-R (27%) and LIE-R (17%), suggesting Zn to be contained in residual minerals. The higher amounts of Fe and S in GUR-R and LIE-R relative to DOR-R (Table A4.1) were also in line with the extraction as well as the speciation results.

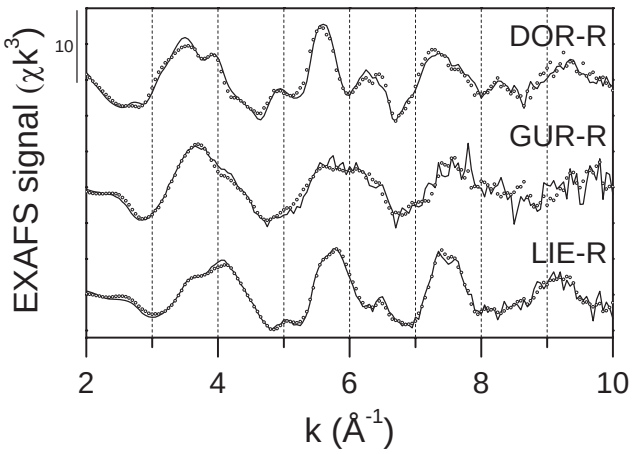

Figure 5.2. EXAFS spectra of limestones samples (R horizons, solid lines) and LCF spectra (dots). LCF results are provided in Table 5.2.

Table 5.2. Linear combination fits of the EXAFS spectra collected on the Zn-rich limestone (R horizons).

Spectrum	Zn-calcite	Zn-Goethite	ZnS	Sum	NSSR
	(%)	(%)	(%)	(%)	(%)
DOR-R[a]	88	———	———	88	6.5
GUR-R	———	92	———	92	18.2
LIE-R	———	34	60	94	4.2

[a]μ-EXAFS spectrum from Zn-rich zone of DOR-R thin-section. Respective bulk EXAFS spectrum contaminated by a signal from metallic Zn due to scattered X-ray radiation, but qualitatively in agreement with μ-EXAFS spectrum.

5.3.3. Principal component analysis and target transform testing

The number of spectral components in the 18 soil EXAFS spectra (5 bulk soil spectra (DOR-Oe, DOR-Ah, DOR-BwC, GUR-Aca, LIE-Aca), 3 spectra from clay fractions (DOR-Ah clay, DOR-BwC clay, GUR-Aca clay) and 10 μ-EXAFS spectra from DOR-BwC (3) GUR-Aca (3) and LIE-Aca (4)) was determined by principal component analysis (PCA). The parameters of the first 8 components from PCA are provided in Table 5.3. The empirical IND function reached a minimum for the first 5 components, suggesting 5 significant spectral components [38], which explained 75% of the total experimental variance. Using these 5 principal components, all soil spectra could be well reproduced (NSSR between 0.01 to 4.8%).

Table 5.3. Results from the principal component analysis of the 8 bulk- and 10 μ-EXAFS spectra collected in the soil horizons.

Component	Eigenvalue	Variance	Cum. Var.[a]	IND[b]
1	134.6	0.385	0.385	0.0600
2	45.2	0.129	0.514	0.0542
3	36.0	0.103	0.617	0.0485
4	28.5	0.081	0.699	0.0425
5	17.5	0.049	0.749	0.0423
6	11.2	0.031	0.781	0.0466
7	10.3	0.029	0.810	0.0519
8	9.67	0.027	0.838	0.0584

[a]Cumulative variance. [b]Indicator function.

Among all tested references, Zn-HIS with intermediate to high Zn loadings (Zn-HIS-2.9, Zn-HIS-4.0, Zn-HIS-6.9) and tetrahedrally coordinated complexed or adsorbed Zn species (Zn-phytate, Zn-sorbed calcite and Zn-sorbed ferrihydrite) had the lowest SPOIL values and were best reconstructed, as judged from their NSSR (Table 5.4, Fig. 5.3). In Zn-HIS with low Zn-loadings, Zn is contained in the vacancies of gibbsitic Al-polymers. With increasing Zn-loading of HIS, Zn speciation shifts to sites with decreasing Al-coordination and ultimately to exchangeably adsorbed Zn [12]. Low SPOIL values were also obtained for ZnS, Zn-calcite and Zn-goethite, which were identified in the oolitic limestones. Among the Zn-bearing phyllosilicates in our database, synthetic and natural Zn-kaolinite had the lowest SPOIL values. The reference spectra of the Zn-kaolinites exhibit similarities to the spectra of Zn-HIS with low Zn loadings (Fig. 5.3). These similarities result from the predominant Zn incorporation into the vacancies of the dioctahedral sheets of kaolinite, resembling the local coordination of Zn in the vacancies of gibbsitic Al-polymers of HIS. Spectral differences between Zn-kaolinite and low-Zn-HIS result from the backscattering contributions from the tetrahedral sheets of kaolinite as well as from potential partial Zn substitution of Zn for Al in the dioctahedral sheets of Zn-kaolinite [12]. Also in Zn-lithiophorite, considered a fair reference based on its SPOIL value, Zn is contained in the vacancies of gibbsitic sheets. The SPOIL values of ZnMg-kerolites were much higher and increased with increasing Zn content, paralleled by an increase in the NSSR of the respective target transforms. In ZnMg-kerolites, Zn is contained in trioctahedral sheets. At low Zn/Mg ratio, Zn is mainly surrounded by second-shell Mg, resulting in a similar local coordination as in low Zn-HIS and Zn-kaolinite [12]. Differences however result from the EXAFS contributions of the two adjacent tetrahedral Si sheets. With increasing Zn content, the spectral features are changing significantly due to the formation of Zn-rich trioctahedral

sheets with substantial backscattering contributions from second-shell Zn. The target transform of Zn adsorbed to the edges of talc (Zn-sorbed talc) had an acceptable SPOIL value and a lower NSSR than Zn-rich kerolites. SPOIL values above 6 suggested that Zn-LDH and pure Zn-kerolite were not relevant in the studied soil materials. In Zn-LDH, Zn is contained in trioctahedral sheets containing Zn and Al, but lacks spectral contributions from tetrahedral sheets as in ZnMg-kerolites. The SPOIL values of phases containing Zn in octahedral sheets thus indicated a clear preference for Zn-HIS and Zn-kaolinites, whereas Zn incorporation into Zn-rich trioctahedral sheets did not seem to be a dominant structural feature in the studied soils.

In adsorbed and complexed Zn species, the first-shell Zn-O signal may dominate the shape of the EXAFS spectrum due to a low number of second-neighbor atoms, the presence of weak low-Z backscatterers, or due to destructive interference of the EXAFS of different types of second neighbor atoms. As a consequence, the EXAFS spectra of adsorbed or complexed species with the same type of first-shell coordination (tetrahedral or octahedral) may be difficult to distinguish in soil spectra with several spectral contributions [11]. In LCF, we therefore only referred to tetrahedrally coordinated sorbed Zn (“sorbed ^{IV}Zn”, reference spectra Zn-phytate, Zn-sorbed calcite, Zn-sorbed ferrihydrite, and low Zn-birnessite) and octahedrally coordinated sorbed Zn (“sorbed ^{VI}Zn”, reference spectra Zn-sorbed goethite, aqueous Zn, and Zn-sorbed talc), indicating the reference used in the best LCF in Tables 5.5-5.7.

Table 5.4. Results from the target transform analysis of the 17 soil EXAFS spectra. Spectra are arranged by increasing SPOIL value. All references except Zn-kerolite and Zn-LDH were included in the LCF analysis.

References	SPOIL[a]	NSSR (%)
Zn-HIS-6.9	0.9	1.5
Zn-phytate	1.2	8.0
Zn-sorbed calcite	1.2	6.2
Zn-HIS-4.0	1.3	3.3
Zn-HIS-2.9	1.3	3.9
syn. Zn-kaolinite	1.4	3.8
Zn-sorbed ferrihydrite	1.5	7.0
Zn-HIS-2.1	1.6	5.6
nat. Zn-kaolinite	2.0	4.8
ZnS	2.0	8.8
low Zn-birnessite	2.1	15.7
Zn-calcite	2.3	15.2
aqueous Zn	2.6	4.3
Zn-goethite	3.0	9.9
Zn-lithiophorite	3.2	13.0
$Zn_{0.06}Mg_{0.94}$-talc	3.3	7.2
$Zn_{0.34}Mg_{0.6}$-talc	4.5	9.5
Zn-ferrihydrite	4.6	36.2
Zn-sorbed goethite	4.8	11.9
Zn-sorbed talc	5.0	8.0
$Zn_{0.6}Mg_{0.4}$-talc	5.3	23.5
$Zn_{0.8}Mg_{0.2}$-talc	5.8	41.7
Zn-kerolite	6.4	50.8
Zn-LDH	6.9	24.4

[a]SPOIL: 0-1.5 excellent; 1.5-3 good, 3-4.5 fair, 4.5-6 acceptable, >6 unacceptable reference [40].

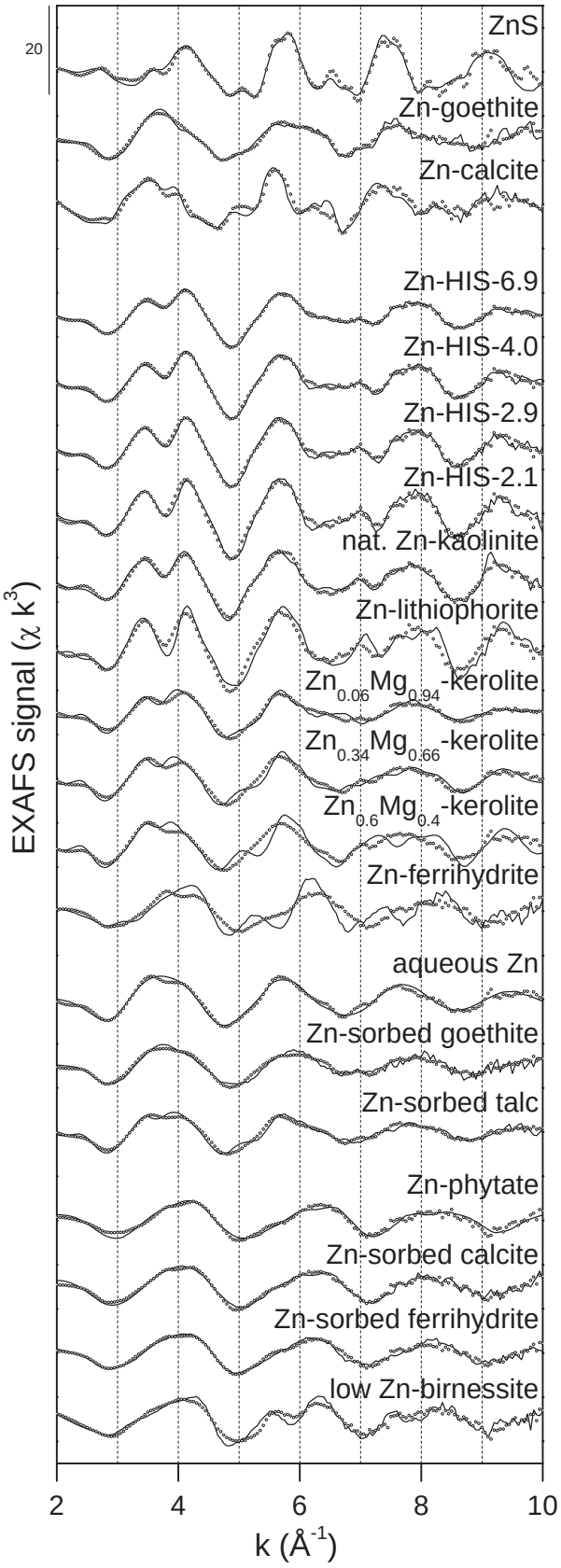

Figure 5.3. Zn K-edge EXAFS spectra for selected Zn compounds and sorbed reference compounds (solid lines) and target transforms (dotted lines, Table 5.4) calculated with the first five components of the principal component analysis (Table 5.3).

5.3.4. Speciation of Zn in the soil samples

For each studied soil, the dominant Zn species were determined by bulk EXAFS spectroscopy. To better delineate the types of Zn species present in the soils, we also analyzed the Zn speciation in selected clay-size isolates by bulk EXAFS as well as the distribution and speciation of Zn in soil thin-sections using μ-XRF and μ-EXAFS spectroscopy.

5.3.4.1. Soil DOR

The distribution of Zn, Fe and Mn in a thin-section of undisturbed material from the DOR-BwC horizon is shown in Figure 5.4. Zn occurs diffusively distributed in the clayey matrix and concentrated in localized Zn-rich spots. The distribution of Zn was closely related to the distribution of Fe, but not to that of Mn. μ-EXAFS spectra collected on selected POI (Fig. 5.4) as well as bulk EXAFS spectra from all soil horizons are shown in Figure 5.5. LCF parameters are provided in Table 5.5.

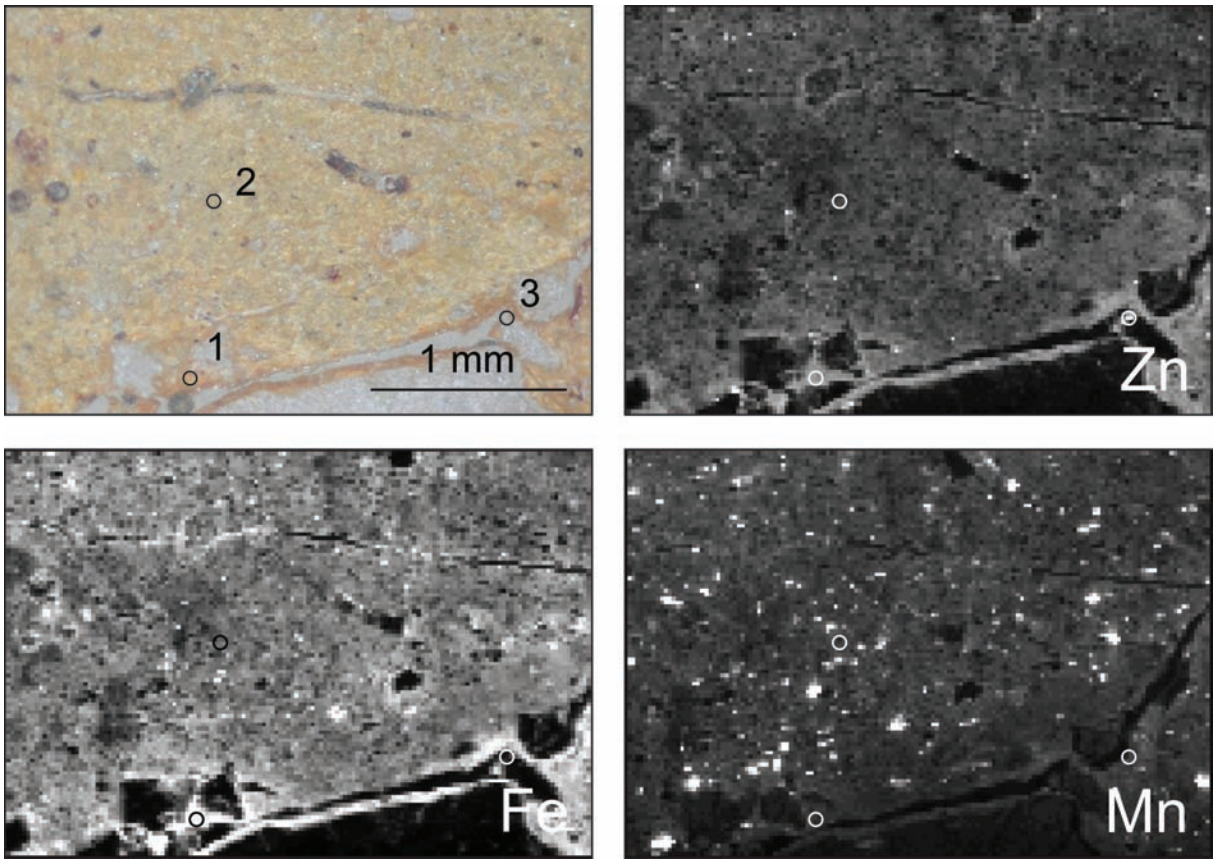

Figure 5.4. Light microscope image of a thin-section from soil DOR-BwC and corresponding μ–XRF maps for Zn, Fe and Mn. The mapped area is 3000×2000 μm² (20×20 μm² resolution, 200 ms dwell time).

In a localized Zn-rich spot next to a calcite grain and lacking correlation with Fe or Mn (DOR-BwC-3), Zn-calcite was identified. The two μ-EXAFS spectra recorded within the clayey matrix of the soil (DOR-BwC-1 and DOR-BwC-2) were nearly identical to the EXAFS spectra from the clay fraction and the bulk soil of the BwC and Ah horizons (Fig. 5.5). This indicated that the Zn speciation in the bulk soil was dominated by Zn associated with minerals in the clay size fraction.

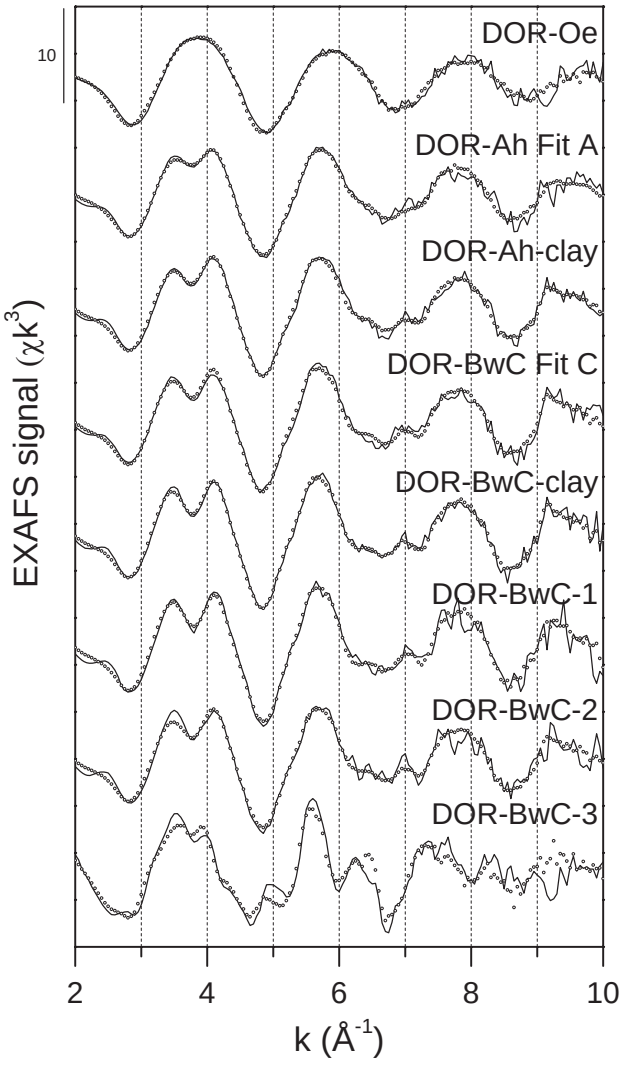

Figure 5.5. Bulk and μ-EXAFS spectra collected in the Oe, Ah and BwC horizons of soil DOR (solid lines) and LCF spectra (dots). LCF results are provided in Table 5.5.

In all these spectra, the first EXAFS oscillation was split at 3.8 $Å^{-1}$, similar to Zn-HIS and Zn-kaolinite reference spectra (Fig. 5.3). For DOR-BwC, a better two-component fit was achieved with Zn-HIS-4.0 and aqueous Zn than with nat. Zn-kaolinite and aqueous Zn. However, addition of Zn-kaolinite in a three-component fit caused a substantial decrease in the NSSR (Table 5.5). The lower NSSR was reflected in a visually improved fit in the *r*-range 3-4.5 Å in Fourier transformed spectrum (Fig. 5.6). Since this region is

sensitive to contributions from next-nearest Si in phyllosilicates [3, 54] which are absent in Zn-HIM [12, 13, 55], the improved LCF strongly suggested that Zn-kaolinite was present in the sample DOR-BwC in addition to Zn-HIM. The Zn-HIS and Zn-kaolinite reference spectra were also present in the best LCF of the EXAFS spectra from the clay size fraction of the Ah and BwC horizons (DOR-Ah-clay, DOR-BwC-clay) as well as the two μ-EXAFS spectra recorded on the soil matrix (BOR-BwC-1, DOR-BwC-2), with similar improvements in *r*-space as reported for DOR-BwC (Fig. 5.6, Table 5.5). In best LCF fits, natural Zn-kaolinite was always preferred over synthetic Zn-kaolinite. In contrast, adding Zn-kaolinite to the LCF of the DOR-Ah EXAFS spectrum did not result in spectral improvements of the fit or a decrease in NSSR (Fig. 5.6, Table 5.5).

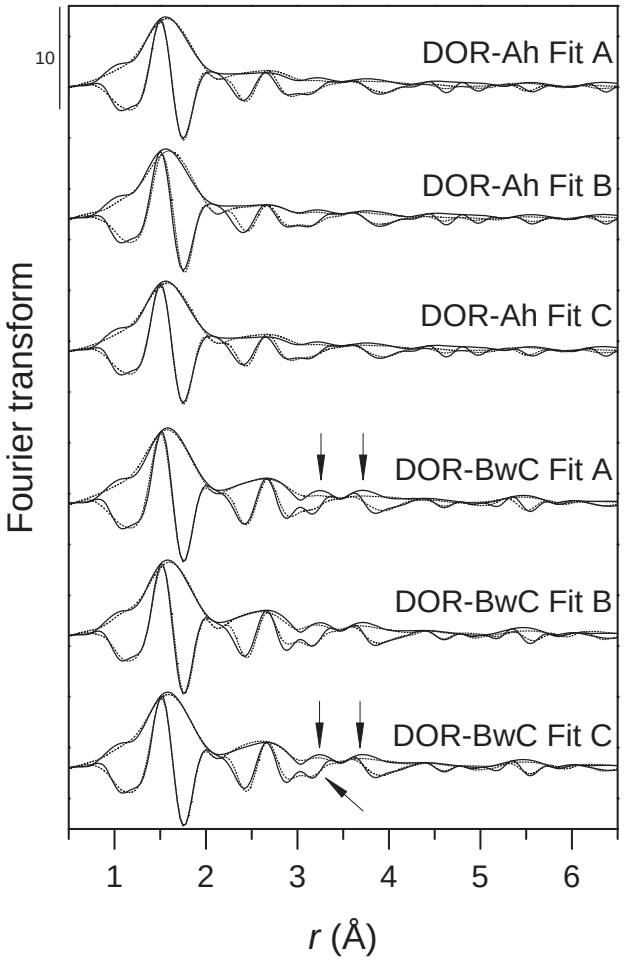

Figure 5.6. Amplitude and imaginary part of the Fourier transformed EXAFS spectra of the samples DOR-Ah and DOR BwC and comparison with Fourier transformed LCF spectra (dots, fits A-C reported in Table 5.5).

Table 5.5. Linear combination fits of the bulk and μ-EXAFS of the DOR-Oe, DOR-Ah, DOR-BwC.

Spectrum	Zn-HIS (%)	nat. Zn-kaolinite (%)	Zn-calcite (%)	sorbed ^{VI}Zn (%)	sorbed ^{IV}Zn	Sum (%)	NSSR (%)
DOR-Oe	———	———	———	55[e]	56[f]	111	5.0
DOR-Ah Fit A	56[a]	———	———	45[e]	———	99	4.5
DOR-Ah Fit B	———	30	———	61[e]	———	91	7.4
DOR-Ah Fit C	53[a]	3	———	44[e]	———	100	4.5
DOR-Ah-clay	49[a]	22	———	32[e]	———	103	2.4
DOR-BwC Fit A	57[b]	———	———	47[e]	———	104	4.8
DOR-BwC Fit B	———	55	———	43[e]	———	98	4.9
DOR-BwC Fit C	32[b]	30	———	39[e]	———	101	3.7
DOR-BwC-clay	32[c]	35	———	34[e]	———	101	2.7
DOR-BwC-1	40[b]	22	———	36[e]	———	98	6.6
DOR-BwC-2	42[d]	15	———	44[e]	———	101	6.4
DOR-BwC-3	———	———	82	———	34[g]	116	17.1

[a]Zn-HIS-6.9, [b]Zn-HIS-4.0, [c]Zn-HIS-2.9, [d]Zn-HIS-2.1. [e]Aqueous Zn. [f]Zn-sorbed ferrihydrite. [g]Zn-sorbed calcite.

5.3.4.2. Soil GUR

The light microscope image of a thin-section from the Aca horizon of soil GUR and corresponding Zn, Fe and Mn distribution maps are shown in Figure 5.7. The Zn distribution indicated localized Zn and Fe rich zones and Zn at lower concentrations associated with FeMn-concretions and the clayey matrix. Bulk and μ-EXAFS spectra and corresponding LCF spectra of the bulk soil (GUR-Aca), the clay size fraction (GUR-Aca-clay) and 3 POI on the soil thin-section (GUR-Aca-1 to GUR-Aca-3) are shown in Figure 5.8. LCF parameters are provided in Table 5.6. The μ-EXAFS spectrum recorded within a FeMn concretion (GUR-Aca-3) exhibited a splitting at 6 $Å^{-1}$, as observed more intensively for birnessite with low Zn surface coverage [56]. Correspondingly, the LCF indicated mainly Zn sorbed to birnessite and ferrihydrite (Table 5.6). On the other hand, the μ-EXAFS spectrum collected in the Fe-rich zone (GUR-Aca-1) closely resembled the bulk soil spectrum having an asymmetric first oscillation maximum at 3.8 $Å^{-1}$. Such spectral features were also present in the spectra of the clay fraction (GUR-Aca-clay) and clayey soil matrix (GUR-Aca-2), although less pronounced (Fig. 5.8). LCF on these spectra indicated Zn-goethite to be a major Zn species in the soil, in agreement with the LCF analysis of the limestone spectrum showing Zn-goethite to be the dominant Zn species (Fig. 5.2, Table 5.2). In addition, LCF of some of the soil EXAFS spectra also indicated minor fractions of nat. Zn-kaolinite, whereas Zn-HIS was not reported for any

spectrum from soil GUR.

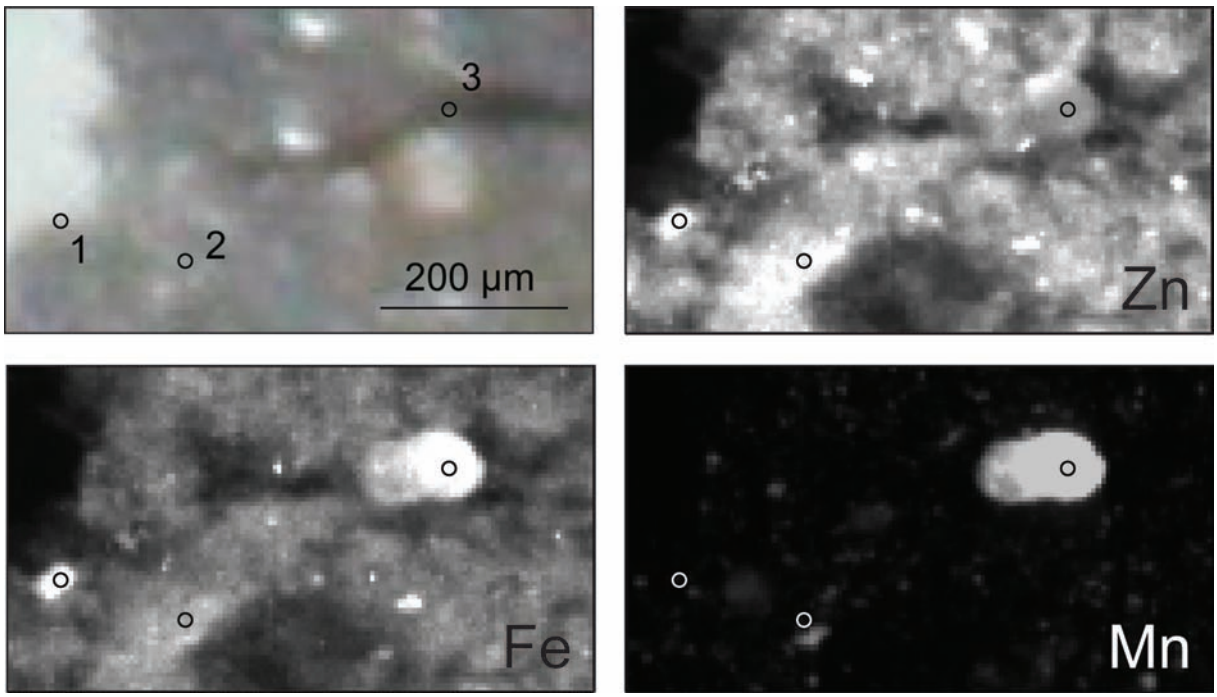

Figure 5.7. Light microscope image of a thin-section from soil GUR-Aca and corresponding µ–XRF maps for Zn, Fe and Mn. The mapped area is 650×350 µm² (5×5 µm² resolution, 100 ms dwell time).

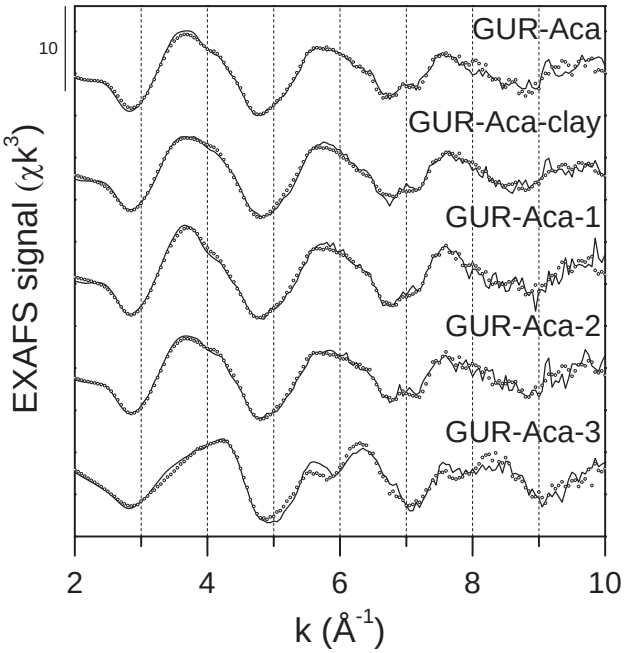

Figure 5.8. Bulk and µ-EXAFS spectra collected in the Aca horizon of soil GUR (solid lines) and LCF spectra (dots). LCF results are provided in Table 5.6.

Table 5.6. Linear combination fits of the bulk and μ-EXAFS of GUR-Aca.

Spectrum	Zn-goethite	nat. Zn-kaolinite	sorbed ^{IV}Zn	sorbed ^{VI}Zn	Sum	NSSR
	(%)	(%)	(%)	(%)	(%)	(%)
GUR1A-Aca	49	16	———	27[e]	92	5.3
GUR1A-Aca-clay	30	13	16[a]	36[f]	95	4.1
GUR1A-Aca-1	53		12[b]	35[f]	100	7.0
GUR1A-Aca-2	55	17	24[b]	———	96	6.8
GUR1A-Aca-3	———	———	40[c] +54[d]	———	94	8.9

[a]Zn-phytate, [b]Zn-sorbed calcite, [c]Zn-sorbed ferrihydrite, [d]low Zn-birnessite. [e]Zn-sorbed goethite, [f]aqueous Zn.

5.3.4.3. Soil LIE

Distribution maps of Zn, Fe and Mn in a thin-section from the Aca horizon of soil LIE are shown in Figure 5.9.

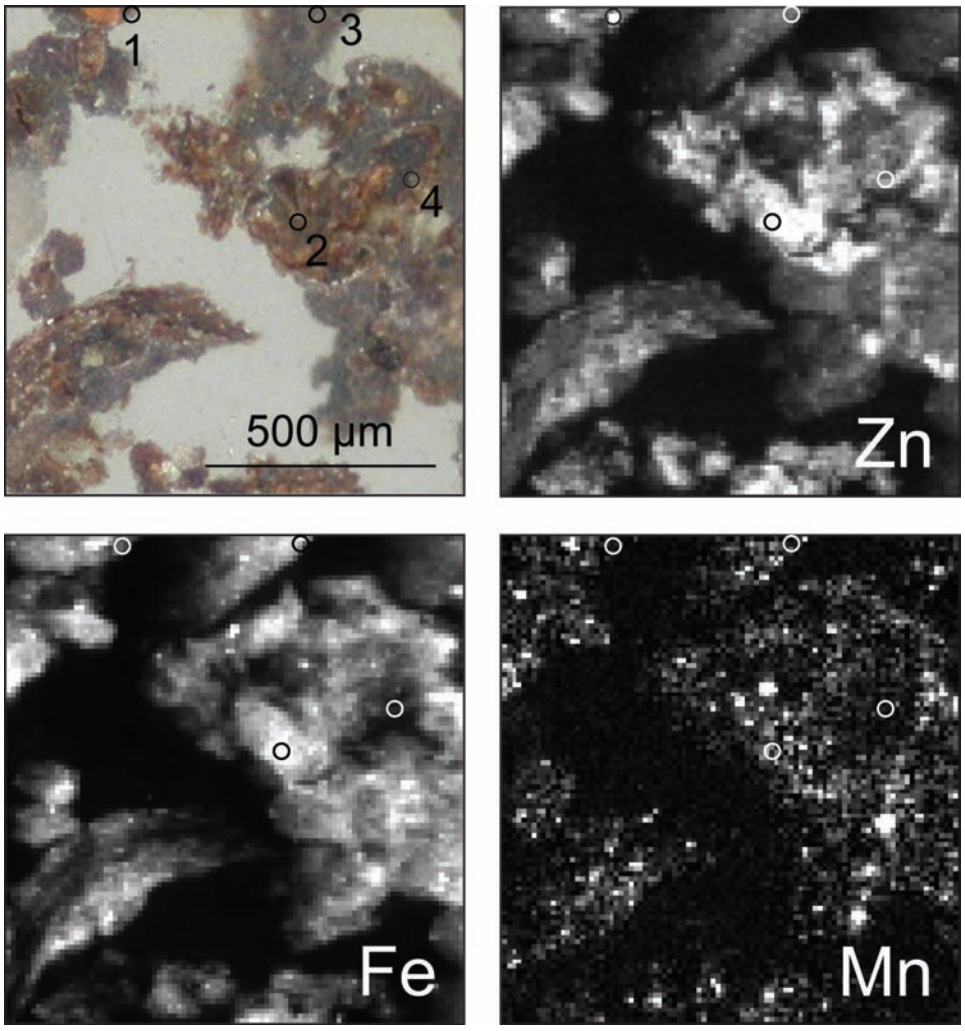

Figure 5.9. Light microscope image of a thin-section from soil LIE-Aca and μ–XRF maps for Zn, Fe and Mn. The mapped area is 1000×1000 μm^2 (10×10 μm^2 resolution, 100 ms dwell time).

The μ-EXAFS spectra from 4 POI on this thin-section and the EXAFS spectrum of the bulk soil are shown in Figure 5.10. Similar to the Aca horizon of soil GUR, the distribution of Zn resembled the distribution of Fe and the μ-EXAFS spectrum of POI 3 (LIE-Aca-3) and the bulk soil spectrum were best fitted with Zn-goethite and minor contributions of nat. Zn-kaolinite and sorbed ^{IV}Zn. At POI 1 locally high Zn levels were not correlated with either Fe or Mn, and the respective μ-EXAFS spectrum (LIE-Aca-1) closely matched the spectrum of ZnS, the dominant Zn species in the corresponding limestone rock (Fig. 5.2, Table 5.2). In contrast, the spectra LIE-Aca-2 and LIE-Aca-4 did not exhibit pronounced high frequency features and LCF returned high fractions of tetrahedrally coordinated adsorbed Zn.

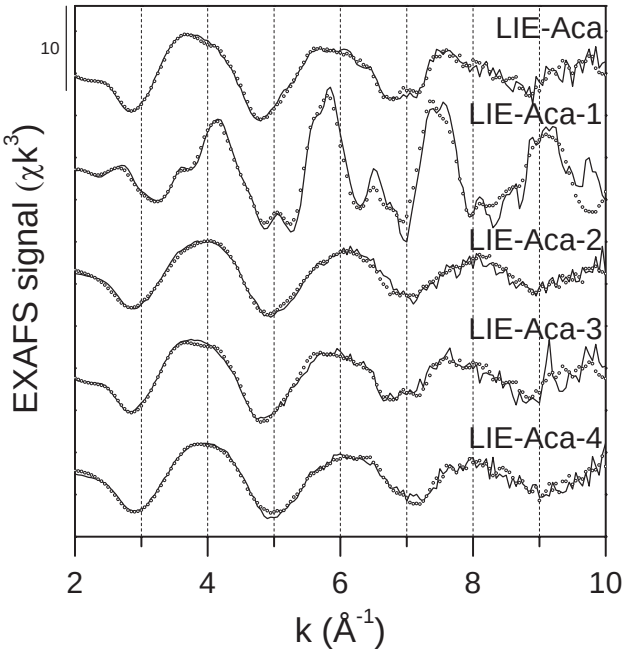

Figure 5.10. Bulk and μ-EXAFS spectra collected in the Aca horizon of soil LIE (solid lines) and LCF spectra (dots). LCF results are provided in Table 5.7.

Table 5.7. Linear combination fits of the bulk and μ-EXAFS of LIE-Aca.

Spectrum	Zn-goethite (%)	ZnS (%)	nat. Zn-kaolinite (%)	sorbed ^{IV}Zn (%)	sorbed ^{VI}Zn (%)	Sum (%)	NSSR (%)
LIE-Aca	58	———	18	25[a]	———	101	6.1
LIE-Aca-1	———	106	———	———	———	106	10.6
LIE-Aca-2	———	———	———	75[a]	23[c]	98	7.0
LIE-Aca-3	45	———	21	33[a]	———	99	11.8
LIE-Aca-4	23	———	———	71[b]	———	94	7.5

[a]Zn-sorbed ferrihydrite, [b]Zn-sorbed calcite. [c]Aqueous Zn.

5.3.5. Sequential extraction

In order to investigate the relation between Zn speciation and Zn fractionation, the geogenically Zn-rich soils and selected Zn reference compounds in pure form or spiked into quartz powder or non-calcareous soil were sequentially extracted. Sequential extraction results are presented in Figure 5.11.

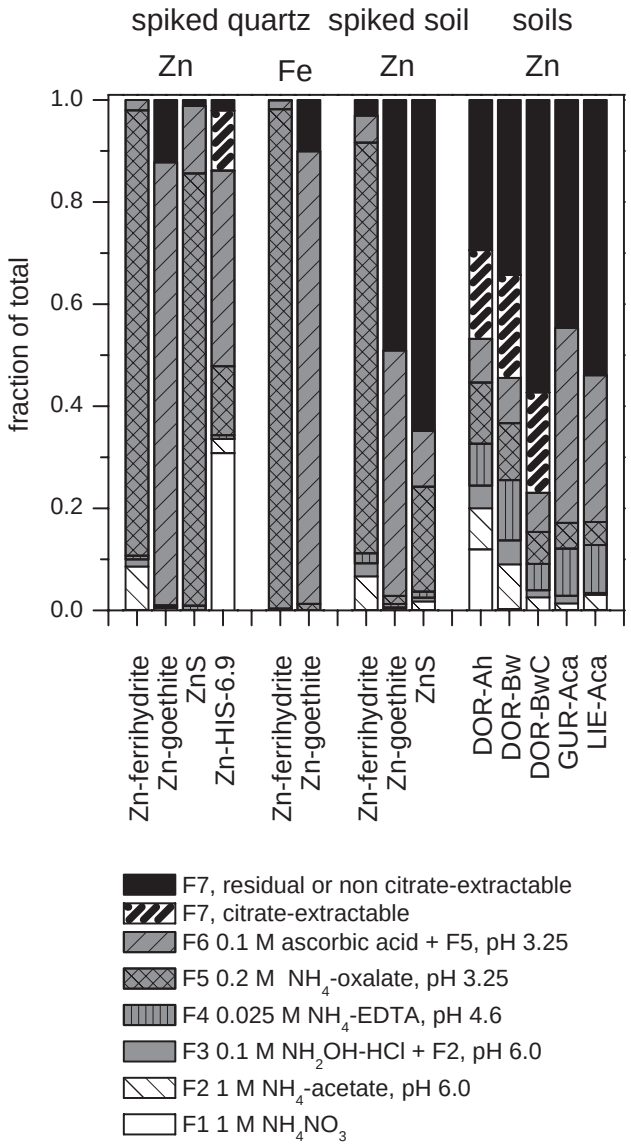

Figure 5.11. Sequential extraction results for quartz (Q) and soil (S) powder spiked with Zn-ferrihydrite, Zn-goethite, ZnS and Zn-HIS-6.9 and for soil samples. Note: only the residual fraction (F7) of Zn-HIS-6.9 and DOR Ah, DOR Bw and DOR BwC was further extracted with Na-citrate (F7, citrate extractable).

Zn-ferrihydrite spiked in quartz powder was mainly extracted in F5, which is intended to remove poorly crystalline iron oxides [44]. However, the acidic (pH 3.25) 0.2 M ammonium oxalate ($(NH_4)_2C_2O_4$) solution used in F5 not only selectively dissolved Zn-ferrihydrite but also mobilized a substantial fraction of ZnS spiked into quartz. Most Zn from Zn-goethite spiked into quartz was extracted in the fraction F6,

which is assumed to dissolve crystalline iron oxides [44]. Most Zn from Zn-HIS-6.9 spiked into quartz was extracted in F1, F4, F5, and F6. The extraction of about 30% of the total Zn from Zn-HIS-6.9 in F1 indicated that Zn was not exclusively sorbed to Al-polymers but also present in exchangeable form in the phyllosilicate interlayer [12]. When spiked into non-calcareous soil rather than quartz powder, Zn from reference materials was extracted in latter extraction steps, demonstrating substantial readsorption or reprecipitation of Zn during sequential soil extraction. The extraction of pure Zn-HIS-6.9 and pure synthetic Zn-kaolinite with Na-citrate [12] confirmed the selectivity of this extraction for hydroxy-Al polymers, mobilizing 78 % of the Zn from Zn-HIS-6.9 but only 15% of the Zn from Zn-kaolinite (not shown in Fig. 5.11).

In the DOR soils, the percentage of mobile and readily mobilisable Zn (fractions F1+F2) decreased with increasing soil pH, i.e., increasing horizon depth. In parallel, the amount of Zn found in the last fraction (F7) increased from the Ah (47 %) to the BwC horizon (77%), indicating a gradual shift to highly stable forms of Zn with depth. In all three soil horizons, additional Na-citrate extraction of the sequentially extracted samples (after step F6) mobilized similar fractions of the total Zn (~20%). The results from the sequential extraction of the Aca horizons from GUR and LIE were nearly identical. Almost all Zn (~80% of total Zn) was extracted in the last two fractions (F6+F7), indicating that Zn was associated with highly recalcitrant phases. From all soils, only minor fractions of Zn were extracted in F3 designed for the dissolution of Mn-oxides [44] and shown to selectively extract birnessite and lithiophorite [12].

5.4. Discussion

5.4.1. Origin and speciation of Zn in limestones

The three oolitic limestones investigated in this work had elevated Zn contents (43-207 mg/kg). The origin of high Zn (and Cd) contents in Jurassic limestones of the Jura mountain range is still unclear. They may result from atmospheric fallouts due to volcanic activities during the Jurassic period [50] or post-sedimentation processes, i.e., hydrothermalism linked to tectonic extension [57]. Regarding the first possibility, phases of volcanism have been identified for the Jurassic period [58, 59]. Rambeau [50] suggested that variations in the quantity of atmospheric metal input (occasional events) and in the depositional environment strongly influence Zn and Cd enrichments in oolitic limestones of the Jura mountain range. Elevated input of organic matter (due to enhanced productivity) into the sediments at the carbonate platform margin may have led to reducing conditions and formation of metal sulfides, whereas in lagoon environments, co-precipitation and micritization may have favored metal incorporation

into carbonate phases [50]. The detection of Zn-calcite in the lagoonal oolitic limestone DOR-R, Zn-goethite in the oolitic barrier limestone GUR-R, and concomitant occurrence of Zn-goethite and sphalerite in the platform margin limestone LIE-R are in qualitative agreement with this enrichment model.

During the Bajocian/Bathonian and Oxfordian, intense hydrothermal activity due to the reactivation of basement structures led to the mineralization of veins, alteration of minerals and illitization in Jurassic sediments of the Jura mountain range, the nearby Black Forest and the Vosges [60]. In the Black Forest, hydrothermal Pb-Zn quartz-fluorite deposits containing sphalerite were dated to the Eocene-Oligocene [61, 62]. Even though mineralization veins were not observed in the limestones investigated here, the occurrence of sphalerite in the limestone LIE-R and in other limestones of the Jura mountain range [57] may also be linked to hydrothermal events. Following this hypothesis, the presence of Zn-containing goethite in the limestones LIE-R and GUR-R and of Zn-calcite in DOR-R could result form the oxidative transformation of hydrothermal sphalerite in contact with meteoric waters. Differences in rock permeability related to differences in rock facies (e.g., micritic versus sparitic matrix in the oolitic limestones DOR-R and GUR-R, respectively) could cause the spatial heterogeneity of the metal enrichments observed in the Jura mountain range [57] and the formation of different Zn species. More detailed chemical and stratigraphical analyses of the respective geological formations will be needed to evaluate the importance of different Zn enrichment pathways and their influence on Zn speciation.

5.4.2. Fate of geogenic Zn species during soil formation

During limestone weathering and soil formation, the identified geogenic Zn species showed different behavior. In soil DOR developed from limestone in which Zn was mainly contained in calcite, Zn was principally associated with pedogenic Zn species. Traces of Zn-calcite were identified by μ-EXAFS in the soil matrix and most likely stemmed from the weathered limestone, although neoformation from dissolved Zn in contact with calcite particles cannot be excluded. The molar ratios Zn/Al, Zn/Si, Zn/Ti and Zn/Fe in the DOR soil samples were substantially smaller than in the limestone DOR-R (Table A4.1). Furthermore, with decreasing soil depth, soil pH gradually decreased from neutral to acidic values (from 7.2 to 4.5) and also TIC contents decreased (from 12 to <1 g/kg) (Table 5.1). Together with the Zn speciation results, these observations indicated that calcite-derived Zn was mostly leached during limestone dissolution and that only a minor fraction of the Zn was retained in the soil.

At Gurnigel and Liestal, the elevated Zn concentrations observed in the soils were to a large extent due to the inheritance of Zn-goethite from the limestone. This interpretation

was based on the EXAFS analyses indicating Zn-goethite to be a major Zn species in the bedrock and sequential extraction data showing Zn-goethite to be highly resistant to acidifying conditions, and thus to pedogenic weathering. The formation of Zn-goethite from the weathering of Zn-Fe spinel has previously been observed in pristine and contaminated soils [7, 20, 63]. However, Zn-goethite in soil GUR and LIE did not form pedogenically but originated from the dissolution of the underlying limestone rock containing Zn-goethite. Based on Zn-goethite fractions from LCF (Table 5.2) and total Zn and Fe contents of the limestones from LIE and GUR (Table A4.1), the Zn contents in goethite from the LIE and GUR limestones were estimated to be 2000 and 13600 mg/kg, respectively. This closely compares to estimated Zn contents of 2000 and 9000 mg/kg Zn in goethite from the respective soil horizons LIE-Aca and GUR-Aca (based on the amounts of Zn and Fe extracted in the fraction F6 of the sequential extraction procedure). Even though sphalerite represented the major Zn species in the limestone from Liestal, it was only detected in traces in the LIE soil, reflecting the oxidation of sulfides in the aerobic soil environment. Both at Gurnigel and Liestal, the molar ratios Zn/Al, Zn/Si, Zn/Ti and Zn/Fe of the limestone and the corresponding soil were of the same order of magnitude (Table A4.1), suggesting limited Zn leaching during soil formation. This can be attributed to the inheritance of geogenic Zn-goethite which resisted transformation during weathering and soil formation as well as to the neutral soil pH of GUR and LIE, which limited the leaching of Zn released from geogenic Zn species.

The relation between Zn-rich limestones and elevated Zn concentrations in soils of the Jura mountain range has previously been reported [25, 49]. These authors suggested that the wide spatial variability of Cd (and Zn) contents observed in soils resulted from variations in the metal concentrations of the underlying rocks. Our results show that not only the Zn content but also the chemical forms of Zn in the limestone rock and the chemical properties (pH, TIC) of the above-lying soil strongly influence soil Zn contents.

5.4.3. Pedogenic Zn species

Our EXAFS analyses indicated that Zn released from the dissolution of geogenic Zn species and retained in the soils was sequestered into Zn-HIM and/or Zn-kaolinite as well as into adsorbed and/or complexed Zn species. Regarding sorbed and complexed forms of Zn, the LCF results (Tables 5.5-5.7) were in line with our earlier observation on contaminated soils that indicated a shift from octahedrally coordinated to tetrahedrally coordinated sorbed/complexed Zn with increasing soil pH. This is due to a decrease of the fraction of exchangeably bound Zn (with octahedral coordination) [14]. In the

following, the formation of Zn-HIM and Zn-kaolinite and the potential for a geogenic origin of these species as well as the relevance of other layered Zn-bearing precipitates will be further discussed.

The LCF analysis of the EXAFS spectra from soil DOR indicated the occurrence of Zn-HIM (Table 5.5). Since only HIV but no HIS was identified by the XRD analysis (Figs. 5.1, A4.1, A4.2), the fitted Zn-HIS fractions likely corresponded to Zn-HIV. The type of Zn-HIS reference used in the best LCF (Zn-HIS-2.1 to Zn-HIS-6.9, corresponding to 2100 mg/kg to 6900 mg/kg Zn content, respectively, Table 5.5) was qualitatively in agreement with a higher Zn loading of HIV in DOR-Ah than DOR-BwC in parallel with a higher Zn content (Table 5.1). According to Pochon [64], HIM in soils of the Jura mountain range have developed from weathered geogenic chlorite and are indicative of post-Würmian (<10000 years) pedogenesis. Furthermore, the trends in Zn-HIS references used in best LCF were in line with an enhanced Zn loading of HIS with higher soil Zn content and lower pH (from the BwC to the Ah horizon), advocating against a geogenic origin of Zn-HIV. Thus, Zn-HIV in soil DOR likely formed via the release of Zn from dissolving geogenic Zn-calcite and subsequent incorporation into pedogenic HIV during soil formation. Similar incorporation of Cu into pedogenic HIV has been reported in soils developed from Cu-rich schists [65]. Zn-HIM has previously been identified in pristine [21, 22] and contaminated soils [12-14] and may represent a dominant Zn species in (mostly acidic) HIM-containing soils, though its capacity for Zn uptake is limited [12]. Even though the XRD analysis of the soils GUR and LIE also indicated significant amounts of HIV, LCF analysis of the soil EXAFS spectra did not indicate a significant fraction of Zn-HIM (Table 5.6 and 5.7). This may either be due to the higher pH of these latter soils (Table 5.1) or to the presence of substantial amounts of Zn-goethite preventing the detection of small amounts of Zn-HIM in the presence of Zn-kaolinite, the second Zn-containing layered phase identified in this work with similar local Zn coordination as in Zn-HIM.

The identification of Zn-kaolinite in all three studied soils was based on LCF (Fig. 5.6, Table 5.5) and sequential extraction data (Fig. 5.11). In soil DOR, the best LCF of the EXAFS spectra from the BwC horizon consistently included Zn-kaolinite, whereas this species was only included in the best LCF to the EXFAS spectrum from the clay fraction of the Ah horizon, but not the bulk soil (Table 5.5, Fig. 5.6). At the same time, the residual fraction F7 decreased from 77% of the total Zn in DOR-BwC to 47% in DOR-Ah, mostly due to a decrease of the non-citrate-extractable fraction (Fig. 5.11). Considering that Zn-HIM is citrate-extractable whereas Zn-kaolinite is not, the trends strongly supported the presence of Zn-kaolinite in soil DOR and its higher fraction in the BwC horizon, which had a higher soil pH than the Ah horizon (whose lower soil

pH likely favored the formation of Zn-HIV). Furthermore, XRD analysis showed that kaolinite was one of the major minerals in the clay size fraction of soil DOR (Figs. 5.1, A4.1, A4.2), which represented ~60 % of the total soil weight (Table 5.1). For the soils LIE and GUR, the results from LCF indicated that most Zn was present as Zn-kaolinite and Zn-goethite and qualitatively matched the sequential extraction results, which showed that ~80% of the total Zn was extracted in the recalcitrant fractions (F6+F7).

Earlier studies on the speciation of Zn in pristine soils identified Zn-HIM and Zn-containing trioctahedral phyllosilicates [21, 22], but the occurrence of Zn-containing dioctahedral phyllosilicate, i.e., Zn-kaolinite, as a major soil Zn species has not been reported before. In previous work, we postulated that Zn-kaolinite was present in the clay size fraction of a slightly contaminated soil [12]. This soil also developed from limestone of the Jura mountain range, but was additionally contaminated by aqueous Zn from corroding power line towers. In the geogenically Zn-rich soils studied here, Zn-kaolinite may have formed during pedogenesis or may have been inherited from the limestone, since traces of kaolinite were detected by XRD in the insoluble limestone residuals (data not shown). Considering the Zn contents of the studied soils, the fractions of Zn-kaolinite obtained by LCF, and assuming the soil clay fraction to contain 25% kaolinite, the Zn content of Zn-kaolinite was estimated to at most ~1000 mg/kg. This concentration compares to Zn contents of 180 mg/kg and 270 mg/kg for the natural and synthetic Zn-kaolinites used as EXAFS references [12]. Assuming all Al in the limestone DOR-R (Table A4.1) to be contained in kaolinite and considering a maximum content of 1000 mg/kg Zn in kaolinite, at most 1% of the total Zn in DOR-R could have been present as Zn-kaolinite. This fraction would have been too small for detection by EXAFS spectroscopy. Considering that the Zn/Al ratio in DOR-R was ~60-100 times higher than in the respective soil samples (Table A4.1), our data do not allow to definitely exclude the possibility that Zn-kaolinite in soil DOR resulted from the residual enrichment of geogenic Zn-kaolinite already present in the limestone rock. However, in the soils GUR and LIE, a geogenic origin of Zn-kaolinite seems unlikely, since only sphalerite and/or Zn-goethite were detected in the limestones and similar molar ratios of Zn relative to Al, Si, Ti and Fe were found for the rock and corresponding soil samples (Table A4.1). Furthermore, percolating waters from soils of the Jura mountain range have previously been shown to be oversaturated with respect to kaolinite [64]. Therefore, our data support the interpretation that Zn-kaolinite in the soils GUR and LIE, and most likely also DOR, was of pedogenic origin.

In a previous study on the speciation of Zn in soils that had been contaminated over periods of years to decades with aqueous Zn from corroding powerline towers, we found Zn-LDH and to a minor extent trioctahedral Zn-phyllosilicates to be important Zn

species [14]. These phases were previously identified in a series of soils contaminated by different forms of Zn, including smelter and foundry emissions or dredged sediments [5-10]. Factors favoring the formation of these phases were higher soil pH and higher Zn concentrations [14]. In the current study, we did not detect these species in the soils GUR and LIE with near neutral pH. This may be due to relatively low Zn levels compared to the previously studied heavily contaminated soils, but may also reflect the limited long-term stability of these phases in the soil environment [11, 66, 67]. As reported by Paquet et al. [17], trioctahedral Zn-rich smectites from ore deposits are unstable upon weathering and evolve to dioctahedral smectites with low Zn contents and finally to Zn-kaolinite and Zn-containing Fe (hydr)oxides. Consequently, the Zn-kaolinite and Zn-goethite, which we identified in ~10000 years old soils, are expected to be stable long-term hosts for Zn in oxic soils. However, the potential of these phases for the immobilization of large amounts of Zn introduced into contaminated soils is determined by their abundance and Zn uptake capacity, the latter likely being limited in the case of Zn-kaolinite.

5.5. Conclusions

The speciation of Zn in naturally Zn-rich soils strongly depends on soil properties and the chemical forms of Zn present in the parent material. Zn in soils developed from the weathering of Zn-rich rocks is either linked to the inheritance of resistant Zn-bearing minerals or dissolution of primary Zn minerals and subsequent redistribution of Zn into pedogenic phases. Zn-containing goethite occurring in Zn-rich limestone is a highly resistant phase, causing its enrichment during limestone dissolution and soil formation. In contrast, sphalerite and Zn-calcite dissolve during pedogenesis. The released Zn may either be leached from the soil or be incorporated into Zn-bearing HIM or kaolinite, which we identified in soils developed over ~10’000 years of soil formation. Thus, Zn-goethite as well as Zn-HIM and Zn-kaolinite are highly resistant in the soil weathering environment and may act as long-term hosts for Zn. In highly contaminated soils, however, the low abundance (especially goethite) and/or the low capacity for Zn uptake (especially HIM and kaolinite) may limit the relevance of these phases for the immobilization of high Zn inputs.

Acknowledgements

We thank Claire Rambeau, Virginie Matera, Natalia Efimenko and Raul Quezada (Neuchâtel University, Switzerland) for help during soil and rock sampling, provision of several samples, and fruitful discussions of geological aspects of this work. Gérome Tokpa (ETH Zurich, Switzerland) is acknowledged for performing the sequential

extraction of the soil samples, André Villard (Neuchâtel University, Switzerland) for the preparation of thin-sections and Kurt Barmettler (ETH Zurich, Switzerland) for his expert help with soil analyses. We thank Guillaume Morin (University of Paris, France) for fruitful discussions on the topic of this study. The spectrum of Zn-sorbed calcite was kindly provided by Evert Elzinga (Rutgers University). Stefan Mangold (XAS, ANKA, Germany), the staff of the Swiss Norwegian beamline (SNBL, ESRF, France) and Matthew A. Marcus (ALS 10.3.2, Berkeley, USA) are acknowledged for their help with EXAFS data acquisition. The Angströmquelle Karlsruhe GmbH (ANKA, Karlsruhe, Germany), the SNBL beamline at the ESRF and the Advanced Light Source (ALS, Berkeley, USA) are acknowledged for providing beamtime. The ALS is supported by the Director, Office of Science, Office of Basic Energy Sciences, Material Sciences Division, of the U.S. Departement of Energy under Contract No. DE-AC03-76SF00098 at Lawrence Berkeley National Laboratory. This research project was financially supported by the Swiss National Science Foundation under contracts no. 200021-101876 and 200020-116592.

References

[1] Alloway, B. J., *Heavy Metals in Soils*. Chapman & Hall: London, 1995.

[2] Ford, R. G.; Sparks, D. L., The nature of Zn precipitates formed in the presence of pyrophyllite. *Environ. Sci. Technol.* 2000, 34, 2479-2483.

[3] Schlegel, M. L.; Manceau, A.; Charlet, L.; Chateigner, D.; Hazemann, J.-L., Sorption of metal ions on clay minerals III. Nucleation and epitaxial growth of Zn phyllosilicate on the edges of hectorite. *Geochim. Cosmochim. Acta* 2001, 65, 4155-4170.

[4] Roberts, D. R.; Ford, R. G.; Sparks, D. L., Kinetics and mechanisms of Zn complexation on metal oxides using EXAFS spectroscopy. *J. Colloid Interface Sci.* 2003, 263, 364-376.

[5] Juillot, F.; Morin, G.; Ildefonse, P.; Trainor, T. P.; Benedetti, M.; Galoisy, L.; Calas, G.; Brown, G. E., Occurrence of Zn/Al hydrotalcite in smelter-impacted soils from northern France: Evidence from EXAFS spectroscopy and chemical extractions. *Am. Mineral.* 2003, 88, 509-526.

[6] Kirpichtchikova, T. A.; Manceau, A.; Spadini, L.; Panfili, F.; Marcus, M. A.; Jacquet, T., Speciation and solubility of heavy metals in contaminated soil using X-ray microfluorescence, EXAFS spectroscopy, chemical extraction, and thermodynamic modeling. *Geochim. Cosmochim. Acta* 2006, 70, 2163-2190.

[7] Manceau, A.; Lanson, B.; Schlegel, M. L.; Harge, J. C.; Musso, M.; Eybert-Berard, L.; Hazemann, J. L.; Chateigner, D.; Lamble, G. M., Quantitative Zn

speciation in smelter-contaminated soils by EXAFS spectroscopy. *Am. J. Sci.* 2000, 300, 289-343.

[8] Nachtegaal, M.; Scheidegger, A. M.; Dahn, R.; Chateigner, D.; Furrer, G., Immobilization of Ni by Al-modified montmorillonite: A novel uptake mechanism. *Geochim. Cosmochim. Acta* 2005, 69, 4211-4225.

[9] Panfili, F. R.; Manceau, A.; Sarret, G.; Spadini, L.; Kirpichtchikova, T.; Bert, V.; Laboudigue, A.; Marcus, M. A.; Ahamdach, N.; Libert, M. F., The effect of phytostabilization on Zn speciation in a dredged contaminated sediment using scanning electron microscopy, X-ray fluorescence, EXAFS spectroscopy, and principal components analysis. *Geochim. Cosmochim. Acta* 2005, 69, 2265-2284.

[10] Voegelin, A.; Pfister, S.; Scheinost, A. C.; Marcus, M. A.; Kretzschmar, R., Changes in zinc speciation in field soil after contamination with zinc oxide. *Environ. Sci. Technol.* 2005, 39, 6616-6623.

[11] Jacquat, O.; Voegelin, A.; Villard, A.; Marcus, M. A.; Kretzschmar, R., Formation of Zn-rich phyllosilicates, Zn-layered double hydroxide and hydrozincite in contaminated calcareous soils. *Geochim. Cosmochim. Acta* 2008, 72, 5034-5057.

[12] Jacquat, O.; Voegelin, A.; Kretzschmar, R., Local coordination of Zn in hydroxy-interlayered minerals and implications for Zn retention in soils. *Geochim. Cosmochim. Acta* 2009, 73, 348-363.

[13] Scheinost, A. C.; Kretzschmar, R.; Pfister, S.; Roberts, D. R., Combining selective sequential extractions, X-ray absorption spectroscopy, and principal component analysis for quantitative zinc speciation in soil. *Environ. Sci. Technol.* 2002, 36, 5021-5028.

[14] Jacquat, O.; Voegelin, A.; Kretzschmar, R., Soil properties controlling Zn speciation and fractionation in contaminated soils. *Submitted* 2008.

[15] Cesàro, G., Sur la fraipontite, silicate basique hydraté de zinc et d'alumine. *Anal. Soc. Geol. Be.* 1927, 50, B106-111.

[16] Merlino, S.; Orlandi, P., Carraraite and zaccagnaite, two new minerals from the Carrara marble quarries: their chemical compositions, physical properties, and structural features. *Am. Mineral.* 2001, 86, 1293-1301.

[17] Paquet, H.; Colin, F.; Duplay, J.; Nahon, D.; Millot, G., Ni, Mn, Zn, Cr-smectites, early and effective traps for transition elements in supergene ore deposits. In *Geochemistry of the earth surface and processes of mineral formation*, Rodriguez-Clemente, R.; Tardy, Y., Eds. Consejo Superior de Investigaciones Científicas: Granada, Spain, 1986; pp 221-229.

[18] Ross, C. S., Sauconite - a clay mineral of the montmorillonite group. *Am. Mineral.* 1946, 31, 411-424.

[19] Rule, A. C.; Radke, F., Baileychlore, the Zn end member of the trioctahedral chlorite series. *Am. Mineral.* 1988, 73, 135-139.

[20] Isaure, M.-P.; Manceau, A.; Geoffroy, N.; Laboudigue, A.; Tamura, N.; Marcus, M. A., Zinc mobility and speciation in soil covered by contaminated dredged sediment using micrometer-scale and bulk-averaging X-ray fluorescence, absorption and diffraction techniques. *Geochim. Cosmochim. Acta* 2005, 69, 1173-1198.

[21] Manceau, A.; Marcus, M. A.; Tamura, N.; Proux, O.; Geoffroy, N.; Lanson, B., Natural speciation of Zn at the micrometer scale in a clayey soil using X-ray fluorescence, absorption, and diffraction. *Geochim. Cosmochim. Acta* 2004, 68, 2467-2483.

[22] Manceau, A.; Tommaseo, C.; Rihs, S.; Geoffroy, N.; Chateigner, D.; Schlegel, M. L.; Tisserand, D.; Marcus, M. A.; Tamura, N.; Zueng-Sang, C., Natural speciation of Mn, Ni, and Zn at the micrometer scale in a clayey paddy soil using X-ray fluorescence, absorption, and diffraction. *Geochim. Cosmochim. Acta* 2005, 60, 4007-3034.

[23] Bitterli-Brunner, P.; Fischer, H.; Herzog, P., Arlesheim (Blatt 80). *Geologischer Atlas der Schweiz 1: 25000* 1984.

[24] Bourquin, P.; Buxtorf, R.; Frei, E.; Lüthi, E.; Muhlethaler, C.; Ryniker, K.; Suter, H., Val de Ruz (Blatt 51). *Geologischer Atlas der Schweiz 1:25000* 1968.

[25] Baize, D.; Sterckeman, T., Of the necessity of knowledge of the natural pedo-geochemical background content in the evaluation of the contamination of soils by trace elements. *Sci. Total Environ.* 2001, 264, 127-139.

[26] Desaules, A.; Sprengart, J.; Wagner, G.; Muntau, H.; Theocharopoulos, S., Description of the test area reference sampling at Dornach. *Sci. Total Environ.* 2000, 264, 17-26.

[27] WRB *Worl Reference Base for Soil Resources 2006-A Framework for International Classification, Correlation and Communication*; Food and Agriculture Organization of the United Nations, Rome, Italy.: 2006.

[28] Loeppert, R. H.; Suarez, D. L., Carbonate and Gypsum. In *Methods of Soil Analysis. Part 3. Chemical Methods*, Soil Science Society of America: Madison, 1996.

[29] Gee, G.; Or, D., Particle size analysis. In *Methods of Soil Analysis. Part 4. Physical Methods*, Dane, J. H.; Topp, C. C., Eds. Soil Science Society of America, Madison, USA: 2002; pp 255-293.

[30] Kimpe, C. R., Soil separation for mineralogical analysis. In *Soil Sampling and Methods of Analysis*, Carter, M. R., Ed. Lewis Publishers: Boca Raton, 1993.

[31] Kimpe, C. R., Clay and silt analysis. In *Soil Sampling and Methods of Analysis*, Carter, M. R., Ed. Lewis Publishers: Boca Raton, 1993.

[32] Brown, G.; Farrow, R., Introduction of glycerol into flakes aggregates by vapour pressure. *Clay Miner. Bull.* 1956, 3, 44-45.

[33] Brunton, G., Vapor pressure glycolation of oriented clay minerals. *Am. Mineral.* 1955, 40, 124-126.

[34] Schwertmann, U.; Cornell, R. M., *Iron Oxides in the Laboratory*. VCH Verlagsgesellschaft, Weinheim: 1991.

[35] Marcus, M. A.; MacDowell, A. A.; Celestre, R. S.; Manceau, A.; Miler, T.; Padmore, H. A.; Sublett, R. E., Beamline 10.3.2 at ALS: a hard X-ray microprobe for environmental and materials science. *J. Synchrotron Rad.* 2004, 11, 239-247.

[36] Ravel, B.; Newville, M., Athena, Artemis, Hephaestus: data analysis for X-ray absorption spectroscopy using IFEFFIT. *J. Synchrotron Rad.* 2005, 12, 537-541.

[37] Webb, S. M., SIXPack: a graphical user interface for XAS analysis using IFEFFIT. *Phys. Scr.* 2005, T115, 1011-1014.

[38] Malinowski, E. R., Determination of the number of factors and the experimental error in a data matrix. *Anal. Chem.* 1977, 49.

[39] Manceau, A.; Tamura, N.; Celestre, R. S.; MacDowell, A. A.; Geoffroy, N.; Sposito, G.; Padmore, H. A., Molecular-scale speciation of Zn and Ni in soil ferromanganese nodules from loess soils of the Mississippi Basin. *Environ. Sci. Technol.* 2003, 37, 75-80.

[40] Malinowski, E. R., Theory of error for target factor analysis with applications to mass spectrometry and nuclear magnetic resonance spectrometry. *Anal. Chim. Acta* 1978, 103, 339-354.

[41] Isaure, M.-P.; Laboudigue, A.; Manceau, A.; Sarret, G.; Tiffrau, C.; Trocellier, P.; Lamble, G. M.; Hazemann, J. L.; Chateigner, D., Quantitative Zn speciation in a contaminated dredged sediment by μ-PIXE, μ-SXRF, EXAFS spectroscopy and principal component analysis. *Geochim. Cosmochim. Acta* 2002, 66, 1549-1567.

[42] Sarret, G.; Balesdent, J.; Bouziri, L.; Garnier, J. M.; Marcus, M. A.; Geoffroy, N.; Panfili, F.; Manceau, A., Zn speciation in the organic horizon of a contaminated soil by micro-x-ray fluorescence, micro- and powder-EXAFS spectroscopy, and isotopic dilution. *Environ. Sci. Technol.* 2004, 38, 2792-2801.

[43] Manceau, A.; Boisset, M. C.; Sarret, G.; Hazemann, R. L.; Mench, M.; Cambier, P.; Prost, R., Direct determination of lead speciation in contaminated soils by EXAFS spectroscopy. *Environ. Sci. Technol.* 1996, 30, 1540-1552.

[44] Zeien, H.; Brümmer, G. W., Chemische Extraktionen zur Bestimmung von Schwermetallbindungsformen in Böden. *Mitt. Dtsch. Bodenkundl. Ges.* 1989, 59, 505-510.

[45] Voegelin, A.; Tokpa, G.; Jacquat, O.; Barmettler, K.; Kretzschmar, R., Zinc fractionation in contaminated soils by sequential and single extractions: Influence of soil properties and zinc content. *J. Environ. Qual.* 2008, 37, 1190-1200.

[46] Tamura, T., Identification of clay minerals from acid soils. *J. Soil Sci.* 1958, 9, 141-147.

[47] Tuchschmid, M. P., Quantifizierung und Regionalisierung von Schwermetall- und Fluorgehalten bodenbildender Gesteine der Schweiz. *Umwelt Materialen 32, Bundesamt für Umwelt, Wald and Lanschaft, Bern, Switzerland.* 1995.

[48] Keller, T.; Desaules, A., Böden der Schweiz: Schadstoffgehalte und Orientierungswerte. *Umwelt Materialen 139, Bundesamt für Umwelt, Wald and Lanschaft, Bern, Switzerland.* 2001.

[49] Dubois, J.-P.; Benitez, N.; Liebig, T.; Baudraz, M.; Okopnik, F., Le cadmium dans les sols du Haut Jura Suisse. In *Les Eléments Traces Métalliques dans les Sols: Approches Fonctionnelles et Spatialles*, Baize, D.; Tercé, M., Eds. 2002.

[50] Rambeau, C., Cadmium anomalies in Jurassic carbonates (Bajocian, Oxfordian) in western and southern Europe. 2006, Ph.D. Thesis, University of Neuchâtel, Switzerland, 261 pp.

[51] Wenk, P.; Bono, R.; Dubois, J. P.; Grenolet, F., Cadmium in Böden und Getreide im Gebiet Blauen/Neuzlingen, Basel-Landschaft. *Mitteilungen Gebiete Lebensmittel Hygiene* 1997, 88, 570-592.

[52] Barnhisel, R. I.; Bertsch, P. M., Chlorites and hydroxy-interlayered vermiculite and smectite. In *Minerals in Soil Environments*, Dixon, J. B.; Weed, S. B., Eds. Soil Science Society of America: Madison, 1989.

[53] Douglas, L. A., Vermiculites. In *Minerals in Soil Environments*, Dixon, J. B.; Weed, S. B., Eds. Soil science society of America: Madison, 1989; pp 635-728.

[54] Manceau, A.; Calas, G., Nickel-bearing clay-minerals. 2. Intracrystalline distribution of nickel - an X-ray absorption study. *Clay Miner.* 1986, 21, 341-360.

[55] Schlegel, M. L.; Manceau, A., Zn incorporation in hydroxy-Al- and Keggin Al-13-intercalated montmorillonite: A powder and polarized EXAFS study.

Environ. Sci. Technol. 2007, 41, 1942-1948.

[56] Manceau, A.; Lanson, B.; Drits, V. A., Structure of heavy metal sorbed birnessite. Part III: Results from powder and polarized extended X-ray absorption fine structure spectroscopy. *Geochim. Cosmochim. Acta* 2002, 66, 2639-2663.

[57] Efimenko, N.; Matera, V.; Adatte, T.; Föllmi, K., Cadmium anomalies in Jurassic carbonates in western and southern Europe: towards the causes and mechanisms. *Geophys. Res. Abstr.* 2008, 10, A-09829.

[58] Jeans, C. V.; Wray, D. S.; Merriman, R. J.; Fisher, M. J., Volcanogenic clays in Jurassic and Cretaceous strata of England and the North Sea basin. *Clay Miner.* 2000, 35, 25-55.

[59] Pankhurst, R. J.; Riley, T. R.; Fanning, C. M.; Kelley, S. P., Episodic silicic volcanism in Patagonia and the Antartic peninsula: chronology of magmatism associated with the break-up of Gondwana. *J. Petrol.* 2000, 41, 605-625.

[60] Wetzel, A.; Allenbach, R.; Allia, V., Reactivated basement structures affecting the sedimentary facies in a tectonically ‘‘quiescent’’ epicontinental basin: an example from NW Switzerland. *Sedim. Geol.* 2003, 157, 153-172.

[61] Schwinn, G.; Wagner, T.; Baatartsogt, B.; Markl, G., Quantification of mixing processes in ore-forming hydrothermal systems by combination of stable isotope and fluid inclusion analyses. *Geochim. Cosmochim. Acta* 2006, 70, 965-982.

[62] von Gehlen, K., Formation of Pb-Zn-F-Ba mineralizations in SW Germany: a status report. *Fortschr. Mineral.* 1987, 65, 87-113.

[63] Manceau, A.; Schlegel, M. L.; Musso, M.; Sole, V. A.; Gauthier, C.; Petit, P. E.; Trolard, F., Crystal chemistry of trace elements in natural and synthetic goethite. *Geochim. Cosmochim. Acta* 2000, 64, 3643-3661.

[64] Pochon, M., Origine et évolution des sols du Haut-Jura suisse : phénomènes d’altération des roches calcaires sous climat tempéré humide. *Denk. Schw. Naturfor. Ges.* 1978, 90, 1-190.

[65] Ildefonse, P.; Manceau, A.; Prost, D.; Groke, M. C. T., Hydroxy-Cu-vermiculite formed by the weathering of Fe-biotites at Salobo, Carajas, Brazil. *Clays Clay Miner.* 1986, 34, 338-345.

[66] Voegelin, A.; Kretzschmar, R., Formation and dissolution of single and mixed Zn and Ni precipitates in soil: Evidence from column experiments and extended X-ray absorption fine structure spectroscopy. *Environ. Sci. Technol.* 2005, 39, 5311-5318.

[67] Voegelin, A.; Scheinost, A. C.; Bühlmann, K.; Barmettler, K.; Kretzschmar, R., Slow formation and dissolution of Zn precipitates in soil - A combined column-transport and XAFS study. *Environ. Sci. Technol.* 2002, 36, 3749-3754.

6. Conclusions

This work focused on the fate of Zn in contaminated and in naturally Zn-rich soils. The aim of this thesis project was (i) to identify the dominant Zn bearing phases as a function of Zn concentration level and soil properties, (ii) to examine the relations between Zn speciation and Zn fractionation in soils contaminated by aqueous Zn from the corrosion of galvanized power line towers and (iii) to understand possible changes in the reactivity of Zn bearing phases through weathering and pedogenesis in naturally Zn-rich soils.

Analysis of 49 contaminated soils by bulk EXAFS spectroscopy indicated that Zn-hydroxy-interlayered minerals (Zn-HIM), Zn-phyllosilicates, Zn-layered double hydroxides (Zn-LDH) and hydrozincite were quantitatively important Zn-bearing phases. Their occurrence was strongly linked to three soil characteristics: soil pH, amount of available sorption sites (i.e., potentical cation exchange capacity (PCEC), calculated from clay and organic carbon content) and total Zn content. The good agreement between sequential extraction data and Zn speciation confirmed that soil pH and the Zn-loading of available sorption sites (i.e., ratio of total Zn in charge equivalent over PCEC) are dominant factors controlling Zn fractionation and demonstrated that Zn fractionation depends on Zn speciation.

In soils with low to intermediate Zn contamination level (i.e., less than ~2000 mg/kg Zn), incorporation of Zn into hydroxy-interlayered minerals has been identified as a major sequestration mechanism. Although the extent of Zn retention increased with soil pH, the amount of Zn in HIM was similar in acidic and neutral soils indicating a Zn loading of HIM close to its sorption capacity. Determination of the coordination environment of Zn in synthetic HIM indicated that with increasing Zn loading, the predominant Zn local coordination environment shifts from the dioctahedral vacancies of gibbsitic hydroxy-polymers to sites with decreasing Al coordination as well as to interlayer exchange sites, confirming the limited presence of high affinity sorption sites for Zn in HIM. The relatively low sorption capacity of HIM does not allow accumulating high levels of Zn in soils but the presence of HIM favors the long-term immobilization of Zn as shown by the resistance of synthetic Zn-HIM in sequential extraction experiments and by the presence of Zn-HIM in naturally enriched soils formed over more than 10’000 years. Hence, amending soil with synthetic HIM could be a possible

remediation strategy in soils being moderately contaminated by aqueous Zn inputs. For heavily contaminated soils, which have to be remediated (i.e., soils bearing more than 2000 mg/kg Zn according to Swiss regulations), this strategy is not suited since very large amounts of HIM would be needed.

In contrast to Zn-HIM, Zn-precipitates have been detected to contribute largely to Zn retention in intermediate to highly contaminated soils of acidic to alkaline pH value. The amount of soil-formed Zn precipitates was shown to increase with increasing soil pH and/or the saturation of sorption sites. The main Zn-precipitate identified was Zn-LDH. Zn-phyllosilicates occurred over a larger range in soil pH and Zn contamination level than Zn-LDH, but in general in lower fractions than either Zn-LDH (or Zn-HIM). Possible reasons for this discrepancy have been proposed and discussed in detail. At present, laboratory studies under controlled chemical conditions are necessary to evaluate the precipitation and transformation mechanisms of Zn-phyllosilicates and Zn-LDH in soils. The formation of hydrozincite may also represent a possible Zn retention pathway, but is limited to environments with extremely high Zn levels and relatively low Al and Si availability. In the sequential extraction experiments, synthetic hydrozincite, Zn-LDH and Zn-phyllosilicate readily dissolved, indicating that Zn bound in these phases is only conditionally immobilized. Monitoring and correcting changes in soil chemical conditions of contaminated soils is therefore a prerequisite to avoid enhanced Zn bioavailability or Zn transport to deeper soil horizons and groundwater following the dissolution of Zn-precipitates. Liming of soils might effectively immobilize Zn by promoting the formation or stabilization of Zn-bearing precipitates but would need to be continuously repeated to compensate for soil acidification processes.

In this study, continental soils contaminated by aqueous Zn from the corrosion of galvanized power lines towers were mainly investigated. Aqueous Zn is also released through the weathering or decomposition of Zn-bearing contaminants. Thus, similar trends in Zn speciation and Zn reactivity may be observed in soils from temperate regions contaminated from Zn in solid or complexed form. In order to complete our worldwide understanding of the relations between soil properties, Zn reactivity and Zn speciation, periodically anoxic soils or soils from boreal or tropical zones need to be investigated. The results from this study are also relevant for other elements such as Ni and Co, which partially exhibit similar geochemical behavior as Zn.

Acknowledgements

THANK YOU TO:

Alain Manceau | Alberte & Georgio | Amandine Courdouan | André Villard | Anke Hofacker | Beate Fulda | Benoît Valley | Calvin & Hobbes | Charlotte Ganter | Charlotte Wüstholz | Christian Bitterli | Christian Mikutta | Claire Rambeau | Claude & Ilham | Corin Studerus | Dipanjan Banerjee | Evert Elzinga | Fabrice Zingg | Farid Juillot | Federica Tamburini | Felix Maurer | Frangine & Doudou | Frank-Andreas Weber | Gerome Tokpa | Guillaume Morin | Iso Christl | Jakob Frommer*** | Jen-How Huang | Jan Wiederhold | Jérôme Spring | Jessica Dittmar | Jon Chorover | Josef Gilli | Kurt Barmettler | Laurie Pesch | Léo & Yann | Léonard Luzieux | Maki Rüegger | Natalia Efimenko | Naraya Carrasco | Maarten Nachtegaal | Marc Schumacher | Martine Docourt | Michael Plötze | Michel Schlegel | Mirjam Kiczka | Orio Okuma | Mam's & Pap's | Paul Borer | Pauline Rais | Petra Reichard | Raoul Quezada | Sabina Pfister | Sarah Hayes | Sof & Pol & Paco | Stefan Egli | Stéphane Affolter | Tomaso Bontognali | Ubald Gasser | Virginie Matera | Yves Brechbühl

...WITH A SPECIAL THANK TO:

Andreas Voegelin and Ruben Kretzschmar for their continuous help and support during the whole PhD.

...AND A VERY SPECIAL THANK TO:

Lou & Marie.

Curriculum vitae

Surname	Jacquat
Given name	Olivier
Date of birth	16.08.1979
Place of birth	La Chaux-de-Fonds, Switzerland
Citizenship	Swiss

School Education

1985-1991	Ecole primaire, Porrentruy, JU
1991-1995	Ecole secondaire, Porrentruy, JU
1995-1998	Gymnase cantonal, Maturité type C (scientifique), Porrentruy, JU

Higher Education

1998-2003	Studies of Earth Sciences Master of Science, mention very good and german distinction Institute of Geology, University of Neuchâtel, Switzerland
2003-2008	Ph.D. studies and work as research and teaching assistant Soil Chemistry Group, ETH Zurich, Switzerland

Occupation

1998-2002	Geologist Paleontology Section of Canton Jura, Porrentruy, Switzerland
2004-2007	Informatics Administrator Soil Chemistry Group, ETH Zurich, Switzerland

Appendix 1

Supporting information to chapter 2

Contents

A1.1. Analysis of EXAFS reference spectra by shell fitting

The EXAFS spectra of the most suitable Zn reference species identified by PCA and TT were analyzed by shell-fitting. Theoretical EXAFS paths were calculated using FEFF 8.2 [1, 2]. Structural models were obtained from the structures of hydrozincite [3], hydrotalcite [4] for Zn-LDH, talc [5] for ZnMg-kerolite references, hopeite [6] for Zn-phytate, franklinite [7] for Zn-sorbed ferrihydrite, and calcite [8] for Zn-sorbed calcite by substituting Zn in the structure where necessary. Path parameters were optimized by minimizing the normalized sum of squared residuals (NSSR = $(\Sigma_i(k^3\chi_{exp}-k^3\chi_{fit})^2)/\Sigma_i(k^3\chi_{exp}{}^2)$) of the fits. Fourier-transformed EXAFS spectra were calculated over the k-range 2-10 Å^{-1} using a Kaiser-Bessel apodization window (window parameter = 2.5). Fits were performed on the Fourier-transformed EXAFS spectra over the *r*-range 1.0-3.4 Å, except for aqueous Zn (1.0-2.1 Å), hydrozincite (1.0-3.7 Å), $Zn_{0.34}Mg_{0.66}$-kerolite (1.0-3.3 Å) and Zn sorbed to calcite (1.0-4.0 Å). The amplitude reduction factor $S_0{}^2$ was fixed at 0.85 [9, 10] and the energy shift ΔE_0 was constrained to be the same for all shells within an individual fit.

The Fourier-transformed spectra and shell-fits are presented in Figure A1.1 and fitting parameters are listed in Table A1.1. In Zn-LDH, all Zn-kerolite samples, and aqueous Zn, Zn is sixfold coordinated with O at an average Zn-O distance of 2.07 Å. In Zn-LDH, Zn is present in trioctahedral sheets and is surrounded by Zn and Al atoms at ~3.12 Å in the second shell. The Zn/Al ratio obtained from the shell fit is affected by the destructive interference of the backscattering waves from scattered Zn and Al atoms, similar as reported for Co- or Ni-LDH [11]. In the Zn-kerolite references, Zn is also located in octahedral sheets (O). In contrast to Zn-LDH, however, these sheets are linked to tetrahedral silicate sheets (T) in a T-O-T arrangement, giving rise to a signal from Si in the second shell [12]. Because of the destructive interference between the Zn-Si and the Zn-Mg signals at shorter distance and the simultaneous destructive interference between light and heavy atoms in the octahedral sheet (as in Zn-LDH), considerable uncertainties are associated with the coordination numbers of second shell Mg, Zn and Si obtained from EXAFS fits [13]. As a consequence of these interferences, the fitted coordination number of second-neighbor Si gradually decreases from the pure Zn-kerolite to the reference with highest Mg content ($Zn_{0.34}Mg_{0.66}$-kerolite) and the coordination number of second shell Mg is underestimated in kerolite references with lower Zn contents ($Zn_{0.6}Mg_{0.4}$-kerolite or $Zn_{0.34}Mg_{0.66}$-kerolite). In k-space, the EXAFS spectra of the Zn-kerolite references exhibit systematic spectral shifts with changes in the amount of light (Mg) and heavy (Zn) atoms in the octahedral sheets (Fig. 2.1). A peak doublet at 3.5 to 4.0 Å^{-1} increases in intensity, as the content of light atoms in the

octahedral sheet increases [12]. It is most prominent in Zn-HIM and Zn-lithiophorite, where Zn in gibbsitic sheets is surrounded by 6 Al atoms (Fig. 2.1) [14, 15]. The upward oscillation around 5 $Å^{-1}$ is specific for Zn-rich phyllosilicates (Fig. 2.1) and originates from backscattering Si cations in the tetrahedral sheets [16]. The peak declines when the content of light atoms in the octahedral sheet increases (Fig. 2.1), as previously reported [16, 17]. In Zn-LDH with a Zn/Al ratio of 2 in the octahedral sheets, but no tetrahedral silicate sheet, a shoulder is observed at around 5 $Å^{-1}$ instead of the well-resolved peak of Zn-rich kerolite phases (Fig 2.1). Another spectral feature allowing distinguishing Zn-rich kerolite from Zn-LDH is found in the k-range 7.5-8.5 $Å^{-1}$ [10, 11]. In Zn-LDH, the presence of Al in the octahedral sheets causes the oscillation to peak at around 8 $Å^{-1}$. The presence of one or two tetrahedral silicate sheets attached to the octahedral sheet, on the other hand, leads to an enhanced upward oscillation at around 8.5 $Å^{-1}$. In *r*-space, the backscattering of the next-nearest Si shell at ~4.5 Å and higher oxygen shells of Zn-phyllosilicates results in a FT peak between 3.4 and 4.3 Å [16, 18], which is absent in the FT of the Zn-LDH spectrum [19, 20] (Fig. A1.1). Thus, Zn-kerolite references with variable Zn/Mg content and Zn-LDH show characteristic spectral features allowing for their distinction in sample spectra.

While the spectrum of aqueous Zn is dominated by the spectral contribution arising from sixfold coordination to O at an average distance of around 2.07 Å, the fitted Zn-O distances and coordination numbers for Zn adsorbed to calcite, Zn adsorbed to ferrihydrite and Zn complexed by phytate reveal that Zn in these references is tetrahedrally coordinated with O at a distance of 1.95-1.97 Å. The 3 references differ in their second shell signal, which is dominated by the contributions from the sorbing/complexing phase. The fit parameters for Zn-sorbed calcite are similar to the values published by Elzinga and Reeder [21]. The fit results indicate that the tetrahedral Zn is adsorbed as an inner-sphere sorption complex on the calcite surface [21]. The second shell of Zn-sorbed ferrihydrite was well reproduced with about 1 Zn atom at 3.22 Å and about 2 Fe atoms at 3.44 Å. Considering the Zn/(Zn+Fe) ratio of 0.04 in this sample, this fit is in agreement with results of Waychunas and coworkers [22]. From EXAFS spectra measured at different surface loadings, they concluded that tetrahedral Zn forms a bidentate edge-sharing complex on ferrihydrite, at a Zn/(Zn+Fe) ratio of less than 0.2, whereas at higher Zn/(Zn+Fe) ratio octahedral Zn polymeric species form. The second shell of Zn complexed by phytate could be well described by P at distances of 3.10 Å and 3.48 Å, in agreement with a previous study [23]. Hydrozincite ($Zn_5(CO_3)_2(OH)_6$) is a layered Zn hydroxycarbonate mineral containing Zn in octahedral and tetrahedral coordination in a 3:2 ratio [3]. The EXAFS spectrum is therefore an average of the contributions from the different Zn sites, as reflected by the fitted first-shell Zn-O

coordination number and distance, which are intermediate between tetrahedral and octahedral coordination. The second shell was best fitted with two Zn subshells at 3.14 and 3.56 Å, in agreement with previous work [24].

Table A1.1. Structural characterization of Zn in reference compounds by shell fitting in *r*-space using theoretical paths. Fits are shown in Figure A1.1.

Samples[a]	Zn-O shell			Zn-X shell				Zn-Y shell					
	R_{Zn-O}[b]	CN[c]	σ^2 (Å^2)[d]	X	R_{Zn-X}[b]	CN[c]	σ^2 (Å^2)[d]	Y	R_{Zn-Y}[b]	CN[c]	σ^2 (Å^2)[d]	ΔE_0 (eV)[e]	NSSR (%)[f]
Zn-LDH	2.07	5.0	0.009	Zn	[h]3.12	3.9	[g]0.010	Al	[h]3.12	1.3	[g]0.010	4.0	0. 9
Zn-kerolite	2.07	5.4	0.009	Zn	3.11	5.9	[g]0.010	Si	3.30	4.7	[g]0.012	6.7	0. 4
$Zn_{0.8}Mg_{0.2}$-kerolite	2.07	5.9	0.009	Zn	3.10	4. 7	[g]0.009	Si	3.33	3.5	[g]0.010	5.8	0. 5
$Zn_{0.6}Mg_{0.4}$-kerolite	2.07	6.1	0.009	Zn	[h]3.10	2.8	[g]0.009	Si	3.32	2.8	[g]0.011	5.9	1.0
				Mg	[h]3.10	[i]1.9	[g]0.009						
$Zn_{0.34}Mg_{0.66}$-kerolite	2.07	6.3	0.010	Mg	3.07	3.8	[g]0.009	Si	3.30	2.5	[g]0.009	5.9	1.5
aqueous Zn	2.07	6.0	0.008	-	-	-	-	-	-	-	-	3.7	1.0
hydrozincite	2.01	4.9	0.011	Zn	3.14	2.6	[g]0.014	Zn	3.56	1.1	[g]0.008	5.3	1.5
Zn-sorbed Cc	1.97	4.4	0.007	C	2.86	2.8	[g]0.010	O	3.12	1.0	[g]0.010	5.4	0. 4
								Ca	3.38	1.2	[g]0.010		
Zn-sorbed Fh	1.97	4.3	0.007	Zn	3.22	0.9	[g]0.009	Fe	3.44	2.4	[g]0.011	4.5	0. 7
Zn-phytate	1.95	3.8	0.007	P	3.10	1.2	[g]0.009	P	3.48	2.7	[g]0.011	9.5	0. 8

[a]Fits were performed over the *r*-range 1.0-3.4 Å, except for aqueous Zn (1.0-2.1), hydrozincite (1.0-3.7), $Zn_{0.34}Mg_{0.66}$-kerolite (1.0-3.3), Zn-sorbed calcite (1.0-4.0), Zn-sorbed ferrihydrite, and Zn-phytate (1.0-3.8). [b]Radial distance; uncertainties are ~ 0.01 Å for Zn-O and 0.01-0.05 for Zn-X/Y shells. [c]Coordination numbers; uncertainties are 0.3-1.0 for Zn-O and 0.4-1.7 for Zn-X/Y shells. [d]Debye Waller parameters; uncertainties are 0.0007-0.0022 Å^2 for Zn-O. [e]Energy shift, constrained to be the same for all shells in a fit, uncertainties are 0.6-1.8 eV. [f]Normalized sum of the squared residuals ($NSSR=\Sigma(data_i\text{-}fit_i)^2/\Sigma data_i^2$). [g]Fixed during shell fits. [h]Constrained to be equal within the fit. [i]CN of Mg fixed to 2/3 of CN of Zn.

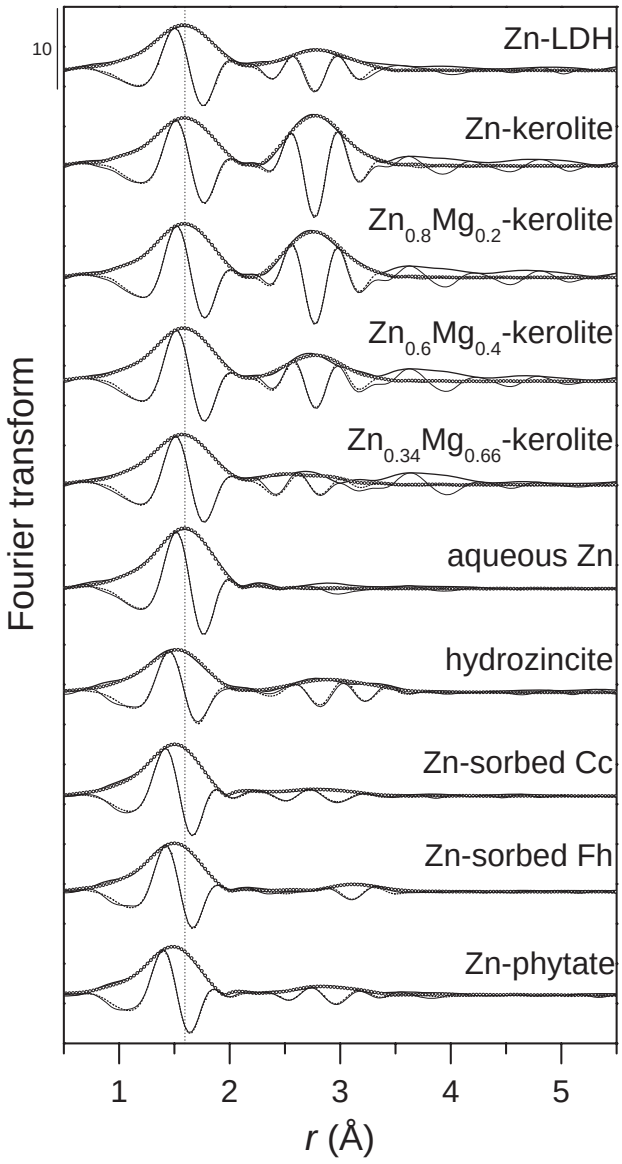

Figure A1.1. Fourier transform magnitudes and imaginary parts (solid lines) of reference samples and corresponding shell fits (dots). Parameters of the shell fits are reported in Table A1.1.

A1.2. Fourier-transformed μ-EXAFS spectra of LUC2-4 and LUC2-8

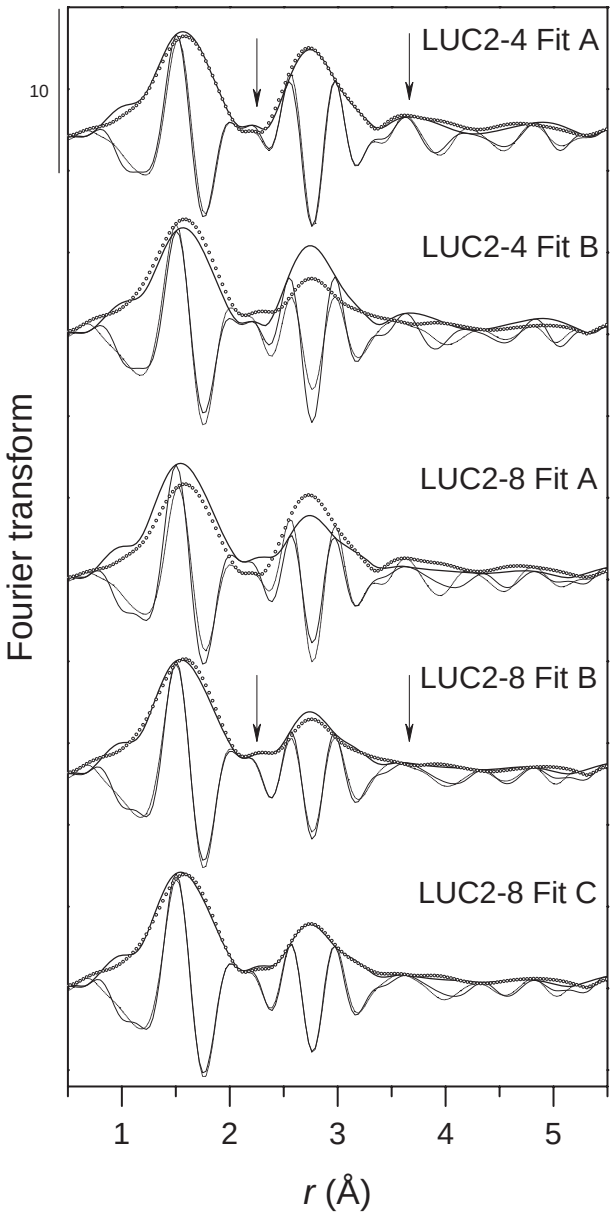

Figure A1.2. Amplitude and imaginary part of the Fourier-transformed μ-EXAFS spectra of LUC2-4 and LUC2-8 (solid lines) and comparison with Fourier-transformed LCF spectra (dots). LCF results are provided in Table 2.5. The spectrum LUC2-4 exhibits a peak in the region 3.4-4.3 Å due to backscattering from next nearest Si and more distant O in phyllosilicates [17, 18]. This peak is absent in the Zn-LDH spectrum [19, 20] (Fig. A1.1), which allows for the distinction between Zn-kerolite and Zn-LDH in experimental spectra.

A1.3. LCF of bulk EXAFS spectra of soils GLO, LUC2, BAS and LAUS

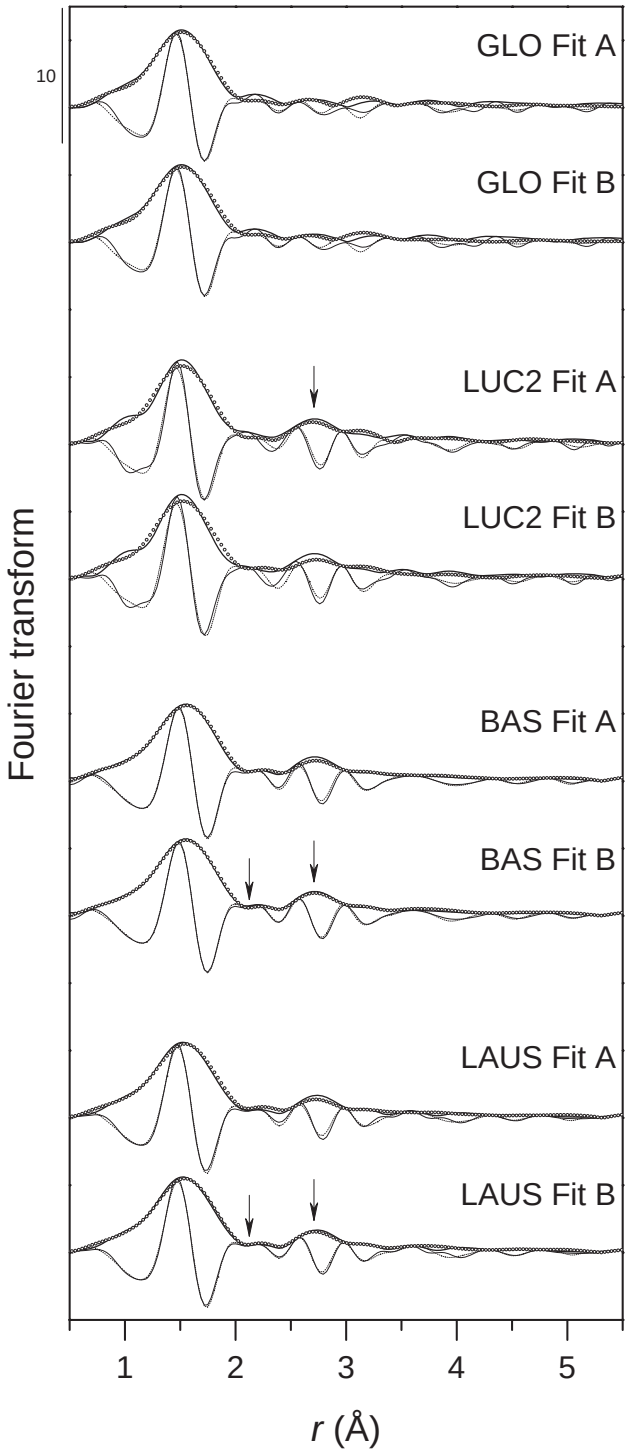

Figure A1.3. Amplitude and imaginary part of the Fourier-transformed bulk EXAFS spectra of the soils GLO, LUC2, BAS and LAUS and comparison with Fourier-transformed LCF spectra (dots). GLO: Fit A with $Zn_{0.6}Mg_{0.4}$-kerolite and Fit B with Zn-LDH. LUC2: Fit A with $Zn_{0.8}Mg_{0.2}$-kerolite and Fit B with Zn-LDH. BAS and LAUS: Fit A with only Zn-LDH and Fit B with Zn-LDH and $Zn_{0.8}Mg_{0.2}$-kerolite (LCF results in Table A1.2).

Table A1.2. Linear combination fits of the bulk EXAFS spectra of soils GLO, LUC2, BAS and LAUS using either Zn-LDH and/or Zn-kerolite.

Spectrum	Zn-LDH (%)	Zn-kerolite[a] (%)	sorbed ^{IV}Zn[b] (%)	aqueous Zn (%)	Sum (%)	NSSR (%)
GLO Fit A	———	17 (60Zn)	54 (Fh)	29	100	4.90
GLO Fit B	20	———	50 (Fh)	31	101	5.02
LUC2 Fit A	———	29 (80Zn)	56 (Fh)	21	106	4.89
LUC2 Fit B	57	———	45 (Fh)	10	112	5.03
BAS Fit A	62	———	22 (Cc)	19	103	1.12
BAS Fit B	40	13 (80Zn)	26 (Cc)	22	101	0.81
LAUS Fit A	58	———	31 (Cc)	14	103	1.62
LAUS Fit B	36	13 (80Zn)	34 (Cc)	17	100	1.29

[a](80Zn): $Zn_{0.8}Mg_{0.2}$-kerolite, (60Zn): $Zn_{0.6}Mg_{0.4}$-kerolite, [b](Cc): Zn-sorbed calcite, (Fh): Zn-sorbed ferrihydrite.

Different LCF of the bulk EXAFS spectra of soils GLO, LUC2, BAS, and LAUS are listed in Table A1.2 and shown in Figure A1.3. For the soil GLO, LCF using either $Zn_{0.6}Mg_{0.4}$-kerolite or Zn-LDH as a proxy for precipitated Zn were of nearly identical quality and returned a similar precipitate fraction. Since only Zn-LDH was detected in the thin section (GLO-5, Table 2.4) and on limestone particles (GLO-WP, Table 2.7), we reported Fit B based on Zn-LDH in Table 2.8. For soil LUC2, LCF with nearly identical NSSR were obtained with either $Zn_{0.8}Mg_{0.2}$-kerolite or Zn-LDH as proxy for precipitated Zn. However, the fit based on $Zn_{0.8}Mg_{0.2}$-kerolite better matched the experimental data in the regions of the second shell (2-3 Å) and of backscattering from next-nearest Si in Zn-kerolites (3-4 Å, Fig. A1.3). Pure $Zn_{0.8}Mg_{0.2}$-kerolite was identified in a soil thin section (LUC2-4, Table 2.5), and also the LCF for limestone particles from soil LUC2 contained $Zn_{0.8}Mg_{0.2}$-kerolite (LUC2-WP, Table 2.7). Fit A was therefore reported for LUC2 in Table 2.8. For the soils BAS and LAUS, LCF based on Zn-LDH were significantly better (based on visual inspection and NSSR) than fits based on any of the ZnMg-kerolite references. However, adding $Zn_{0.8}Mg_{0.2}$-kerolite to fits based on Zn-LDH further reduced the NSSR and led to visual improvements in the LCF in the region of the second shell (Fig. A1.3). Fits B from Table A1.2 are therefore reported for BAS and LAUS in Table 2.8.

A1.4. Light microscope images of limestone particles from soil SIS

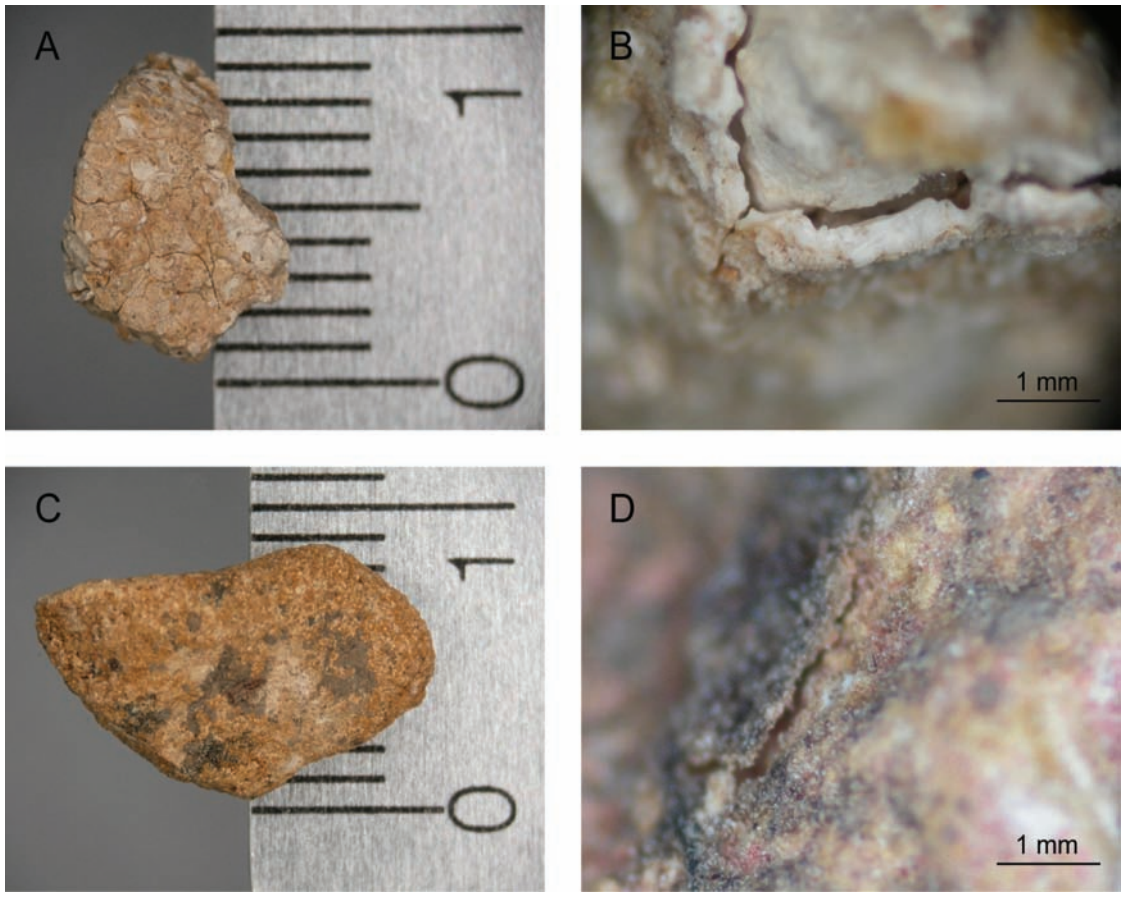

Figure A1.4. Light microscope images of a white (A, B) and a red limestone particle (C, D) from soil SIS. The scale in the panels A and C represents 1 cm.

A1.5. XRD patterns of crusts of white limestone particles from soils SIS, LAUS and BAS

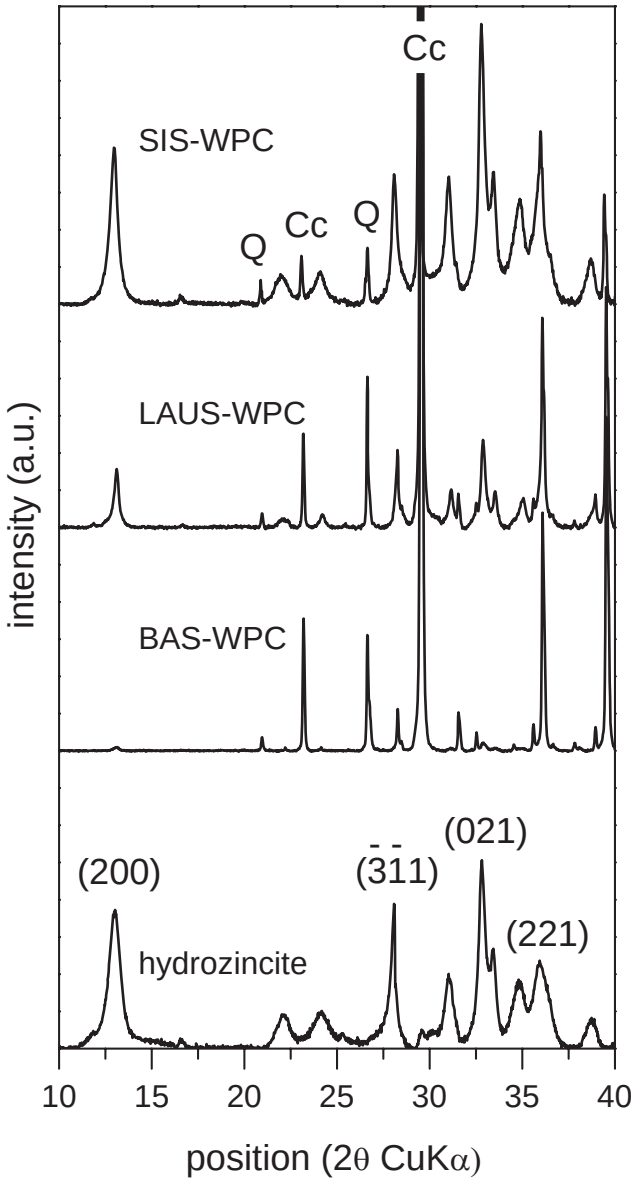

Figure A1.5. X-ray diffraction patterns of the crusts from limestone particles from the soils SIS, LAUS and BAS and of hydrozincite (Cc: calcite, Q: quartz).

A1.6. Sequential soil extraction results for Zn, Fe and Mn

The amounts of Zn, Fe and Mn sequentially extracted from soils GLO, LUC2, BAS, LAUS, TAL and SIS, using the procedure of Zeien and Brümmer [25] are provided in Table A1.3. The extractions were carried out in duplicates. Relative standard deviations for relative fractions were lower than 10%. Extracts F1 to F6 were measured using ICP-OES and the residual fraction F7 was measured by XRF (further details on the sequential extraction are provided in the Materials and Methods section and in Voegelin et al. [26]). On average, the sum of extracted Zn deviated by 12% from the total Zn content determined by XRF. The larger deviations of 15-19% observed for soils GLO, LAUS, and TAL may be due to analytical errors (either of the analysis of the extractions or the XRF measurements) or due to sample heterogeneity.

From all soils, only minor fractions of total Fe were extracted in the fractions F1 to F4. About half of the total Fe was extracted in fractions F5 and F6 designed for the removal of amorphous and crystalline Fe-(hydr)oxides, the other half being retained in the residual fraction. Substantial percentages of total Mn were extracted in the fraction 3 intended to remove reducible Mn contained in Mn(hydr)-oxides. In contrast to Fe and Mn, substantial fractions of soil Zn (29% in GLO, 59-83% in other soils) were extracted in the first two fractions considered to remove mobile and mobilisable Zn, respectively [26].

Table A1.3. Amounts of Zn, Fe and Mn (in mg/kg) extracted using the sequential extraction procedure of Zeien and Brümmer [25].

Samples	F1	F2	F3	F4	F5	F6	F7[a]	Sum F1-F7[a]	Total Zn[b]
Zn	(mg/kg)								
GLO	49	395	225	338	284	84	144	1519	1322
LUC2	52	843	53	55	59	42	185	1287	1398
BAS	1413	5683	916	2371	1135	148	169	11836	12170
LAUS	1888	7745	1797	3323	981	171	211	16115	13810
TAL	1480	5467	385	337	320	203	195	8386	7040
SIS	2150	13680	3602	6011	1153	313	251	27160	30090
Fe	(mg/kg)								
GLO	0.1	0.0	14	980	3961	13713	21770	40437	35820
LUC2	0.8	21	60	359	18032	2468	3610	8322	11250
BAS	0.2	0.9	15	850	5773	8868	18150	33656	29630
LAUS	0.0	0.6	23	1342	6367	22710	17860	48302	38300
TAL	0.8	3.6	75	331	425	8988	10700	20523	15950
SIS	1.6	5.5	17	998	1986	13182	13830	30020	29150
Mn	(mg/kg)								
GLO	50	121	710	96	82	59	148	1265	1048
LUC2	1.3	101	310	24.	38	6.2	84	564	688
BAS	38	54	189	36	107	32	109	564	562
LAUS	33	97	648	59	138	67	120	1161	891
TAL	9.1	53	42	49	6.7	9.7	105	274	253
SIS	60	116	227	33	34	32	140	642	623

[a]Sum of element content extracted in fractions F1 to F7. [b]Measured by XRF.

References

[1] Ankudinov, A. L.; Ravel, B.; Rehr, J. J.; Conradson, S. D., Real-space multiple-scattering calculation and interpretation of x-ray-absorption near-edge structure. *Phys. Rev. B* 1998, 58, 7565-7576.

[2] Rehr, J. J.; Albers, R. C., Theoretical approaches to x-ray absorption fine structure. *Rev. Mod. Phys.* 2000, 72, 621-653.

[3] Ghose, S., Crystal structure of hydrozincite $Zn_5(OH)_6(CO_3)_2$. *Acta Crystallogr.* 1964, 17, 1051-1057.

[4] Allmann, R.; Jepsen, H. P., Die Struktur des Hydrotalkits. *Neues Jahrbuch für Mineralogie Monatshefte* 1969, 544-551.

[5] Perdikatsis, B.; Burzlaff, H., Structural refinement of talc $Mg_3[(OH)_2Si_4O_{10}]$. *Z. Kristallogr.* 1981, 156, 177-186.

[6] Hill, R. J.; Jones, J. B., Crystal structure of hopeite. *Am. Mineral.* 1976, 61, 987-995.

[7] Lucchesi, S.; Russo, U.; Della Giusta, A., Cation distribution in natural Zn-spinels: Franklinite. *Eur. J. Mineral.* 1999, 11, 501-511.

[8] Graf, D. L., Crystallographic tables for the rhombohedral carbonates. *Am. Mineral.* 1961, 46, 1283-1316.

[9] O'Day, P.; Rehr, J. J.; Zabinsky, S. I.; Brown, G. E. J., Extended X-ray absorption fine structure (EXAFS) analysis of disorder and multiple-scattering in complex crystalline solids. *J. Am. Chem. Soc.* 1994, 116, 2938-2949.

[10] Voegelin, A.; Kretzschmar, R., Formation and dissolution of single and mixed Zn and Ni precipitates in soil: Evidence from column experiments and extended X-ray absorption fine structure spectroscopy. *Environ. Sci. Technol.* 2005, 39, 5311-5318.

[11] Scheinost, A. C.; Sparks, D. L., Formation of layered single- and double-metal hydroxide precipitates at the mineral/water interface: A multiple-scattering XAFS analysis. *J. Colloid Interface Sci.* 2000, 223, 167-178.

[12] Schlegel, M. L.; Manceau, A.; Charlet, L.; Hazemann, J. L., Adsorption mechanisms of Zn on hectorite as a function of time, pH, and ionic strength. *Am. J. Sci.* 2001, 301, 798-830.

[13] Manceau, A.; Calas, G., Nickel-bearing clay-minerals. 2.Intracrystalline distribution of nickel - an X-ray absorption study. *Clay Miner.* 1986, 21, 341-360.

[14] Manceau, A.; Marcus, M. A.; Tamura, N.; Proux, O.; Geoffroy, N.; Lanson, B., Natural speciation of Zn at the micrometer scale in a clayey soil using X-ray fluorescence, absorption, and diffraction. *Geochim. Cosmochim. Acta* 2004, 68, 2467-2483.

[15] Scheinost, A. C.; Kretzschmar, R.; Pfister, S.; Roberts, D. R., Combining selective sequential extractions, X-ray absorption spectroscopy, and principal component analysis for quantitative zinc speciation in soil. *Environ. Sci. Technol.* 2002, 36, 5021-5028.

[16] Schlegel, M. L.; Manceau, A.; Charlet, L.; Chateigner, D.; Hazemann, J.-L., Sorption of metal ions on clay minerals III. Nucleation and epitaxial growth of Zn phyllosilicate on the edges of hectorite. *Geochim. Cosmochim. Acta* 2001, 65, 4155-4170.

[17] Schlegel, M. L.; Manceau, A., Evidence for the nucleation and epitaxial growth

of Zn phyllosilicate on montmorillonite. *Geochim. Cosmochim. Acta* 2006, 70, 901-917.

[18] Manceau, A.; Chateigner, D.; Gates, W. P., Polarized EXAFS, distance-valence least-squares modeling (DVLS), and quantitative texture analysis approaches to the structural refinement of Garfield nontronite. *Phys. Chem. Mater.* 1998, 25 (5), 347-365.

[19] Panfili, F. R.; Manceau, A.; Sarret, G.; Spadini, L.; Kirpichtchikova, T.; Bert, V.; Laboudigue, A.; Marcus, M. A.; Ahamdach, N.; Libert, M. F., The effect of phytostabilization on Zn speciation in a dredged contaminated sediment using scanning electron microscopy, X-ray fluorescence, EXAFS spectroscopy, and principal components analysis. *Geochim. Cosmochim. Acta* 2005, 69, 2265-2284.

[20] Voegelin, A.; Pfister, S.; Scheinost, A. C.; Marcus, M. A.; Kretzschmar, R., Changes in zinc speciation in field soil after contamination with zinc oxide. *Environ. Sci. Technol.* 2005, 39, 6616-6623.

[21] Elzinga, E. J.; Reeder, R. J., X-ray absorption spectroscopy study of Cu^{2+} and Zn^{2+} adsorption complexes at the calcite surface: Implications for site-specific metal incorporation preferences during calcite crystal growth. *Geochim. Cosmochim. Acta* 2002, 66, 3943-3954.

[22] Waychunas, G. A.; Fuller, C. C.; Davis, J. A., Surface complexation and precipitate geometry for aqueous Zn(II) sorption on ferrihydrite: I. X-ray absorption extended fine structure spectroscopy analysis. *Geochim. Cosmochim. Acta* 2002, 66, 1119-1137.

[23] Sarret, G.; Saumitou-Laprade, P.; Bert, V.; Proux, O.; Hazemann, J. L.; Traverse, A.; Marcus, M. A.; Manceau, A., Forms of zinc accumulated in the hyperaccumulator Arabidopsis halleri. *Plant Physiol.* 2002, 130, 1815-1826.

[24] Charnock, J. M.; Schofield, P. F.; Henderson, C. M. B.; Cressey, G.; Cressey, B. A., Cu and Zn ordering in aurichalcite. *Mineralo. Mag.* 1996, 60, 887-896.

[25] Zeien, H.; Brümmer, G. W., Chemische Extraktionen zur Bestimmung von Schwermetallbindungsformen in Böden. *Mitt. Dtsch. Bodenkundl. Ges.* 1989, 59, 505-510.

[26] Voegelin, A.; Tokpa, G.; Jacquat, O.; Barmettler, K.; Kretzschmar, R., Zinc fractionation in contaminated soils by sequential and single extractions: Influence of soil properties and zinc content. *J. Environ. Qual.* 2008, 37, 1190-1200.

Appendix 2

Supporting information to chapter 3

Contents

A2.1. Reference EXAFS spectra used in linear combination fits

In addition to the reference spectra of Zn-HIS, Zn-sorbed gibbsite, aqueous Zn, Zn-kaolinite, and Zn-lithiophorite shown in Figure 3.2, additional reference spectra were included in the analysis of soil EXAFS spectra by linear combination fitting (LCF). ZnMg-kerolite phases with high to intermediate Zn/Mg ratio (Zn/(Zn+Mg) = 0.8, 0.6, and 0.34) were synthesized as described elsewhere [1]. The EXAFS spectra are characterized by a peak doublet at 3.5 to 4.0 $Å^{-1}$ and an upward oscillation at ~5 $Å^{-1}$. With increasing Mg content in the octahedral sheets, the peak doublet at 3.5 to 4.0 $Å^{-1}$ becomes more pronounced, whereas the upward oscillation at ~5 $Å^{-1}$ decreases in intensity. In *r*-space, a higher Mg content results in a lower magnitude of the second shell. In Zn-sorbed goethite (2900 mg/kg Zn), Zn is predominantly octahedrally coordinated and forms an inner-sphere sorption complex [2]. Compared to the first-shell peaks of the Fourier-transformed spectra of the ZnMg-kerolite phases, aqueous Zn and Zn-sorbed goethite, the first shell peaks of Zn-phytate and low Zn-birnessite are located at lower distances, indicating the tetrahedral coordination of Zn. An EXAFS spectrum of Zn-phytate containing Zn coordinated to 4 phosphate groups has previously been used as a proxy for Zn bound to organic phosphate groups [3]. In low Zn-birnessite, Zn is also tetrahedally coordinated [4]. The synthesis of Zn-phytate and low Zn-birnessite has been described in an earlier study [1].

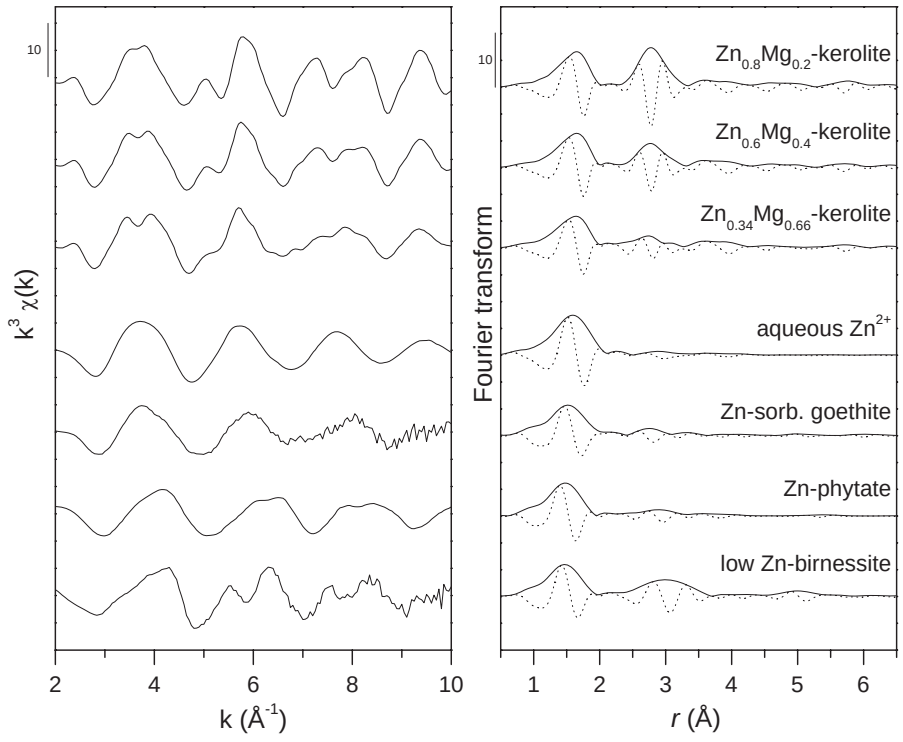

Figure A2.1. EXAFS spectra and Fourier transform of adsorbed/complexed Zn species used in addition to Zn-HIS-6.9-pH5 in the LCF analysis.

A2.2. LCF and shell-fits of reference EXAFS spectra shown in Figure 3.2

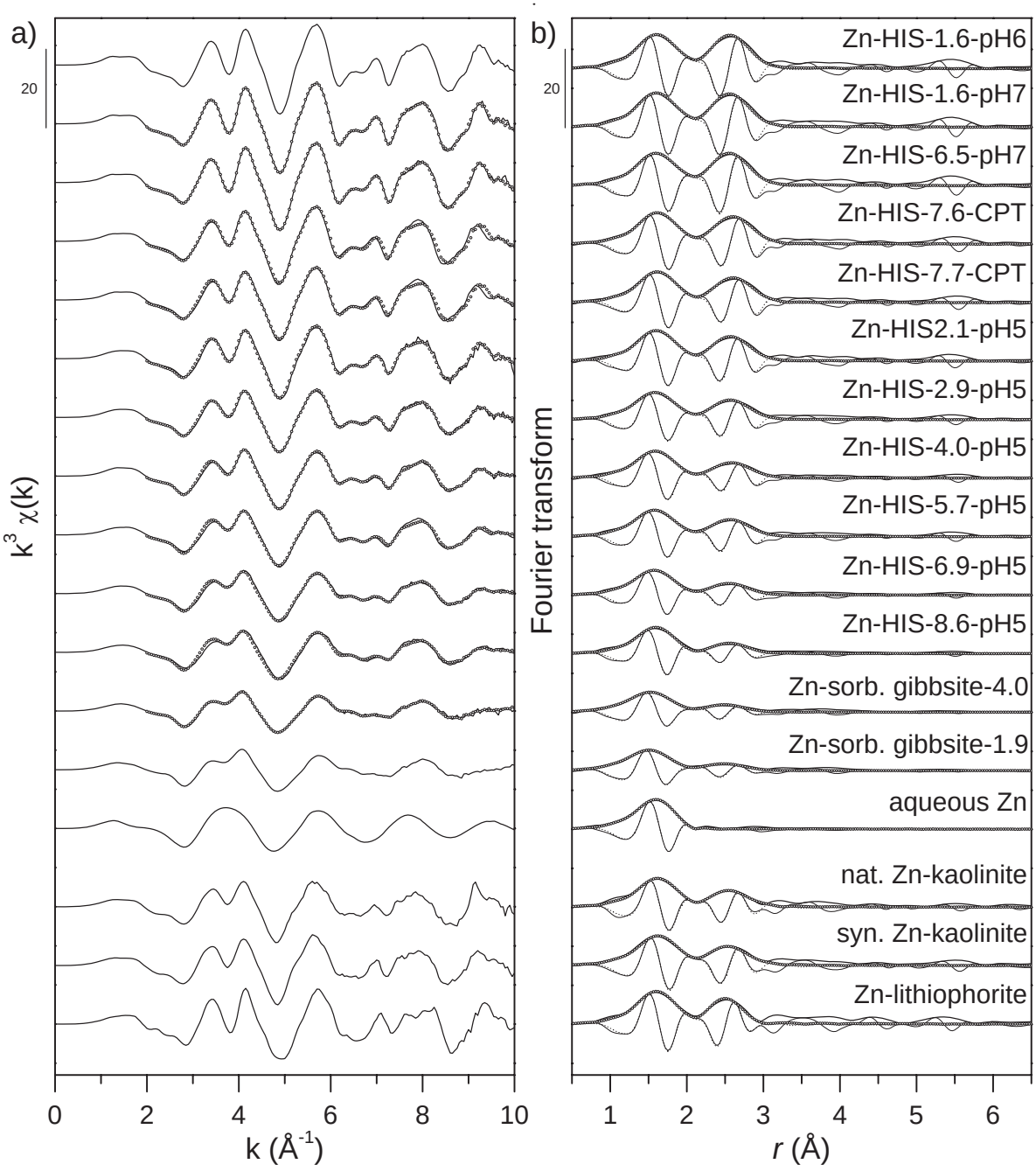

Fig. A2.2. EXAFS spectra (a) and Fourier transform magnitudes and imaginary parts (b) of Zn-HIS, Zn-sorbed gibbsite, Zn-kaolinite and Zn-lithiophorite including the LCF fits (a) to Zn-HIS references for which fit parameters are reported in Table 3.3 and the shell-fits (b) to all plotted references listed for which detailed fit parameters are provided in Table A2.1.

Table A2.1. Parameters (± uncertainties) obtained from shell-fits to the reference spectra shown in Figures 3.2 and A2.2. Fitted spectra are shown in Fig. A2.2.

Samples	Path	R_{Zn-O}	±	CN	±	σ^2 (Å^2)	±	ΔE_0 (eV)[a]	±	NSSR (%)[b]
Zn-HIS-1.6-pH6	Zn-O	2.08	0.01	6.9	1.4	0.008	0.003	7.4	1.9	0.9
	Zn-Al	3.04	0.02	6.6[c]	1.6	0.004[d]	0.004			
	Zn-O	3.28	0.05	6.6[c]	1.6	0.004[d]	0.004			
Zn-HIS-1.6-pH7	Zn-O	2.08	0.01	6.8	1.5	0.007	0.003	7.1	2.0	1.0
	Zn-Al	3.04	0.02	6.6[c]	1.7	0.004[d]	0.004			
	Zn-O	3.28	0.06	6.6[c]	1.7	0.004[d]	0.004			
Zn- HIS-6.5-pH7	Zn-O	2.08	0.01	6.8	1.4	0.008	0.003	6.9	0.1	0.9
	Zn-Al	3.03	0.01	6.7[c]	1.6	0.005[d]	0.004			
	Zn-O	3.28	0.04	6.7[c]	1.6	0.005[d]	0.004			
Zn-HIS-7.6-CPT	Zn-O	2.08	0.01	6.3	1.1	0.008	0.002	7.5	1.8	0.7
	Zn-Al	3.06	0.02	5.4[c]	1.6	0.005[d]	0.005			
	Zn-O	3.27	0.07	5.4[c]	1.6	0.005[d]	0.005			
Zn-HIS-7.7-CPT	Zn-O	2.08	0.01	6.1	1.1	0.008	0.002	7.9	1.8	0.8
	Zn-Al	3.06	0.02	4.7[c]	1.4	0.004[d]	0.005			
	Zn-O	3.28	0.07	4.7[c]	1.4	0.004[d]	0.005			
Zn-HIS-2.1-pH5	Zn-O	2.08	0.01	6.1	1.1	0.008	0.002	7.4	1.8	0.8
	Zn-Al	3.04	0.02	4.6[c]	1.2	0.004[d]	0.004			
	Zn-O	3.27	0.06	4.6[c]	1.2	0.004[d]	0.004			
Zn-HIS-2.9-pH5	Zn-O	2.07	0.01	6.3	1.2	0.010	0.002	6.9	1.9	0.9
	Zn-Al	3.04	0.02	3.9[c]	1.2	0.004[d]	0.005			
	Zn-O	3.28	0.06	3.9[c]	1.2	0.004[d]	0.005			
Zn-HIS-4.0-pH5	Zn-O	2.07	0.01	6.1	1.0	0.010	0.002	6.9	0.1	0.8
	Zn-Al	3.04	0.02	3.6[c]	1.1	0.005[d]	0.005			
	Zn-O	3.28	0.05	3.6[c]	1.1	0.005[d]	0.005			
Zn-HIS-5.7-pH5	Zn-O	2.07	0.01	5.8	0.9	0.009	0.002	7.2	1.7	0.7
	Zn-Al	3.05	0.02	3.1[c]	1.0	0.004[d]	0.005			
	Zn-O	3.27	0.07	3.1[c]	1.0	0.004[d]	0.005			
Zn-HIS-6.9-pH5	Zn-O	2.06	0.01	5.8	0.9	0.010	0.002	6.9	0.1	0.8
	Zn-Al	3.04	0.02	2.6[c]	0.9	0.005[d]	0.005			
	Zn-O	3.29	0.05	2.6[c]	0.9	0.005[d]	0.005			

[a]Energy shift; set equal for all shells in a fit. [b]Normalized sum of the squared residuals ($NSSR=\Sigma(data_i\text{-}fit_i)^2/\ \Sigma(data_i)^2$). [c,d]Set equal for Zn-Al and Zn-O/Si paths within individual fit. [e]CN of Zn-Si constrained to 1/3 of CN of Zn-Al during fit.

Table A2.1. continued.

Samples	Path	R_{Zn-O}	±	CN	±	σ^2 (Å^2)	±	ΔE_0 (eV)[a]	±	NSSR (%)[b]
Zn-HIS-8.6-pH5	Zn-O	2.06	0.01	5.3	0.9	0.008	0.002	8.0	1.8	1.0
	Zn-Al	3.04	0.02	2.1[c]	0.9	0.004[d]	0.006			
	Zn-O	3.30	0.07	2.1[c]	0.9	0.004[d]	0.006			
Zn-sorbed gibbsite-4.0	Zn-O	2.04	0.02	5.8	1.0	0.013	0.002	4.6	1.9	0.9
	Zn-Al	3.01	0.02	1.7[c]	0.8	0.005[d]	0.006			
	Zn-O	3.28	0.07	1.7[c]	0.8	0.005[d]	0.006			
Zn-sorbed gibbsite-1.9	Zn-O	2.03	0.02	5.8	1.0	0.012	0.002	3.6	2.1	0.9
	Zn-Al	3.01	0.03	1.7[c]	0.9	0.005[d]	0.008			
	Zn-O	3.26	0.08	1.7[c]	0.9	0.005[d]	0.008			
aqueous Zn	Zn-O	2.08	0.01	6.3	0.5	0.008	0.001	6.1	0.9	0.2
nat. Zn-kaolinite	Zn-O	2.09	0.02	5.9	1.3	0.008	0.002	7.1	2.5	1.1
	Zn-Al	3.05	0.03	4.3	2.1	0.004[d]	0.006			
	Zn-Si	3.16	0.16	1.4[e]	0.7	0.004[d]	0.006			
syn. Zn-kaolinite	Zn-O	2.10	0.02	6.5	1.3	0.008	0.002	7.2	2.2	1.1
	Zn-Al	3.05	0.02	6.9	2.4	0.009[d]	0.010			
	Zn-Si	3.13	0.23	2.3[e]	0.8	0.009[d]	0.010			
Zn-lithiophorite	Zn-O	2.07	0.02	6.3	1.5	0.007	0.002	7.3	2.4	0.7
	Zn-Al	2.99	0.03	4.5[c]	2.4	0.002	0.006			
	Zn-O	3.27	0.07	4.5[c]	2.4	0.004	0.016			

[a]Energy shift; set equal for all shells in a fit. [b]Normalized sum of the squared residuals ($NSSR=\Sigma(data_i\text{-}fit_i)^2/\ \Sigma(data_i)^2$). [c,d]Set equal for Zn-Al and Zn-O/Si paths within individual fit. [e]CN of Zn-Si constrained to 1/3 of CN of Zn-Al during fit.

A2.3. Fourier-filtered EXAFS spectra of Zn-HIS-1.6-pH6

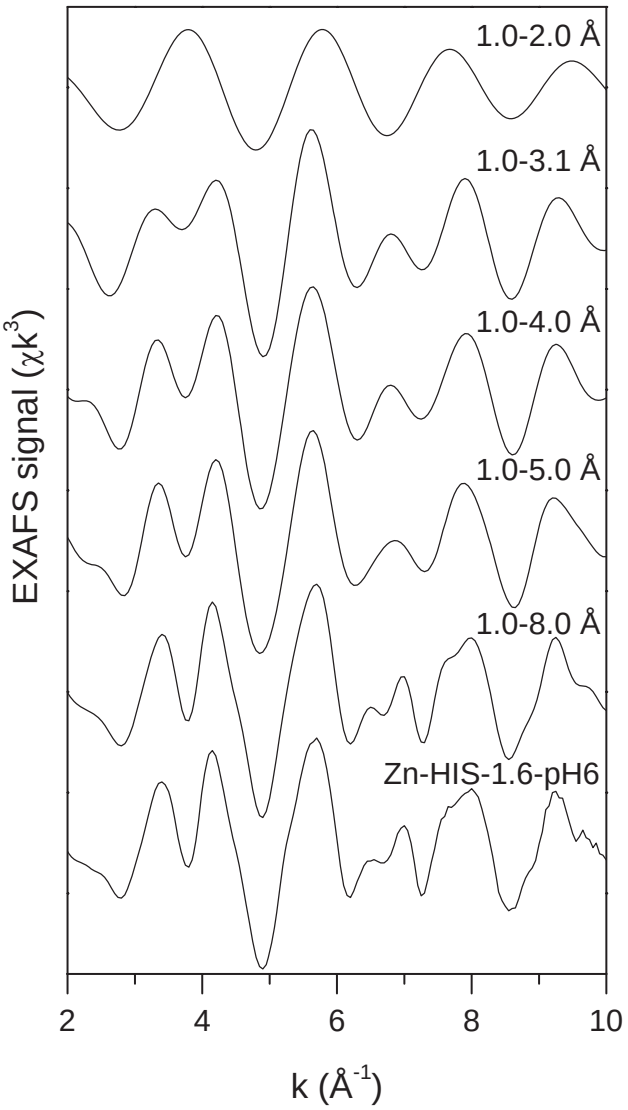

Figure A2.3. EXAFS spectra of Zn-HIS-1.6-pH6 backtransformed over increasing *r*-range and corresponding experimental EXAFS spectrum. The splitting at 3.8 $Å^{-1}$ mainly results from backscattering contributions in the (non phase-shifted) *r*-range 3.1-5 Å, with minor contributions from the *r*-ranges 2-3.1 and 5-8 Å.

A2.4. Clusters used for EXAFS simulations (Fig. 3.4)

Three different model clusters were used for Zn K-edge spectra simulations. The first cluster was constructed by placing one central Zn atom into the dioctahedral vacancy of a gibbsitic cluster ("unfilled" gibbsitic cluster). The second cluster had a similar structure but with all vacancies filled with Zn ("filled" gibbsitic cluster). The third cluster was constructed by substituting one Al atom in the center of a gibbsitic cluster by one Zn atom ("substituted" gibbsitic cluster).

A2.4.1. Unfilled gibbsitic cluster

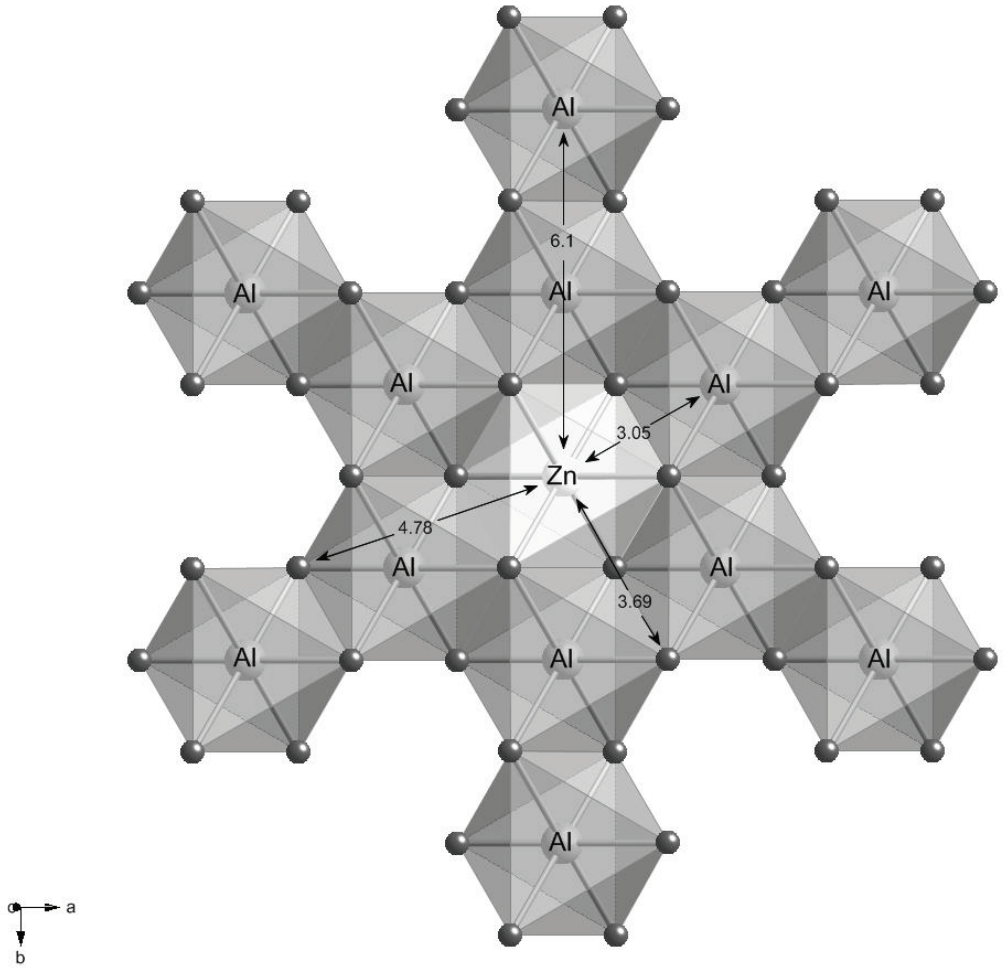

Figure A2.4. Structure of the "unfilled gibbsitic" cluster used for Zn K-edge spectra simulations. The distance between atoms is given in Å. Dark spheres represent O atoms.

A2.4.2. Filled gibbsitic cluster

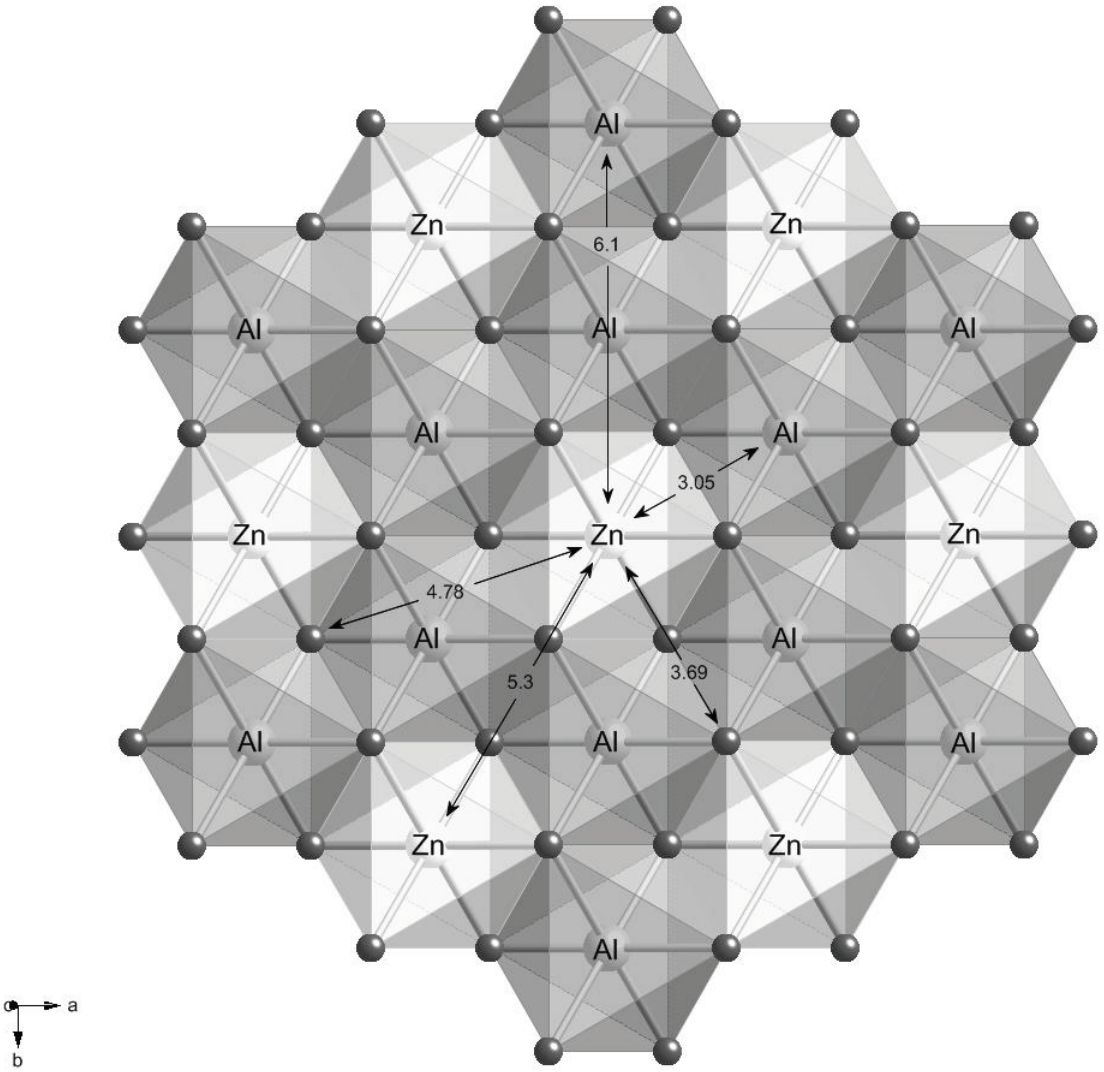

Figure A2.5. Structure of the "filled gibbsitic cluster" used for Zn K-edge spectra simulations. The distance between atoms is given in Å. Dark spheres represent O atoms.

A2.4.3. Substituted gibbsitic cluster

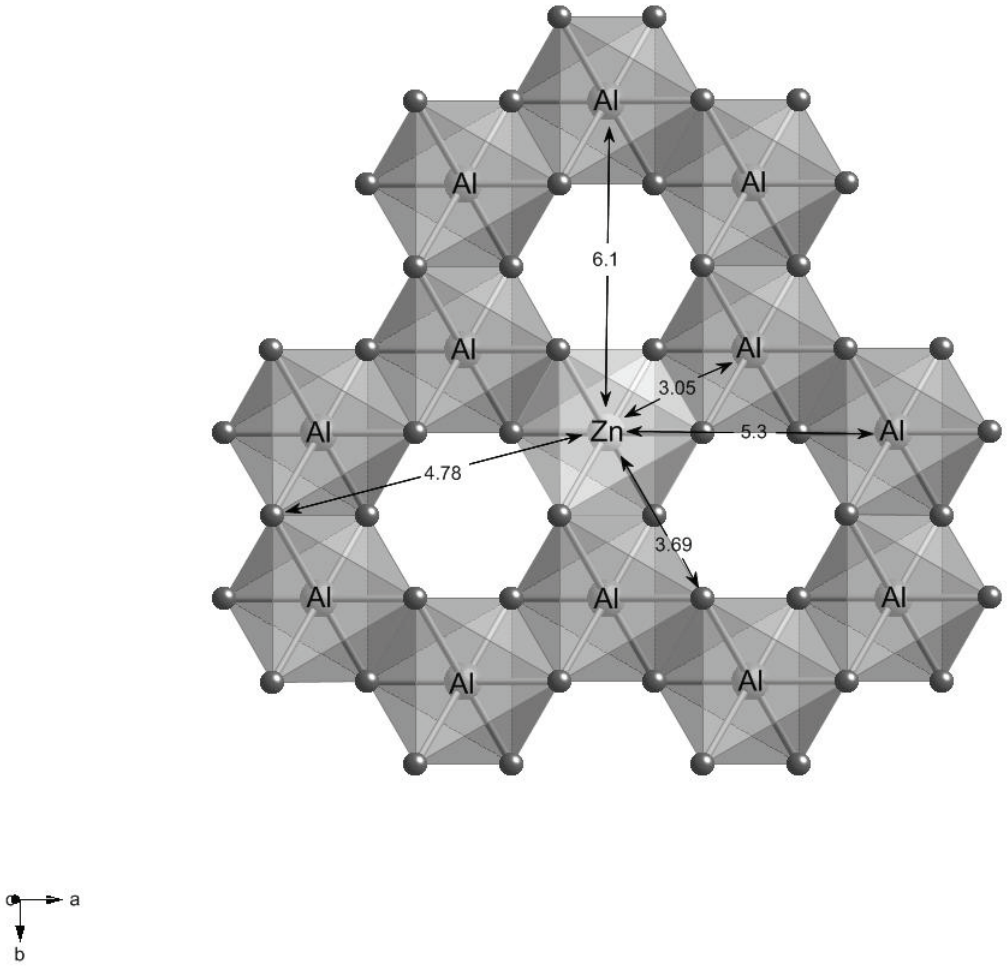

Figure A2.6. Structure of the "substituted gibbsitic cluster" used for Zn K-edge spectra simulations. The distance between atoms is given in Å. Dark spheres represent O atoms.

A2.5. X-ray diffraction patterns of oriented soil clay fractions

A2.5.1. Soils MOM, SAR, CHI

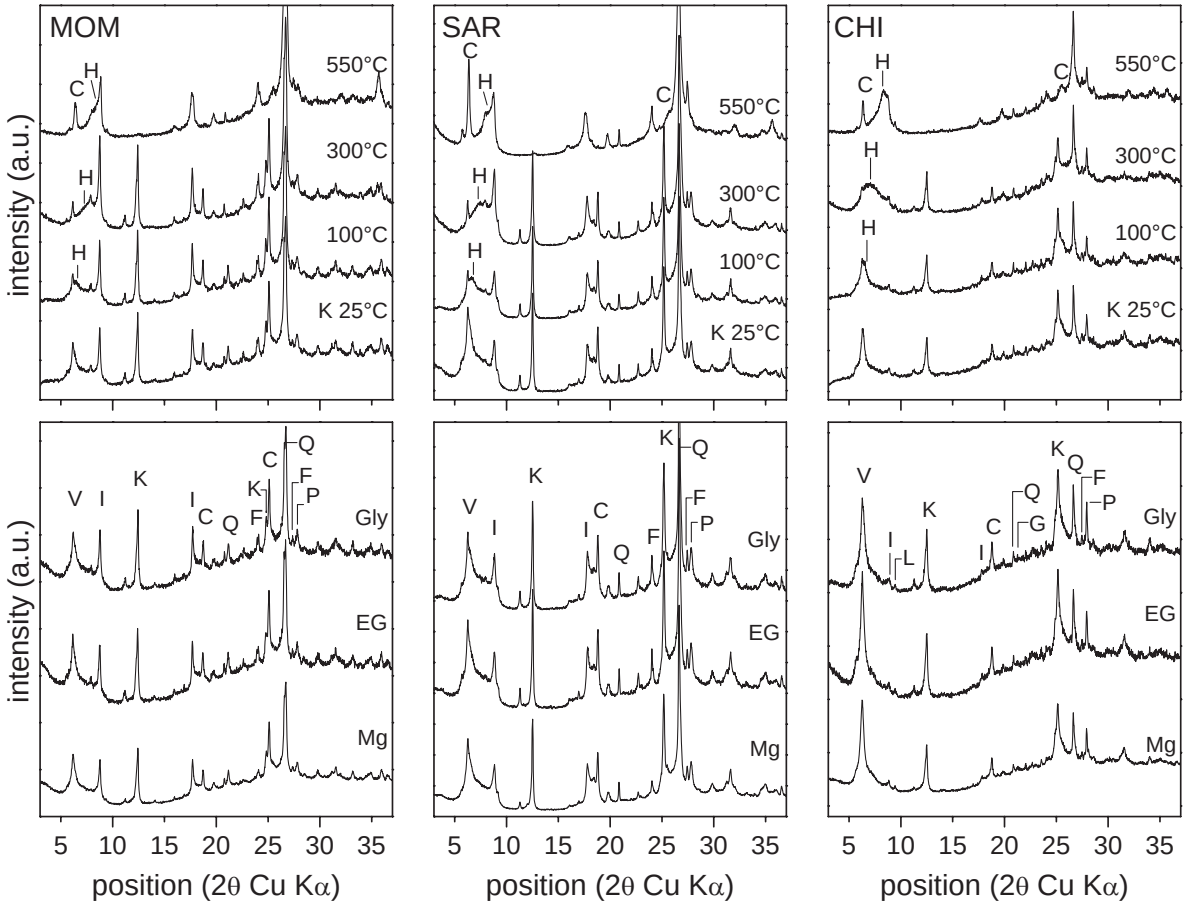

Figure A2.7. XRD patterns collected on oriented preparations of the <2 μm size fraction . Lower panel: Mg-saturated slides in air-dried state (Mg) and after ethylene glycol (EG) and glycerol solvation (Gly). Upper panel: K-saturated slides (K) after ex situ thermal treatment. C: chlorite; F: K-feldspar; H: hydroxy-interlayered vermiculite; I: illite; K: kaolinite; M: mica; L: lithiophorite; P: plagioclase; Q: quartz; V: vermiculite.

A2.5.2. Soil BUN and BIB2

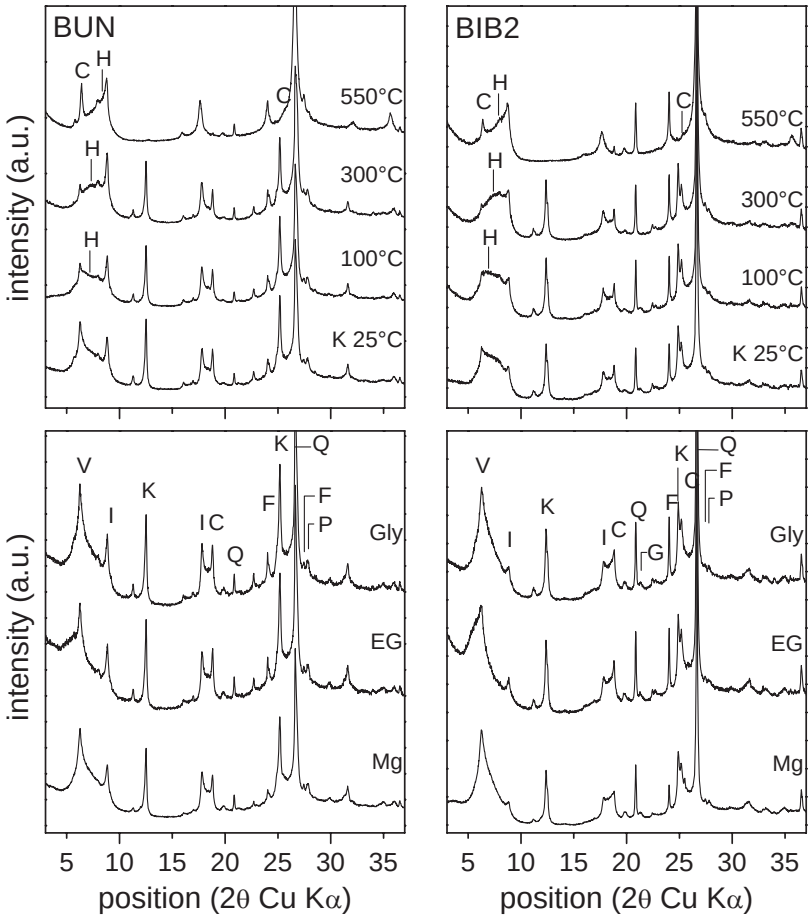

Figure A2.8. XRD patterns collected on oriented preparations of the <2 μm size fraction of soil BUN. Lower panel: Mg-saturated slides in air-dried state (Mg) and after ethylene glycol (EG) and glycerol solvation (Gly). Upper panel: K-saturated slides (K) after ex situ thermal treatment. C: chlorite; F: K-feldspar; H: hydroxyl-interlayered vermiculite; I: illite; K: kaolinite; P: plagioclase; Q: quartz; V: vermiculite.

A2.5.3. Na-citrate treatment

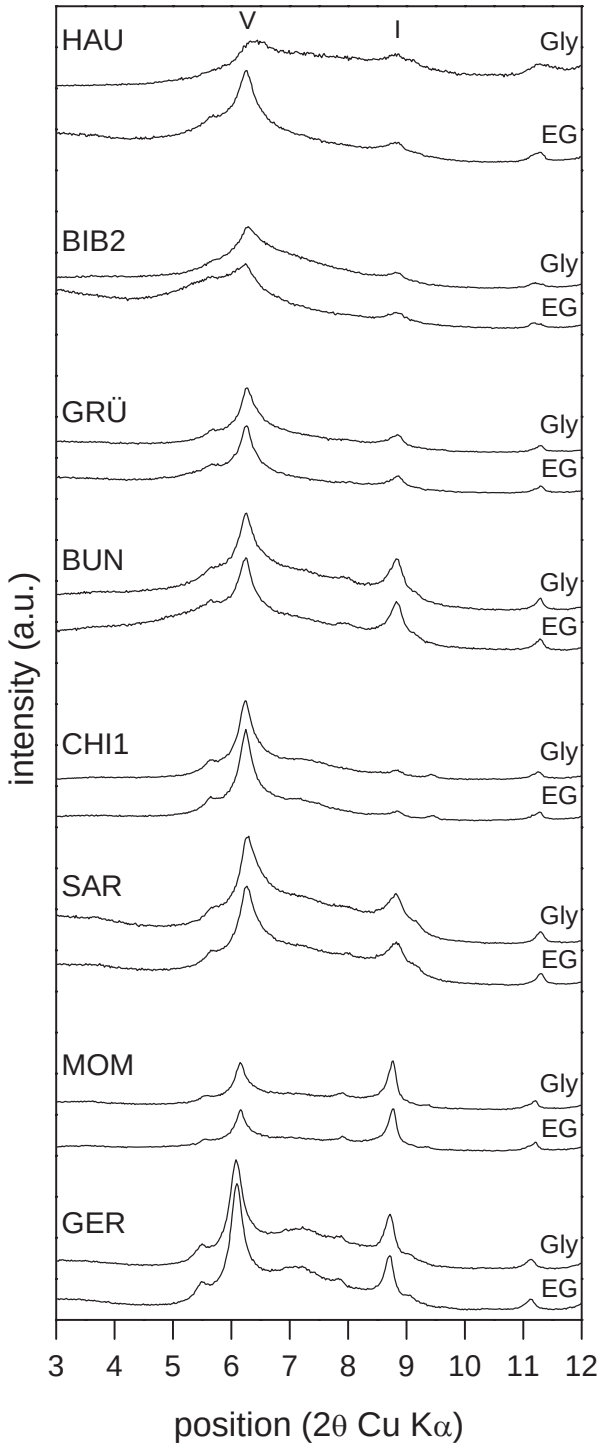

Figure A2.9. XRD patterns collected on oriented mounts of the <2 μm size fraction of all soils after treatment with 0.3 M Na-citrate for the removal of interlayered hydroxy-Al (see sections 3.2.2 and 3.2.8 for details). The 14.2 Å peak of the hydroxy-Al extracted and Mg-saturated clay fractions does not shift to higher d-spacings after ethylene glycol (EG) and glycerol solvation (Gly), suggesting that the HIM in the soils are mainly HIV and not HIS. I: illite; V: vermiculite.

A2.6. µ-XRF mapping of soil GRÜ

Element mapping of a thin section (resin Araldit 2020, thickness 150 µm) of soil GRÜ was carried out at the beamline 10.3.2 at the Advanced Light Source (ALS, Berkeley, USA). Distribution maps were collected at 10 keV (Zn and Fe) and 7.012 keV (Mn and Si) incident photon energies with a resolution of 20x20 µm² or 3x3 µm² and dwell times of 200 or 100 ms/points. The black-white scale for the XRF maps was defined by the minimum pixel value (black) and the 90-percentile pixel value (white).

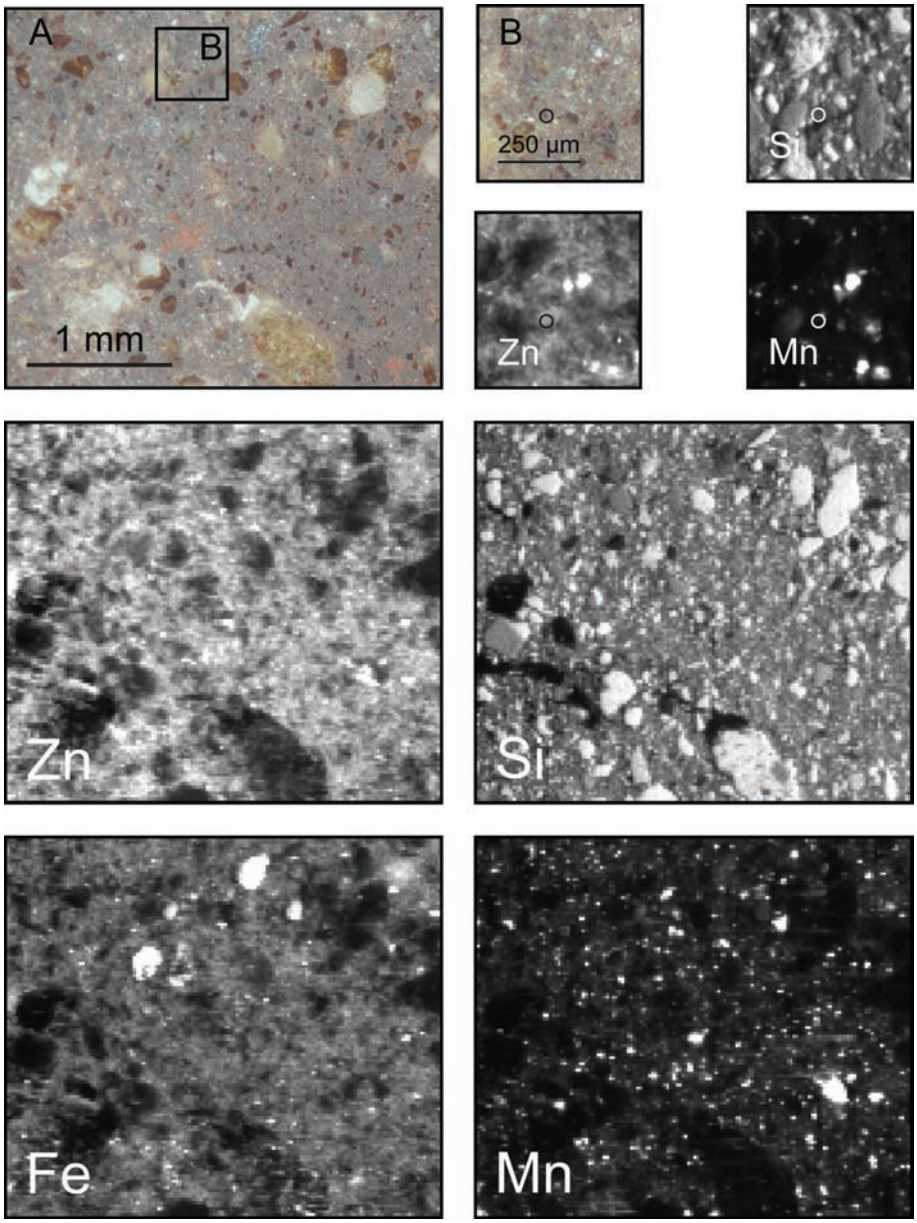

Figure A2.10. Light microscope images of the GRÜ soil thin section and corresponding µ-XRF maps. (A) Coarse map of a 3000×2500 µm² area (20×20 µm² resolution). (B) and (C) Fine maps of 500×500 µm² area (3×3 µm² resolution). Circle on maps B indicates the location where the µ-EXAFS spectrum (GRÜ-µ) was collected.

References

[1] Jacquat, O.; Voegelin, A.; Villard, A.; Marcus, M. A.; Kretzschmar, R., Formation of Zn-rich phyllosilicates, Zn-layered double hydroxide and hydrozincite in contaminated calcareous soils. *Geochim. Cosmochim. Acta* 2008, 72, 5037-5054.

[2] Schlegel, M. L.; Manceau, A.; Charlet, L., EXAFS study of Zn and ZnEDTA sorption at the goethite (alpha-FeOOH)/water interface. *J. Phys. IV* 1997, 7, 823-824.

[3] Sarret, G.; Saumitou-Laprade, P.; Bert, V.; Proux, O.; Hazemann, J. L.; Traverse, A.; Marcus, M. A.; Manceau, A., Forms of zinc accumulated in the hyperaccumulator Arabidopsis halleri. *Plant Physiol.* 2002, 130, 1815-1826.

[4] Manceau, A.; Lanson, B.; Drits, V. A., Structure of heavy metal sorbed birnessite. Part III: Results from powder and polarized extended X-ray absorption fine structure spectroscopy. *Geochim. Cosmochim. Acta* 2002, 66, 2639-2663.

Appendix 3

Supporting information to chapter 4

Contents

A3.1. Selected physical and chemical properties and Zn content of the investigated soils

Table A3.1. Selected physical and chemical properties and Zn content of soil samples containing Zn-HIM (group A).

Soil	Geology / Landuse[a]	pH	TOC	TIC	Texture (g/kg)			ECEC[b]	Tower age[c]	Total Zn	Exch. Zn[d]
		($CaCl_2$)	(g/kg)	(g/kg)	Clay	Silt	Sand	($mmol_c$/kg)	(years)	(mg/kg)	(mg/kg)
HAU	limestone / M	6.9	42	0.2	227	320	453	102	35	276	<1
BIB2	conglomerate / M	6.1	36	1.1	324	344	333	232	74	871	21
GRÜ	glacial till / M	6.0	36	0.3	253	363	384	149	45	852	99
BUN	conglomerate / M	5.5	44	-	215	455	330	121	53	852	139
CHI3	orthogneiss / F	5.9	61	-	76	180	734	154	17	1634	262
LUC3	dolomite / M	5.3	9	-	115	348	537	31	55	647	204
CHI1	orthogneiss / F	4.9	14	-	42	149	809	8	53	971	118
SAR	schist / M	4.6	52	-	105	700	195	79	44	251	35
LEI	glacial till / M	4.6	33	-	142	429	429	59	48	1301	676
MOM	paragneiss / M	4.6	37	-	77	302	621	34	43	1039	286
AVE	orthogneiss / F	4.2	97	-	182	187	630	95	26	345	161
GER	alluvium / M	4.1	27	-	48	348	604	43	40	403	104

[a]F: forest, M: meadow. [b]Effective cation exchange capacity. [c]Indicating age of soil contamination. [d]Exchangeable Zn in 0.1 M $BaCl_2$ at solution-soil-ratio of 30 mL/g.

Table A3.2. Selected physical and chemical properties and Zn content of soil samples containing <30% of total Zn in Zn-precipitates (group B).

Soil	Geology / Landuse[a]	pH	TOC	TIC	Texture (g/kg)			ECEC[b]	Tower age[c]	Total Zn	Exch. Zn[d]
		($CaCl_2$)	(g/kg)	(g/kg)	Clay	Silt	Sand	($mmol_c$/kg)	(years)	(mg/kg)	(mg/kg)
LUC2	dolomite / M	7.3	33	87	88	131	781	181	55	1398	12
GLO	Limestone / M	6.6	49	1.2	451	319	230	411	30	1322	194
ZIE2	conglomerate / M	6.5	95	13	175	426	399	333	42	3351	282
CAR	schist / M	5.9	61	-	172	459	369	198	43	3378	856
LUC1	dolomite / M	5.8	55	-	120	237	643	120	55	4974	1845
DUR	orthogneiss / M	5.7	73	-	77	302	621	152	55	9136	2774
MIC	sandstone / M	5.4	43	-	178	323	500	160	56	5167	2834
MOR	limestone / M	5.1	73	-	142	442	416	241	56	4269	2235

[a]M: meadow. [b]Effective cation exchange capacity. [c]Indicating age of soil contamination. [d]Exchangeable Zn in 0.1 M $BaCl_2$ at solution-soil-ratio of 30 mL/g.

Table A3.2. Selected physical and chemical properties and Zn content of soil samples containing 30 to 60% of total Zn in Zn-precipitates (group C).

Soil	Geology / Landuse[a]	pH ($CaCl_2$)	TOC (g/kg)	TIC (g/kg)	Texture (g/kg)			ECEC[b] ($mmol_c$/kg)	Tower age[c] (years)	Total Zn (mg/kg)	Exch. Zn[d] (mg/kg)
					Clay	Silt	Sand				
ALT	alluvium / M	6.9	95	5.0	142	260	598	327	n.a.	8592	292
WOL	glacial till / W	6.6	63	1.8	360	400	240	362	31	1793	238
ERS1	alluvium / M	6.5	21	3.3	95	238	667	116	n.a.	1649	124
FON	paragneiss / M	6.5	94	3.0	173	111	716	193	53	10450	1103
CHI2	orthogneiss / F	6.4	23	5.2	71	164	765	126	n.a.	3027	399
ETZ	glacial till / M	6.4	37	3.9	212	313	475	199	53	2240	234
BAS	limestone / M	6.4	74	4.4	382	434	184	341	30	12170	2548
BRU	paragneiss / M	6.2	21	1.1	96	204	700	84	72	8827	1296
TRE	conglomerate / F	6.2	26	0.7	396	278	325	281	56	6971	1309
LAUS	limestone / M	6.2	44	6.5	406	348	246	251	39	13780	2838
UDL	sandstone / M	6.2	35	2.3	177	271	552	170	44	4418	848
GOLD	conglomerate / M	6.0	60	1.7	128	469	403	148	52	4988	1283
LAU	conglomerate / M	5.9	44	-	290	417	293	195	56	7538	1650
WAS	orthogneiss / F	5.9	102	-	164	168	668	197	62	3666	680
BIB3	conglomerate / M	5.8	59	-	334	370	296	168	42	6613	1603
FLU	schist / F	5.7	67	-	127	229	644	181	44	8558	1927
MOT	alluvium / M	5.3	33	-	79	313	607	108	n.a.	4749	1803
ALTA	paragneiss / F	5.3	68	-	119	281	600	180	72	4778	1714

[a] F: forest, M: meadow, W: wetland. [b]Effective cation exchange capacity. [c]Indicating age of soil contamination (n.a: no information available) [d]Exchangeable Zn in 0.1 M $BaCl_2$ at solution-soil-ratio of 30 mL/g.

Table A3.4. Selected physical and chemical properties and Zn content of soil samples containing >60% of total Zn in Zn-precipitates (group D).

Soil	Geology / Landuse[a]	pH ($CaCl_2$)	TOC (g/kg)	TIC (g/kg)	Texture (g/kg)			ECEC[b] ($mmol_c$/kg)	Tower[c] age[c] (years)	Total Zn (mg/kg)	Exch. Zn[d] (mg/kg)
					Clay	Silt	Sand				
BON	alluvium / M	7.7	33	21	82	318	600	179	52	1046	4
TAL	limestone / F	7.5	14	8.9	108	244	648	99	39	6055	20
ERS2	paragneiss / M	7.4	26	4.6	107	200	693	93	ND	5342	54
PER	glacial till / M	7.0	27	21	160	444	396	174	44	1923	<1
BAL	glacial till / M	6.9	56	5	287	386	327	364	24	1602	10
BOD	alluvium / M	6.5	59	5.4	116	152	732	135	ND	3300	141
SIS	limestone / F	6.5	59	17	309	288	403	464	39	30090	3051
GÖS	orthogneiss / F	6.3	19	1.8	38	207	755	71	ND	3653	327
BRUN	alluvium / M	5.8	78	-	166	469	365	223	56	19410	3745
AMS	alluvium / M.	5.7	35	-	142	612	246	101	44	5371	1053
DEG	paragneiss / M	5.6	33	-	145	149	706	95	72	6841	1741

[a]F: forest, M: meadow. [b]Effective cation exchange capacity. [c]Indicating age of soil contamination (ND: unknown). [d]Exchangeable Zn in 0.1 M $BaCl_2$ at solution-soil-ratio of 30 mL/g.

A3.2. Linear combination fit results

Table A3.5. Linear combination fits of the EXAFS spectra for soils containing Zn-HIM (group A).

Spectrum	Zn-HIM[a] (%)	Zn-kerolite[b] (%)	Zn-LDH (%)	sorbed ^{IV}Zn[c] (%)	sorbed ^{VI}Zn[d] (%)	Sum (%)	NSSR (%)
HAU	84 (6.9)	15 (60Zn)	———	———	———	99	4.50
BIB2	50 (6.9)	24 (60Zn)	———	———	29 (Go)	103	3.56
GRÜ	52 (6.9)	13 (60Zn)	———	———	36 (Go)	101	2.50
BUN	54 (6.9)	15 (34Zn)	———	———	33 (Go)	102	2.16
CHI3	22 (6.9)	———	32	19 (Po)	36 (Go)	109	3.95
LUC3	46 (8.6)	29 (60Zn)	———	29 (Fh)	———	105	3.49
CHI1	34 (6.9)	48 (60Zn)	———	16 (Ph) + 16 (Bi)	———	114	2.32
SAR	75 (6.9)	24 (60Zn)	———	———	———	99	5.05
LEI	29 (8.6)	13 (60Zn)	———	20 (Fh)	40 (Aq)	102	3.68
MOM	36 (6.9)	———	———	———	22 (Aq) + 43 (Go)	101	3.78
AVE	17 (8.6)	———	———	41 (Fh)	41 (Aq)	99	6.00
GER	29 (6.9)	18 (80Zn)	———	29 (Ph)	31 (Aq)	107	3.87

[a](6.9): Zn-HIS-6.9, (8.6): Zn-HIS-8.6. [b](80Zn): $Zn_{0.8}Mg_{0.2}$-kerolite, (60Zn): $Zn_{0.6}Mg_{0.4}$-kerolite, (34Zn): $Zn_{0.34}Mg_{0.66}$-kerolite. [c](Po): Zn-phosphate, (Fh): Zn-sorbed ferrihydrite, (Ph): Zn-phytate, (Bi): low Zn-birnessite. [d](Aq): aqueous Zn, (Go): Zn-sorbed goethite.

Table A3.6. Linear combination fits of the EXAFS spectra for soils containing <30% of total Zn in Zn-precipitates (group B).

Spectrum	Zn-kerolite[a] (%)	Zn-LDH (%)	sorbed ^{IV}Zn[b] (%)	sorbed ^{VI}Zn[c] (%)	Sum (%)	NSSR (%)
LUC2	29 (80Zn)	———	56 (Cc)	21 (Aq)	106	4.89
GLO	———	20	50 (Fh)	31 (Aq)	101	5.00
ZIE2[d]	———	33	57 (Fh)	23 (Go)	113	3.18
CAR	24 (60Zn)	———	37 (Fh)	40 (Aq)	101	1.75
LUC1	16 (80Zn)	———	68 (Fh)	24 (Aq)	108	1.78
DUR	12 (80Zn)	———	42 (Fh)	43 (Aq)	97	2.49
MIC	12 (80Zn)	———	65 (Fh)	31 (Aq)	107	2.39
MOR	21 (34Zn)	———	46 (Fh)	43 (Go)	111	4.29

[a](80Zn): $Zn_{0.8}Mg_{0.2}$-kerolite, (60Zn): $Zn_{0.6}Mg_{0.4}$-kerolite, (34Zn): $Zn_{0.34}Mg_{0.66}$-kerolite, [b](Cc): Zn-sorbed calcite, (Fh): Zn-sorbed ferrihydrite, [c](Aq): aqueous Zn, (Go): Zn-sorbed goethite. [d]LCF results normalized over 100% give 29 % of Zn-LDH.

Table A3.7. Linear combination fits of the EXAFS spectra for soils containing 30 to 60% of total Zn in Zn-precipitates (group C).

Spectrum	Zn-LDH	Zn-kerolite[a]	sorbed ^{IV}Zn[b]	sorbed ^{VI}Zn[c]	Sum	NSSR
	(%)	(%)	(%)	(%)	(%)	(%)
ALT	34	10 (80Zn)	66 (Fh)	———	110	2.25
WOL	54	———	47 (Fh)	20 (Aq)	121	2.41
ERS1	67	———	18 (Cc)	28 (Aq)	113	3.52
FON	43	23 (60Zn)	45 (Fh)	———	111	1.36
CHI2	46	17 (34Zn)	50 (Fh)	———	113	3.18
ETZ	49	———	43 (Cc)	14 (Aq)	106	2.15
BAS	40	13 (80Zn)	26 (Cc)	22 (Aq)	101	0.81
BRU	41	17 (34Zn)	54 (Fh)	———	112	1.81
TRE	48	16 (80Zn)	42 (Fh)	16 (Aq)	122	2.17
LAUS	36	13 (80Zn)	34 (Cc)	17 (Aq)	100	1.29
UDL	45	20 (34Zn)	49 (Fh)	———	114	3.35
GOLD	43	———	31 (Cc)	29 (Aq)	103	3.32
LAU	56	———	23 (Cc)	28 (Aq)	107	2.67
WAS	46	———	42 (Fh)	26 (Aq)	114	2.56
BIB3	50	12 (80Zn)	24 (Cc)	23 (Aq)	109	1.73
FLU	35	13 (80Zn)	44 (Fh)	22 (Aq)	114	2.37
MOT	47	———	40 (Fh)	30 (Aq)	117	1.12
ALTA	42	———	41 (Fh)	32 (Aq)	115	2.65

[a](80Zn): $Zn_{0.8}Mg_{0.2}$-kerolite, (60Zn): $Zn_{0.6}Mg_{0.4}$-kerolite, (34Zn): $Zn_{0.34}Mg_{0.66}$-kerolite. [b](Fh): Zn-sorbed ferrihydrite, (Cc): Zn-sorbed calcite. [c](Aq): aqueous Zn.

Table A3.8. Linear combination fits of the EXAFS spectra for soils containing >60% of total Zn in Zn-precipitates (group D).

Spectrum	Zn-LDH	Zn-kerolite[a]	hydrozincite	sorbed ^{IV}Zn[b]	sorbed ^{VI}Zn[c]	Sum	NSSR
	(%)	(%)	(%)	(%)	(%)	(%)	(%)
BON	73	———	———	35 (Cc)	———	108	4.72
TAL	———	25 (80Zn)	52	24 (Cc)	———	101	3.58
ERS2	73	———	———	40 (Ph)	———	113	2.90
PER	63	14 (80Zn)	———	———	35 (Go)	112	1.91
BAL	72	———	———	27 (Fh)	13 (Aq)	112	2.27
BOD	75	———	———	42 (Fh)	———	117	2.22
SIS	30	———	51	———	16 (Aq)	97	1.05
GÖS	85	———	———	37 (Fh)	———	122	3.00
BRUN	89	———	———	25 (Cc)	———	114	4.36
AMS	46	23 (80Zn)	———	35 (Fh)	11 (Aq)	115	1.65
DEG	52	16 (34Zn)	———	45 (Fh)	———	113	1.35

[a](80Zn): $Zn_{0.8}Mg_{0.2}$-kerolite, (34Zn): $Zn_{0.34}Mg_{0.66}$-kerolite. [b](Cc): Zn -orbed calcite, (Ph): Zn-phytate, (Fh): Zn-sorbed ferrihydrite. [c](Go): Zn-sorbed goethite, (Aq): aqueous Zn.

A3.3. Distribution plots of soil properties and Zn content

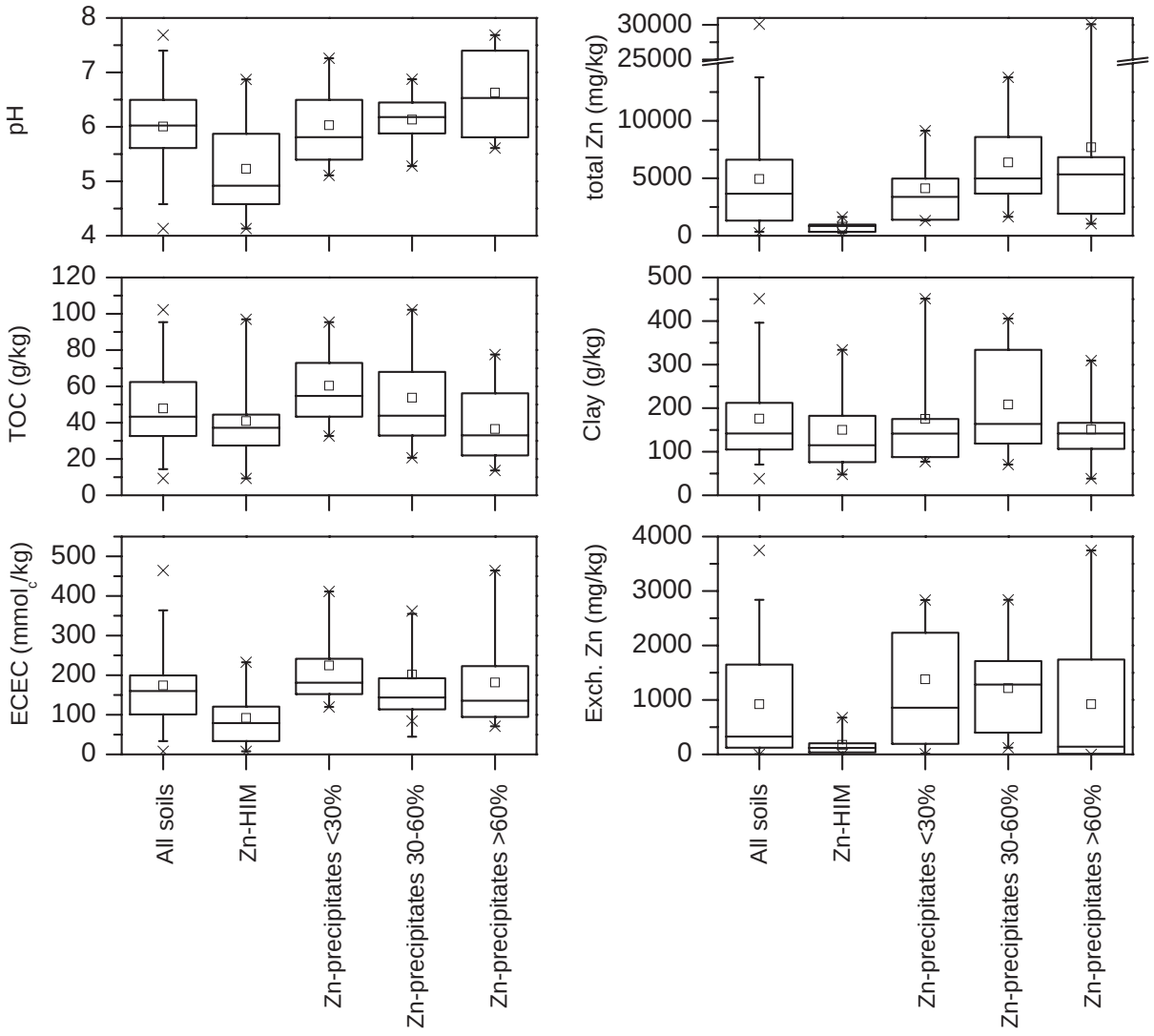

Figure A3.1. Summarizing comparison of the LCF results as a function of soil properties and Zn content. Box cover the 25th to 75th percentile range (including the median (line dividing boxes) and the arithmetic mean (square)), bars cover the 5th to 95th percentile range and crosses indicate the maximum and minimum values.

A3.4. Extracted Zn fractions versus LCF results

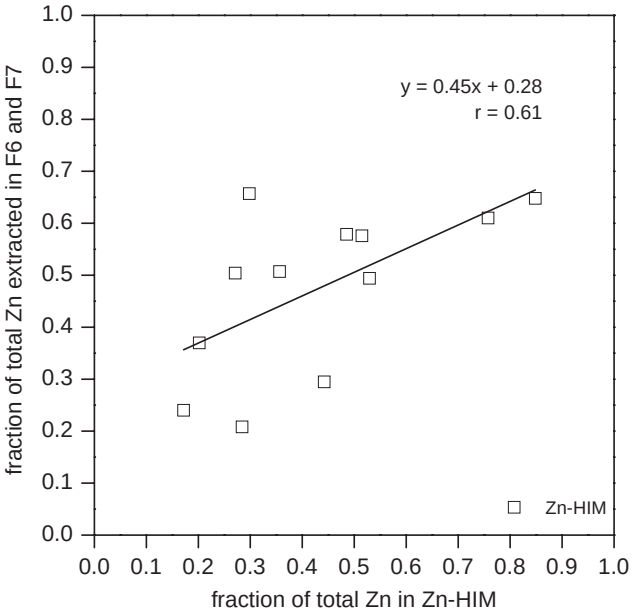

Figure A3.2. Comparison between the fraction of total Zn sequentially extracted in F6 and F7 and the fraction of Zn-HIM determined by LCF.

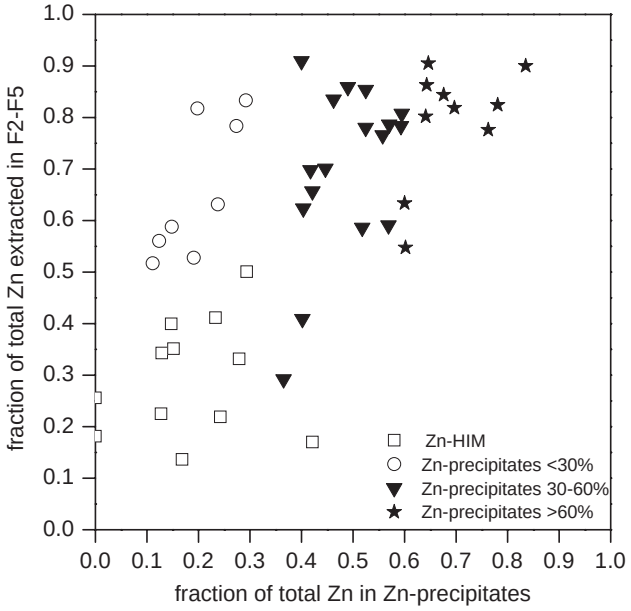

Figure A3.3. Comparison between the fraction of total Zn sequentially extracted in F2-F5 and the fraction of Zn-precipitates determined by LCF.

Appendix 4

Supporting information to chapter 5

Contents

A4.1. Total element contents and molar Zn/element ratios in soil and limestone samples

Table A4.1. Total contents of Mg, Al, Si, S, Ca, Ti, Fe, Zn, and Cd and molar ratios of Zn over Al, Si, S, Ti and Fe.

Soil	Horizon	Total element contents (mg/kg)									Molar element ratios (×100)				
		Mg	Al	Si	S	Ca	Ti	Fe	Zn	Cd	Zn/Al	Zn/Si	Zn/S	Zn/Ti	Zn/Fe
DOR	Oe	823	5367	16000	2173	18360	394	4922	318	2.9	2.4	0.9	7.2	59	5.5
	Ah	3470	60220	182400	356	8456	3939	45210	783	11.2	0.5	0.2	11	15	1.5
	Bw	4560	69380	186000	272	17550	4158	50790	734	15.1	0.4	0.2	132	13	1.2
	BwC	4300	70440	162500	162	45690	4201	55440	476	13.6	0.3	0.1	144	8.3	0.7
	R	370	297	748	6	386600	5	413	207	17.3	29	12	1720	3040	43
GUR	Aca	1450	19450	71970	2050	31400	2117	46370	864	15.4	1.8	0.5	21	30	1.6
	R	1060	770	2421	254	389500	37	1992	43	1.4	2.3	0.8	8.3	86	1.8
LIE	Aca	2350	26560	92840	1166	99500	2526	40550	237	2.4	0.4	0.1	10	6.9	0.5
	R	5710	13200	46580	220	299600	1109	10660	92	1.0	0.3	0.1	21	6.1	0.7

A4.2. XRD patterns of soil clay fractions after Na-citrate treatment

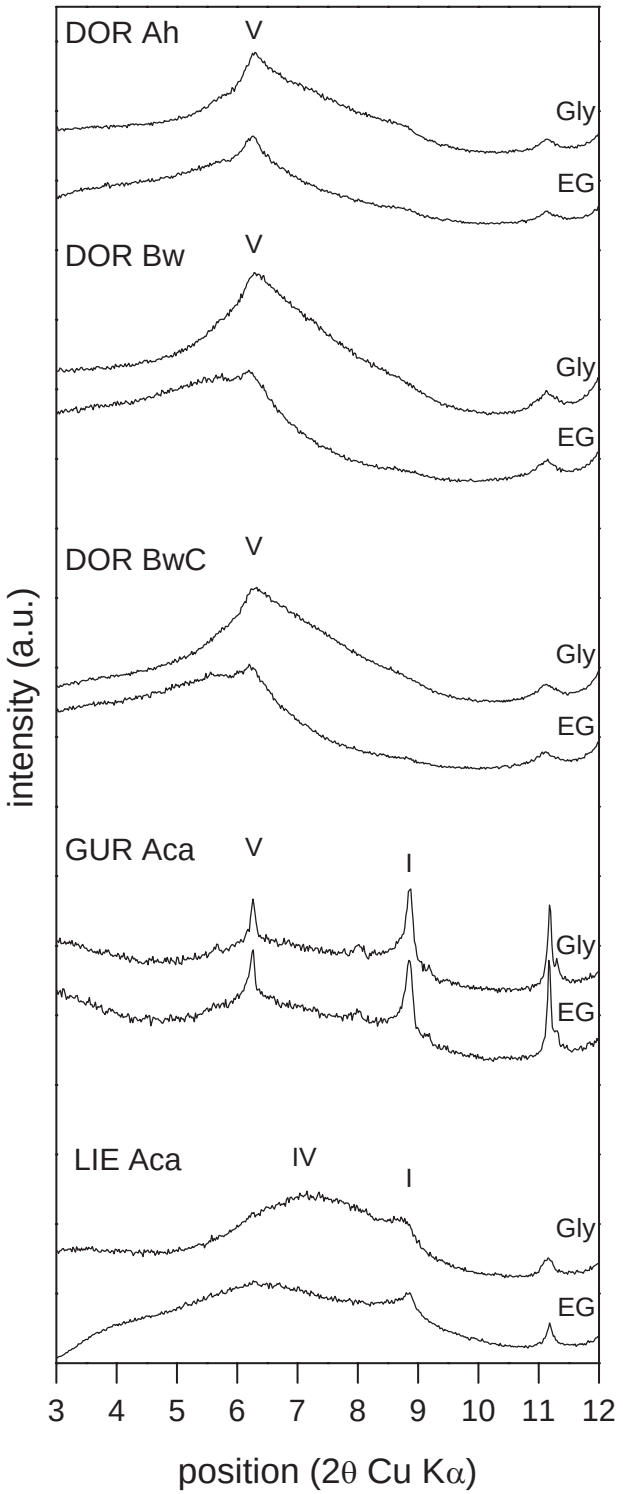

Figure A4.1. XRD patterns collected on oriented mounts of the <2 μm size fraction of all soils after treatment with 0.3 M Na-citrate for the removal of hydroxy-Al polymers from the interlayers (see sections 5.2.3 and 5.2.9 for details). The 14.2 Å peak of the hydroxy-Al extracted and Mg-saturated clay fractions does not shift to higher d spacings after ethylene glycol (EG) and glycerol salvation (Gly), suggesting that HIM in the soils are mainly HIV and not HIS. I: illite; V: vermiculite, IV: illite-vermiculite.

A4.3. Clay mineralogy of the soil horizons DOR Ah and DOR Bw

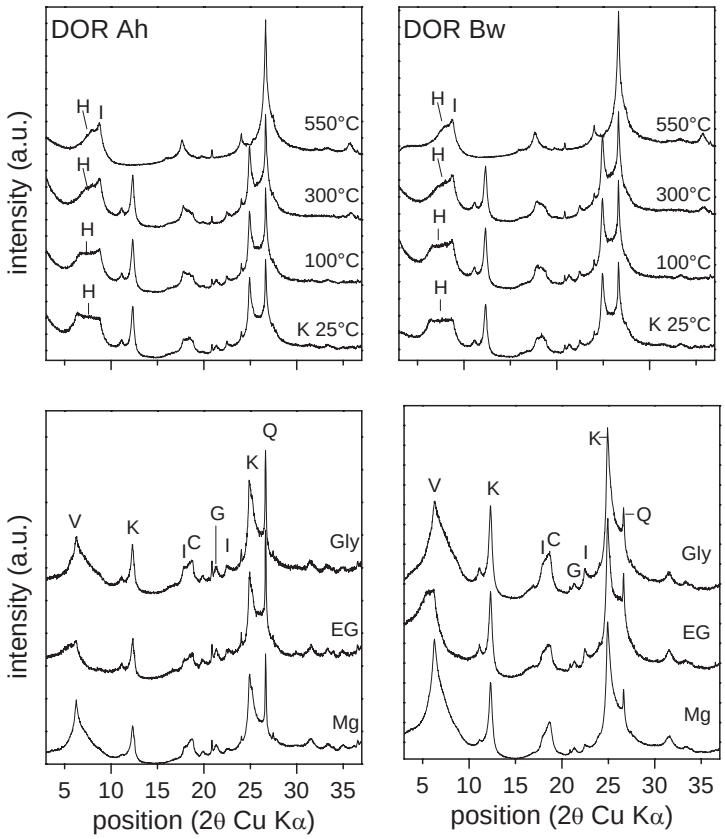

Figure A4.2. XRD patterns collected on oriented mounts of the <2 μm size fraction of the soil samples DOR Ah and DOR Bw. Lower panel: Mg-saturated slides in air-dried state (Mg) and after ethylene glycol (EG) and glycerol solvation (Gly). Upper panel: K-saturated slides (K) after ex situ thermal treatment. F: K-feldspar; H: hydroxyinterlayered vermiculite; I: illite; K: kaolinite; M: mica; P: plagioclase; Q: quartz; V: vermiculite.

Appendix 5

Contents

A5.1. Locations of soil samples

Table A5.1. Locations of soil samples.

Soil	Location	Canton	Swiss coordinates	Altitute (m)	Tower number	Compagny	Year of construction
ALT	Altdorf	UR	691300/190500	450	NA	SBB	NA
ALTA	Altanca	TI	694600/153100	1400	9047	ATEL	1932
AMS	Amsteg	UR	693600/181300	500	41	CKW/SBB	1960
AVE	Avegno	TI	701500/117000	300	NA	SES	1978
BAL	Zürich/Bal	ZU	688000/247100	638	8	EWZ	1978
BAS	Bassecourt	JU	586500/243200	460	1	FMB	1974
BIB2	Ziegelbrücke/Biberlichopf	SG	724300/221700	600	32	NOK	1930
BIB3	Ziegelbrücke/Biberlichopf	SG	724300/221700	600	105	NOK	1962
BOD	Bodio	TI	712000/138700	350	NA	SBB	NA
BON	Bonaduz	GR	750200/187600	600	NA	SBB	1952
BRU	Brugnasco	TI	692800/153200	1400	9052	ATEL	1932
BRUN	Brunnen	SZ	690100/206900	440	9476	ATEL	1948
BUN	Willisau/Bunegg	LU	642800/217400	660	172	BKW	1951
CAR	Carrera	GR	742200/183600	900	72	NOK	1961
CHI1	Chironico	TI	708300/142200	780	128	ATEL	1951
CHI2	Chironico	TI	708400/142300	780	12	AET	NA
CHI3	Chironico	TI	708400/142300	780	62	SBB	1968/1987
DEG	Deggio	TI	697600/152300	200	4038	ATEL	1932
DUR	Medel/Durschei	GR	707800/166400	1400	9271	ATEL	1949
ERS1	Erstfeld/Niderhofen	UR	681700/186700	460	40	SBB/EWA	NA
ERS2	Erstfeld	UR	693400/185100	480	37	SBB	NA
ETZ	Etznerlen/Sal	LU	654100/217100	740	209	BKW	1951
FLU	Flüelen	UR	690900/195400	660	87	SBB	1960
FON	Sementina/Fontanella	TI	718700/115800	500	22	ATEL	1951
GER	Gerra	TI	713200/114500	200	19	Versazca SA	1964
GLO	Glovelier	JU	582600/244500	520	15	FMB	1974
GOLD	Goldau	SZ	683330/210700	740	9503	ATEL	1948
GÖS	Göschenen	UR	688300/170800	980	10	EWA/CKW	NA
GRÜ	Gossau/Grüt	ZU	701100/241300	540	404	NOK	1959
HAU	Haut-Geneveys	NE	557400/21400	870	53	ENSA	1969
LAU	Lauerz	SZ	687400/208700	650	9488	ATEL	1948
LAUS	Lausen	BL	624800/257400	390	453	EGL	1965
LEI	Leidenberg	AG	635500/234700	480	8	NOK	1956

NA: not available.

Table A5.1. continued.

Soil	Location	Canton	Swiss coordinates	Altitute (m)	Tower number	Compagny	Year of construction
LUC1	Lucmagno Passo	TI	704200/157800	1900	9244	ATEL	1949
LUC2	Lucmagno Passo	TI	704300/157400	1900	9243	ATEL	1949
LUC3	Lucmagno Passo	TI	704400/156900	1870	9241	ATEL	1949
MIC	Udligenswil/Michelskreuz	LU	673700/270100	670	9540	ATEL	1948
MOM	Disentis/Mompe Tujetsch	GR	706700/171500	1300	19	KVR	1961
MOR	Morschach	UR	690600/204600	770	9469	ATEL	1948
MOT	Motto	TI	717800/142800	440	35	BLENIO SA	NA
PER	Perlen	LU	670500/218800	440	192	CKW	1960
SAR	Sargans-Mels	SG	749000/212200	840	96	NOK	1960
SIS	Sissach	BL	628200/259300	620	465	EGL	1965
TAL	Bubendorf/Talhaus	BL	623600/256500	390	446	EGL	1965
TRE	Arth/Treichi	ZG	680200/214100	420	9519	ATEL	1948
UDL	Udligenswil	LU	674900/218100	600	177	CKW	1960
WAS	Wassen/Oberwiler	UR	689000/174100	1000	9139	ATEL	1932
WOL	Wolfhausen/Rüti	ZU	704000/234900	500	533	NOK	1973
ZIE2	Ziegelbrücke/Niederurnen	SG	724500/221300	420	186	NOK	1962

NA: not available.